

AD _____

Award Number: U01FVU08EEJNEFEFFIJ

TITLE: O~^\ãáb\ÁN&æ^\"bÁà~ãÁR↔´ã~ËO~↑*|\æäÁÚ~↑~&ãá*â]Á~àÁ
R↔´ã~ää↑á&æÁ↔^ÃÑ~^æ

PRINCIPAL INVESTIGATOR: Þ]á^ÁPÈÁÞ~æäæãÊÁŞåÈÈÈ

CONTRACTING ORGANIZATION: U^↔{æǻ↔\]Ã~àĀS~\ăæĀĒ↑æ
 ĀĀĀĀĀĀĀĀĀĀĀĀĀĀĀĀĀĀĀĀĀS~\ăæĀĒ↑æĒÅØSĀĤIJI I IJĀ

REPORT DATE: 03/15/2023

TYPE OF REPORT: $\hat{O} \leftrightarrow \hat{a} \rightarrow$

PREPARED FOR: U.S. Army Medical Research and Materiel Command
Fort Detrick, Maryland 21702-5012

DISTRIBUTION STATEMENT:

Approved for public release; distribution unlimited

The views, opinions and/or findings contained in this report are those of the author(s) and should not be construed as an official Department of the Army position, policy or decision unless so designated by other documentation.

REPORT DOCUMENTATION PAGE				Form Approved OMB No. 0704-0188	
Public reporting burden for this collection of information is estimated to average 1 hour per response, including the time for reviewing instructions, searching existing data sources, gathering and maintaining the data needed, and completing and reviewing this collection of information. Send comments regarding this burden estimate or any other aspect of this collection of information, including suggestions for reducing this burden to Department of Defense, Washington Headquarters Services, Directorate for Information Operations and Reports (0704-0188), 1215 Jefferson Davis Highway, Suite 1204, Arlington, VA 22202-4302. Respondents should be aware that notwithstanding any other provision of law, no person shall be subject to any penalty for failing to comply with a collection of information if it does not display a currently valid OMB control number. PLEASE DO NOT RETURN YOUR FORM TO THE ABOVE ADDRESS.					
1. REPORT DATE (DD-MM-YYYY) 01-01-2011		2. REPORT TYPE Final		3. DATES COVERED (From - To) 1 JAN 2006 - 31 DEC 2010	
4. TITLE AND SUBTITLE Contrast Agents for Micro-Computed Tomography of Microdamage in Bone				5a. CONTRACT NUMBER	
				5b. GRANT NUMBER W81XWH-06-1-0196	
				5c. PROGRAM ELEMENT NUMBER	
6. AUTHOR(S) Ryan K. Roeder, Ph.D. E-Mail: rroeder@nd.edu				5d. PROJECT NUMBER	
				5e. TASK NUMBER	
				5f. WORK UNIT NUMBER	
7. PERFORMING ORGANIZATION NAME(S) AND ADDRESS(ES) University of Notre Dame Notre Dame, IN 46556				8. PERFORMING ORGANIZATION REPORT NUMBER	
9. SPONSORING / MONITORING AGENCY NAME(S) AND ADDRESS(ES) U.S. Army Medical Research and Materiel Command Fort Detrick, Maryland 21702-5012				10. SPONSOR/MONITOR'S ACRONYM(S)	
				11. SPONSOR/MONITOR'S REPORT NUMBER(S)	
12. DISTRIBUTION / AVAILABILITY STATEMENT Approved for Public Release; Distribution Unlimited					
13. SUPPLEMENTARY NOTES					
14. ABSTRACT Novel methods were investigated for detecting damaged bone tissue using contrast-enhanced micro-computed tomography (micro-CT). The presence, spatial location, and accumulation of fatigue microdamage in machined human cortical bone specimens and whole rat femora was non-destructively detected in vitro after labeling by barium sulfate precipitation, and was validated by conventional histology. Micro-CT enabled non-destructive imaging and provided 3-D spatial information, which are not possible using conventional histology. These new methods are immediately useful for in vitro scientific studies investigating the etiology of fatigue and fragility fractures in bone. Functionalized Au NPs were demonstrated to enable targeted delivery and labeled microdamage was detected using synchrotron radiation computed tomography with absorption edge subtraction. Therefore, the results of this study suggest that the ambitious goal of non-invasive (in vivo) imaging of microdamage in bone could be feasible with improvements in commercial scientific and clinical CT instruments.					
15. SUBJECT TERMS Bone; Microdamage; Computed Tomography, Contrast Agents; Barium Sulfate; Gold; Nanoparticles					
16. SECURITY CLASSIFICATION OF:			17. LIMITATION OF ABSTRACT UU	18. NUMBER OF PAGES 133	19a. NAME OF RESPONSIBLE PERSON USAMRMC
a. REPORT U	b. ABSTRACT U	c. THIS PAGE U			19b. TELEPHONE NUMBER (include area code)

Table of Contents

	<u>Page</u>
Introduction.....	4
Body.....	4
Key Research Accomplishments.....	11
Reportable Outcomes.....	12
Conclusion.....	16
References.....	16
Appendices.....	17

INTRODUCTION

Accumulation of microdamage in bone tissue can lead to an increased risk of fracture, including stress fractures in active individuals and fragility fractures in the elderly [1,2]. Current methods for detecting microdamage are inherently invasive, destructive, tedious and two-dimensional [3]. These limitations inhibit evaluating the effects of microdamage on whole bone strength and prohibit detecting microdamage *in vivo*. Therefore, we have investigated novel methods for detecting microdamage in bone using micro-computed tomography (micro-CT) and contrast agents with higher X-ray attenuation than bone. The presence, spatial location, and accumulation of microdamage in cortical and trabecular bone specimens was nondestructively detected using micro-CT after labeling tissue specimens with barium sulfate (BaSO_4) [4-6]. However, specimens were stained *in vitro* via a precipitation reaction, which was non-specific to damage and not biocompatible. Therefore, we have also investigated the synthesis and functionalization of gold and BaSO_4 nanoparticles for targeted contrast agents [7,8]. The objectives of the project were to: 1) develop damage-specific contrast agents, with greater X-ray attenuation than bone, for micro-computed tomography (micro-CT) of microdamage; 2) evaluate the X-ray attenuation, deliverability and specificity of contrast agent formulations; and, 3) quantify the effects of the contrast agent on micro-CT images in damaged and undamaged bone, and correlate the measurements to traditional measures of microdamage. ***This final report comprehensively summarizes research activities and results for the entire project period (Jan. 2006 to Jan. 2011). Whenever possible, results for each task/aim in the approved Statement of Work refer to journal manuscripts, which are included as Appendices.***

BODY

Task 1: Develop damage-specific contrast agents, with greater X-ray attenuation than bone, for micro-computed tomography (micro-CT) of microdamage (Months 1-24).

Aim 1.1 Synthesize barium sulfate (BaSO_4) nanoparticles with a mean size less than 10 nm (Months 1-6).

Completed. BaSO_4 nanoparticles were synthesized using a nanoemulsion technique (**Appendix 1**, Meagher *et al.*, 2011). Additionally, in order to circumvent challenges that were encountered in stabilizing and functionalizing BaSO_4 nanoparticles (described below), gold nanoparticles (Au NPs) were also prepared using the citrate reduction method (**Appendix 2**, Zhang *et al.*, 2010).

Aim 1.2 Stabilize and functionalize colloidal dispersions of BaSO_4 nanoparticles with (macro)molecules containing multiple carboxy, hydroxyl and/or phosphonate ligands able to simultaneously bind with both the nanoparticle and calcium ions exposed on surfaces created by microdamage in bone (Months 1-24).

Completed. BaSO_4 nanoparticles were stabilized by encapsulation with cross-linked dextran to enable aqueous dispersion (**Appendix 1**, Meagher *et al.*, 2011). Due to greater than anticipated challenges in the preparation of dextran-encapsulated BaSO_4 and resultant delays, functionalization was not completed within the project period, but is ongoing within our lab. However, Au NPs were readily functionalized with either carboxylate, phosphonate, or bisphosphonate ligands for targeted labeling of calcium in damaged bone tissue (**Appendix 2**, Zhang *et al.*, 2010; **Appendix 3**, Ross and Roeder, 2011).

Aim 1.3 Synthesize iodinated molecules containing multiple phosphonate ligands with a high binding affinity for calcium ions exposed on surfaces created by microdamage in bone (Months 1-24).

Obviated. Soon after this proposal was submitted, another research group in Ireland reported the preparation of iodinated molecules functionalized with carboxylate ligands which were only able to be detected using micro-CT when precipitated in powder form rather than when in a deliverable molecular form [9,10]. Moreover, success with bisphosphonate functionalized Au NPs (Aim 1.2) further obviated the need for this aim.

Task 2: Evaluate the X-ray attenuation, deliverability and specificity of contrast agent formulations (Months 6-36).

Aim 2.1 Measure the particle size and/or molecular weight of the contrast agent (Months 1-12).

Completed. As-synthesized and dextran-encapsulated BaSO₄ nanoparticles exhibited a spherical morphology and narrow size distributions with particle diameters less than 10 and 40 nm, respectively (**Appendix 1**, Meagher *et al.*, 2011). Functionalized Au NPs were spherical and relatively monodispersed with a mean (\pm standard deviation) particle diameter of 10-15 (\pm 1-2) nm and aspect ratio of \sim 1 (\pm 0.1) (**Appendix 2**, Zhang *et al.*, 2010; **Appendix 3**, Ross and Roeder, 2011). There was no apparent change in particle size or morphology between as-synthesized and functionalized Au NPs.

Aim 2.2 Measure the mass attenuation and partial volume effect of known concentrations of the contrast agents on micro-CT images (Months 7-18).

Completed. Dextran-encapsulated BaSO₄ nanoparticles exhibited a nearly three-fold increase in X-ray attenuation compared to a commercial, microscale BaSO₄ contrast agent (**Appendix 1**, Meagher *et al.*, 2011). This effect was most likely due to enhanced X-ray scattering with increased specific surface area and is being further investigated with Au NPs of varying size.

Micro-CT detection limits were investigated using an imaging phantom comprising an array of gold islands deposited into acid-etched aluminum substrates using photolithography. The array consisted of square islands ranging in size from 1 to 100 μ m, and deposited to thicknesses of 1 μ m, 500 nm and 100 nm (**Fig. 1**). Aluminum is well-known to exhibit similar X-ray attenuation to cortical bone tissue and is therefore used for commercial/clinical X-ray phantoms. Specimen edge effects were mitigated by "sandwiching" the gold islands against another polished aluminum surface, such that edge detection was aluminum-gold-aluminum without the presence of air. A commercial, polychromatic benchtop micro-CT (Scanco μ CT-80, 10 μ m resolution) was able to reliably detect islands as small as 20 x 20 x 1 μ m and 30 x 30 x 0.5 μ m, but was not able to detect any islands at 100 nm thickness (**Fig. 2**). A user proposal was awarded for beam time using the Advanced Photon Source (APS) at the Argonne National Laboratory (ANL) in order to investigate the same imaging phantom using monochromatic synchrotron radiation computed tomography (SRCT). Gold island phantoms were imaged by SRCT at a resolution of 2.5 μ m and an energy level just above the L_{III} edge of gold at 12.018 keV. The low energy of the L_{III} edge required a small sample thickness; therefore, phantoms were sectioned to a 1 x 1 mm cross-sectional area. In contrast to the polychromatic micro-CT, monochromatic SRCT was able to detect gold islands of all sizes (**Fig. 3**). The brightness of gold islands was proportional to the island thickness.

The minimum mass fraction for micro-CT imaging of a contrast agent in a given matrix was calculated theoretically by relating the fractional abundance of the contrast agent added to the change in the mass attenuation coefficient [11]. The minimum mass fraction of gold in bone tissue at a photon energy of 70 keV was calculated to be 0.023, which corresponds to a volume fraction of 0.002. Therefore, \sim 22 Au NPs, 20 nm in diameter, would be required for detection in a 1 μ m³ volume of bone matrix. Backscattered SEM micrographs of glutamic acid functionalized Au NPs bound to damaged bone surfaces (**Appendix 2**, Zhang *et al.*, 2010) showed a surface coverage near this theoretical detection limit.

The results to date suggest that the necessarily small size and low concentration of Au NPs labeling damaged bone is at or below the detection limits of current, commercially available micro-CT scanners. However, the detection of a Au NP contrast agent in bone tissue may be feasible with reasonable improvements in commercially available micro-CT systems. SRCT enabled a 20-fold decrease in the volumetric size of gold islands able to be detected compared to polychromatic micro-CT. Thus, this detection difference was only partially attributable to the 4-fold difference in the resolution of the imaging systems. The improved detection limit of SRCT demonstrated that X-ray computed tomography was able to image small quantities of gold by tailoring monochromatic radiation to take advantage of absorption-edge effects associated with the contrast agent. Thus, beam filtration to tailor photon energies and improved detector systems are improvements that can be readily implemented in future commercial micro-CT systems. Moreover, SRCT provided improved resolution and tailored, monochromatic radiation, which also enabled the detection of fatigue microcracks labeled with functionalized Au NPs, as described below under Aim 3.1.

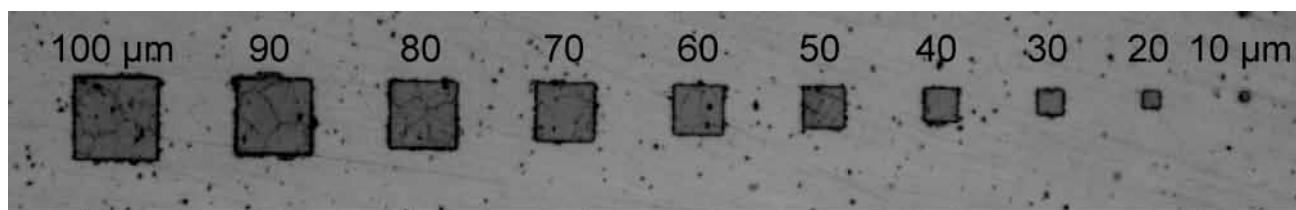


Fig. 1. Optical micrograph showing a single row from an array of gold islands on the imaging phantom. The area of each gold island decreased from the left, 100 x 100 μm, to the right, 10 x 10 μm.

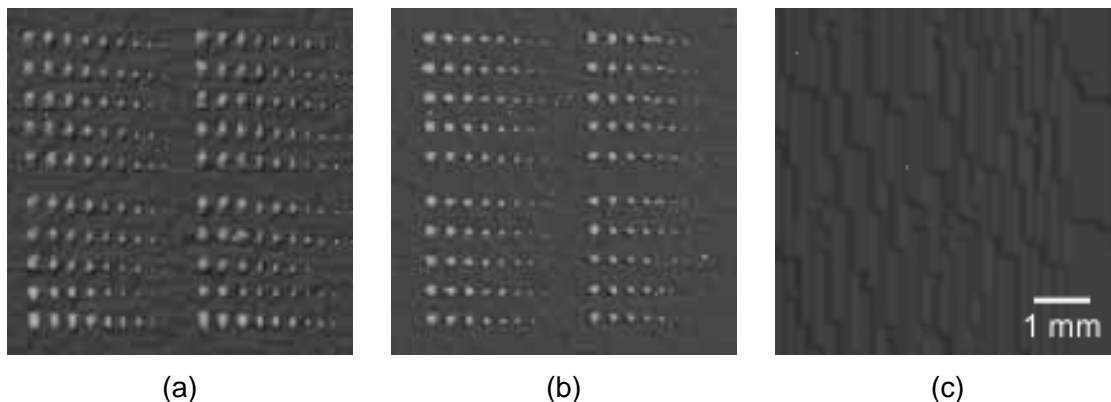


Fig. 2. Reconstructed polychromatic micro-CT images at 10 μm resolution for gold islands deposited to a thickness of (a) 1 μm, (b) 500 nm and (c) 100 nm.

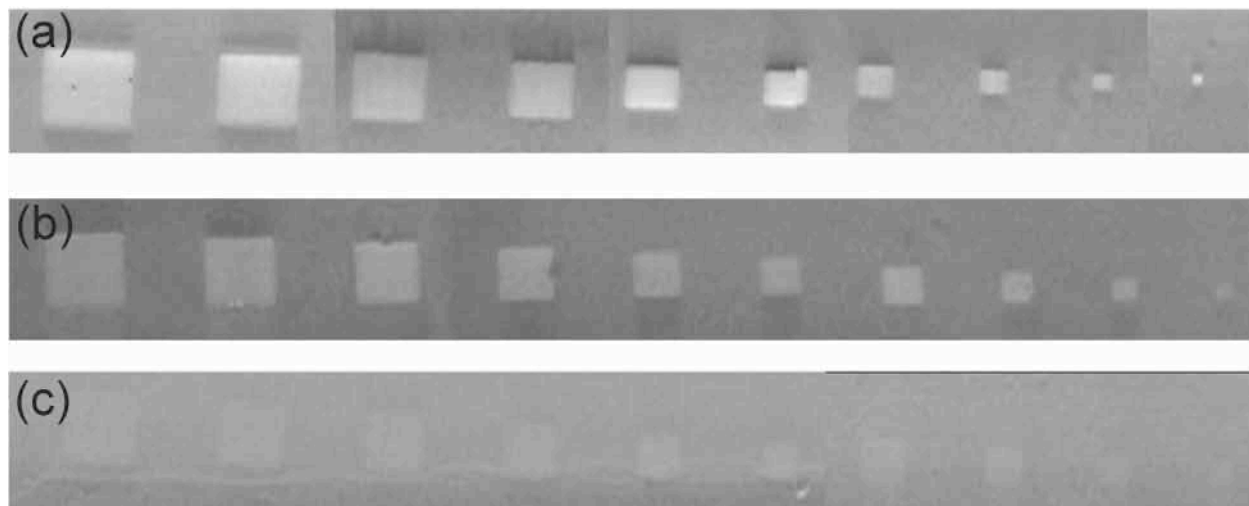


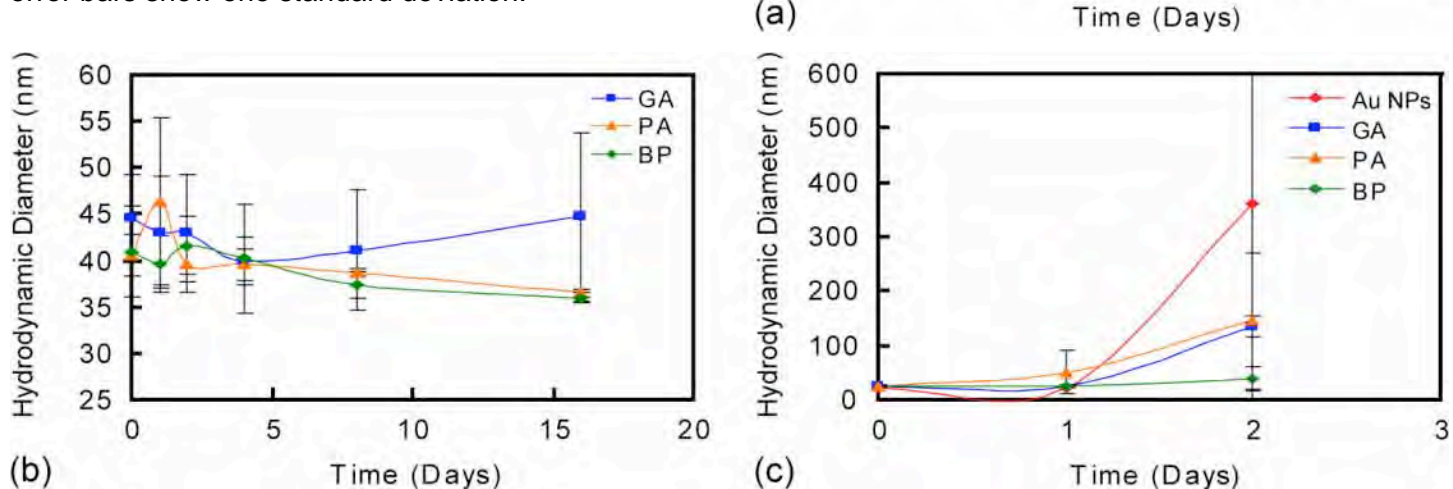
Fig. 3. Reconstructed island cross-sections imaged by SRCT showing, (a) 1000 nm, (b) 500 nm, and (c) 100 nm thick gold islands on an aluminum substrate. The islands are shown in decreasing size from left to right, 100 x 100 μm to 10 x 10 μm.

Aim 2.3 Determine the stability of the contrast agent in phosphate buffered saline, simulated body fluid (SBF) and/or fetal bovine serum (FBS) (Months 13-24).

Completed. The stability of functionalized Au NPs in DI water, phosphate buffered saline (PBS) and 10% fetal bovine serum (FBS) was investigated as a function of time under ambient conditions by measuring the hydrodynamic particle diameter using dynamic light scattering. As-synthesized and functionalized Au NPs were stable in DI water as indicated by a constant mean hydrodynamic particle diameter over 16 days (**Fig. 4a**). In PBS, as-synthesized Au NPs coagulated immediately, but functionalized Au NPs were stable over 16 days (**Fig. 4b**). The presence of a highly ionic media, such as PBS, disrupted the electrostatic stabilization of as-synthesized Au NPs. However, surface functionalization imparted steric stabilization, which was resilient to

ionic media. Long-term stability measurements in FBS were prohibited by the instability of the serum media itself after 2 days, which was verified in serum alone. However, as-synthesized and functionalized Au NPs were stable after 1-2 days, with bisphosphonate functional groups imparting the greatest stability (**Fig. 4c**).

Fig. 4. Colloidal stability of glutamic acid (GA), phosphonic acid (PA) and bisphosphonate (BP) functionalized Au NPs measured by the mean hydrodynamic particle diameter as a function of time in (a) DI water, (b) PBS or (c) FBS. The particle size was constant with time in water and PBS, indicating colloidal stability. Note that as-synthesized Au NPs coagulated immediately in PBS. FBS stability was measured only over the course of 2 days due to the instability of serum media. Each data point represents the mean of three measurements and error bars show one standard deviation.



Aim 2.4 Validate the specificity of the contrast agent for microdamage using machined surfaces of bovine cortical bone (Months 19-30).

Completed. The binding affinity of functionalized Au NPs for targeted delivery to bone mineral was investigated *in vitro* using hydroxyapatite (HA) crystals as a synthetic analog. Bisphosphonate functionalized Au NPs exhibited the most rapid binding kinetics and greatest binding affinity for HA, followed by glutamic acid and phosphonic acid (**Appendix 3**, Ross and Roeder, 2011). Functionalized Au NPs exhibited lower overall binding in FBS compared to de-ionized water, but relative differences between functional groups were similar. Bisphosphonate functionalized Au NPs also exhibited the most visible labeling of damaged tissue (scratches) in optical (**Fig. 5**) and backscattered SEM micrographs (**Fig. 6**). Specimens were scratched with a scalpel to induce controlled surface damage and then soaked in a solution of functionalized Au NPs.

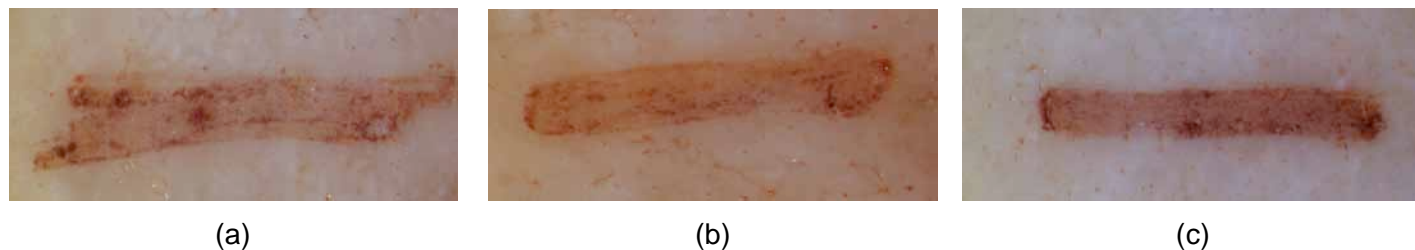


Fig. 5. Optical micrographs of bovine cortical bone surface damage labeled with (a) glutamic acid, (b) phosphonic acid, and (c) bisphosphonate functionalized Au NPs, showing the characteristic red color of Au NPs labeling the scratched surface. Note that the width of the scratch is approximately the same as in Fig. 6.

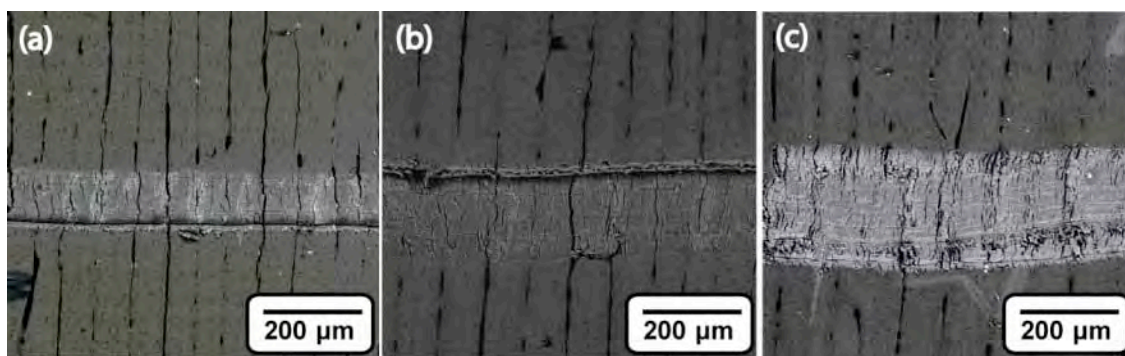


Fig. 6. Backscattered SEM micrographs of bovine cortical bone surface damage (scratch) labeled with (a) glutamic acid, (b) phosphonic acid, and (c) bisphosphonate functionalized Au NPs, showing enhanced contrast between damaged and non-damaged tissue correlating to the binding affinity of each functional group.

Aim 2.5 Measure diffusivity of the contrast agent into both cortical and trabecular bone tissue (Months 25-36).

Partially completed. The diffusivity was not able to be quantitatively measured within the project period due to initially unsuccessful attempts to develop a suitable experimental model and turnover in lab personnel working on this aim. However, diffusivity was qualitatively verified and quantitative methods have been developed for future work.

As-prepared Au NPs were conjugated with fluorescein (**Fig. 7a**) in order to track the diffusion of Au NPs in bone tissue. UV-vis spectroscopy showed that the Au NPs remained dispersed and fluorescein retained its characteristic epifluorescence (**Fig. 7b**). Therefore, we have prepared a dual contrast agent able to be imaged by X-ray and epifluorescence. A scratch test similar to that described in Aim 2.4 showed that the dual contrast agent exhibited specificity for damage (**Fig. 7c**).

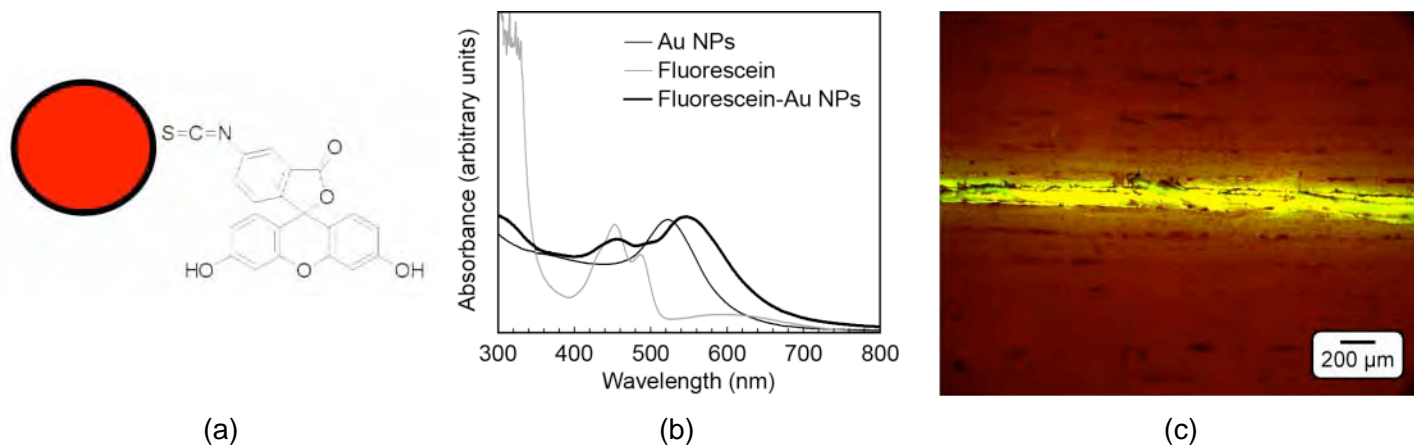
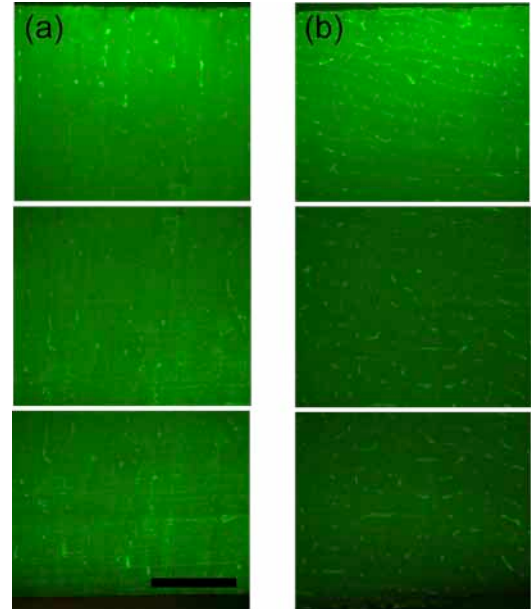


Fig. 7. (a) Schematic diagram showing functionalization of Au NPs with fluorescein. (b) UV-vis spectra measured for as-prepared Au NPs, fluorescein, and Au NPs functionalized with fluorescein. (c) Optical micrograph under UV epifluorescence showing a scratch on the surface of a bovine cortical bone specimen stained by Au NPs functionalized with fluorescein (yellow-green).

Two experimental models were developed for investigating the diffusivity of functionalized Au NPs in bone tissue. The first model used bone tissue specimens as a membrane separating a functionalized Au NP solution from DI water (or PBS). For the second model, a 5 mm cube of cortical bone tissue was embedded in polymethylmethacrylate and sectioned with a diamond wafer saw to expose one specimen to contrast agent solutions. Using this model, fluorescein functionalized Au NPs were qualitatively verified to readily diffuse into bovine cortical bone tissue (**Fig. 8**). The fluorescence intensity for diffusion was greater in the longitudinal direction than the transverse direction, as expected, due to the orientation of vasculature in the tissue.

Transport *in vivo* would be expected to be further enhanced by blood flow and load-induced fluid flow. Quantitative measurements of diffusivity were inhibited by difficulty correlating levels of fluorescence to gold concentration. However, inductively coupled plasma optical emission spectroscopy (ICP-OES) or similar analytical methods can be used in the future to quantitatively measure gold concentrations after acid digestion of thin sections of the bone tissue specimen.

Fig. 8. Optical micrographs using green epifluorescence of fluorescein functionalized Au NP diffusion through a 5 mm bovine cortical bone specimen after 4 h in either the (a) longitudinal or (b) transverse anatomic direction. The rows of images show the top surface of the specimen where diffusion originated, middle, and bottom of the specimen depth. The fluorescence intensity for diffusion was greater in the longitudinal direction than the transverse direction, as expected, due to the orientation of vasculature in the tissue. The scale bar corresponds to 1 mm.



Task 3: Quantify the effects of the contrast agent on micro-CT images in damaged and undamaged bone, and correlate the measurements to traditional measures of microdamage (Months 25-48).

Due to the need to use SRCT in order to detect the functionalized Au NP contrast agent, experiments for Task 3 were revised to move forward with a precipitated BaSO₄ stain. While this stain is not damage-specific or biocompatible (e.g., suited for *ex vivo* studies only), it can be imaged using a polychromatic micro-CT common to research labs and has enabled non-destructive, three-dimensional (3-D) investigation of microdamage accumulation for the first time. Experiments for Aim 3.1 were also able to be investigated for bisphosphonate functionalized Au NPs with SRCT using the APS at ANL, as described below.

Aim 3.1 Quantify the measured mass attenuation in rectangular notched and un-notched human cortical bone bending specimens, and correlate micro-CT measurements to the microdamage density measured by fluorescent staining and microscopy (Months 25-42).

Completed. Several studies were conducted in support of this aim, utilizing notched bovine cortical bone beams loaded in cyclic four-point bending (**Appendix 4**, Leng *et al.*, 2008), notched dentin specimens (**Appendix 5**, Landrigan *et al.*, 2010), and un-notched human cortical bone specimens loaded in cyclic uniaxial tension (**Appendix 6**, Landrigan *et al.*, 2011). Note that investigation of un-notched specimens was originally proposed to be conducted using four-point bending fatigue; however, experiments demonstrated a number of inherent problems in the use of four-point bending for the study of fatigue microdamage in cortical bone (**Appendix 7**, Landrigan *et al.*, 2009). In further support of these studies, a novel micro-CT imaging phantom was also investigated for improved accuracy in the calibration of linear attenuation coefficients with levels of mineral density in bone tissue (**Appendix 8**, Deuerling *et al.*, 2010).

Taken together, these studies demonstrated that contrast-enhanced micro-CT was able to detect the presence, spatial location, and progressive accumulation of fatigue microdamage in human cortical bone specimens *in vitro* using a precipitated BaSO₄ stain. Quantitative measurements of damage accumulation were validated against conventional histological methods using basic fuchsin (**Appendix 6**, Landrigan *et al.*, 2011). Thus, contrast-enhanced micro-CT enabled non-destructive imaging and 3-D spatial information, which

are not possible using conventional histological methods, and is immediately useful in the study of bone tissue mechanics, including the etiology of fatigue and fragility fractures.

A commercial, polychromatic benchtop micro-CT scanner (Scanco μ CT-80, 10 μ m resolution) was not able to detect damaged bone tissue labeled with functionalized Au NPs at the size (10-15 nm) and surface density (see Aim 2.4) investigated. However, fatigue microcracks labeled with bisphosphonate functionalized Au NPs were able to be detected by SRCT using absorption edge subtraction (**Appendix 9**, Ross and Roeder, 2010). A subsequent user proposal for beam time at ANL was awarded to repeat this experiment. A total of 15 samples were stained and imaged: 5 control samples with no loading, 5 samples loaded to a 5% elastic modulus loss, and 5 samples loaded to a 10% elastic modulus loss. These levels of mechanical degradation were previously shown to correspond to increased levels damage which were able to be distinguished using a precipitated BaSO_4 contrast agent and polychromatic micro-CT [4]. These experiments generated a large volume of image data which was just received in the last month from ANL staff for our own analysis.

Aim 3.2 Quantify locations and levels of microdamage in trabecular bone subjected to torsional loading, and validate the measurements by comparing to fluorescent staining and microscopy (Months 37-48).

Completed. On-axis cylindrical trabecular bone specimens were prepared from bovine femora using established methods [12]. Fifteen specimens were loaded in torsion to 4% shear strain, 3 specimens were loaded in uniaxial compression to 2% strain, and 2 specimens were used as unloaded controls. All specimens were subsequently stained by BaSO_4 precipitation and imaged by micro-CT (Scanco μ CT-80, $\sim 10 \mu$ m resolution) using methods adapted from a previous study, which also included validation against histological measurements [6]. The volume of each specimen was subdivided into inner, middle, and outer regions, corresponding to increasing levels of strain for specimens loaded in torsion. Damage was measured by the ratio of stain volume to bone volume (SV/BV) in segmented images (**Fig. 9**). The amount of microdamage measured by micro-CT (SV/BV) increased from the unloaded control group to groups loaded in uniaxial compression to 2% strain and torsion to 4% shear strain (**Fig. 10**). Microdamage in loaded groups increased from the inner to outer regions of the specimens, but these differences were not statistically significant. *Post hoc* power analysis indicated that group sizes need to be increased to at least 20 specimens per group. Moreover, the greater amount of staining in the outer region for the unloaded control group and the group loaded in uniaxial compression suggested that the staining protocol was not optimized for this experiment.

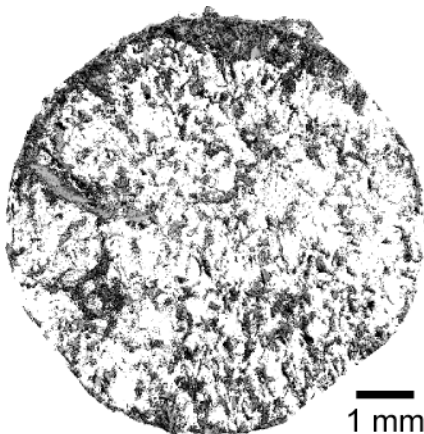


Fig. 9. Segmented, 3-D micro-CT reconstruction of a bovine trabecular bone specimen loaded in torsion to 4% shear strain and stained by BaSO_4 .

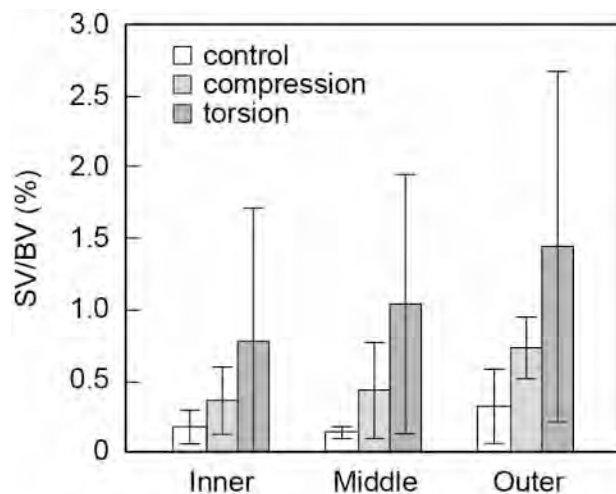


Fig. 10. The amount of microdamage measured by micro-CT (SV/BV) increased from the unloaded control group to groups loaded in uniaxial compression to 2% strain and torsion to 4% shear strain ($p < 0.05$, Kruskal-Wallis). Microdamage in loaded groups increased from the inner to outer regions of the specimens, but differences were not statistically significant. Error bars span one standard deviation.

Aim 3.3 Quantify microdamage in whole rat femurs subjected to bending (Months 37-48).

Completed. The presence, spatial location, and accumulation of fatigue microdamage in whole rat femora loaded in cyclic three-point bending was detected *in vitro* using contrast-enhanced micro-CT with a precipitated BaSO₄ stain (**Appendix 10**, Turnbull and Roeder, 2011). Moreover, cracks in whole human molars were also imaged by contrast-enhanced micro-CT (**Appendix 5**, Landrigan *et al.*, 2010).

KEY RESEARCH ACCOMPLISHMENTS

- Barium sulfate (BaSO₄) nanoparticles were synthesized using nanoemulsions, stabilized by coating with cross-linked dextran, and exhibited a three-fold increase in X-ray attenuation compared to a commercial, microscale contrast agent.
- Gold nanoparticles (Au NPs) were synthesized using the citrate reduction method and surface functionalized with L-glutamic acid, 2-aminoethylphosphonic acid, and alendronate, which exhibit a primary amine for binding gold opposite carboxylate, phosphonate, and bisphosphonate groups, respectively, for targeting calcium. Au NPs were also surface functionalized with fluorescein for a dual contrast agent suitable for both epifluorescent and X-ray imaging.
- Functionalized Au NPs exhibited stability in physiological solutions, deliverability via diffusion into bone tissue, a high binding affinity for bone mineral, and specificity for damaged bone tissue. Bisphosphonate functionalized Au NPs exhibited the strongest binding affinity for bone mineral and the most visible labeling of damaged tissue.
- Fatigue microcracks labeled with bisphosphonate functionalized Au NPs were able to be detected by synchrotron radiation computed tomography using absorption edge subtraction.
- Contrast-enhanced micro-CT using a precipitated BaSO₄ stain was able to detect the presence, spatial location, and accumulation of fatigue microdamage in notched bovine cortical bone beams loaded in cyclic four-point bending, un-notched human cortical bone specimens loaded in cyclic uniaxial tension, and whole rat femora loaded in cyclic three-point bending.
- Quantitative measurements of damage accumulation by contrast-enhanced micro-CT were validated against conventional histological methods using basic fuchsin.

REPORTABLE OUTCOMES

Journal Publications (accepted or in print)

R.D. Ross and R.K. Roeder, "Binding Affinity of Surface Functionalized Gold Nanoparticles for Hydroxyapatite," *J. Biomed. Mater. Res.*, accepted pending revision.

M.D. Landrigan, J. Li, T.L. Turnbull, D.B. Burr, G.L. Niebur and R.K. Roeder, "Contrast-Enhanced Micro-Computed Tomography of Fatigue Microdamage Accumulation in Human Cortical Bone," *Bone*, **48** [3] 443-450 (2011). [doi:10.1016/j.bone.2010.10.160](https://doi.org/10.1016/j.bone.2010.10.160)

J.M. Deuerling, D.J. Rudy, G.L. Niebur and R.K. Roeder, "Improved accuracy of cortical bone mineralization measured by polychromatic micro-computed tomography using a novel high mineral density composite calibration phantom," *Med. Phys.*, **37** [9] 5138-5145 (2010). [doi:10.1118/1.3480507](https://doi.org/10.1118/1.3480507)

Z. Zhang, R.D. Ross and R.K. Roeder, "Preparation of functionalized gold nanoparticles as a targeted X-ray contrast agent for damaged bone tissue," *Nanoscale*, **2** [4] 582-586 (2010). [doi:10.1039/b9nr00317g](https://doi.org/10.1039/b9nr00317g) Featured in RSC's Highlights in Chemical Science, January 29, 2010.

M.D. Landrigan, J.C. Flatley, T.L. Turnbull, J.J. Kruzic, J.L. Ferracane, T.J. Hilton and R.K. Roeder, "Detection of dentinal cracks using contrast-enhanced micro-computed tomography," *J. Mech. Behav. Biomed. Mater.*, **3** [2] 223-227 (2010). [doi:10.1016/j.jmbbm.2009.10.003](https://doi.org/10.1016/j.jmbbm.2009.10.003)

M.D. Landrigan and R.K. Roeder, "Systematic error in mechanical measures of damage during four-point bending fatigue of cortical bone," *J. Biomechanics*, **42** [9] 1212-1217 (2009). [doi:10.1016/j.jbiomech.2009.03.016](https://doi.org/10.1016/j.jbiomech.2009.03.016)

H. Leng, X. Wang, R.D. Ross, G.L. Niebur and R.K. Roeder, "Micro-computed tomography of fatigue microdamage in cortical bone using a barium sulfate contrast agent," *J. Mech. Behav. Biomed. Mater.*, **1** [1] 68-75 (2008). [doi:10.1016/j.jmbbm.2007.06.002](https://doi.org/10.1016/j.jmbbm.2007.06.002)

X. Wang, D.B. Masse, H. Leng, K.P. Hess, R.D. Ross, R.K. Roeder and G.L. Niebur, "Detection of trabecular bone microdamage by micro-computed tomography," *J. Biomechanics*, **40** [15] 3397-3403 (2007). [doi:10.1016/j.jbiomech.2007.05.009](https://doi.org/10.1016/j.jbiomech.2007.05.009)

Journal Publications (submitted or in preparation)

M.J. Meagher, B. Leone, Z. Zhang and R.K. Roeder, "Enhanced X-Ray Contrast with Dextran-Encapsulated Barium Sulfate Nanoparticles Prepared Using Nanoemulsions," *ACS Nano*, to be submitted this month.

T.L. Turnbull and R.K. Roeder, "Detection of fatigue microdamage in whole rat femora using contrast-enhanced micro-computed tomography," *J. Biomechanics*, to be submitted this month.

R.D. Ross and R.K. Roeder, "The Effect of Particle Diameter on the X-ray Attenuation of Gold Nanoparticles," in preparation.

R.D. Ross and R.K. Roeder, "Specificity of Functionalized Gold Nanoparticles to Damaged Bone Tissue," in preparation.

R.D. Ross and R.K. Roeder, "Detection of Fatigue Microdamage Labeled with Bisphosphonate Functionalized Gold Nanoparticles using Micro-CT with Adsorption Edge Subtraction," in preparation.

Conference Proceedings and Abstracts

M.J. Meagher, B. Leone, R.D. Ross, Z. Zhang and R.K. Roeder, "Preparation and Stabilization of Barium Sulfate Nanoparticles for X-Ray Contrast Agents," *Functionalized Nanobiomaterials for Medical Applications, MRS Workshop Series*, Denver, CO (2010).

R.D. Ross and R.K. Roeder, "Functionalized Gold Nanoparticles as a Targeted X-ray Contrast Agent for Mineralized Tissue," *Functionalized Nanobiomaterials for Medical Applications, MRS Workshop Series*, Denver, CO (2010).

Principal Investigator: Roeder, Ryan K.

T.L. Turnbull and R.K. Roeder, "Detection of Fatigue Microdamage in Whole Rat Femora Using Contrast-Enhanced Micro-Computed Tomography," *Proc. of the 2010 Summer Bioengineering Conference (ASME)*, Naples, FL, 19506 (2010). 1st place in the Ph.D. Student Paper Competition – Poster Presentation, Biofluids and Biotransport Engineering and Other.

M.D. Landrigan, J. Li, D.B. Burr, G.L. Niebur and R.K. Roeder, "Non-Destructive Measurement of Fatigue Microdamage Accumulation using Contrast-Enhanced Micro-Computed Tomography: Validation by Conventional Histology," *Trans. of the 56th Annual Meeting of the Orthopaedic Research Society*, New Orleans, LA, **35**, 336 (2010).

R.D. Ross and R.K. Roeder, "Functionalized Gold Nanoparticles for Targeted Labeling of Damaged Bone Tissue in X-Ray Tomography," *Trans. of the 56th Annual Meeting of the Orthopaedic Research Society*, New Orleans, LA, **35**, 1368 (2010).

R.K. Roeder, R.D. Ross, T.L. Turnbull, J.C. Flatley and M.D. Landrigan, "Micro-Computed Tomography of Cracks and Damage in Mineralized Tissues," *Composites at Lake Louise 2009*, Lake Louise, Canada (2009). Invited.

R.K. Roeder, R.D. Ross, Z. Zhang, M.D. Landrigan and G.L. Niebur, "Contrast Agents for Micro-Computed Tomography of Microdamage in Bone," *Military Health Research Forum 2009*, Kansas City, MO, 1500 (2009). Invited.

R.D. Ross, L. Cole, M. Rivers and R.K. Roeder, "X-ray Tomography of Damaged Bone Tissue Labeled with Functionalized Gold Nanoparticles," *Users Week 2009*, Advanced Photon Source, Argonne National Laboratory (2009).

R.D. Ross and R.K. Roeder, "Functionalized Gold Nanoparticle X-ray Contrast Agents for Bone Tissue," *Trans. of the 35th Annual Meeting of the Society for Biomaterials*, San Antonio, TX, **32**, 8 (2009).

J.M. Deuerling, D.J. Rudy, G.L. Niebur and R.K. Roeder, "Cortical Bone Mineralization Measured by Quantitative Micro-Computed Tomography Using a Non-Linear Calibration of Attenuation and Mineral Density," *Trans. of the 55th Annual Meeting of the Orthopaedic Research Society*, Las Vegas, NV, **34**, 2145 (2009).

M.D. Landrigan, G.L. Niebur and R.K. Roeder, "Detection of Fatigue Microdamage in Human Cortical Bone Using Micro-Computed Tomography," *Trans. of the 55th Annual Meeting of the Orthopaedic Research Society*, Las Vegas, NV, **34**, 2143 (2009).

M.D. Landrigan and R.K. Roeder, "Comparison of Measures of Mechanical Degradation During Four-Point Bending Fatigue of Cortical Bone," *Trans. of the 55th Annual Meeting of the Orthopaedic Research Society*, Las Vegas, NV, **34**, 322 (2009).

M.D. Landrigan, H. Leng, R.D. Ross, C. Berasi, X. Wang, G.L. Niebur and R.K. Roeder, "Imaging Microdamage in Bone Using a Barium Sulfate Contrast Agent," *2009 TMS Annual Meeting*, San Francisco, CA (2009).

R.D. Ross and R.K. Roeder, "Molecular Surface Modification of Gold Nanoparticles to Impart Specificity to Damaged Bone Tissue," *2009 TMS Annual Meeting*, San Francisco, CA (2009).

R.D. Ross and R.K. Roeder, "Imaging Damaged Bone Tissue Labeled with Functionalized Gold Nanoparticle Contrast Agents," *2009 TMS Annual Meeting*, San Francisco, CA (2009). 2nd place in the Graduate Division of the Biological Materials Science Symposium Student Poster Contest. NSF/ARO Travel Award Recipient.

R.K. Roeder, "A Paradigm for the Integration of Biology into Materials Science and Engineering," *2008 TMS Annual Meeting*, New Orleans, LA (2008).

R.D. Ross, Z. Zhang and R.K. Roeder, "Functionalized Gold Nanoparticles as an X-ray Contrast Agent for Bone Microdamage," *2008 TMS Annual Meeting*, New Orleans, LA (2008). 1st place in the Graduate Division of the Biological Materials Science Symposium Student Poster Contest. NSF Travel Award Recipient.

R.K. Roeder, Z. Zhang, R.D. Ross, M.D. Landrigan and H. Leng, "Noninvasive Imaging of Microdamage in Bone," *Materials Science and Technology 2007 (MS&T '07)*, Detroit, MI (2007). Invited.

Principal Investigator: Roeder, Ryan K.

M.D. Landrigan and R.K. Roeder, "Systematic Error in the Measure of Microdamage by Modulus Degradation During Four-Point Bending Fatigue," *Proc. of the 2007 Summer Bioengineering Conference (ASME)*, Keystone, CO, 175238 (2007). Honorable mention in the Ph.D. Student Paper Competition – Poster Presentation, Solid Mechanics, Design and Rehabilitation.

Z. Zhang, R.D. Ross and R.K. Roeder, "Functionalized Gold Nanoparticles as a Damage Specific Contrast Agent for Bone," *Trans. of the 33rd Annual Meeting of the Society for Biomaterials*, Chicago, IL, **30**, 93 (2007).

M.J. Meagher, Z. Zhang, and R.K. Roeder, "Precipitation of a Barium Sulfate Nanoparticle Contrast Agent Using Microemulsions," *2007 TMS Annual Meeting*, Orlando, FL (2007).

H. Leng, X. Wang, J. Du, G.L. Niebur and R.K. Roeder, "Fatigue Microdamage Mechanisms in Plexiform Bone Differ from Osteonal Bone," *Trans. of the 52nd Annual Meeting of the Orthopaedic Research Society*, Chicago, IL, **31**, 1757 (2006).

X. Wang, H. Leng, J. Du, R.K. Roeder and G.L. Niebur, "Three Dimensional Imaging of Fatigue Microdamage in Bovine Cortical Bone," *Trans. of the 52nd Annual Meeting of the Orthopaedic Research Society*, Chicago, IL, **31**, 1756 (2006).

Personnel Report (including new degrees and employment)

Name	Role	Period	% Effort	Degrees	Current Position
Ryan K. Roeder	PI	1/06-1/11	8	n/a	promoted to Associate Professor with tenure in 2007
Glen L. Niebur	co-PI	1/06-1/11	8	n/a	promoted to Associate Professor with tenure in 2006
Zhenyuan Zhang	PA	6/06-12/07	100	n/a	Postdoc, Duke University
Huijie Leng	GA	1/06-10/06	100	PhD (2006)	Assoc. Prof., Dept. of Orthopaedics, Peking Univ. Hospital, Beijing, China
Matt D. Landrigan	GA	6/06-5/09	100	PhD (2009)	Research Scientist, Biomet Corp.
Ryan D. Ross	GA	8/06-1/11	100		PhD Candidate at Notre Dame
Jackie Garrison	GA	1/08-8/08	100		PhD Candidate at Notre Dame
Travis L. Turnbull	GA	5/09-1/11	100		pursuing PhD at Notre Dame
Justin M. Deuerling	GA	9/09-5/10	100	PhD (2010)	defended dissertation in Dec. 2010
Matt J. Meagher	UGRA	6/06-8/06	summer	BS (2008)	pursuing PhD at Notre Dame
Paul Baranay	UGRA	6/07-8/07	summer		pursuing BS at MIT
Carl Berasi	UGRA	1/07-5/09	unpaid	BS (2009)	attending medical school
Erin Heck	UGRA	1/07-5/07	unpaid	BS (2009)	unknown
Jimmy Buffi	UGRA	8/07-5/08	unpaid	BS (2008)	pursuing PhD at Northwestern
David J. Rudy	UGRA	12/07-5/10	part time		pursuing BS at Notre Dame
Bridget Leone	UGRA	6/08-8-08	summer	BS (2009)	attending medical school
John C. Flatley	UGRA	6/09-8/09	summer	BS (2010)	pursuing MS at Notre Dame
Allison Cudworth	UGRA	1/09-5/10	unpaid	BS (2010)	pursuing MS at Trinity College (Ireland)

Note that PA = postdoctoral associate, GA = graduate assistant, UGRA = undergraduate research assistant.

Principal Investigator: Roeder, Ryan K.

Research Grants and Opportunities Applied For (awarded)

GUP-24309, Quantification of Gold Nanoparticle Concentrations Labeling Damaged Bone Tissue, Station 2-IDE, Advanced Photon Source, Argonne National Laboratory, nine shifts, February 25-28, 2011.

GUP-21884, X-Ray Tomography of Damaged Bone Tissue Labeled with Gold Nanoparticles: Validation by X-Ray Fluorescence, Station 2-IDE, Advanced Photon Source, Argonne National Laboratory, six shifts March 31-April 2, 2010.

GUP-21074, X-Ray Tomography of Damaged Bone Tissue Labeled with Gold Nanoparticles: Validation by X-Ray Fluorescence, Station 2-BM, Advanced Photon Source, Argonne National Laboratory, six shifts, April 21-23, 2010.

GUP-12889, X-ray Tomography of Damage Accumulation in Bone Tissue Labeled with Functionalized Gold Nanoparticles, Station 2-BM, Advanced Photon Source, Argonne National Laboratory, six shifts November 12-14, 2009.

GUP-10463, Detection of Gold Nanoparticles in Bone Tissue Using X-ray Tomography, Station 13-BMD, Advanced Photon Source, Argonne National Laboratory, three shifts October 9-10, 2008 and three shifts February 27-28, 2009.

Research Grants and Opportunities Applied For (pending)

NIH NIAMS R21, Effects of Intracortical Porosity on Microdamage Accumulation and Fracture Risk, PI, (2011-2013).

NIH NIDCR R01 (subcontract from the Oregon Health and Science University), Enhancing Risk Diagnosis for Predicting Clinical Outcomes of Cracked Teeth, PI, (2011-2015).

Research Grants and Opportunities Applied For (declined)

U.S. Army Medical Research and Materiel Command (USAMRMC), Congressionally Directed Medical Research Programs (CDMRP), Peer Reviewed Medical Research Program (PRMRP), Non-Invasive Detection of Fatigue Microdamage in Rat Ulnae Using Contrast-Enhanced Micro-Computed Tomography, PI, (2011-2014).

GUP-22594, Phase Contrast X-Ray Tomography for the Detection of Mineralized Tissue Labeled by Functionalized Gold Nanoparticles, Station 2-BM, Advanced Photon Source, Argonne National Laboratory, 24 shifts, 2010-2012.

NIH NIDCR RC1 (subcontract from the Oregon Health and Science University), Enhanced Diagnosis of Caries and Cracks in Teeth, PI, (2009-2011).

CONCLUSION

Deliverable, targeted X-ray contrast agents for damaged bone tissue were investigated using functionalized nanoparticles. Functionalized Au NPs were demonstrated to enable targeted delivery for non-invasive detection of microdamage using micro-CT. However, detection of damaged tissue labeled by functionalized Au NPs was thus far limited to the use of synchrotron radiation computed tomography in order to utilize monochromatic radiation for gold absorption edge subtraction. Therefore, the results of this study suggest that the ambitious goal of non-invasive (*in vivo*) imaging of microdamage in bone could be feasible with improvements in commercial scientific and clinical CT instruments. For example, beam filtration to tailor photon energies and improved detector systems are improvements that could be implemented into commercial micro-CT systems. A biocompatible, deliverable, damage-specific contrast agent could enable clinical assessment of bone quality and damage accumulation, and scientific study of damage processes *in situ*.

Contrast-enhanced micro-CT using a precipitated BaSO₄ stain was demonstrated to enable non-destructive, 3-D detection and imaging of microdamage in machined cortical bone specimens and whole rat femora. Limitations of these methods included that the precipitated BaSO₄ stain was non-specific and non-biocompatible. However, contrast-enhanced micro-CT enabled non-destructive imaging and provided 3-D spatial information which are not possible using conventional histology. Therefore, these new methods are immediately useful for *in vitro* scientific studies investigating the etiology of fatigue and fragility fractures in bone.

REFERENCES

1. D.B. Burr, M.R. Forwood, D.P. Fyhrie, R.B. Martin, M.B. Schaffler, and C.H. Turner, "Bone Microdamage and Skeletal Fragility in Osteoporotic and Stress Fractures," *J. Bone Miner. Res.*, **12** [1] 6-15 (1997).
2. B.D. Chapurlat and P.D. Delmas, "Bone microdamage: a clinical perspective," *Osteoporos. Int.*, **20**, 1299-1308 (2009).
3. T.C. Lee, S. Mohsin, D. Taylor, R. Parkesh, T. Gunnlaugsson, F.J. O'Brien, M. Giehl, and W. Gowin, "Detecting microdamage in bone," *J. Anat.*, **203**, 161-172 (2003).
4. M.D. Landrigan, J. Li, T.L. Turnbull, D.B. Burr, G.L. Niebur and R.K. Roeder, "Contrast-Enhanced Micro-Computed Tomography of Fatigue Microdamage Accumulation in Human Cortical Bone," *Bone*, **48** [3] 443-450 (2011). [doi:10.1016/j.bone.2010.10.160](https://doi.org/10.1016/j.bone.2010.10.160)
5. H. Leng, X. Wang, R.D. Ross, G.L. Niebur and R.K. Roeder, "Micro-computed tomography of fatigue microdamage in cortical bone using a barium sulfate contrast agent," *J. Mech. Behav. Biomed. Mater.*, **1** [1] 68-75 (2008). [doi:10.1016/j.jmbbm.2007.06.002](https://doi.org/10.1016/j.jmbbm.2007.06.002)
6. X. Wang, D.B. Masse, H. Leng, K.P. Hess, R.D. Ross, R.K. Roeder and G.L. Niebur, "Detection of trabecular bone microdamage by micro-computed tomography," *J. Biomechanics*, **40** [15] 3397-3403 (2007). [doi:10.1016/j.jbiomech.2007.05.009](https://doi.org/10.1016/j.jbiomech.2007.05.009)
7. R.D. Ross and R.K. Roeder, "Binding Affinity of Surface Functionalized Gold Nanoparticles for Hydroxyapatite," *J. Biomed. Mater. Res.*, accepted pending revision.
8. Z. Zhang, R.D. Ross and R.K. Roeder, "Preparation of functionalized gold nanoparticles as a targeted X-ray contrast agent for damaged bone tissue," *Nanoscale*, **2** [4] 582-586 (2010). [doi:10.1039/b9nr00317g](https://doi.org/10.1039/b9nr00317g)
9. R. Parkesh, T.C. Lee, T. Gunnlaugsson and W. Gowin, "Microdamage in bone: Surface analysis and radiological detection," *J. Biomechanics*, **39**, 1552-1556 (2006).
10. R. Parkesh, W. Gowin, T.C. Lee, and T. Gunnlaugsson, "Synthesis and evaluation of potential CT (computer tomography) contrast agents for bone structure and microdamage analysis," *Org. Biomol. Chem.*, **4**, 3611-3617 (2006).
11. K. Kouris, N. M. Spyrou, and D. F. Jackson, "Minimum Detectable Quantities of Elements and Compounds in a Biological Matrix," *Nucl. Instrum. Methods*, **187**, 539-545 (1981).
12. X. Wang, X. Liu and G.L. Niebur, "Preparation of on-axis cylindrical trabecular bone specimens using micro-CT imaging," *J. Biomech. Eng.*, **126**, 122-125 (2004).

APPENDICES (attached reprints)

1. M.J. Meagher, B. Leone, Z. Zhang and R.K. Roeder, "Enhanced X-Ray Contrast with Dextran-Encapsulated Barium Sulfate Nanoparticles Prepared Using Nanoemulsions," *ACS Nano*, to be submitted this month (2011).
2. Z. Zhang, R.D. Ross and R.K. Roeder, "Preparation of functionalized gold nanoparticles as a targeted X-ray contrast agent for damaged bone tissue," *Nanoscale*, **2** [4] 582-586 (2010). [doi:10.1039/b9nr00317g](https://doi.org/10.1039/b9nr00317g)
Featured in RSC's Highlights in Chemical Science, January 29, 2010.
3. R.D. Ross and R.K. Roeder, "Binding Affinity of Surface Functionalized Gold Nanoparticles for Hydroxyapatite," *J. Biomed. Mater. Res.*, accepted pending revision (2011).
4. H. Leng, X. Wang, R.D. Ross, G.L. Niebur and R.K. Roeder, "Micro-computed tomography of fatigue microdamage in cortical bone using a barium sulfate contrast agent," *J. Mech. Behav. Biomed. Mater.*, **1** [1] 68-75 (2008). [doi:10.1016/j.jmbbm.2007.06.002](https://doi.org/10.1016/j.jmbbm.2007.06.002)
5. M.D. Landrigan, J. Li, T.L. Turnbull, D.B. Burr, G.L. Niebur and R.K. Roeder, "Contrast-Enhanced Micro-Computed Tomography of Fatigue Microdamage Accumulation in Human Cortical Bone," *Bone*, **48** [3] 443-450 (2011). [doi:10.1016/j.bone.2010.10.160](https://doi.org/10.1016/j.bone.2010.10.160)
6. M.D. Landrigan, J.C. Flatley, T.L. Turnbull, J.J. Kruzic, J.L. Ferracane, T.J. Hilton and R.K. Roeder, "Detection of dentinal cracks using contrast-enhanced micro-computed tomography," *J. Mech. Behav. Biomed. Mater.*, **3** [2] 223-227 (2010). [doi:10.1016/j.jmbbm.2009.10.003](https://doi.org/10.1016/j.jmbbm.2009.10.003)
7. M.D. Landrigan and R.K. Roeder, "Systematic error in mechanical measures of damage during four-point bending fatigue of cortical bone," *J. Biomechanics*, **42** [9] 1212-1217 (2009). [doi:10.1016/j.jbiomech.2009.03.016](https://doi.org/10.1016/j.jbiomech.2009.03.016)
8. J.M. Deuerling, D.J. Rudy, G.L. Niebur and R.K. Roeder, "Improved accuracy of cortical bone mineralization measured by polychromatic micro-computed tomography using a novel high mineral density composite calibration phantom," *Med. Phys.*, **37** [9] 5138-5145 (2010). [doi:10.1118/1.3480507](https://doi.org/10.1118/1.3480507)
9. R.D. Ross and R.K. Roeder, "Functionalized Gold Nanoparticles for Targeted Labeling of Damaged Bone Tissue in X-Ray Tomography," *Trans. of the 56th Annual Meeting of the Orthopaedic Research Society*, New Orleans, LA, **35**, 1368 (2010).
10. T.L. Turnbull and R.K. Roeder, "Detection of fatigue microdamage in whole rat femora using contrast-enhanced micro-computed tomography. *J. Biomechanics*, to be submitted this month.

Enhanced X-Ray Contrast with Dextran-Encapsulated Barium Sulfate Nanoparticles Prepared Using Nanoemulsions

Matthew J. Meagher, Bridget Leone, Zhenyuan Zhang, and Ryan K. Roeder

Department of Aerospace and Mechanical Engineering
Bioengineering Graduate Program
University of Notre Dame
Notre Dame, Indiana 46556

Submitted to: *ACS Nano*

Running Title: Barium Sulfate Nanoparticle Contrast Agents

Keywords: Barium Sulfate; Nanoparticles; Nanoemulsion; Dextran; Contrast Agent

Correspondence: Ryan K. Roeder, Ph.D.
Associate Professor
Department of Aerospace and Mechanical Engineering
Bioengineering Graduate Program
148 Multidisciplinary Research Building
University of Notre Dame
Notre Dame, Indiana 46556

Phone: (574) 631-7003
Fax: (574) 631-2144
Email: rroeder@nd.edu

Funding Sources: U.S. Army Medical Research and Materiel Command (W81XWH-06-1-0196) through the Peer Reviewed Medical Research Program (PR054672)

ABSTRACT

BaSO₄ has also been recently investigated as a radiographic contrast agent for non-invasive, three-dimensional (3-D) imaging of fatigue cracks and microcracks in mineralized tissues using micro-computed tomography (micro-CT). A deliverable contrast agent would require BaSO₄ nanoparticles less than 40 nm in diameter in order to be transported through the lacunar-canalicular network to microdamage in bone. BaSO₄ nanoparticles < 40 nm in diameter were synthesized using water-in-oil nanoemulsions and stabilized in aqueous media by cross-linked dextran encapsulation. The X-ray attenuation of BaSO₄ nanoparticles was compared to an equal concentration of a commercial, micro-scale BaSO₄ contrast agent. A nearly three-fold increase in X-ray attenuation was observed in the synthesized BaSO₄ nanoparticles.

INTRODUCTION

The high X-ray attenuation and reasonable biocompatibility of barium sulfate (BaSO_4) has led to clinical use as a contrast agent for gastrointestinal radiography¹ and as a radiopacifier in polymethylmethacrylate bone cement.² Current commercial products for either application use microscale BaSO_4 particles. However, the increased specific surface area of nanoparticles can enhance X-ray scattering and therefore provide greater radiographic contrast.³

BaSO_4 has also been recently investigated as a radiographic contrast agent for non-invasive, three-dimensional (3-D) imaging of fatigue cracks and microcracks in mineralized tissues using micro-computed tomography (micro-CT).⁴⁻⁷ However, this technique is limited to *in vitro* histology, as BaSO_4 particles are precipitated within tissue using staining solutions that are not biocompatible. A deliverable contrast agent would require BaSO_4 nanoparticles less than 40 nm in diameter in order to be transported through the lacunar-canalicular network to microdamage in bone.^{8,9}

Previous attempts to synthesize submicron BaSO_4 particles have ranged from direct precipitation, possibly including anionic polyelectrolytes and other additives, to water-in-oil micro- or nanoemulsions.¹⁰⁻¹⁴ The ideal synthesis route for the preparation of a deliverable BaSO_4 nanoparticle contrast agent should allow for precise control of particle diameter.

Water-in-oil micro- and nanoemulsions provide a stable, reliable reaction template for the synthesis of nanoparticles by controlling crystal growth and limiting agglomeration (Fig. 1).^{11,15-18} Aqueous droplets suspended via a surfactant in the oil phase limits (1) primary crystal growth by controlling the available amount of reactants in each aqueous droplet^{11,12,15,17} and (2) agglomeration by serving as a physical barrier to contact between the precipitated nanoparticles. The amount of available reactants can be controlled by the salt concentration with aqueous

droplets and the droplet size.¹³ The thermodynamic principles governing water-in-oil nanoemulsions allows for precise control of the droplet size primarily through water/oil/surfactant ratios.^{11,12,15,17} However, once the nanoparticles are collected and the stabilizing effects of the nanoemulsion are removed, the nanoparticles tend to agglomerate and form large aggregates that are not readily dispersed.

Encapsulation of nanoparticles within a hydrophilic biopolymer, such as dextran, has been utilized for the dispersion of nanoscale iron oxide as a contrast agent for magnetic resonance imaging.¹⁹⁻²¹ Encapsulation of BaSO₄ nanoparticles with cross-linked dextran (Fig. 2) would not only confer the hydrophilicity necessary to stabilize the nanoparticles in aqueous solution, but could also provide a platform for the covalent attachment of functional groups necessary for targeted delivery.

The objective of this study was to prepare and characterize a BaSO₄ nanoparticle contrast agent with colloidal stability in aqueous solutions. BaSO₄ nanoparticles were synthesized using water-in-oil nanoemulsions and stabilized by cross-linked dextran encapsulation. The X-ray attenuation of BaSO₄ nanoparticles was compared to an equal concentration of a commercial, micro-scale BaSO₄ contrast agent.

EXPERIMENTAL METHODS

BaSO₄ Nanoparticle Synthesis

Barium sulfate was synthesized through a simple precipitation reaction,



where the diameter of the synthesized particles was controlled using water-in-oil nanoemulsions. Solutions of barium chloride, $\text{BaCl}_2 \cdot 2\text{H}_2\text{O}$ (Fluka, ACS Reagent, 99% purity), and ammonium chloride, $(\text{NH}_4)_2\text{SO}_4$ (Sigma-Aldrich, 99.999% purity), were prepared in concentrations ranging from 0.1 M to 0.3 M. Nanoemulsions were prepared comprising 90 vol% cyclohexane, C_6H_6 (Sigma-Aldrich, Plus 99.9% purity), as the oil phase and 10 vol% of a surfactant blend. The surfactant blend was prepared by combining Triton X-100 (Fluka, BioXtra) and 1-hexanol (Sigma-Aldrich, Reagent Grade, 98% purity) at a weight ratio of 4.5:1. Nanoemulsions for each salt solution were prepared by adding 1.2 vol% of the salt solution and mixing until isotropic. BaCl_2 and $(\text{NH}_4)_2\text{SO}_4$ nanoemulsions were added together and stirred vigorously for 90 min to allow equilibration between the aqueous phase droplets, facilitating precipitation (Fig. 1).

Dextran Encapsulation of BaSO_4 Nanoparticles

Two additional nanoemulsions were prepared via the procedure described above, one containing an aqueous phase of 8.3 wt% dextran (from *Leuconostoc mesenteroides*, Sigma, average molecular weight 9,000-11,000) and 0.002 M epichlorohydrin (Sigma).¹⁹ The dextran-containing nanoemulsion was added to the BaSO_4 -containing nanoemulsion and mixed for 90 min. After the dextran- BaSO_4 microemulsion had equilibrated, the epichlorohydrin-containing nanoemulsion was added and the resulting nanoemulsion was mixed for an additional 90 min.

Nanoparticle Collection

Synthesized nanoparticles were collected by breaking the nanoemulsion through the addition of 12.5 vol% acetone and centrifugation at 5,000 RPM for 10 min. Following centrifugation, the supernatant was removed from the solution and the collected particles were

washed with ethanol. The centrifugation and washing procedure was repeated three times. Excess ethanol was evaporated at 80-90°C.

Characterization

The droplet size distribution of each nanoemulsion, and the particle size distribution of as-synthesized and dextran-encapsulated BaSO₄ nanoparticles, was measured using dynamic light scattering (DLS, Zetasizer Nano-ZS, Malvern Instruments) on a 1 mL sample in a quartz cuvette. The crystallographic phase and composition of as-synthesized nanoparticles was verified by X-ray diffraction (XRD) using Cu K α radiation generated at 40 kV and 30 mA (X1 Advanced Diffraction System, Scintag, Inc.). Nanoparticles were examined over 15-90° two-theta with a step size of 0.02° and a steptime of 0.04 s. The primary crystallite size was measured from peak broadening in XRD using the Scherrer equation and Warren's Method.²² The morphology and particle size distribution of as-synthesized and dextran-encapsulated BaSO₄ nanoparticles was measured by transmission electron microscopy (TEM, Hitachi H-600). Specimens were prepared by immersing carbon-coated grids in BaSO₄-containing solutions. The electrokinetic potential (ζ -potential) was measured via electrophoretic mobility (Zetasizer, Malvern Instruments).²³

The X-ray contrast of BaSO₄ nanoparticles was measured using micro-CT. Dextran-encapsulated BaSO₄ nanoparticles were suspended in aqueous medium and placed in capillary tubes at a concentration of 0.01 g BaSO₄/mL H₂O. A commercial, microscale BaSO₄ suspension (individual particles 834 \pm 370 nm) was diluted in aqueous media to an identical concentration and also placed in capillary tubes. Settling of the microscale suspension was prevented by dissolving polyvinyl alcohol (PVA) in the capillary tubes for both microscale and nanoscale

BaSO₄. The relative X-ray attenuation of these solutions was measured using a benchtop micro-CT system (μ CT-80, Scanco Medical AG, Brüttisellen, Switzerland) at 70 kVp, 114 mA, and 400 ms integration time for 10 slices with a 10 μ m voxel size. The measured linear attenuation coefficient was converted to Hounsfield units (HU) using an internal calibration against air (-1000 HU) and water (0 HU).

RESULTS AND DISCUSSION

Nanoemulsion Characterization

The isotropic phase of the water-in-oil nanoemulsion was qualitatively characterized by optical clarity and decreased kinematic viscosity. Kinematic viscosity measurements above 3 mPa·s typically indicated an anisotropic microemulsion, while kinematic viscosity measurements of approximately 2.7 mPa·s or less typically indicated an isotropic nanoemulsion. Once equilibrated, an isotropic nanoemulsion remained stable for at least 7 days, as evidenced by stable droplet size distributions measured via DLS. Nanoemulsions containing BaCl₂ and (NH₄)₂SO₄ reactants, as well as precipitated BaSO₄ nanoparticles, exhibited a narrow mean droplet size distribution with a mean droplet diameter of approximately 4.72 nm (Fig. 2). Nanoemulsions containing dextran-encapsulated BaSO₄ nanoparticles also exhibited a monodispersed droplet size distribution, but a slightly larger aqueous droplet diameter than the constituent nanoemulsions (Fig. 3a).

For nanoemulsions containing 0.3 M salt solutions, a theoretical yield of 4.8×10^{-4} moles (0.112 g) of BaSO₄ was expected. Following reaction, approximately 4.2×10^{-4} moles (0.100 g) of BaSO₄ was typically collected for a yield of 89.3%. Losses from the theoretical yield were attributed to incomplete exchange of Ba²⁺ and SO₄²⁻ salts between nanoemulsion droplets.

Synthesis of BaSO₄ nanoparticles required controlling the nucleation and growth rate, as well as the rate of agglomeration. To this end, aqueous droplets in the W/O nanoemulsion system served as nanoreactors by, encapsulating the aqueous reactant environment within a surfactant film.^{9,13,15} In other words, the aqueous droplets served as templates for the nanoparticles, as the droplet size limited the amount of reactants available for reaction and provided an upper limit for particle growth.^{16-18,27}

Nanoparticle Characterization

As-synthesized nanoparticles readily agglomerated when collected and redispersed in polar solvents such as water. Therefore, as-synthesized nanoparticles were redispersed in cyclohexane for accurate characterization via DLS and TEM. DLS confirmed that nearly all particles exhibited a diameter < 15 nm (Fig. 3). As-synthesized BaSO₄ nanoparticles redispersed in cyclohexane were directly observed to exhibit monodispersed spherical, or ellipsoidal particles equiaxed nanoparticles with diameters < 15 nm (Fig. 3b). The crystallographic phase of the as-synthesized nanoparticles was verified to be BaSO₄ by XRD (Fig. 5). The primary crystallite size, estimated from peak-broadening, was approximately 27 nm.

Nanoparticle Dispersion

As-synthesized BaSO₄ nanoparticles remained stable and dispersed while contained within the aqueous nanoemulsion droplets. However, the stabilizing presence of the nanoemulsion is not suited for the intended biological application. When the stabilizing effects of the nanoemulsion were removed in the absence of an external stabilizing agent, the BaSO₄ nanoparticles readily formed agglomerates at least 250 nm in diameter. While the collected,

agglomerated nanoparticles were readily redispersed in organic solvents such as cyclohexane, aqueous dispersion was inhibited by a low measured ζ -potential of < 10 mV at neutral pH. The ζ -potential required for electrostatic stabilization of colloidal particles is typically taken as ± 25 mV.²⁴ Nanoparticles with surface charge values less than 25 mV, will agglomerate until the aggregate is large enough to resist attractive forces stemming from the electrokinetic potential.²⁴

Dextran-encapsulation of BaSO₄ nanoparticles stabilized particles less than < 40 nm in diameter (Fig. 4b) while dispersed in aqueous medium. This result was supported by TEM and DLS. Dextran encapsulation has proved to be an effective method for aqueous dispersion of BaSO₄ nanoparticles. The stabilizing effects of the cross-linked dextran coating resulted from the steric barrier and hydrophilicity. Dextran is soluble in water, and readily dispersed in aqueous media. Dextran has been previously utilized to provide hydrophilicity to iron-oxide based MRI contrast agents. The methods used in this study for dextran-encapsulation resulted in an increased hydrodynamic diameter of the as-synthesized nanoparticles from 4 nm to 40 nm which could limit transport through applications involving targeted delivery to cells and tissues. On the other hand, 40 nm particles could be well suited for radiopacifiers and gastrointestinal transport.

X-Ray Attenuation

Dextran-encapsulated BaSO₄ nanoparticles exhibited a 2.6 times greater X-ray attenuation compared to a commercial microscale solution at the same concentration (Fig. 6). This results is attributed to the nanoparticles increased surface area per volume of BaSO₄ compared with the microscale suspension. The increased surface area results in greater scattering of X-rays, which increases attenuation. These results indicate that smaller BaSO₄

particles may allow clinicians to use smaller masses of contrast agents to achieve the desired level of contrast.

CONCLUSIONS

Precipitation within the controlled environment provided by a nanoemulsion allowed for precise control of particle size at < 15 nm in diameter. Encapsulation of BaSO₄ nanoparticles by cross-linked dextran enabled aqueous dispersion. Dextran-encapsulated BaSO₄ nanoparticles exhibited a nearly three-fold increased in X-ray attenuation compared to a commercial, microscale BaSO₄ contrast agent used clinically.

ACKNOWLEDGEMENTS

This research was supported by the U.S. Army Medical Research and Materiel Command (W81XWH-06-1-0196) through the Peer Reviewed Medical Research Program (PR054672). We acknowledge the Notre Dame Integrated Imaging Facility (NDIIF) for the use of TEM.

REFERENCES

1. Skucas, J. *Radiographic Contrast Agents*; Wolters Kluwer Law & Business, 1989, 10-76.
2. Lewis, G. Properties of acrylic bone cement: state of the art review. *J. Biomed. Mater. Res. (Appl. Biomater.)* **1997**, 38, 155.
3. Xu, C., Tung, G., and Shouheng, S. Size and Concentration Effect of Gold Nanoparticles on X-ray Attenuation As Measured on Computed Tomography. *Chem. Mater.* **2008**, 20, 4167.

4. Landrigan, M., Li, J., Turnbull, T., Burr, D., Niebur, G., and Roeder, R. Contrast-enhanced micro-computed tomography of fatigue microdamage accumulation in human cortical bone. *Bone* **2010**, 10, 160.
5. Landrigan, M., Flatley, J., Turnbull, T., Kruzic, J., Ferracane, J., Hilton, T., and Roeder, R. Detection of dentinal cracks using contrast-enhanced micro-computed tomography. *J. Mech. Behav. Biomed. Mater.* **2010**, 3, 223.
6. Leng, H., Wang, X., Ross, R., Niebur, G., and Roeder, R. Micro-computed tomography of fatigue microdamage in cortical bone using a barium sulfate contrast agent. *J. Mech. Behav. Biomed. Mater.* **2008**, 1, 68.
7. Wang, X., Masse, D., Leng, H., Hess, K., Ross, R., Roeder, R., and Niebur, G. Detection of trabecular bone microdamage by micro-computed tomography. *J. Biomech.* **2007**, 15, 3397.
8. Knothe-Tate, M., Niederer, P., Knothe, U. In Vivo Tracer Transport Through the Lacunocanalicular System of Rat Bone in an Environment Devoid of Mechanical Loading. *Bone* **1998**, 22, 107.
9. O'Brien, F., Taylor, D., Dickson, G., Lee, T. Visualisation of three-dimensional microcracks in compact bone. *J. Anat.* **2000**, 197, 413.
10. Bala, H., Fu, W., Zhao, J., Ding, X., Jiang, Y., Yu, K., and Wang, Z. Preparation of BaSO₄ nanoparticles with self-dispersing properties. *Colloid Surface A*, 2005, 252, 129.
11. Hopwood, J. and Mann, S. Synthesis of Barium Sulfate Nanoparticles and Nanofilaments in Reverse Micelles and Microemulsions. *Chem. Mater.* **1997**, 9, 1819.
12. Ivanova, N., Rudelev, D., Summ, B., and Chalykh, A. Synthesis of Barium Sulfate Nanoparticles in Water-in-Oil Microemulsion Systems. *Colloid J.* **2001**, 63, 714.
13. Li, S., Xu, J., and Luo, G. Control of crystal morphology through supersaturation ratio and mixing conditions. *J. Crystal Growth* **2007**, 304, 219.

14. Qi, Limin, Ma, J., Cheng, H., and Zhao, Z. Preparation of BaSO₄ nanoparticles in non-ionic w/o microemulsions. *Colloids Surface A* **1996**, 108, 117.
15. Eastoe, J. and Dalton, J. Dynamic surface tension and adsorption mechanisms of surfactants at the air-water interface. *Adv. Colloid Interfac.* **2000**, 85, 103.
16. Koetz, J., Bahnemann, J., Lucas, G., Tiersch, B., and Kosmella, S. Polyelectrolyte-modified microemulsions as new templates for the formation of nanoparticles. *Colloids Surface A* **2004**, 250, 423.
17. Lam, A., Falk, N., and Schechter, R.. The thermodynamics of microemulsions. *Colloids Surface A* **1987**, 120, 30.
18. Niemann, B., Veit, P., and Sundmacher, K. Nanoparticle Precipitation in Reverse Microemulsions: Particle Formation Dynamics and Tailoring of Particle Size Distributions. *Langmuir* **2008**, 24, 4320.
19. Cullility, B. *Elements of X-Ray Diffraction*; Addison-Wesley Publishing Company, Inc.: Reading, MA, 1978, 281-285.
20. Jarrett, B., Frendo, M., Vogan, J., and Louie, A. Size-controlled synthesis of dextran sulfate coated iron oxide nanoparticles for magnetic resonance imaging. *Nanotechnology* **2007**, 18, 1.
21. Özdemir, C., Çolak, N., and Güner, A. Solution dynamics of the dextran/crosslinking agent systems. *J. Appl. Polym. Sci.* **2007**, 105, 1177.
22. Hang, J., Zhan, Y., Shi, L., and Feng, X. Electrokinetic properties of barite nanoparticles suspensions in different electrolyte media. *J. Mater. Sci.*, **2007** 42, 9611.
23. Schwarzer, H. and Peukert, W. Tailoring particle size through nanoparticle precipitation. *Chem. Eng. Commun.* **2004**, 191, 580.

24. Schwarzer, H. and Peukert., W. Experimental Investigation into the Influence of Mixing on Nanoparticle Precipitation. *Chem. Eng. Technol.* **2002**, 25, 657.
25. Schwarzer, H. and Peukert, W. Prediction of aggregation kinetics based on surface properties of nanoparticles. *Chem. Eng. Sci.* **2005**, 60, 11 .
26. Siano, D., Bock, J., Myer, P., and Russel, W. Thermodynamics and hydrodynamics of a nonionic microemulsion. *Colloids Surface A* **1987**, 26, 171.
27. Laurent, S., Forge, D., Port, M., Roch, A., Robic, C., Vander Elst, L., Muller, R. Magnetic Iron Oxide Nanoparticles: Synthesis, Stabilization, Vectorization, Physicochemical Characterizations, and Biological Applications. *Chem. Rev.* **2008**, 108, 2064.
28. Hounsfield, G. Computed Medical Imaging. *Med. Phys.* **1980**, 7, 283.

TABLES

Table 1. X-Ray Attenuation of Biological Tissues and BaSO₄ Contrast Agents

Material	X-Ray Attenuation (HU)
cortical bone ²⁸	990
as-synthesized BaSO ₄ nanoparticles (0.01 g/mL)	243
commercial, microscale BaSO ₄ (0.01 g/mL)	92
muscle ²⁸	40
fat ²⁸	-80

FIGURE CAPTIONS

Figure 1. Schematic diagram showing solute transfer between nanoemulsion droplets. The surfactant stabilized aqueous droplets suspended in the oil phase controlled crystal growth by limiting the concentration of reactants (Ba^{2+} and SO_4^{2-}) available for reaction, and limited agglomeration by preventing precipitated BaSO_4 nanoparticles from contacting each other.

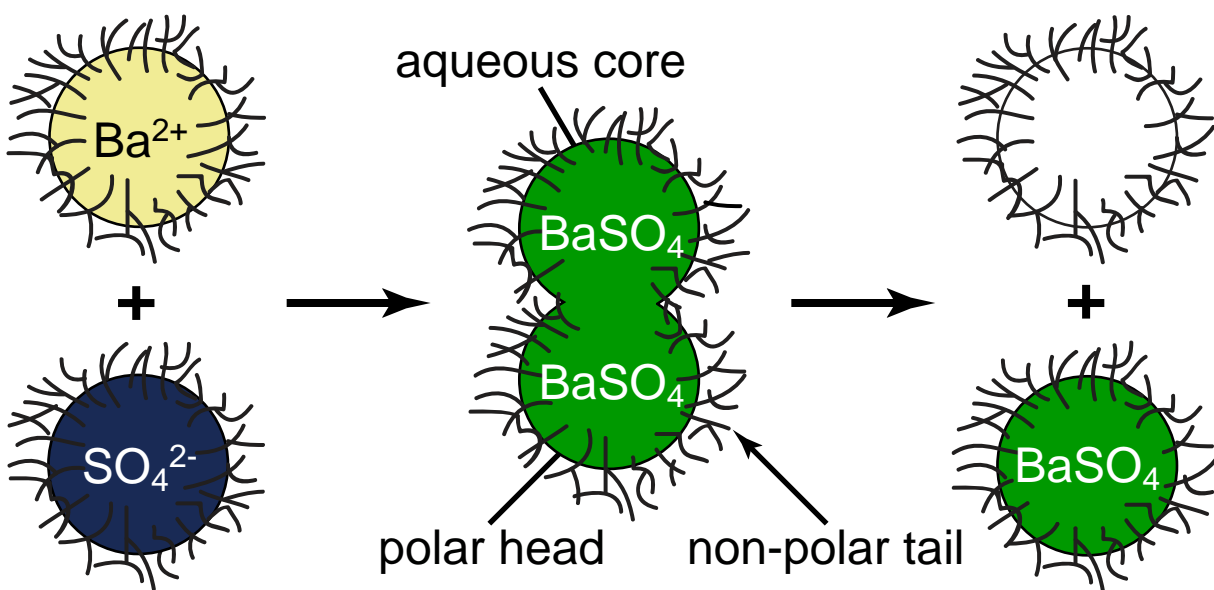
Figure 2. Schematic diagram showing encapsulation of BaSO_4 nanoparticles with dextran, a hydrophilic polysaccharide, to facilitate dispersion in aqueous media.

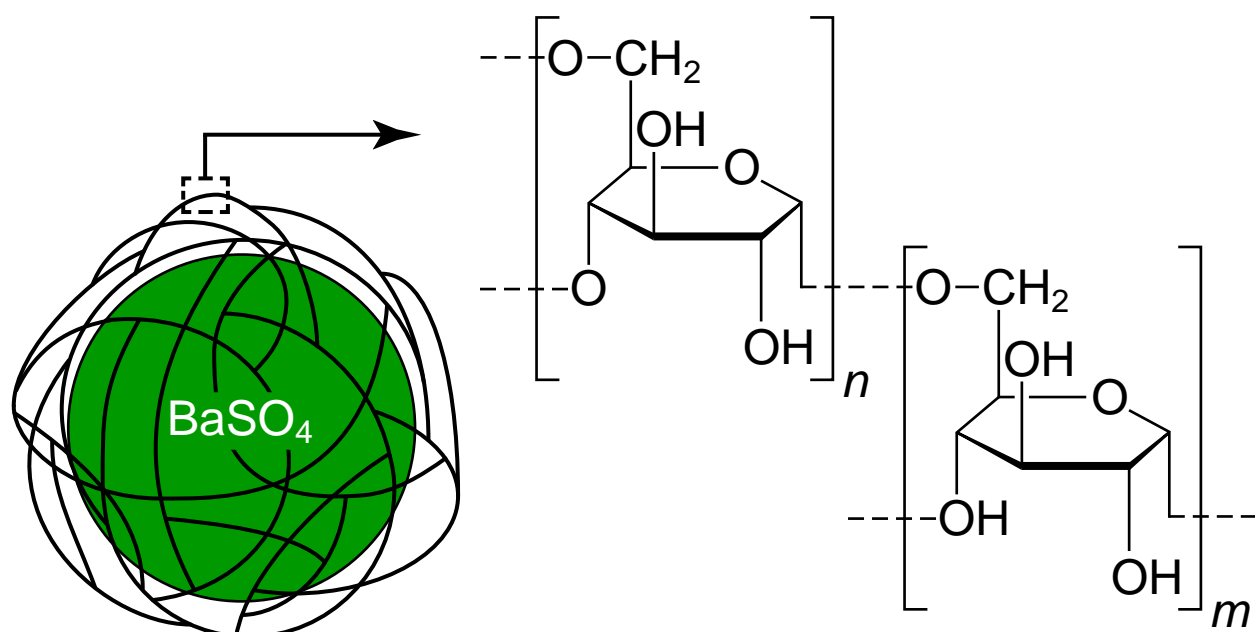
Figure 3. (a) Droplet size distributions measured by DLS for nanoemulsions containing Ba^{2+} , SO_4^{2-} , BaSO_4 , and dextran-encapsulated BaSO_4 . (b) Particle size distributions measured by DLS for as-synthesized BaSO_4 nanoparticles redispersed in cyclohexane and dextran-encapsulated BaSO_4 nanoparticles redispersed in water.

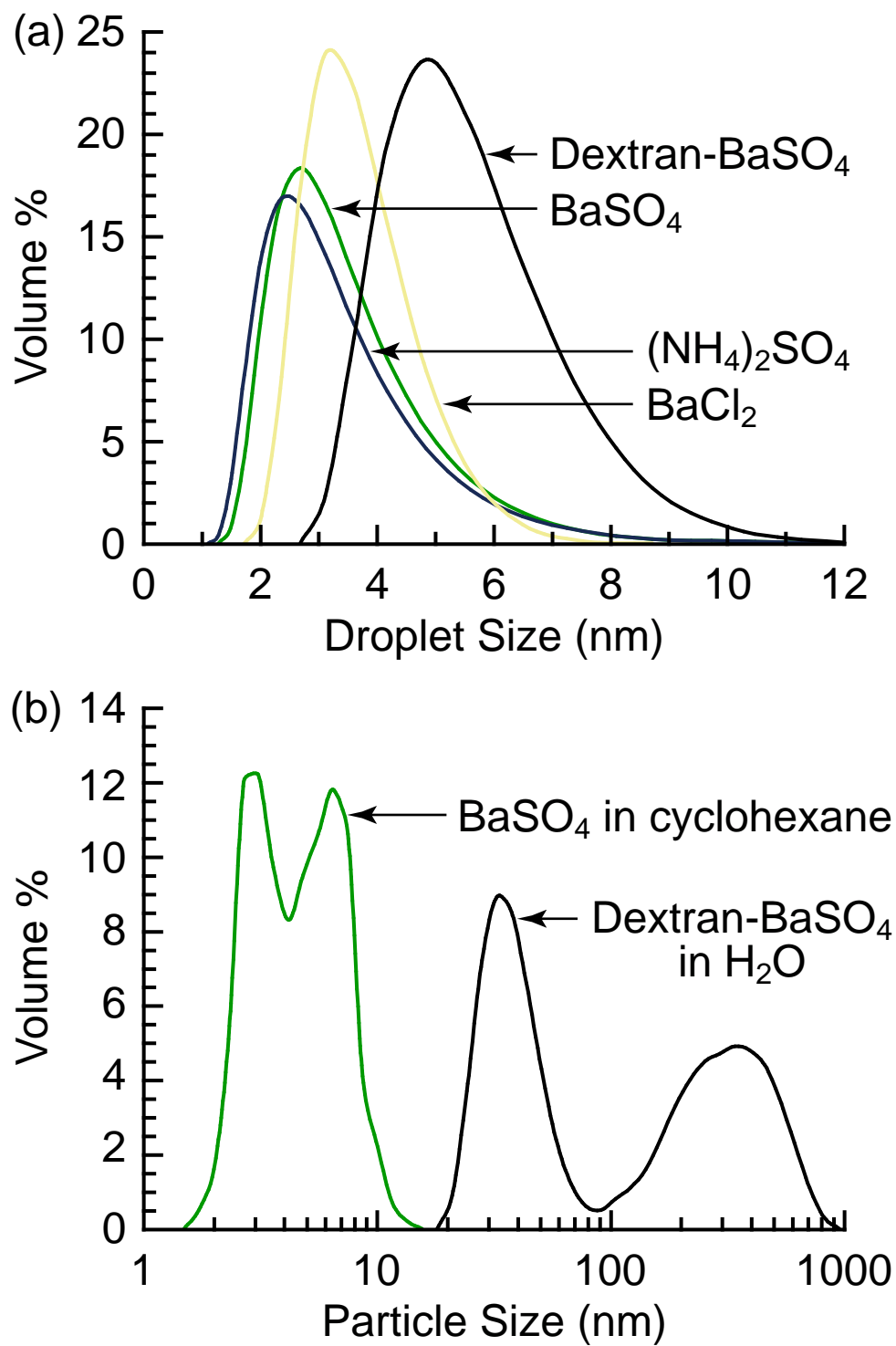
Figure 4. TEM micrographs showing (a) as-synthesized BaSO_4 nanoparticles and (b) as-synthesized, dextran-coated BaSO_4 nanoparticles.

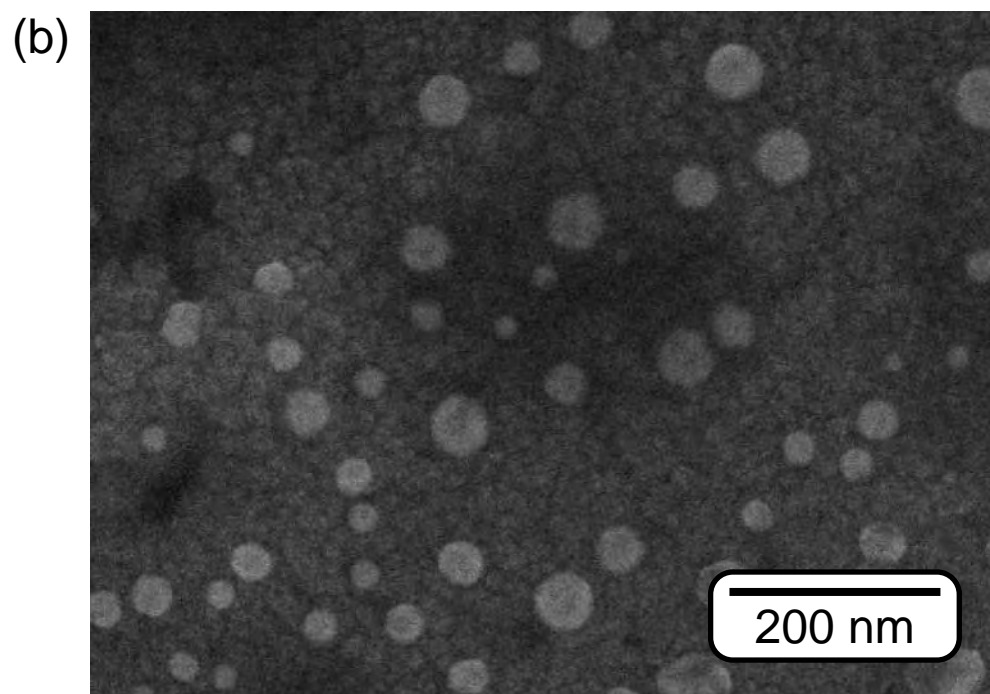
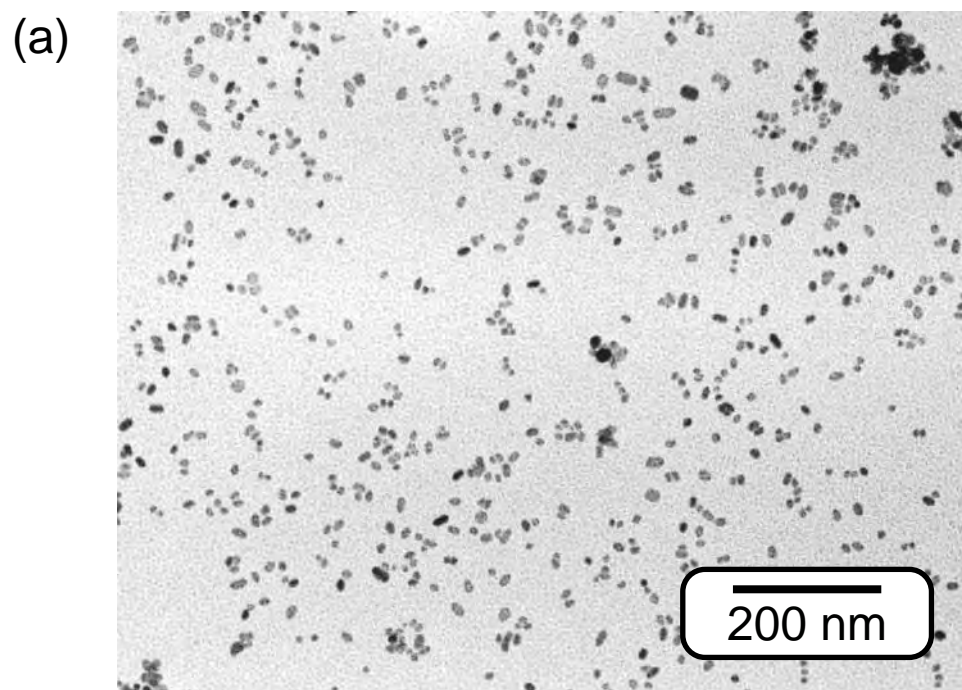
Figure 5. XRD pattern of as-synthesized BaSO_4 nanoparticles. All peaks correspond to BaSO_4 (JCPDS 24-1035)²⁹.

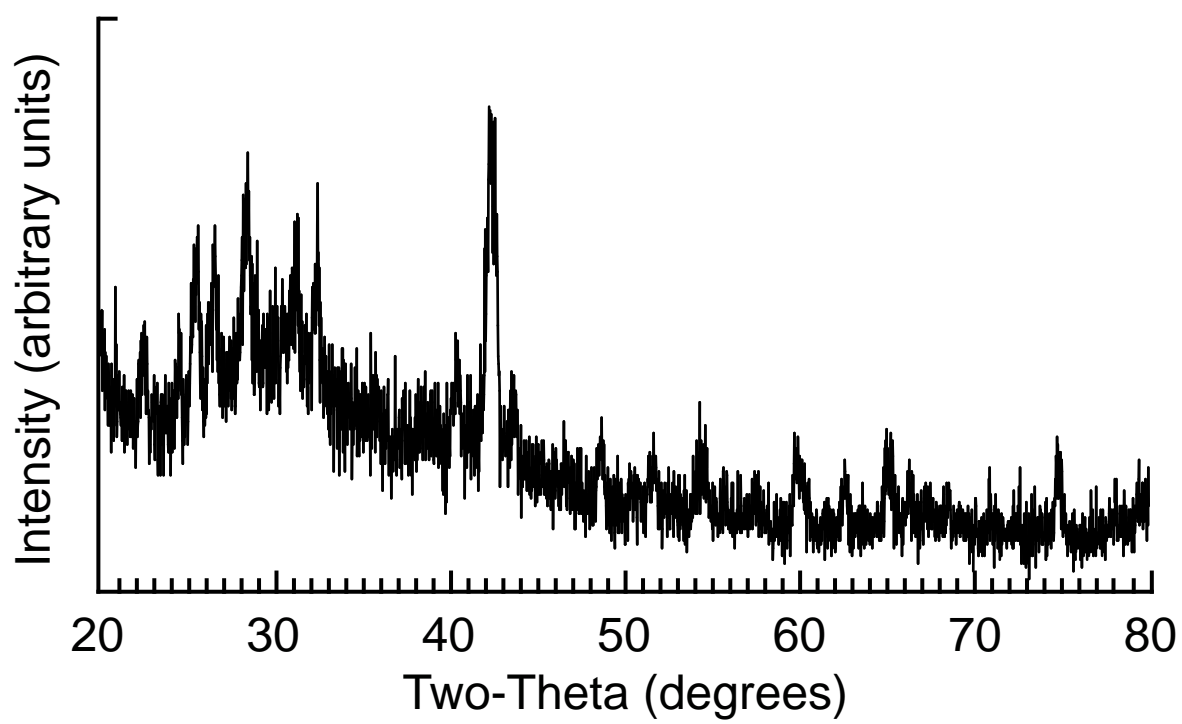
Figure 6. The X-ray attenuation of a microscale commercially available BaSO_4 suspension at a concentration of 0.01 g/mL BaSO_4 is approximately 92 ± 15 HU. The X-ray attenuation of as-synthesized BaSO_4 nanoparticles at a concentration of 0.01 g/mL BaSO_4 is approximately 243 ± 24 HU, a 2.64-fold increase over the commercially available suspension.

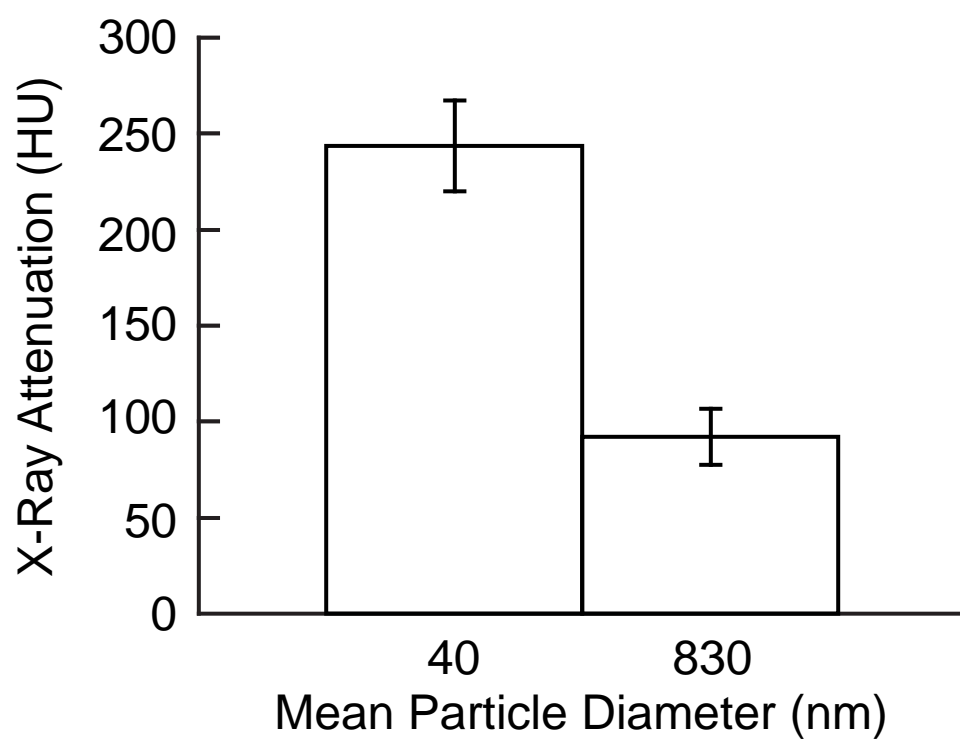












Preparation of functionalized gold nanoparticles as a targeted X-ray contrast agent for damaged bone tissue

Zhenyuan Zhang,[†] Ryan D. Ross and Ryan K. Roeder*

Received (in Cambridge, UK) 21st October 2009, Accepted 10th December 2009

First published as an Advance Article on the web 27th January 2010

DOI: 10.1039/b9nr00317g

Conventional methods used to image and quantify microdamage in bone tissue are limited to thin histological sections. Therefore recent studies have begun to investigate methods for non-destructive, three-dimensional (3-D) detection and imaging of microdamage in bone tissue. The objective of this study was to investigate gold nanoparticles (Au NPs) as a potential damage-specific X-ray contrast agent due to their relative biocompatibility, ease of surface functionalization, colloidal stability, and high X-ray attenuation. Au NPs were prepared using a citrate reduction reaction to ~15 or 40 nm diameter, and functionalized with glutamic acid for targeting damaged bone tissue. As-synthesized and functionalized Au NPs were spherical, relatively monodispersed, and exhibited aqueous colloidal stability. Functionalized Au NPs were demonstrated to target damaged bovine cortical bone tissue as visually evidenced by surface scratches turning a characteristic red color after soaking in functionalized Au NP solutions. Individual Au NPs were observed on the surface of damaged tissue using backscattered electron imaging and atomic force microscopy. Therefore, functionalized Au NPs are a promising candidate for a targeted X-ray contrast agent for damaged bone tissue.

Introduction

Repetitive loading of bone tissue can lead to the accumulation of microdamage, observed histologically as microcracks or diffuse damage, and the degradation of mechanical properties.^{1–4} Therefore, microdamage accumulation in bone has been implicated with clinical scenarios for increased risk of fracture, including stress fractures in active individuals and fragility fractures in the elderly. However, the role of microdamage in clinical bone fragility is not well understood due, in part, to limited capabilities for detecting microdamage non-destructively.

Contrast agents are used to aid detection of microdamage and differentiate artefactual damage created during specimen preparation. Current imaging techniques – including transmitted light microscopy using stains,^{5–7} epifluorescence microscopy using fluorochrome stains or chelating agents,^{8–10} laser scanning confocal microscopy using fluorochromes,^{11,12} and backscattered electron microscopy using heavy metal stains¹³ – are limited to thin histological sections, which are inherently invasive, destructive, tedious and two-dimensional.¹⁴ These limitations inhibit evaluating the effects of microdamage on whole bone strength and prohibit detecting microdamage *in vivo*.

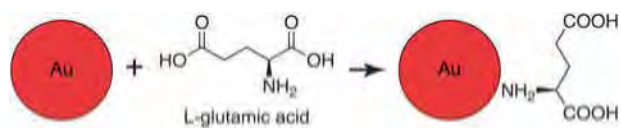
Recent studies have begun to investigate methods for non-destructive, three-dimensional (3-D) detection and imaging of microdamage in bone tissue. X-Ray tomography using high energy, monochromatic synchrotron radiation has sufficient resolution to directly image microcracks in bone,¹⁵ but is neither readily available nor amenable to imaging large numbers of

tissue specimens that are relatively large in size. Therefore, contrast agents have been investigated to enable the use of lower resolution, but commercially available, micro-computed tomography (micro-CT) instruments. Micro-CT has been used to detect microdamage *in vitro* using iodinated,^{14,16,17} lead sulfide,^{18,19} and barium sulfate^{20–22} contrast agents. In particular, non-destructive, 3-D imaging of the presence, spatial location and accumulation of microdamage in bone tissue was recently demonstrated for the first time using contrast-enhanced micro-CT with a precipitated BaSO₄ stain.^{20–22} While this approach is expected to find increased use in the study of mineralized tissues, precipitation staining is non-specific to damage and the staining solutions are not biocompatible, limiting use to *in vitro* studies. Positron emission tomography (PET) was able to detect regions of damaged tissue *in vivo* using a sodium fluoride tracer.^{23,24} However, the resolution of this technique is relatively low and tracer uptake is not specific to microcracks but rather cellular activity in the vicinity of microcracks.

A deliverable, biocompatible and damage-specific X-ray contrast agent could have potential for use *in vivo*. Typical microcracks in bone are less than 10 µm in width,¹² and nutrients are transported to bone cells through Haversian canals (~50 µm diameter) and canaliculi (~0.1–1 µm diameter).²⁵ Therefore, the contrast agent must be nanoscale in order to be delivered through vasculature to microcracks. Gold nanoparticles (Au NPs) were recently investigated as a vascular contrast agent, exhibiting high X-ray attenuation, colloidal stability and biocompatibility.^{26,27} Moreover, Au NPs are readily synthesized²⁸ and functionalized through surface adsorption of molecules with thiols²⁹ or amines.^{30,31} Fluorochromes with carboxylate functional groups (e.g., calcein) are well-known to target microcracks by chelating calcium ions on the surfaces of exposed bone mineral crystals.^{9,10} Therefore, glutamic acid,

Department of Aerospace and Mechanical Engineering, University of Notre Dame, Notre Dame, Indiana, 46556, USA. E-mail: rroeder@nd.edu; Fax: +1 (574) 631-2144; Tel: +1 (574) 631-7003

[†] Current address: Department of Chemistry, Duke University, Durham, NC 27708, USA



Scheme 1 Schematic diagram showing a Au NP surface functionalized with glutamic acid (not to scale), which exhibits a primary amine for binding to the gold surface opposite carboxylate groups for targeting microcracks by chelating calcium ions on the surfaces of exposed bone mineral crystals.

a natural amino acid with a primary amine opposite carboxylate groups, was considered a logical choice for surface functionalization of Au NPs to target microdamage in bone tissue (Scheme 1). Glutamic acid residues in proteins such as osteonectin were shown to promote binding affinity for hydroxyapatite,^{32,33} a synthetic analog for bone mineral.

Therefore, the objective of this study was to prepare and characterize functionalized Au NPs as a targeted X-ray contrast agent for damaged bone tissue. Au NPs were prepared using a citrate reduction reaction, and functionalized with glutamic acid for targeting damaged bone tissue (Scheme 1). Alternatively, damaged bone surfaces were functionalized with glutamic acid for targeting Au NPs in order to enable imaging by atomic force microscopy (AFM).

Experimental methods

Synthesis of Au NPs

Monodispersed Au NPs, ~15 nm in diameter, were synthesized by a citrate reduction reaction using the Turkevich method.²⁸ Briefly, 0.1 g $\text{HAuCl}_4 \cdot 3\text{H}_2\text{O}$ ($\geq 99.9\%$, Aldrich) was added to 400 mL of de-ionized (DI) water, heated to boiling, and 50 mL of a solution containing 1% trisodium citrate dihydrate (ACS reagent $>99.0\%$, Aldrich) was added to the boiling solution under vigorous stirring. The solution was boiled for an additional 20 min, and the volume was adjusted to 500 mL with DI water after cooling. The resultant colloidal solution was wine red with a gold concentration of ~ 0.5 mM. Larger Au NPs, ~40 nm in diameter, were prepared using a modification of the Turkevich method with a lower [citrate]/[Au] ratio.³⁴ 0.1021 g trisodium citrate dihydrate in 20 mL water was added to the 400 mL boiling solution containing 0.1018 g $\text{HAuCl}_4 \cdot 3\text{H}_2\text{O}$ under vigorous stirring. For reproducible results, the [citrate]/[Au] molar ratio was controlled at ~ 1.34 .

Functionalization of Au NPs

14 mL 2% polyvinyl alcohol (PVA 10–98, $M_w = 61\,000$, Fluka) was added to 236 mL of the as-synthesized 0.5 mM solution containing 15 or 40 nm Au NPs. 5.8 g or 1.8 g ion exchange resin (Amberlite MB-150, Sigma) was added to remove citrate ions from the 15 nm or 40 nm Au sol, respectively. The solution was stirred overnight and subsequently filtered (grade 3 filter paper, Whatman) to remove the ion exchange resin. 4 mL or 2 mL of an aqueous solution containing 10 mM L-glutamic acid ($\geq 99.5\%$, Fluka) were added to the 15 or 40 nm Au sol, respectively, and the solution was stirred for 2 days. Note that this was a large excess of glutamic acid relative to the amount calculated to be required for one full monolayer on the surface of Au NPs for

their size and concentration. Excess glutamic acid was removed using dialysis membrane tubing (Spectra/Por, MWCO = 3500 kDa, Spectrum Laboratories) in a 3000 mL beaker containing DI water, which was changed every 2–3 h for a total of 12 cycles. The functionalized Au NPs were filtered (grade 3 filter paper, Whatman) to remove particle coagulation that may have occurred during dialysis.

Labeling damaged bone tissue

Bovine cortical bone specimens were sectioned on a diamond wafer saw to $\sim 5 \times 5 \times 2$ mm, soaked in 0.5 mM calcein (ICN Biomedicals) for 20 min under vacuum (~ 50 mmHg) to mask machining damage, and rinsed in DI water. Specimens were scratched with a scalpel to induce controlled surface damage,¹⁰ exposing calcium ions in the mineral phase, and labeled using one of two methods. Damaged bone specimens were soaked for 2 days under vacuum (~ 50 mmHg) in a solution containing functionalized Au NPs (Scheme 1), 15 or 40 nm in size. After labeling damage with Au NPs, specimens were rinsed with DI water and dried under ambient conditions.

Alternatively, in order to enable imaging by AFM, damaged bone surfaces, were functionalized with glutamic acid for targeting Au NPs. 15 nm Au NPs were mixed with PVA, ion exchange resin was added to remove citrate ions, and the mixture was stirred overnight, as described above. Upon filtration, the Au NP solution was dialyzed and filtered again to further remove citrate ions. Damaged bone specimens were soaked in a solution containing 10 mM glutamic acid for 5 h. Specimens were rinsed with DI water, soaked 2 days under vacuum (~ 50 mmHg) in a solution containing Au NPs, rinsed with DI water, and dried under ambient conditions.

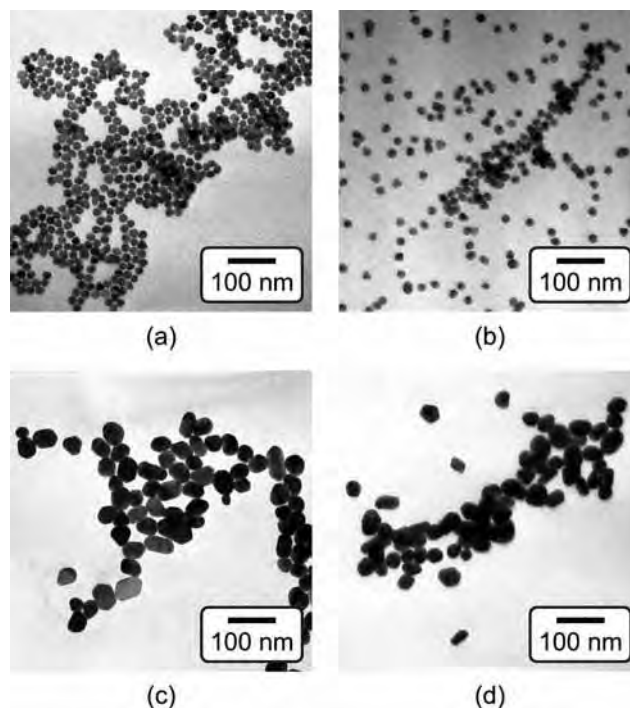


Fig. 1 TEM micrographs of as-synthesized (a) 15 nm and (c) 40 nm Au NPs, and functionalized (b) 15 nm and (d) 40 nm Au NPs, showing that the particle size did not change after functionalization.

Characterization

The mean particle diameter, particle size distribution, and morphology before and after functionalization were measured by transmission electron microscopy (TEM, Hitachi H-600) at 75 kV accelerating voltage (Fig. 1). Specimens were prepared by immersing carbon-coated grids in Au NP solutions. The maximum and minimum particle diameters were measured for a sample size of 116 particles per group. The mean particle diameter and aspect ratio were calculated as the mean and ratio, respectively, of the average of maximum and minimum diameter. The particle size distribution was measured using both TEM and dynamic light scattering (DLS, Zetasizer Nano-ZS, Malvern Instruments) (Fig. 2). Ultraviolet-visible (UV-Vis) absorption spectra (Varian Cary 50 Spectrophotometer) were collected before and after functionalization to verify colloidal stability and the concentration of Au NPs in solution using Beer's Law (Fig. 3).

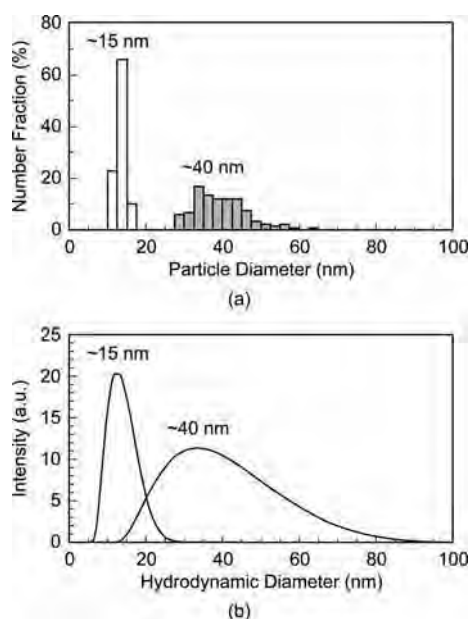


Fig. 2 Particle size distributions of as-synthesized 15 and 40 nm Au NPs measured by (a) TEM and (b) dynamic light scattering (DLS). Note that DLS measures the hydrodynamic particle diameter, which was in close agreement with TEM.

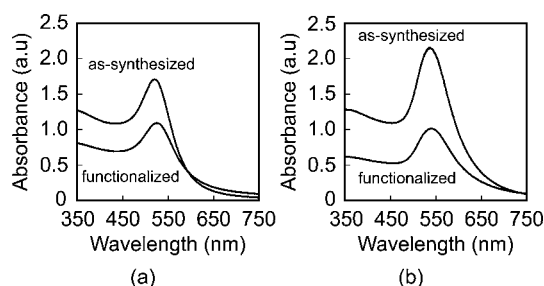


Fig. 3 UV-vis spectra of (a) 15 nm and (b) 40 nm Au NPs, showing no change in the position of plasmon bands between as-synthesized and functionalized Au NPs. Absorbance was normalized to a 1 cm optical path.

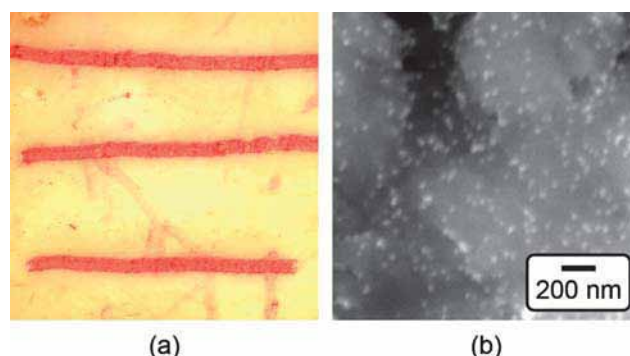


Fig. 4 (a) Optical micrograph of scratches on the surface of a bovine cortical bone specimen labeled by 15 nm functionalized Au NPs, as shown by the characteristic red color. The width of the image is approximately 7 mm. (b) Backscattered SEM micrograph showing the surface of a scratch labeled by 15 nm functionalized Au NPs (bright spots).

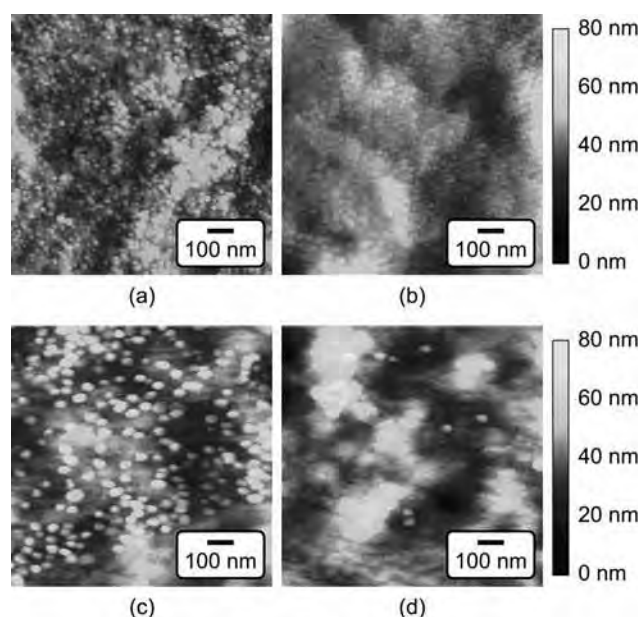


Fig. 5 Tapping mode AFM images of the (a,c) damaged and (b,d) undamaged tissue surfaces on bovine cortical bone specimens labeled by (a,b) 15 nm and (c,d) 40 nm functionalized Au NPs. Note that images of undamaged tissue surface showed little or no presence of Au NPs.

Damaged bone tissue labeled by Au NPs was characterized using reflected light microscopy (SMZ 800, Nikon Instruments Inc.), and scanning electron microscopy (SEM, Evo 50, LEO Electron Microscopy Ltd.) with backscattered electron imaging (BEI) at an accelerating voltage of 20 kV and working distance of 6.5 mm (Fig. 4). Note that image contrast in BEI is primarily due to compositional differences in atomic number, with increasing atomic number resulting in increased intensity. Damaged bone tissue labeled by Au NPs was also imaged using tapping mode AFM (AFM, Nanoscope[®] IIIa, Digital Instruments) (Fig. 5).

Results and discussion

As-synthesized and functionalized Au NPs were spherical, relatively monodispersed, and exhibited aqueous colloidal stability.

The mean (\pm standard deviation) particle diameter of as-synthesized Au NPs measured from TEM micrographs was 13.4 (\pm 1.2) and 39.5 (\pm 7.1) nm (Fig. 1 and Fig. 2a). The particle size distributions measured by TEM and DLS were in close agreement, showing a narrow size distribution for 15 nm Au NPs and a broader size distribution for 40 nm Au NPs (Fig. 2). As-synthesized Au NPs were mostly spherical with some evidence of faceting, which was more pronounced for 40 nm Au NPs (Fig. 1). The mean (\pm standard deviation) aspect ratio of as-synthesized Au NPs measured from TEM micrographs was 1.1 (\pm 0.1) and 1.3 (\pm 0.2) for 15 and 40 nm particles, respectively. There was no apparent change in the particle size or morphology observed by TEM after functionalization (Fig. 1). Moreover, characteristic plasmon bands were observed at 520 and 536 nm for as-synthesized 15 and 40 nm Au NPs, respectively, and exhibited no apparent changes after functionalization, indicating colloidal stability (Fig. 3).

As-synthesized Au NPs were surface functionalized with L-glutamic acid in order to target damaged bone tissue (Scheme 1). However, citrate ions, which functioned as both a reducing agent and stabilizer in the preparation of Au NPs,²⁸ have three carboxylate groups which exhibit binding affinity for damaged bone tissue. Therefore, citrate ions were first removed in order to prevent interference with functionalized Au NPs for targeting damaged bone tissue. PVA was added to sterically stabilize the as-synthesized Au NPs while removing citrate ions by ion exchange resin. PVA is uncharged and was therefore not expected to interfere with the functionalization step or the binding of functionalized Au NPs to damage tissue. (Note that subsequent work has demonstrated the ability to add glutamic acid in the presence of citrate and remove both citrate and excess glutamic acid by dialysis, avoiding the addition of PVA.) After adding a large excess of glutamic acid relative to the amount required for one full monolayer coverage on Au NP surfaces, solutions were dialyzed to remove excess glutamic acid. Note that glutamic acid has amine and carboxylate functional groups which both exhibit affinity for gold surfaces. However, amines exhibit a stronger affinity to gold surfaces, displacing carboxylates.^{35,36} Therefore, the primary amine group was expected to adsorb to the Au NP surface, leaving carboxylate groups available for chelating calcium ions on the surfaces of exposed bone mineral crystals (Scheme 1). The concentration of Au NPs remaining in solution after functionalization was 64 and 47% of the as-synthesized concentration (0.5 mM) for 15 and 40 nm Au NPs, respectively (Fig. 3). After the final dialysis and filtration steps, 47 and 39% of the as-synthesized concentration remained for 15 and 40 nm Au NPs, respectively (not shown).

Specificity for damaged bone tissue was demonstrated with bovine cortical bone specimens by masking machining damage with calcein, scratching the surface with a scalpel, and soaking the specimen in functionalized Au NP solutions. Functionalized Au NPs were able to target surface scratches as visually evidenced by a characteristic red color (Fig. 4a). Similar results were obtained for either 15 or 40 nm functionalized Au NPs. Backscattered electron imaging also detected high contrast between the scratch and adjacent tissue, where increased brightness in the scratch was indicative of the higher atomic number of Au NPs compared to calcium phosphate. At higher magnification, individual Au NPs bound to the damaged tissue

were imaged as bright spots on the surface of scratched tissue (Fig. 4b). AFM of damaged tissue labeled by functionalized Au NPs was unsuccessful for reasons that remained unclear. Possible reasons included a relatively greater variability in surface roughness or lower density in surface coverage of functionalized Au NPs.

Damaged bone surfaces were also functionalized with glutamic acid prior to labeling with Au NPs in order to enable high resolution imaging by AFM. The carboxylate groups of glutamic acid were expected to chelate calcium ions on the surfaces of exposed bone mineral crystals, similar to fluorochromes such as calcein. Bone specimens were subsequently soaked in Au NP solutions such that Au NPs were able to bind with amine groups on glutamic acid and thus target damaged bone surfaces. AFM images showed individual Au NPs bound to damaged tissue surfaces and little or no Au NPs on undamaged tissue surfaces (Fig. 5). The surface coverage on damaged tissue appeared to be more dense than labeling with functionalized Au NPs. However, the use of functionalized Au NPs is more desirable for a deliverable contrast agent. Furthermore, note that the glutamic acid solution exhibited pH \sim 3.5 which could demineralize the tissue over greater lengths of time than those utilized in this study.

This work is the first to our knowledge to demonstrate targeted labeling of damaged bone tissue using a nanoparticle X-ray contrast agent. A biocompatible, deliverable, and damage-specific contrast agent with greater X-ray attenuation than bone could enable non-destructive, three-dimensional and non-invasive (*in vivo*) imaging of microdamage in bone. Such a contrast agent would have the potential to enable clinical assessment of bone quality and damage accumulation, and scientific study of damage processes *in situ*. However, this ambitious goal will require much further work. The relative binding affinities of various potential functional groups, such as carboxylates and bisphosphonates, must be investigated. Preliminary efforts have highlighted the difficulty of obtaining sufficient signal for detection by commercially available, polychromatic micro-computed tomography (micro-CT) instruments with \sim 10 μ m resolution despite the relatively high X-ray attenuation of gold, due to the necessarily small size and concentration of Au NPs labeling damaged bone tissue. Therefore, the use of monochromatic synchrotron radiation may be advantageous in order to maximize contrast by edge subtraction imaging just above and below the energy of gold absorption peaks.

Conclusions

Au NPs were prepared using a citrate reduction reaction to \sim 15 or 40 nm diameter, and functionalized with glutamic acid for targeting damaged bone tissue. As-synthesized and functionalized Au NPs were spherical, relatively monodispersed, and exhibited aqueous colloidal stability. Functionalized Au NPs were demonstrated to target damaged bone tissue, which was verified by visual staining, backscattered electron imaging and atomic force microscopy of surface scratches compared to undamaged tissue. Therefore, functionalized Au NPs are a promising candidate for a targeted X-ray contrast agent for damaged bone tissue.

Acknowledgements

This research was supported by the U.S. Army Medical Research and Materiel Command (W81XWH-06-1-0196) through the Peer Reviewed Medical Research Program (PR054672). TEM was made available through the Notre Dame Integrated Image Facility (NDIIF). The Notre Dame Radiation Laboratory (NDRL) is gratefully acknowledged for use of the AFM and UV-vis spectroscopy.

References

- 1 D. B. Burr, M. R. Forwood, D. P. Fyhrie, R. B. Martin, M. B. Schaffler and C. H. Turner, *J. Bone Miner. Res.*, 1997, **12**, 6–15.
- 2 D. B. Burr, C. H. Turner, P. Naick, M. R. Forwood, W. Ambrosius, M. S. Hasan and R. Pidaparti, *J. Biomech.*, 1998, **31**, 337–345.
- 3 T. C. Lee, F. J. O'Brien and D. Taylor, *Int. J. Fatigue*, 2000, **22**, 847–853.
- 4 R. B. Martin, *Calcif. Tissue Int.*, 2003, **73**, 101–107.
- 5 H. M. Frost, *Henry Ford Hosp. Med. Bull.*, 1960, **8**, 25–35.
- 6 D. B. Burr and T. Stafford, *Clin. Orthop. Relat. Res.*, 1990, 305–308.
- 7 D. B. Burr and M. Hooser, *Bone*, 1995, **17**, 431–433.
- 8 T. C. Lee, E. R. Myers and W. C. Hayes, *J. Anat.*, 1998, **193**, 179–184.
- 9 T. C. Lee, T. L. Arthur, L. J. Gibson and W. C. Hayes, *J. Orthop. Res.*, 2000, **18**, 322–325.
- 10 F. J. O'Brien, D. Taylor and T. C. Lee, *J. Biomech.*, 2002, **35**, 523–526.
- 11 P. Zioupos and J. D. Currey, *J. Mater. Sci.*, 1994, **29**, 978–986.
- 12 F. J. O'Brien, D. Taylor, G. R. Dickson and T. C. Lee, *J. Anat.*, 2000, **197**, 413–420.
- 13 M. B. Schaffler, W. C. Pitchford, K. Choi and J. M. Riddle, *Bone*, 1994, **15**, 483–488.
- 14 T. C. Lee, S. Mohsin, D. Taylor, R. Parkesh, T. Gunnlaugsson, F. J. O'Brien, M. Giehl and W. Gowin, *J. Anat.*, 2003, **203**, 161–172.
- 15 R. K. Nalla, J. S. Stölken, J. H. Kinney and R. O. Ritchie, *J. Biomech.*, 2005, **38**, 1517–1525.
- 16 R. Parkesh, T. C. Lee, T. Gunnlaugsson and W. Gowin, *J. Biomech.*, 2006, **39**, 1552–1556.
- 17 R. Parkesh, W. Gowin, T. C. Lee and T. Gunnlaugsson, *Org. Biomol. Chem.*, 2006, **4**, 3611–3617.
- 18 H. Leng, J. J. VanDersarl, G. L. Niebur and R. K. Roeder, *Trans. Orthop. Res. Soc.*, 2005, **30**, 665.
- 19 S. Y. Tang and D. Vashishth, *Bone*, 2007, **40**, 1259–1264.
- 20 X. Wang, D. B. Masse, H. Leng, K. P. Hess, R. D. Ross, R. K. Roeder and G. L. Niebur, *J. Biomech.*, 2007, **40**, 3397–3403.
- 21 H. Leng, X. Wang, R. D. Ross, G. L. Niebur and R. K. Roeder, *J. Mech. Behav. Biomed. Mater.*, 2008, **1**, 68–75.
- 22 M. D. Landrigan, G. L. Niebur and R. K. Roeder, *Trans. Orthop. Res. Soc.*, 2009, **34**, 332.
- 23 J. Li, M. A. Miller, G. D. Hutchins and D. B. Burr, *Bone*, 2005, **37**, 819–824.
- 24 M. J. Silva, B. A. Uthgenannt, J. R. Rutlin, G. R. Wohl, J. S. Lewis and M. J. Welch, *Bone*, 2006, **39**, 229–236.
- 25 M. L. K. Tate, P. Niederer and U. Knothe, *Bone*, 1998, **22**, 107–117.
- 26 J. F. Hainfield, D. N. Slatkin and H. M. Smilowitz, *Phys. Med. Biol.*, 2004, **49**, N309–N315.
- 27 J. F. Hainfield, D. N. Slatkin, T. M. Focella and H. M. Smilowitz, *Br. J. Radiol.*, 2006, **79**, 248–253.
- 28 J. Turkevich, P. C. Stevenson and J. Hillier, *Discuss. Faraday Soc.*, 1951, **11**, 55–75.
- 29 M. Brust, J. Fink, D. Bethell, D. J. Schiffrin and C. Kiely, *J. Chem. Soc., Chem. Commun.*, 1995, 1655–1656.
- 30 D. V. Leff, L. Brandt and J. R. Heath, *Langmuir*, 1996, **12**, 4723–2730.
- 31 M. Aslam, L. Fu, M. Su, K. Vijayamohan and V. P. Dravid, *J. Mater. Chem.*, 2004, **14**, 1795–1997.
- 32 M. E. Bolander, M. F. Young, L. W. Fisher, Y. Yamada and J. D. Termine, *Proc. Natl. Acad. Sci. U. S. A.*, 1988, **85**, 2919–2923.
- 33 R. Fujisawa, Y. Wada, Y. Nodasaka and Y. Kuboki, *Biochim. Biophys. Acta, Protein Struct. Mol. Enzymol.*, 1996, **1292**, 53–60.
- 34 G. Frens, *Nature Phys. Sci.*, 1973, **241**, 20–22.
- 35 L. M. Liz-Marzán, M. Giersig and P. Mulvaney, *Langmuir*, 1996, **12**, 4329–4335.
- 36 Z. Y. Zhang, A. Berg, H. Levanon, R. W. Fessenden and D. Meisel, *J. Am. Chem. Soc.*, 2003, **125**, 7959–7963.

**Highlights in
Chemical Science**

Chemical science news from across RSC Publishing.



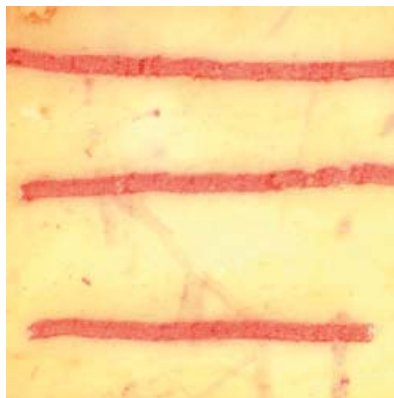
Gold nanoparticles highlight bone damage

29 January 2010

American scientists have demonstrated three-dimensional imaging of damaged bone tissue using functionalised gold nanoparticles that could be used in vivo.

Repetitive stress to bone tissue causes tiny cracks or scratches, known as microdamage, which increases the risk of fractures and can be a major concern for the physically active and elderly. Research into how this condition relates to bone fragility is critical for the early diagnosis of fractures.

Current imaging techniques are limited to thin sections of bone and are invasive and destructive explains Ryan Roeder at the University of Notre Dame. By attaching glutamic acid to gold nanoparticles, Roeder's team synthesised an X-ray contrast agent that could be used to accurately image microdamage non-destructively in vivo.



Scratched bone tissue can be imaged using the new technique

The amine group anchors the amino acid to the gold, leaving the carboxylate free to attach to the bone mineral that becomes exposed when the surface is damaged, explains Roeder. This allows the damage to be detected using X-ray techniques, such as CT scans. The particle's nanoscale size also means that it can be transported via blood capillaries into micro-sized cracks.

'There isn't an alternative known system to do non-destructive three dimensional imaging of damage,' says Roeder.

Thorfinnur Gunnlaugsson, an expert in medicinal chemistry at the University of Dublin, Ireland recognises the merits of Roeder's achievements. 'This is a real step forward. I'm delighted to see this work,' he enthuses.

'The beauty of the nanoparticles is they have a very large surface area, so you can populate them very highly [with amino acid], which means you can get higher concentrations and to a more targeted area,' he adds.

Having demonstrated the effectiveness of the nanoparticle system, Roeder and his team are now looking at its deliverability through tissue, further increasing its potential for use in vivo.

Yuandi Li

Enjoy this story? Spread the word using the 'tools' menu on the left or add a comment to the Chemistry World blog.

[Link to journal article](#)

Preparation of functionalized gold nanoparticles as a targeted X-ray contrast agent for damaged bone tissue

Zhenyuan Zhang, Ryan D. Ross and Ryan K. Roeder, *Nanoscale*, 2010

DOI: 10.1039/b9nr00317g



Journal of Biomedical
Materials Research
Part A

Binding Affinity of Surface Functionalized Gold Nanoparticles for Hydroxyapatite

Journal:	<i>Journal of Biomedical Materials Research: Part A</i>
Manuscript ID:	JBMR-A-10-0690
Wiley - Manuscript type:	Original Article
Date Submitted by the Author:	14-Oct-2010
Complete List of Authors:	Ross, Ryan; University of Notre Dame, Aerospace and Mechanical Engineering Roeder, Ryan; University of Notre Dame, Aerospace and Mechanical Engineering
Keywords:	Gold Nanoparticles, Hydroxyapatite, Targeted Delivery, Contrast Agent, Bisphosphonate

SCHOLARONE™
Manuscripts

Binding Affinity of Surface Functionalized Gold Nanoparticles for Hydroxyapatite

Ryan D. Ross and Ryan K. Roeder

Department of Aerospace and Mechanical Engineering
Bioengineering Graduate Program
University of Notre Dame
Notre Dame, Indiana 46556

Submitted to: *Journal of Biomedical Materials Research, Part A*

Running Title: Hydroxyapatite binding affinity of functionalized gold nanoparticles

Keywords: Gold Nanoparticles; Hydroxyapatite; Binding Affinity; Targeted Delivery; Contrast Agent; Bisphosphonate

Correspondence: Ryan K. Roeder, Ph.D.
Associate Professor
Department of Aerospace and Mechanical Engineering
Bioengineering Graduate Program
148 Multidisciplinary Research Building
University of Notre Dame
Notre Dame, Indiana 46556

Phone: (574) 631-7003
Fax: (574) 631-2144
Email: rroeder@nd.edu

Funding Sources: U.S. Army Medical Research and Materiel Command (W81XWH-06-1-0196) through the Peer Reviewed Medical Research Program (PR054672)

ABSTRACT

Gold nanoparticles (Au NPs) have been investigated for a number of biomedical applications, including drug and gene delivery vehicles, thermal ablation therapy, diagnostic sensors, and imaging contrast agents. Surface functionalization with molecular groups exhibiting calcium affinity can enable targeted delivery of Au NPs to calcified tissue, including damaged bone tissue. Therefore, the objective of this study was to investigate the binding affinity of functionalized Au NPs for targeted delivery to bone mineral, using hydroxyapatite (HA) crystals as a synthetic analog *in vitro*. Au NPs were synthesized to a mean particle size between 10-15 nm and surface functionalized with either L-glutamic acid, 2-aminoethylphosphonic acid, or alendronate, which exhibit a primary amine for binding gold opposite carboxylate, phosphonate, or bisphosphonate groups, respectively, for targeting calcium. Bisphosphonate functionalized Au NPs exhibited the most rapid binding kinetics and greatest binding affinity for HA, followed by glutamic acid and phosphonic acid. All functional groups reached complete binding after 24 h. Equilibrium binding constants in de-ionized water, determined by linear regression of Langmuir isotherms, were 3.82, 0.72, 0.25 mg/L for bisphosphonate, carboxylate, and phosphonate functionalized Au NPs, respectively. Functionalized Au NPs exhibited lower overall binding in fetal bovine serum compared to de-ionized water, but relative differences between functional groups were similar.

INTRODUCTION

Gold nanoparticles (Au NPs) have been investigated for a number of biomedical applications,^{1,2} including drug and gene delivery vehicles,^{3,4} thermal ablation therapies,^{4,5} diagnostic sensors,^{6,7} and imaging contrast agents.⁸⁻¹¹ The utility of Au NPs in these applications is derived from multiple factors including the ease of synthesizing monodispersed nanoparticles, colloidal stability, biocompatibility, surface plasmon resonance, and high X-ray attenuation. Moreover, Au NPs are readily surface functionalized with molecular groups for cellular targeting and delivery, as well as enhancing colloidal stability. Surface functionalization with molecular groups exhibiting calcium affinity could enable targeted delivery of Au NPs to mineralized tissue, including fatigue microdamage in bone tissue,¹² as well as calcifications in soft tissue associated with cancer or musculoskeletal injury.

Microdamage accumulates in bone tissue during repetitive loading in the form of microcracks and diffuse damage.^{13,14} The accumulation of microdamage has been implicated in clinical fracture susceptibility, including fatigue fractures in active individuals, such as military recruits, fragility fractures in the elderly, and the effects of long-term antiresorptive treatments for osteoporosis.^{13,14} However, the role of microdamage in clinical bone fragility remains poorly understood due, in part, to limitations in available methods for detection and imaging.¹⁴

Current methods for imaging microdamage in bone tissue are limited to histological sections, which are inherently two-dimensional (2-D), destructive, invasive, and tedious.¹⁵ The first and most common method has been *en bloc* staining with basic fuchsin in ethanol.¹⁵⁻¹⁷ Basic fuchsin exhibits protein affinity, but primarily acts as a space-occupying dye.¹⁵ Therefore, microdamage must be distinguished from non-specific staining under observation in transmitted light or epifluorescent microscopy. More recently, fluorophores, such as xyleneol and calcein,

which employ iminodiacetate moieties for calcium-chelation, have been used as damage-specific labels for epifluorescent microscopy.^{15,18,19} Moreover, sequential labeling with fluorophores exhibiting differing binding affinity enabled the measurement of spatiotemporal variation in damage events, including crack propagation^{18,19} and modes of loading.²⁰ Additionally, calcium-specific photoinduced electron transfer sensor molecules have been investigated for the ability to “switch-on” fluorescence upon chelation to calcium ions in damaged tissue.^{21,22} However, both light and epifluorescent microscopy are inherently 2-D. Three-dimensional (3-D) spatial information can only be ascertained from serial sectioning^{23,24} which is destructive and tedious. Laser scanning confocal microscopy has been used to provide limited depth of field for 3-D imaging of damage in histological sections labeled with fluorophores.^{25,26}

X-ray computed tomography has been proposed for non-destructive and 3-D imaging of damage using contrast agents with higher X-ray attenuation than bone tissue. The presence, spatial variation, and accumulation of microdamage in both cortical and trabecular bone specimens was detected using micro-computed tomography (micro-CT) after staining tissue with a precipitated barium sulfate (BaSO_4) contrast agent.²⁷⁻²⁹ While this technique enabled non-destructive and 3-D detection of microdamage *in vitro*, the precipitated BaSO_4 stain was not damage-specific and the staining solutions were not biocompatible. Iodinated molecules were investigated as a damaged-specific X-ray contrast agent,^{30,31} but were only detected using micro-CT when precipitated in powder form.

Functionalized Au NPs were recently investigated as a targeted X-ray contrast agent for labeling microdamage in bone tissue.¹² Gold exhibits greater X-ray attenuation than other commonly used X-ray contrast agents containing barium and iodine.³² Au NPs exhibited high X-ray attenuation and biocompatibility as an intravascular X-ray contrast agent in mice after intravenous administration.⁹⁻¹¹ Functionalized Au NPs also exhibit relatively high water

solubility and low viscosity compared to iodinated molecular contrast agents. Finally, gold surfaces are readily functionalized through adsorption of thiols³³⁻³⁵ and amines,³⁶⁻³⁹ which can be used to attach molecules which target calcium ions on bone mineral crystals exposed on the surface of microcracks.

The objective of this study was to investigate the binding affinity of functionalized Au NPs for targeted delivery to bone mineral, using hydroxyapatite crystals as a synthetic analog *in vitro*. Au NPs were surface functionalized with either L-glutamic acid, 2-aminoethylphosphonic acid, or alendronate (Fig. 1). Glutamic acid is a naturally occurring amino acid with known affinity for calcium phosphates.^{40,41} Moreover, glutamic acid functionalized Au NPs were previously shown to target damaged bone tissue.¹² However, phosphonate and particularly bisphosphonate groups are known to provide strong binding affinity to calcium phosphates.⁴²⁻⁴⁴ Bisphosphonates, such as alendronate, are widely used clinically to suppress bone resorption as a pharmacological treatment for osteoporosis and other bone-related diseases.¹⁴

EXPERIMENTAL METHODS

Gold Nanoparticle (Au NP) Synthesis and Functionalization

Au NPs were synthesized to a mean particle diameter of 10-15 nm using the citrate reduction method.⁴⁵ Briefly, 0.1 g $\text{HAuCl}_4 \cdot 3\text{H}_2\text{O}$ ($\geq 99.9\%$, Aldrich) was added to 400 mL of deionized (DI) water and the solution was boiled vigorously while stirring. A 1% solution of trisodium citrate dehydrate (ACS reagent, $>99.0\%$, Sigma) was added to the boiling solution at a mass ratio of 5:1 HAuCl_4 to sodium citrate and left boiling for an additional 20 min. The solution volume was then adjusted to a total of 500 mL using DI water. The resulting Au NP solution had a gold concentration of ~ 0.5 mM and a wine red color.

Au NPs were prepared for functionalization by first removing excess citrate ions. 1.5 mL 2% polyvinyl alcohol (PVA 10-98, $M_w = 61000$, Fluka) was added to 24 mL Au NP solution, followed by 0.6 g ion exchange resin (Amberlite MB-150, Sigma). The resulting solution was stirred overnight and subsequently filtered (Grade 3, Whatman) to remove spent ion exchange resin. Au NPs were surface functionalized by adding 1 mL of a 0.01 M solution of either L-glutamic acid ($\geq 99.5\%$, Fluka), 2-aminoethylphosphonic acid (99%, Aldrich), or alendronate sodium trihydrate ($\geq 97\%$, Sigma) (Fig. 1). The solution was left to equilibrate under mild stirring overnight. Excess functionalization molecules were removed by dialysis tubing (Spectra/Por, MWCO = 3500, Spectrum Laboratories) against DI water for a total of three days, changing the water solution at least twice daily.

The mean particle diameter and particle size distributions were measured before and after functionalization by transmission electron microscopy (TEM, Hitachi H-600) at 75 kV accelerating voltage. TEM specimens were prepared by dropping a solution of functionalized Au NPs onto carbon-coated grids and evaporating the solvent. The particle diameter and aspect ratio were characterized by the mean and standard deviation from measurements on a total of 100 particles per functional group. Ultraviolet-visible (UV-vis) spectra (Varian Cary 3 spectrophotometer) were collected before and after functionalization to verify colloidal stability and relative concentrations of the particles within solution.

Surface functionalization of Au NPs was verified using diffuse reflectance infrared Fourier transform spectroscopy (DRIFTS, Bruker Tensor 27) at 4 cm^{-1} with 64 total scans. Particles were functionalized as outlined above, except without the presence of PVA and without the use of ion exchange resin prior to functionalization and dialysis, in order to prevent PVA from interfering with the detection of functional groups. After dialysis, functionalized Au NPs were collected by evaporation at 40°C and 25 in Hg below atmospheric pressure. The dried

powders were diluted in KBr (IR grade, 99+%, Acros Organics) at a ratio of ~1:200 by mass. Fourier transform-infrared (FT-IR) spectra were collected over frequencies of 4000-500 cm^{-1} and normalized to the background spectra for KBr alone. FT-IR peaks used to identify functional groups on Au NPs were determined by comparison to corresponding FT-IR spectra for stock solutions of the functional molecules.

Binding Affinity of Functionalized Au NPs

Two separate binding experiments were performed to investigate the binding affinity of functionalized Au NPs for bone mineral, using hydroxyapatite (HA) crystals as a synthetic analog. Calcium-deficient HA single crystal whiskers were synthesized using the chelate decomposition method, as described in detail elsewhere.⁴⁶ As-synthesized HA crystals exhibited a mean length of ~18 μm and mean width of ~2 μm .⁴⁶ The specific surface area of the crystals was 5.63 m^2/g as measured by Brunauer-Emmett-Teller (BET) N_2 adsorption (Autosorb-1, Quantachrome Instruments).

The first set of experiments investigated the kinetics of binding. 10 ± 0.1 mg HA whiskers were added to DI water, followed by a measured volume of functionalized Au NP solution, for a final volume of 15 ml containing a gold concentration of 0.1 mg/L. Solutions were placed onto a test tube rotator and allowed to incubate for 0.25, 0.5, 1, 2, 4, 8, 12, and 24 h. After the predetermined time, solutions were centrifuged at 2,000 rpm for 2 min to separate HA crystals and bound Au NPs from Au NPs remaining in solution. Percent binding was defined as the concentration (mg Au/L) of Au NPs remaining in the supernatant solution after binding, subtracted from the initial concentration of Au NPs in solution, and divided by the initial

concentration of Au NPs. Binding of functionalized Au NPs to the surface of HA crystals was verified by TEM after dispersing the collected HA crystals onto carbon-coated grids.

A second set of experiments investigated the effect of concentration on binding affinity by plotting the binding isotherm for each functional group. The binding affinity of functionalized Au NPs for HA crystals was determined separately in DI water and 10% fetal bovine serum (FBS, Omega Scientific). The binding affinity of as-synthesized, citrate stabilized Au NPs was also measured as a control. Experiments were performed using the same methods outlined above for the binding kinetics, except the incubation time was held constant at 4 h and the initial gold concentration was varied. The kinetics of binding revealed that after 4 h 30-80% of Au NPs were bound to HA crystals depending on the functional group. This incubation time was also comparable to previous studies investigating bisphosphonate functionalized protein binding to HA surfaces.^{43,44}

Binding isotherms were plotted as the amount of gold bound per mass of HA crystals added, V (mg Au/g HA), versus the initial gold concentration, $[S]$ (mg Au/L), for both DI water and FBS. Plotted binding data was modeled as a Langmuir isotherm,

$$V = \frac{V_{\max}[S]}{K + [S]} \quad (1)$$

where V is the amount of functionalized Au NPs bound per mass of HA crystals (mg/g), V_{\max} is the maximum surface binding (mg/g), $[S]$ is the initial concentration of gold (mg/L), and K is the equilibrium binding constant (mg/L). The equilibrium binding constant, K , and maximum binding of functionalized Au NPs on HA crystals, V_{\max} , were measured from Langmuir isotherms using linear least squares regression,

$$\frac{[S]}{V} = \frac{K}{V_{\max}} + \frac{[S]}{V_{\max}} \quad (2)$$

plotting the value of the initial gold concentration in solution over the amount of gold bound for each test, $[S]/V$, versus the initial gold concentration, $[S]$.

The gold concentration in control and supernatant solutions was measured using inductively coupled plasma-optical emission spectroscopy (ICP-OES, Optima 7000, PerkinElmer). Solutions were acidified to 2% v/v HCl prior to analysis. Calibration curves were created by diluting certified standard gold solutions (SPEX CertiPrep). All binding tests were performed in triplicate, reporting the mean and first standard deviation.

RESULTS AND DISCUSSION

Characterization of Functionalized Au NPs

Functionalized Au NPs were spherical and relatively monodispersed (Fig. 2). There was no apparent change in particle size or morphology between as-synthesized and functionalized Au NPs. The mean (\pm standard deviation) particle diameter was 11.40 (\pm 1.36), 13.57 (\pm 1.43), and 12.79 (\pm 1.58) nm for glutamic acid, phosphonic acid, and bisphosphonate functionalized Au NPs, respectively, with an aspect ratio of 1.09 (\pm 0.07), 1.12 (\pm 0.10), and 1.09 (\pm 0.07), respectively. The plasmon resonance peak remained constant at \sim 530 nm for functionalized Au NPs, indicating that the colloidal suspension remained stable and free from coagulation after functionalization (Fig. 3). The plasmon resonance band broadened slightly upon surface functionalization, due to the adsorption of amine groups.

Gold surface adsorption was expected to occur through the terminal amine group present in each functional molecule (Fig. 1). Previous studies have suggested that the amine-gold surface interaction is relatively strong and stable.³⁶⁻³⁹ Adsorption of terminal amines facilitated the availability of carboxylate, phosphonate, and bisphosphonate groups for binding to calcium

on HA crystals, which was qualitatively verified by FT-IR (Fig. 4). As-synthesized, citrate stabilized Au NPs exhibited peaks corresponding to alkyl groups which were not apparent for functionalized Au NPs. The hydroxyl peak was broadened and shifted to lower wavenumbers for functionalized Au NPs due to the presence of primary amine groups. Carbonyl peaks were most prominent for glutamic acid functionalized and as-synthesized, citrate stabilized Au NPs. Phosphonic acid and bisphosphonate functionalized Au NPs exhibited strong peaks corresponding to phosphonyl groups. The location of these peaks were similar to a previous study on phosphonic acid functionalized Au NPs.⁴⁷ Taken together, the FT-IR spectra suggested the Au NPs exhibited the intended terminal surface functionality, although the amount of surface coverage and citrate displacement was not quantified.

Functionalized Au NP Binding to HA Crystals

Binding of functionalized Au NPs to HA crystal surfaces was confirmed by TEM (Fig. 5). Bisphosphonate functionalized Au NPs exhibited more rapid binding kinetics compared to glutamic acid or phosphonic acid functionalized Au NPs, reaching complete binding after 8 h in DI water (Fig. 6). Glutamic acid and phosphonic acid functionalized Au NPs exhibited similar binding kinetics, reaching near complete binding by 24 h in DI water. Thus, kinetic tests suggested differences in binding affinity between different functional groups, requiring further binding experiments.

Binding affinity isotherms for functionalized Au NPs exhibited large differences between functional groups (Fig. 7). Bisphosphonate functionalized Au NPs exhibited the greatest binding affinity to the surface of HA crystals, as evidenced by a comparatively greater amount of gold bound per HA (mg/g) and greater saturation concentration. Binding isotherms for glutamic acid,

phosphonic acid, and bisphosphonate functionalized Au NPs in DI water exhibited correlation coefficients (R^2) of 0.997, 0.998, and 0.988, respectively, after linearization, supporting Langmuir kinetics. The equilibrium binding constant, K , and the maximum surface binding, V_{\max} , were greatest for bisphosphonate functionalized Au NPs followed by glutamic acid and phosphonic acid (Table I). The maximum surface binding was also normalized by the specific surface area of the HA crystals to obtain a measure of the maximum binding of functionalized Au NPs per surface area of HA, V_{\max}^* (mg Au/m² HA) (Table I).

The high binding affinity of bisphosphonate functionalized Au NPs was expected and consistent with previous studies investigating bisphosphonate functionalized model proteins, such as albumin,⁴²⁻⁴⁴ and poly(D,L-lactide-co-glycolide) nanoparticles.⁴⁸ As-synthesized Au NPs exhibited significantly lower binding affinity than the lowest of functionalized Au NPs in DI water and did not follow Langmuir kinetics ($R^2 = 0.27$) (Fig. 8). Therefore, differences in binding affinity between functional groups were attributed to the calcium-affinity of the functional group and not a simple electrostatic interaction.

The overall binding affinity of functionalized Au NPs was decreased in FBS compared to DI water, but relative differences in binding affinity between functional groups remained consistent. However, binding isotherms for functionalized Au NPs in FBS did not display Langmuir kinetics and, therefore, could not be linearized to determine the binding constants. Non-Langmuir binding behavior in serum solutions was also previously observed by Uludag *et al.*⁴² Non-equilibrium binding of functionalized Au NPs to HA crystals in FBS may be attributed to a number of possible competitive binding effects, including (1) competition between soluble calcium ions and HA surfaces for binding functionalized Au NPs, (2) competition of soluble proteins and functionalized Au NPs for HA surfaces, (3) interactions between bound Au NPs through shared interactions with either soluble calcium or soluble proteins, (4) place-exchange

1
2
3 reactions between functional groups and thiol or amine containing proteins in solution, or (5)
4
5 some combination of these mechanisms.
6
7
8
9

10 **Implications for Targeted Delivery**

11
12
13
14 A damage-specific X-ray contrast agent could enable non-invasive and 3-D imaging of
15
16 fatigue microdamage in bone. The results of this study suggest that, of the functional groups
17
18 investigated, bisphosphonate functionalized Au NPs would provide the highest surface density
19
20 (cf., Table I) for labeling damage bone tissue and, therefore, the greatest contrast enhancement in
21
22 X-ray tomography. Fatigue microcracks in human cortical bone specimens labeled by
23
24 bisphosphonate functionalized Au NPs were able to be detected by synchrotron X-ray
25
26 tomography in a preliminary study.⁴⁹ On the other hand, release and clearance of the contrast
27
28 agent in clinical use would likely require functional groups with intermediate binding affinity,
29
30 similar to L-glutamic acid in this study. For example, γ -carboxyglutamic acid is a post-
31
32 translationally modified amino acid which has been identified in proteins with hydroxyapatite
33
34 affinity.⁵⁰ Further work will be required to determine the appropriate balance between the
35
36 contrast enhancement and clearance of the agent. The significance of the present study was in
37
38 demonstrating the ability to tailor and quantify the binding affinity for these objectives.
39
40
41
42
43
44

45 An additional concern for the use of bisphosphonate functionalized Au NPs as an
46
47 imaging contrast agent is the pharmacological activity of bisphosphonates, which are commonly
48
49 used to treat osteoporosis by inhibiting the cellular remodeling process to prevent additional loss
50
51 of bone mass. The mechanism by which bisphosphonates are able to inhibit osteoclast activity is
52
53 directly related to the presence of nitrogen.⁵¹ Nitrogen-containing bisphosphonates, such as
54
55 alendronate, have been shown to selectively inhibit a specific enzymatic pathway necessary for
56
57
58
59
60

osteoclast function, while bisphosphonates that do not contain nitrogen are incorporated into toxic ATP analogs that cause apoptosis.⁵¹ However, the nitrogen in alendronate is in the form of a primary amine, which was bound to the surface of Au NPs. Therefore, the pharmacological activity may have been passivated. The effects amine binding to gold surfaces on cellular activity is unknown and will depend upon potential intracellular place-exchange reactions between thiol and amine-containing molecules.^{1,3}

Amongst the expansive body of research for active targeting of Au NPs for biological applications,¹⁻⁴ there has not, to our knowledge, been prior investigation on the binding affinity of functionalized Au NPs for mineralized tissue. While the main motivation for this study was in the use of Au NPs as a targeted contrast agent for labeling damaged bone tissue, other applications are readily envisioned for the detection of calcifications in soft tissue associated with cancer or musculoskeletal injury, and as drug delivery vehicles.

CONCLUSIONS

Gold nanoparticles (Au NPs) were synthesized to a mean particle diameter between 10-15 nm and surface functionalized with either L-glutamic acid, 2-aminoethylphosphonic acid, or alendronate, which exhibit a primary amine for gold surface adsorption opposite carboxylate, phosphonate or bisphosphonate groups, respectively, for targeting calcium. Bisphosphonate functionalized Au NPs exhibited the most rapid binding kinetics and greatest binding affinity for HA, followed by glutamic acid and phosphonic acid. Functionalized Au NPs exhibited lower overall binding in fetal bovine serum compared to de-ionized water, but relative differences between functional groups were similar. The high binding affinity of bisphosphonate

functionalized Au NPs for HA could lead to improved labeling of damage bone tissue and enhanced-contrast in X-ray tomography.

ACKNOWLEDGEMENTS

This research was supported by the U.S. Army Medical Research and Materiel Command (W81XWH-06-1-0196) through the Peer Reviewed Medical Research Program (PR054672). The authors acknowledge the Center for Environmental Science and Technology (CEST) at the University of Notre Dame for the use of ICP-OES and UV-vis spectroscopy, as well as the Notre Dame Integrated Imaging Facility (NDIIF) for the use of TEM. Timothy L. Conrad is gratefully acknowledged for preparing the HA crystals used in binding experiments.

REFERENCES

1. Sperling RA, Rivera Gil P, Zhang F, Zanella M, Parak WJ. Biological applications of gold nanoparticles. *Chem Soc Rev* 2008;37:1896-1908.
2. Huang X, Jain PK, El-Sayed IH, El-Sayed MA. Gold nanoparticles: interesting optical properties and recent applications in cancer diagnostics and therapy. *Nanomedicine* 2007;2(5):681-693.
3. Ghosh P, Han G, De M, Kim CK, Rotello VM. Gold nanoparticles in delivery applications. *Adv Drug Delivery Rev* 2008;60:1307-1315.
4. Pissuwan D, Valenzuela SM, Cortie MB. Therapeutic possibilities of plasmonically heated gold nanoparticles. *Trends Biotechnol* 2006;24(2):62-67.
5. Hirsch LR, Stafford RJ, Bankson JA, Sershen SR, Rivera B, Price RE, Hazle JD, Halas NJ, West JL. Nanoshell-mediated near-infrared thermal therapy of tumors under magnetic

- resonance guidance. *Proc Nat Acad Sci* 2003;100(23):13540-13554.
6. Elghanian R, Storhoff JJ, Mucic RC, Letsinger RL, Mirkin CA. Selective colorimetric detection of polynucleotides based on the distance-dependent optical properties of gold nanoparticles. *Science* 1997;277(5329):1078-1081.
 7. Möller R, Fritzsche W. Metal nanoparticle-based detection for DNA analysis. *Curr Pharm Biotechnol* 2007;8(5):274-285.
 8. Hayat MA. *Colloidal Gold: Principles, Methods and Applications*, Vol. 1. San Diego: Academic Press, 1989.
 9. Hainfield JF, Slatkin DN, Focella TM, Smilowitz HM. Gold nanoparticles: an new X-ray contrast agent. *Brit J Radiol* 2006;79(3):248-253.
 10. Cai Q-Y, Kim SH, Choi KS, Kim SY, Byun SJ, Kim KW, Park SH, Juhng SK, Yoon KH. Colloidal gold nanoparticles as a blood-pool contrast agent for X-ray computed tomography in mice. *Invest Radiol* 2007;42(12):797-806.
 11. Kim D, Park S, Lee JH, Jeong YY, Jon S. Antibiofouling polymer-coated gold nanoparticles as a contrast agent for in vivo X-ray computed tomography imaging. *J Am Chem Soc* 2007;129:7661-7665.
 12. Zhang Z, Ross RD, Roeder RK. Preparation of functionalized gold nanoparticles as a targeted X-ray contrast agent for damaged bone tissue. *Nanoscale* 2010;2(4):582-586.
 13. Burr DB, Forwood MR, Fyhrie DP, Martin RB, Schaffler MB, Turner CH. Bone microdamage and skeletal fragility in osteoporotic and stress fractures. *J Bone Miner Res* 1997;12(1):6-15.
 14. Chapurlat BD, Delmas PD. Bone microdamage: a clinical perspective. *Osteoporos Int* 2009;20:1299-1308.
 15. Lee TC, Mohsin S, Taylor D, Parkesh R, Gunnlaugsson T, O'Brien FJ, Giehl M, Gowin W.

- Detecting microdamage in bone. *J Anat* 2003;203:161-172.
16. Frost HM. Presence of microscopic cracks in vivo in bone. *Henry Ford Hosp Med Bull* 1960;8:25-35.
17. Burr DB, Hooser M. Alterations to the en bloc basic fuchsin staining protocol for the demonstration of microdamage produced in vivo. *Bone* 1995;17(4):431-433.
18. O'Brien FJ, Taylor D, Lee TC. An improved labelling technique for monitoring microcrack growth in compact bone. *J Biomechanics* 2002;35:523-526.
19. O'Brien FJ, Taylor D, Lee TC. Microcrack accumulation at different intervals during fatigue testing of compact bone. *J Biomechanics* 2003;36:973-980.
20. Wang X, Niebur GL. Microdamage propagation in trabecular bone due to changes in loading mode. *J Biomechanics* 2006;39:781-790.
21. Parkesh R, Mohsin S, Lee TC, Gunnlaugsson T. Histological, spectroscopic, and surface analysis of microdamage in bone: toward real-time analysis using fluorescent sensors. *Chem Mater* 2007;19:1656-1663.
22. Parkesh R, Lee TC, Gunnlaugsson T. Fluorescence imaging of bone cracks (microdamage) using visibly emitting 1,8-naphthalimide-based PET sensors. *Tetrahedron Lett* 2009;50:4114-4116.
23. Mohsin S, O'Brien FJ, Lee TC. Microcracks in compact bone: a three-dimensional view. *J Anat* 2006;209:119-124.
24. Bigley RF, Singh M, Hernandez CJ, Kazakia GJ, Martin RB, Keaveny TM. Validity of serial milling-based imaging system for microdamage quantification. *Bone* 2008;42:212-216.
25. Zioupos P, Currey JD. The extent of microcracking and the morphology of microcracks in damaged bone. *J Mater Sci* 1994;29:978-986.
26. O'Brien FJ, Taylor D, Dickson GR, Lee TC. Visualization of three-dimensional microcracks

- in compact bone. *J Anat* 2000;197:413-420.
27. Wang X, Masse DB, Leng H, Hess KP, Ross RD, Roeder RK, Niebur GL. Detection of trabecular bone microdamage by micro-computed tomography. *J Biomechanics* 2007;40:3397-3403.
28. Leng H, Wang X, Ross RD, Niebur GL, Roeder RK. Micro-computed tomography of fatigue microdamage in cortical bone using a barium sulfate contrast agent. *J Mech Behav Biomed Mater* 2008;1(1):68-75.
29. Landrigan MD, Li J, Turnbull TL, Burr DB, Niebur GL, Roeder RK. Contrast-enhanced micro-computed tomography of fatigue microdamage accumulation in human cortical bone. *Bone*, submitted.
30. Parkesh R, Gowin W, Lee TC, Gunnlaugsson T. Synthesis and evaluation of potential CT (computer tomography) contrast agents for bone structure and microdamage analysis. *Org Biomol Chem* 2006;4:3611-3617.
31. Parkesh R, Lee TC, Gunnlaugsson T, Gowin W. Microdamage in bone: Surface analysis and radiological detection. *J Biomechanics* 2006;39:1552-1556.
32. Hubbell JH, Seltzer SM. Table of X-ray Mass Attenuation Coefficients and Mass Energy-Absorption Coefficients (version 1.4); National Institute of Standards and Technology: Gaithersburg, MD, 2004. Available at <http://physics.nist.gov/xaamdi>.
33. Giersig M, Mulvaney P. Preparation of ordered colloid monolayers by electrophoretic deposition. *Langmuir* 1993;9:3408-3413.
34. Brust M, Walker M, Bethell D, Schiffrin DJ, Whyman R. Synthesis of thiol-derivatized gold nanoparticles in a 2-phase liquid-liquid system. *J Chem Soc, Chem Commun* 1994;7:801-802.
35. Brust M, Fink J, Bethell D, Schiffrin DJ, Kiely C. Synthesis and reactions of functionalised

- gold nanoparticles. *J Chem Soc, Chem Commun* 1995(16):1655-1656.
36. Leff DV, Brandt L, Heath JR. Synthesis and characterization of hydrophobic, organically-soluble gold nanocrystals functionalized with primary amines. *Langmuir* 1996;12:4723-2730.
37. Kumar A, Mandal S, Selvakannan PR, Pasricha R, Mandale AB, Sastry M. Investigation into the interaction between surface-bound alkylamines and gold nanoparticles. *Langmuir* 2003;19:6277-6282.
38. Selvakannan PR, Mandal S, Phadtare S, Pasricha R, Sastry M. Capping of gold Nanoparticles by the amino acid lysine renders them water-dispersable. *Langmuir* 2003;19:3545-3549.
39. Aslam M, Fu L, Su M, Vijayamohanan K, Dravid VP. Novel one-step synthesis of amine-stabilized aqueous colloidal gold nanoparticles. *J Mater Chem* 2004(14):1795-1997.
40. Bolander ME, Young MF, Fisher LW, Yamada Y, Termine JD. Osteonectin cDNA sequence reveals potential binding regions for calcium and hydroxyapatite and shows homologies with both a basement membrane protein (SPARC) and a serine proteinase inhibitor (ovomucoid). *Proc Nat Acad Sci* 1988;85:2919-2923.
41. Fujisawa R, Wada Y, Nodasaka Y, Kuboki Y. Acidic amino acid-rich sequences as binding sites of osteonectin to hydroxyapatite crystals. *Biochim Biophys Acta* 1996;1292:53-60.
42. Uludag H, Kousinioris N, Gao T, Kantoci D. Bisphosphonate conjugation to proteins as a means to impart bone affinity. *Biotechnol Prog* 2000;16:258-267.
43. Bansal G, Wright JEI, Zhang S, Zernicke RF, Uludag H. Imparting mineral affinity to proteins with thiol-labile disulfide linkages. *J Biomed Mater Res* 2005;74A(4):618-628.
44. Wright JEI, Gittens SA, Bansal G, Kitov PI, Sindrey D, Kucharski C, Uludag H A comparison of mineral affinity of bisphosphonate-protein conjugates constructed with disulfide and thioether linkages. *Biomaterials* 2006;26:769-784.
45. Turkevich J, Stevenson PC, Hillier J. A study of the nucleation and growth processes in the

synthesis of colloidal gold. Discuss Faraday Soc 1951;(11):55-75.

46. Roeder RK, Converse GL, Leng H, Yue W. Kinetic effects on hydroxyapatite whiskers synthesized by the chelate decomposition method. J Am Ceram Soc 2006;89(7):2096-2104.

47. Fiurasek P, Reven L. Phosphonic and sulfonic acid-functionalized gold nanoparticles: A solid-state NMR study. Langmuir 2007;23:2857-2866.

48. Choi SW, Kim JH. Design of surface-modified poly(D,L-lactide-co-glycolide) nanoparticles for targeted drug delivery to bone. J Control Release 2007;122(1):24-30.

49. Ross RD, Roeder RK. Functionalized gold nanoparticles for targeted labeling of damaged bone tissue in X-ray tomography Trans Orthop Res Soc 2010;35:1368.

50. Price PA, Otsuka AS, Poser JW, Kristaponis J, Raman N. Characterization of a gamma-carboxyglutamic acid-containing protein from bone. Proc Natl Acad Sci 1976;73(5):1447-1451.

51. Reszka AA, Rodan GA. Bisphosphonate mechanism of action. Curr Rheumatol Rep 2003;5(1):65-74.

TABLES

Table I. The equilibrium binding constant, K (mg/L), maximum HA surface binding, V_{\max} (mg Au/g HA), and maximum HA surface binding normalized to the specific surface area of HA crystals, V_{\max}^* (mg Au/m² HA), for glutamic acid (GA), phosphonic acid (PA), and bisphosphonate (BP) functionalized Au NPs, derived from linearization of Langmuir isotherms.

Group	K (mg/L)	V_{\max} (mg/g)	V_{\max}^* (mg/m ²)
GA-Au NPs	0.72	1.22	0.22
PA-Au NPs	0.25	0.48	0.085
BP-Au NPs	3.82	7.33	1.30

FIGURE CAPTIONS

Figure 1. Gold nanoparticles (Au NPs) were surface functionalized with (a) L-glutamic acid, (b) 2-aminoethylphosphonic acid, or (c) alendronate, which exhibit a primary amine for binding to gold surfaces opposite (a) carboxylate, (b) phosphonate, or (c) bisphosphonate functional groups, respectively, for binding to calcium on bone mineral crystals exposed within damaged bone tissue.

Figure 2. Particle size distributions and representative TEM micrographs of (a) glutamic acid (GA), (b) phosphonic acid (PA), and (c) bisphosphonate (BP) functionalized Au NPs. The scale bar in each micrograph represents 100 nm. The mean (\pm standard deviation) particle diameter was 11.40 (\pm 1.36), 13.57 (\pm 1.43), and 12.79 (\pm 1.58) nm for GA-, PA-, and BP-Au NPs, respectively.

Figure 3. UV-vis spectra of as-synthesized Au NPs compared to glutamic acid (GA), phosphonic acid (PA), and bisphosphonate (BP) functionalized Au NPs, showing a consistent plasmon resonance peak at \sim 530 nm, which indicated that the particle size did not change and the colloid was stable after surface functionalization.

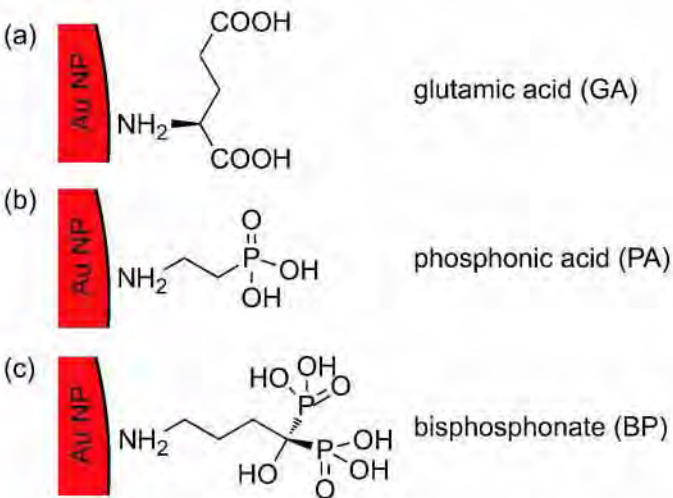
Figure 4. FT-IR spectra of as-synthesized, citrate stabilized Au NPs compared to glutamic acid (GA), phosphonic acid (PA), and bisphosphonate (BP) functionalized Au NPs, confirming the presence of functional groups on gold surfaces. As-synthesized, citrate stabilized Au NPs and GA-Au NPs exhibited carboxylate functionality, while PA- and BP-Au NPs exhibited phosphonate functionality. Note that all peaks were verified by comparison to corresponding FT-IR spectra for stock solutions of the functional molecules.

Figure 5. TEM micrographs showing (a) glutamic acid (GA), (b) phosphonic acid (PA), and (c) bisphosphonate (BP) functionalized Au NPs bound to the surface of HA crystals after 4 h in a solution containing a gold concentration of 0.1 mg/L in DI water.

Figure 6. Binding kinetics of glutamic acid (GA), phosphonic acid (PA), and bisphosphonate (BP) functionalized Au NPs to HA crystals in DI water, showing the mean mass percent of Au NPs bound as a function of incubation time. Error bars show one standard deviation. Percent binding was defined as the concentration (mg Au/L) of Au NPs remaining in the supernatant solution after binding, subtracted from the initial concentration of Au NPs in solution, and divided by the initial concentration of Au NPs.

Figure 7. Binding isotherms for (a) glutamic acid (GA), (b) phosphonic acid (PA), and (c) bisphosphonate (BP) functionalized Au NPs in both DI water and FBS. Note that the scale of axes is changed in (c) due to the significantly greater binding affinity of BP-AuNPs. Binding in DI water exhibited Langmuir kinetics with the binding constants shown in Table I. Binding in FBS did not exhibit equilibrium binding due to competition of soluble species present within serum solutions.

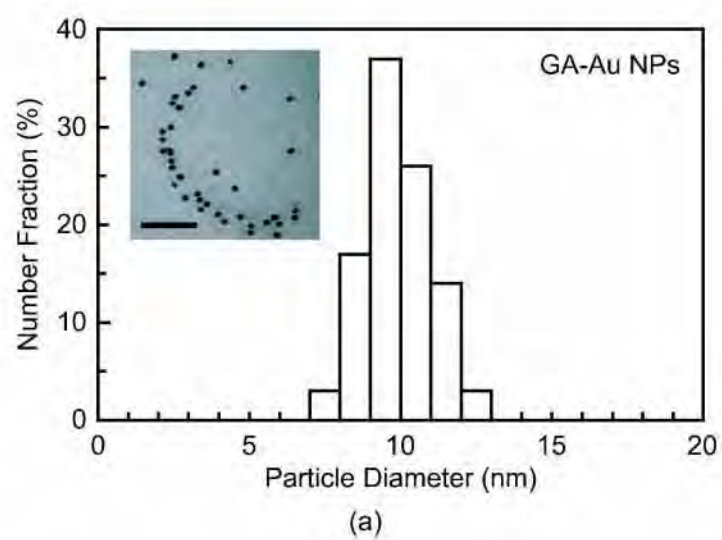
Figure 8. Binding isotherm for as-synthesized Au NPs in DI water. The low binding affinity relative to functionalized Au NPs (Fig. 7) verified that binding was due to the calcium-specific functional groups rather than electrostatic interactions.



Ross and Roeder

Figure 1

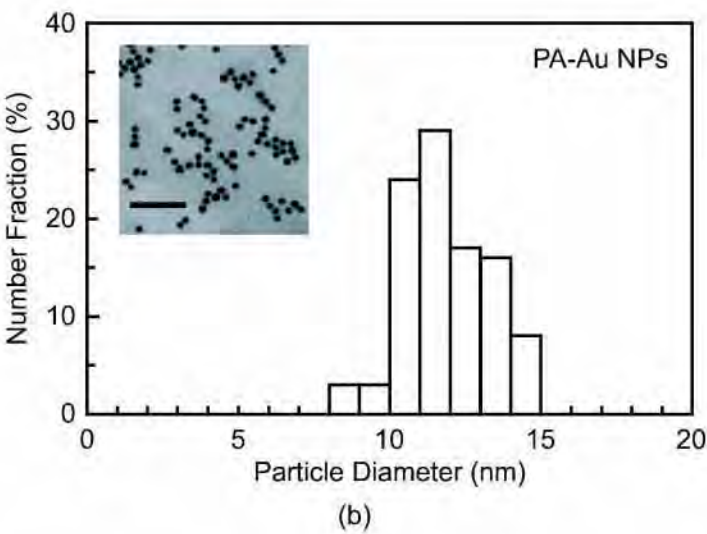
215x279mm (600 x 600 DPI)



Ross and Roeder

Figure 2a

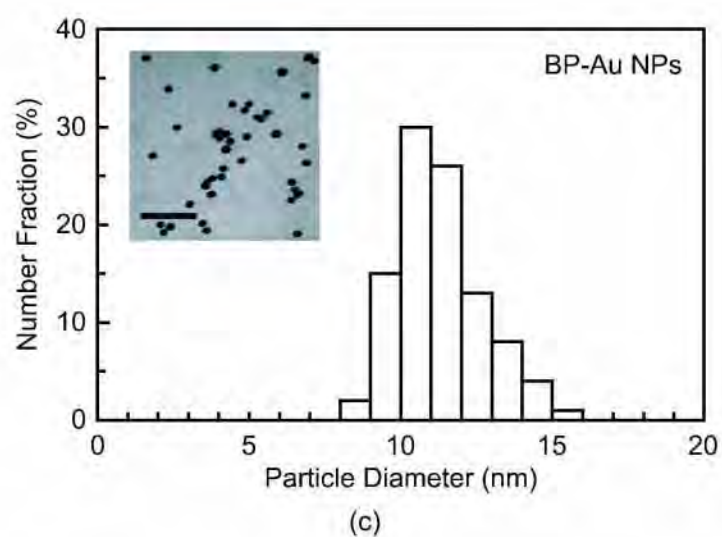
215x279mm (600 x 600 DPI)



Ross and Roeder

Figure 2b

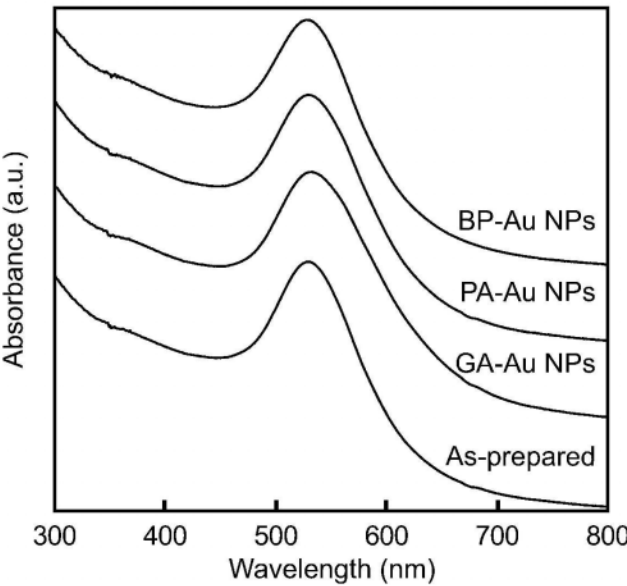
215x279mm (600 x 600 DPI)



Ross and Roeder

Figure 2c

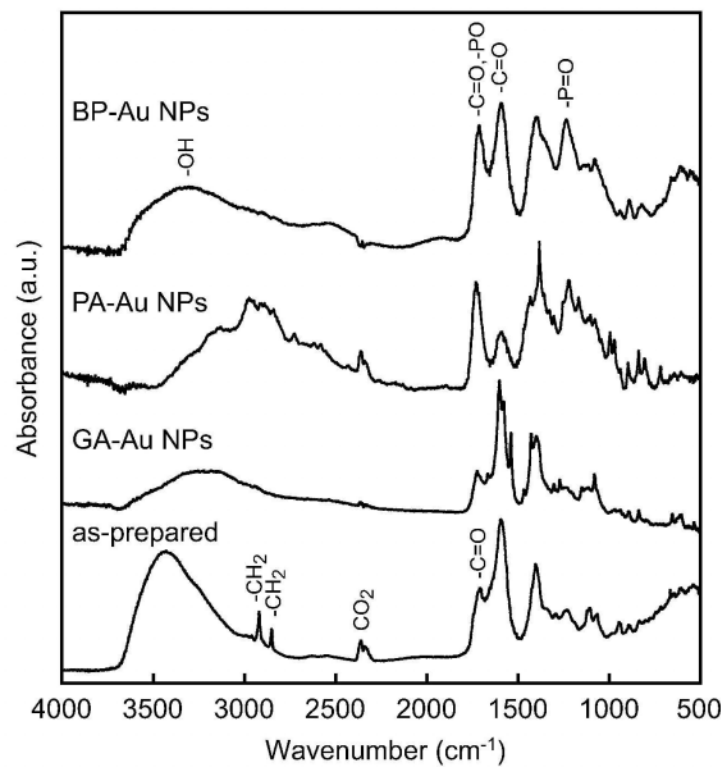
215x279mm (600 x 600 DPI)



Ross and Roeder

Figure 3

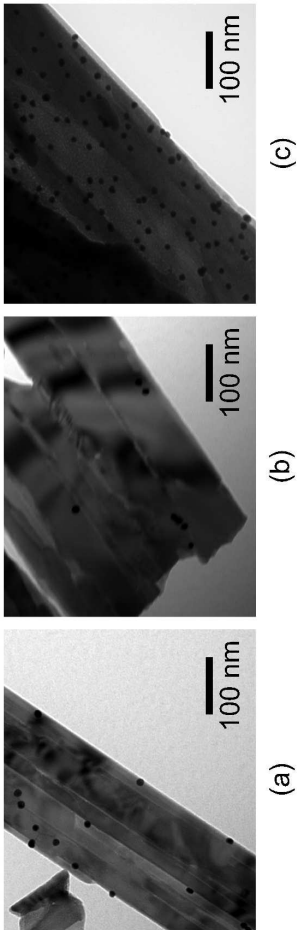
215x279mm (600 x 600 DPI)



Ross and Roeder

Figure 4

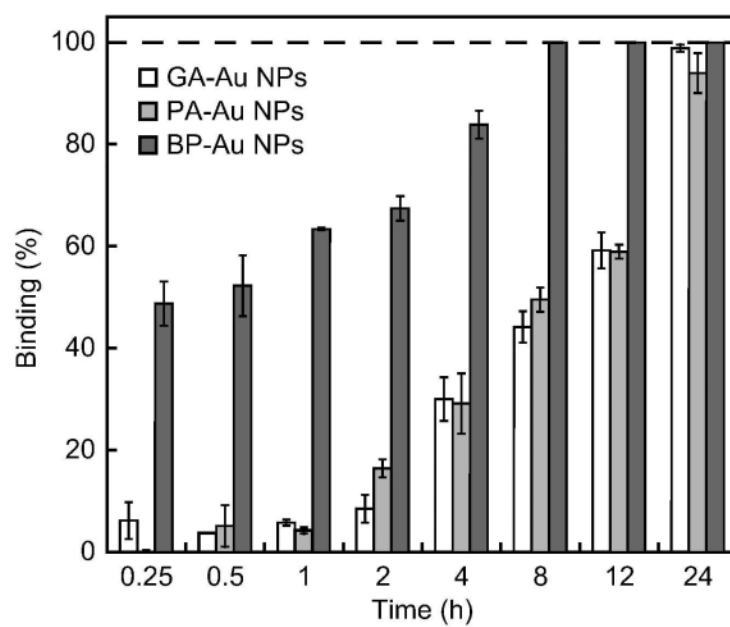
215x279mm (600 x 600 DPI)



Ross and Roeder

Figure 5

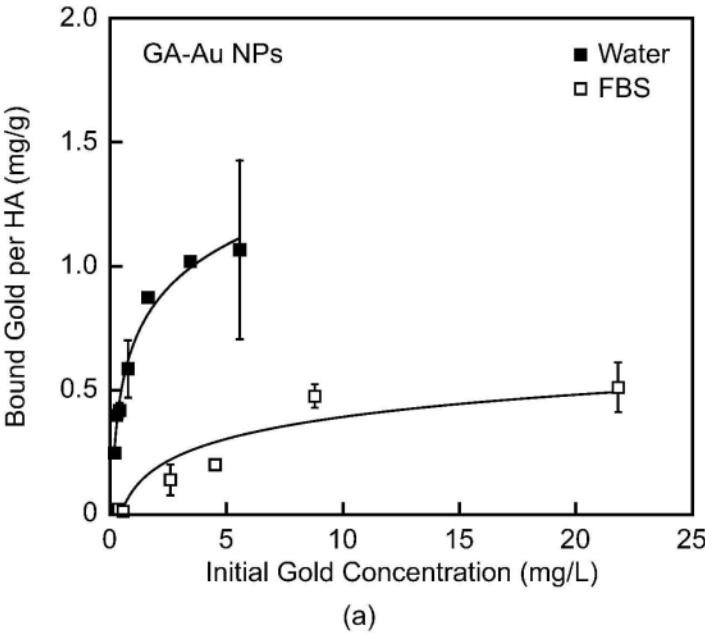
215x279mm (600 x 600 DPI)



Ross and Roeder

Figure 6

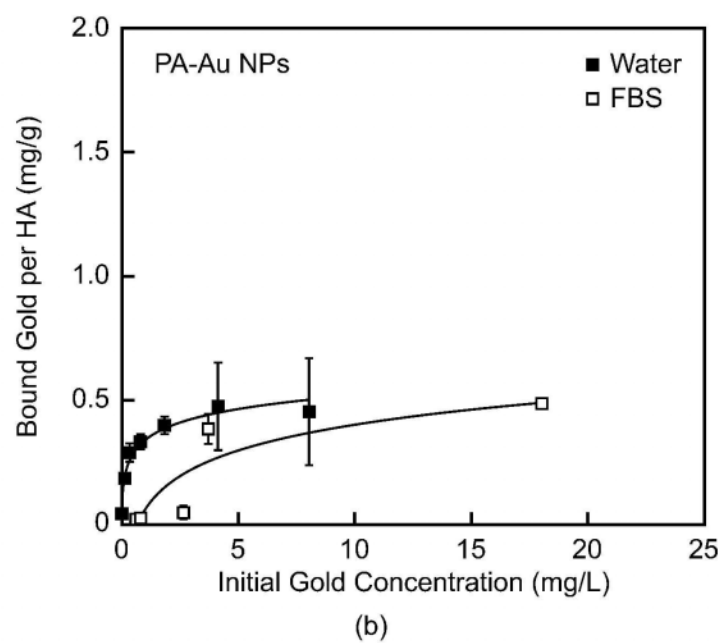
215x279mm (600 x 600 DPI)



Ross and Roeder

Figure 7a

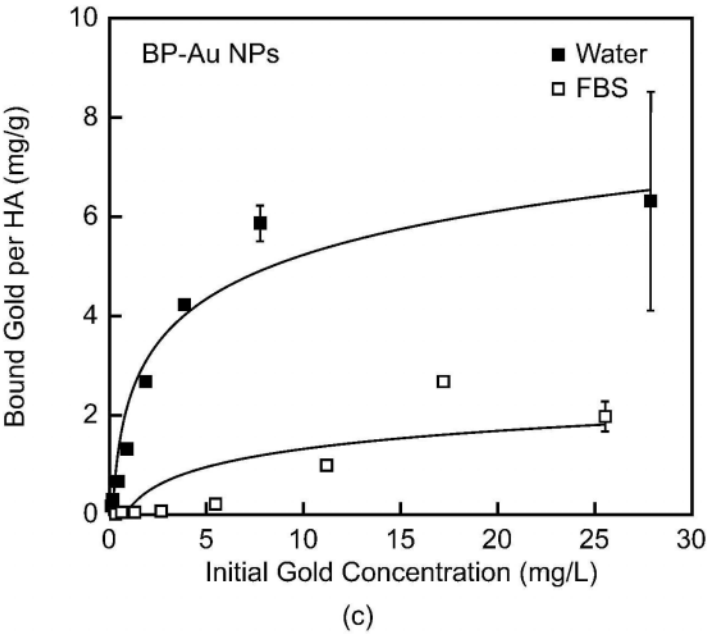
215x279mm (600 x 600 DPI)



Ross and Roeder

Figure 7b

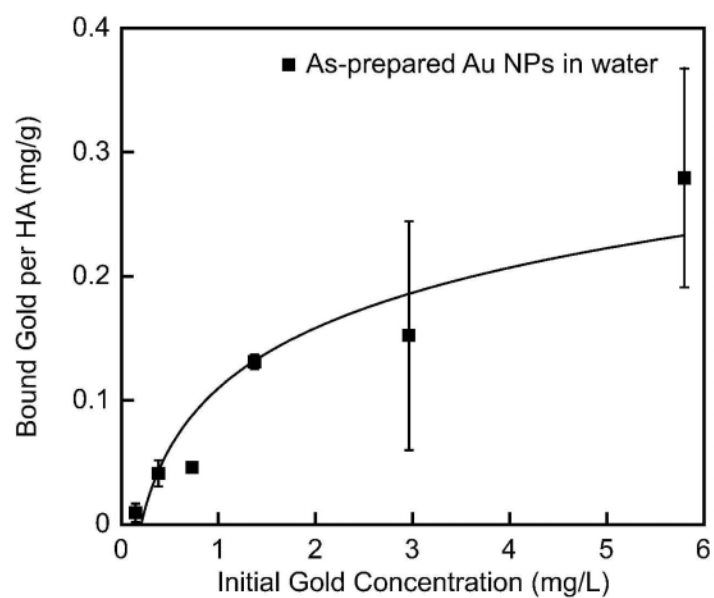
215x279mm (600 x 600 DPI)



Ross and Roeder

Figure 7c

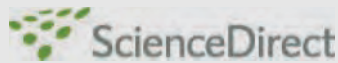
215x279mm (600 x 600 DPI)



Ross and Roeder

Figure 8

215x279mm (600 x 600 DPI)

available at www.sciencedirect.comjournal homepage: www.elsevier.com/locate/jmbbm

Research paper

Micro computed tomography of fatigue microdamage in cortical bone using a barium sulfate contrast agent

Huijie Leng¹, Xiang Wang², Ryan D. Ross, Glen L. Niebur, Ryan K. Roeder*

Department of Aerospace and Mechanical Engineering, The University of Notre Dame, Notre Dame, IN 46556, United States

ARTICLE INFO

Article history:

Received 4 May 2007

Received in revised form

31 May 2007

Accepted 4 June 2007

Published online 31 July 2007

Keywords:

Fatigue microdamage

Cortical bone

Micro-computed tomography

Contrast agents

Barium sulfate

ABSTRACT

Accumulation of microdamage during fatigue can lead to increased fracture susceptibility in bone. Current techniques for imaging microdamage in bone are inherently destructive and two-dimensional. Therefore, the objective of this study was to image the accumulation of fatigue microdamage in cortical bone using micro-computed tomography (micro-CT) with a barium sulfate (BaSO_4) contrast agent. Two symmetric notches were machined on the tensile surface of bovine cortical bone beams in order to generate damage ahead of the stress concentrations during four-point bending fatigue. Specimens were loaded to a specified number of cycles or until one notch fractured, such that the other notch exhibited the accumulation of microdamage prior to fracture. Microdamage ahead of the notch was stained *in vitro* by precipitation of BaSO_4 and imaged using micro-CT. Reconstructed images showed a distinct region of bright voxels around the notch tip or along propagating cracks due to the presence of BaSO_4 , which was verified by backscattered electron imaging and energy dispersive spectroscopy. The shape of the stained region ahead of the notch tip was consistent with principal strain contours calculated by finite element analysis. The relative volume of the stained region was correlated with the number of loading cycles by non-linear regression using a power law. This study demonstrates new methods for the non-destructive and three-dimensional detection of fatigue microdamage accumulation in cortical bone *in vitro*, which may be useful to gain further understanding into the role of microdamage in bone fragility.

© 2007 Elsevier Ltd. All rights reserved.

1. Introduction

Healthy bone is crucial to overall human health. Bone provides structural support for the body, protects soft tissues and organs, produces red blood cells, stores essential minerals and transmits muscular forces during movement (Jee, 2001). Microdamage accumulates in bone tissue *in vivo*

due to repetitive loading and is observed in the form of microcracks or diffuse damage (Burr et al., 1997; Martin, 2003). *In vitro* studies have shown that microdamage accumulation has a detrimental effect on the mechanical properties of cortical bone (Jepsen and Davy, 1997; Schaffler et al., 1989). However, *in vivo*, microdamage is repaired by, and may signal, bone remodeling (Burr et al., 1985; Martin, 2003; Martin and

* Corresponding author. Tel.: +1 574 631 7003; fax: +1 574 631 2144.

E-mail address: rroeder@nd.edu (R.K. Roeder).

¹ Current Address: Department of Mechanical Engineering, University of Texas at San Antonio, San Antonio, TX 78249, United States.

² Current Address: Department of Orthopaedic Surgery, University of California, Davis, Sacramento, CA 95817, United States.

Burr, 1982; Mori and Burr, 1993). Thus, excessive accumulation of microdamage prior to remodeling can lead to increased fracture susceptibility. However, the role of microdamage in clinical bone fragility is not yet well understood, in part due to limited capabilities for imaging and measuring microdamage accumulation both *in vivo* and *in vitro*.

Current imaging techniques, such as ultraviolet light microscopy using fluorescent stains or chelating agents (Burr and Stafford, 1990; Lee et al., 2000; O'Brien et al., 2002, 2005), backscattered electron imaging (BEI) using a lead-uranyl acetate stain (Schaffler et al., 1994), laser scanning confocal microscopy (LSCM) using fluorescent stains (O'Brien et al., 2000; Zioupos and Currey, 1994) and serial imaging using fluorescent stains (O'Brien et al., 2000), require the preparation of many histologic sections which are inherently destructive and two-dimensional. LSCM provides limited depth of field for three-dimensional (3D) imaging of labeled microdamage, but the sample preparation is destructive and the depth of field is not sufficient to image whole microcracks and tissue architecture.

A non-destructive and 3D imaging technique would enable measurement of the spatial density of microdamage accumulation, which could be correlated to local variations in mechanical loading, bone mineral density (BMD) or microarchitecture. Therefore, recent studies have begun to investigate non-invasive, 3D imaging techniques. Positron emission tomography (PET) was used to image microdamage *in vivo* with a sodium fluoride (Na^{18}F) contrast agent (Li et al., 2005; Silva et al., 2006). Micro-computed tomography (micro-CT) was used to detect microdamage *in vitro* with lead sulfide (PbS) (Leng et al., 2005), barium sulfate (BaSO_4) (Wang et al., *in press*) or iodinated (Parkesh et al., 2006, 2007) contrast agents. In particular, BaSO_4 was proposed as a more benign alternative to lead-based stains. BaSO_4 was also considered a logical choice for a contrast agent with potential for future use *in vivo* due to high x-ray attenuation and reasonable biocompatibility. BaSO_4 is currently used clinically as a contrast agent for gastrointestinal radiography (Skucas, 1989) and as a radiopacifier in polymethylmethacrylate bone cement (Lewis, 1997).

The objective of this study was to non-destructively and three-dimensionally image microdamage accumulation in cortical bone *in vitro* using micro-CT with a BaSO_4 contrast agent. The BaSO_4 stain employed in this study was previously used to label microdamage *in vitro* in trabecular bone specimens that were damaged by an overload (Wang et al., *in press*). In this study, similar methods were used to detect the progressive accumulation of fatigue microdamage ahead of a notch in cortical bone specimens.

2. Materials and methods

Twenty-four parallelepiped beams, $4 \times 4 \times 50\text{--}60$ mm, were sectioned from the cortex at the mid-diaphysis of a single bovine tibia. Two symmetric notches were machined on the periosteal surface of the beams, which were loaded in tension under bending, in order to concentrate damage ahead of the notch during loading. The notches were machined 10 mm

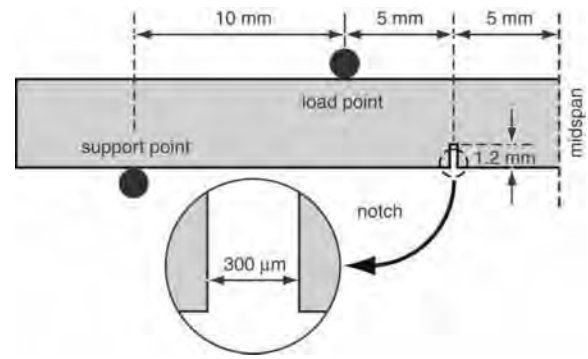


Fig. 1 – Schematic diagram of a double-notched beam in four-point bending sectioned at the midspan, showing loading points and dimensions.

apart to a depth of 1.2 mm and width of $300\ \mu\text{m}$ using a low-speed diamond wafer saw (Fig. 1). As-prepared beams were wrapped in gauze, hydrated with buffered saline solution, and stored at $-20\ ^\circ\text{C}$ in airtight containers prior to mechanical testing and staining.

Specimens were randomly divided into six groups which were loaded in four-point bending fatigue to 0 (unloaded control), 1×10^5 , 2×10^5 , 3×10^5 , 4×10^5 and 5×10^5 cycles. A 5 N compressive preload was initially applied to each beam and the displacement was set to zero. Beams were loaded using an electromagnetic test instrument (ELF 3300, ElectroForce Systems Group of Bose Corp., Eden Prairie, MN) under displacement control (0.1 mm minimum and 0.3 mm maximum deflection) at a frequency of 2 Hz, while soaking in de-ionized water under ambient conditions. Loading was stopped after reaching the designated number of cycles or when fracture occurred at one of the notches, such that the unfractured notch exhibited the accumulation of microdamage prior to fracture (Nalla et al., 2003, 2005). Specimens that fractured prior to the designated number of cycles were reassigned to the appropriate group based on the number of cycles to failure. Load and displacement data were recorded continuously for 10 s for every 100 s. The beam stiffness (S , N/mm) was calculated as the secant from the maximum and minimum loads and displacements for each loading cycle recorded. The relative stiffness was calculated as the ratio of the stiffness at a given number of loading cycles to the initial stiffness and was correlated to the number of loading cycles using least-squares linear regression (JMP 5.1, SAS Institute, Inc., Cary, NC).

After mechanical loading, all beams were sectioned at the midspan (Fig. 1). For each beam, a specimen half with a notch that did not fracture was stained by BaSO_4 precipitation, soaking in an equal parts mixture of 1 M barium chloride (certified ACS crystal, Fisher Scientific, Fair Lawn, NJ) in de-ionized water, buffered saline and acetone for 7 days, followed by an equal parts mixture of 1 M sodium sulfate (anhydrous powder, Fisher Scientific, Fair Lawn, NJ) in de-ionized water, buffered saline and acetone for 7 days, both under vacuum (50 mm Hg). Barium chloride and sodium sulfate staining solutions were neutralized by the addition of sodium hydroxide (ACS reagent, Sigma Chemical, St. Louis, MO) and nitric acid (ACS reagent, Aldrich Chemical,

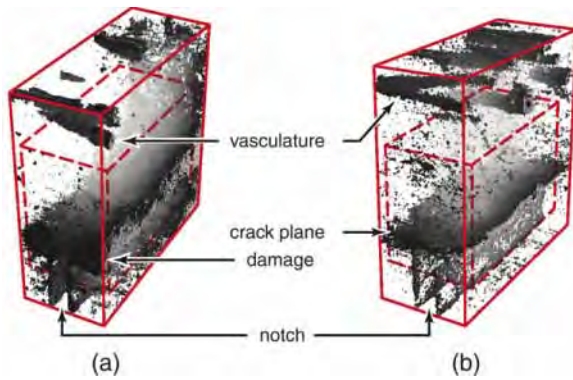


Fig. 2 – Three-dimensional micro-CT images reconstructed from transverse slices of specimens loaded to 5×10^5 cycles and stained with BaSO_4 , showing (a) a typical specimen with a damaged region ahead of the notch and (b) a specimen with a macroscopic crack propagating laterally from the notch tip. The entire region imaged is shown by the solid box ($1.6 \times 4.0 \times 4.0$ mm) and the subregion is shown by the dashed box ($1.6 \times 2.0 \times 3.6$ mm). Note that BaSO_4 also stained the endosteal vasculature shown at the top of each image and free surfaces of the beam, such as around the notch shown at the bottom of each image.

Milwaukee, WI), respectively. The staining mechanism was a simple and benign precipitation reaction where $\text{BaCl}_2(\text{aq}) + \text{Na}_2\text{SO}_4(\text{aq}) \rightarrow \text{BaSO}_4(\text{s}) + 2\text{NaCl}(\text{aq})$ (Leng et al., 2004).

Stained specimens were imaged using micro-CT (μCT -80, Scanco Medical AG, Bassersdorf, Switzerland) at 10 μm resolution, 70 kVp voltage and 113 μA current with slices taken either transversely or longitudinally. For transverse slices, a 1.6 mm long region of the entire specimen cross-section, which fully spanned the notch, was scanned using a 200 ms integration time. Longitudinal slices were imaged to a depth of 0.8 mm in the center of the specimen cross-section using a 300 ms integration time. In order to remove the effect of excess BaSO_4 staining on the free surfaces of beams and within vasculature located near the endosteal surface, images reconstructed from transverse slices were also analyzed within a $1.6 \times 2.0 \times 3.6$ mm subregion surrounding the notch tip. This subregion was located 1.4 mm from the endosteal surface, 0.6 mm from the periosteal surface and 0.2 mm from the beam sides (Fig. 2). Gaussian smoothing was applied to suppress noise and 3D images were thresholded in order to show the BaSO_4 stain.

Damage was quantified from the micro-CT image intensity histogram which, after removing background pixels, represents the volume of material at a given image intensity. After staining with BaSO_4 , the otherwise symmetric Gaussian distribution for bone was skewed to higher intensities due to the presence of BaSO_4 (Fig. 3). Therefore, the single, asymmetric Gaussian peak in the image intensity histogram was fit as the sum of two symmetric Gaussian peaks, which represented the two known sources of x-ray attenuation (bone and BaSO_4), using a non-linear least-squares algorithm (Fig. 3). The relative volume of stain was measured as the ratio of the BaSO_4 integrated peak intensity relative to the total integrated peak intensity. Non-linear regression was used to

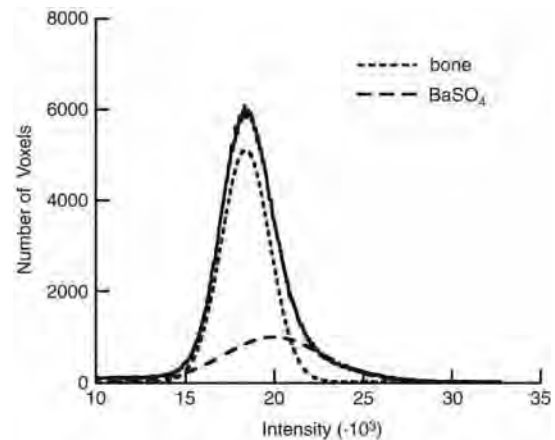


Fig. 3 – Representative micro-CT image intensity histogram showing bone and BaSO_4 peaks fit using a two-peaked Gaussian function.

correlate the relative peak intensity for BaSO_4 to the number of loading cycles using a power law (JMP 5.1, SAS Institute, Inc., Cary, NC). Regression analysis was conducted with all 24 specimens and after the exclusion of outlier specimens, which included two specimens that were over-stained and four specimens with macroscopic cracks present at the notch.

Selected specimens were also imaged by scanning electron microscopy (SEM) using backscattered electron imaging (BEI) (Evo 50, LEO Electron Microscopy Ltd., Cambridge, UK) at an accelerating voltage of 20 kV and a working distance of 7 mm. Note that image contrast in BEI is primarily due to compositional differences in atomic number, with increasing atomic number resulting in increased intensity. The elemental composition was also measured by electron probe microanalysis (EPMA) using energy dispersive spectroscopy (EDS) (INCA x-sight model 7636, Oxford Instruments America, Concord, MA). Specimens were embedded in poly(methylmethacrylate), sectioned with a low-speed diamond wafer saw, polished with a series of diamond compounds to a 0.25 μm final finish, washed with methanol, dried overnight in an oven at 90 °C and coated with Au-Pd by sputter deposition.

Finite element analysis (FEA) was used to qualitatively compare principal strain contours around the notch to micro-CT images of the staining. The finite element model was created with four-node plane strain elements and analyzed with ABAQUS (v.6.3, ABAQUS, Inc., Providence, RI). Isotropic material properties were assigned to the bone tissue, using an elastic modulus of 18 GPa (Reilly and Burstein, 1974) and Poisson's ratio of 0.3. Displacement bounding conditions were applied to simulate the maximum deflection in four-point bending.

3. Results

Micro-CT images of damaged specimens showed high-intensity voxels within the bone tissue in regions ahead of the notch tip, as well as on surfaces associated with specimen

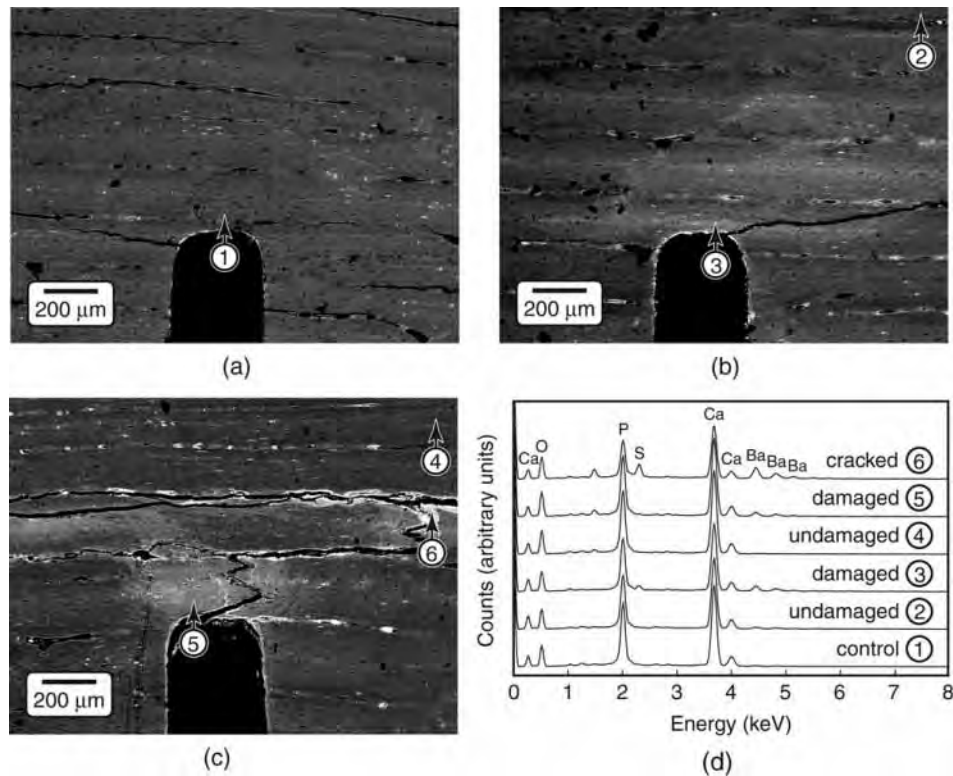


Fig. 4 – SEM micrographs using BEI showing (a) an unloaded control specimen and specimens loaded to 5×10^5 cycles exhibiting (b) microdamage accumulation ahead of the notch and (c) a crack that propagated from the notch. All specimens were stained with BaSO_4 . (d) The elemental composition was measured using EDS at the locations shown in undamaged tissue, damaged tissue and the within the crack. Note that the specimen shown in Fig. 4(a) is the same as that shown in Fig. 6 (unloaded control); the specimen shown in Fig. 4(b) is the same as that shown in Fig. 2(a) and Fig. 6 (5×10^5 cycles); and the specimen shown in Fig. 4(c) is the same as that shown in Figs. 2(b) and 9.

edges, propagating cracks and vasculature (Fig. 2). These high-intensity voxels were observed at higher resolution and shown to be due to the presence of precipitated BaSO_4 using BEI and EDS, respectively (Fig. 4). The highest image intensity and highest levels of elemental barium (Ba) and sulfur (S) were detected within propagating cracks (Fig. 4, location 6) or vasculature (Fig. 2). Lower levels of Ba and S were detected in damaged tissue ahead of the notch, which appeared at an intermediate image intensity (Fig. 4, locations 3 and 5). The stain was virtually undetectable within the unloaded control specimen or regions of tissue far away from the notch, where the lowest image intensity was observed and no damage was expected (Fig. 4, locations 1, 2 and 4). Note that the absence of BaSO_4 within cracks allowed drying cracks (e.g., Fig. 4(a), (b)) to be distinguished from cracks that initiated and propagated during loading (e.g., Fig. 4(c)). Higher-magnification SEM micrographs revealed the presence of individual BaSO_4 crystals, less than $5 \mu\text{m}$ in size, on the surfaces of propagating cracks (Fig. 5(a)) and diffuse staining within damaged tissue (Fig. 5(b)). Thus, BaSO_4 staining enhanced the contrast of tissue that was damaged during loading which enabled imaging by micro-CT using a suitable threshold intensity.

The amount of staining ahead of the notch tip visibly increased with an increased number of loading cycles, as shown by representative two-dimensional micro-CT images

from different specimens (Fig. 6). Note that unloaded control specimens exhibited negligible staining ahead of the notch but did exhibit staining of vasculature and the free surfaces of beams (Fig. 4(a) and Fig. 6). Furthermore, the shape of stained regions ahead of the notch tip was qualitatively consistent with principal strain contours calculated by FEA, which exhibited a characteristic kidney shape of high intensity immediately ahead of the notch (Fig. 7).

The amount of staining was measured from micro-CT image histograms by the ratio of the BaSO_4 integrated peak intensity relative to the overall integrated peak intensity (Fig. 3), and was correlated with the number of loading cycles using a power-law regression (Fig. 8, Table 1). The strength and significance of the correlation was improved using a subregion that excluded the free surfaces of beams and endosteal vasculature (Fig. 2, Table 1). The correlation was also improved by excluding two specimens that were observed to be over-stained and four specimens that exhibited macroscopic cracks propagating from the imaged notch, rather than only microdamage ahead of the notch (Fig. 8, Table 1).

4. Discussion

The accumulation of microdamage during fatigue was non-destructively and three-dimensionally imaged in notched

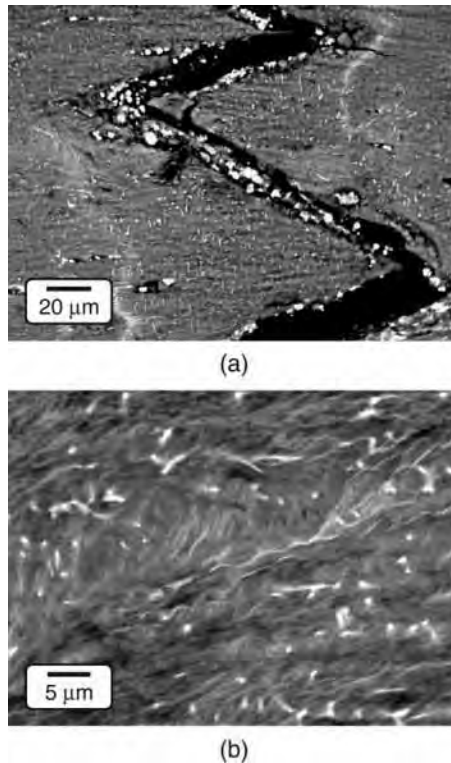


Fig. 5 – Higher-magnification SEM micrographs using BEI for specimens loaded to 5×10^5 cycles showing (a) a crack that propagated from the notch (Fig. 4(c)) and (b) diffuse staining of damage ahead of the notch (Fig. 4(b), location 3). Note the presence of BaSO_4 crystals within the crack, staining of canaliculi, and characteristic wavy lines for diffuse damage.

bovine cortical bone beams *in vitro* using micro-CT with a new BaSO_4 staining technique (Figs. 2 and 6). BaSO_4 was precipitated within damaged tissue, cracks and vasculature, and enhanced the intensity of voxels in micro-CT due to the higher x-ray attenuation of BaSO_4 relative to bone tissue (Figs. 2 and 4). The amount of staining was measured from the image intensity histogram and correlated with the number of loading cycles using a power-law regression (Fig. 8). Thus, this

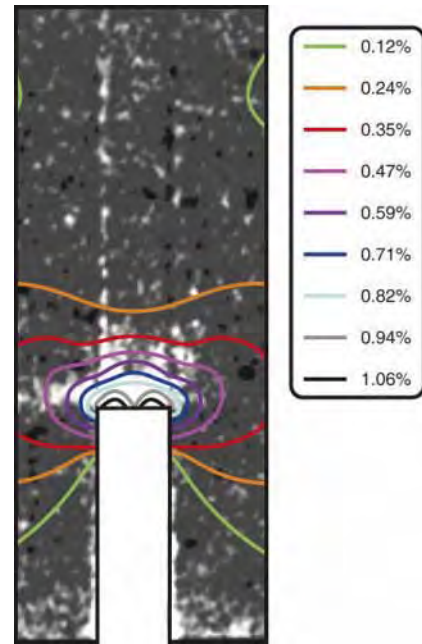


Fig. 7 – Two-dimensional micro-CT image of a specimen loaded to 1×10^5 cycles showing the shape of the stained region ahead of the notch in comparison to principal strain contours calculated by FEA.

study demonstrated the feasibility of non-destructive and three-dimensional detection of microdamage in cortical bone *in vitro* using micro-CT with a suitable contrast agent.

Staining occurred via a simple and benign precipitation reaction (Leng et al., 2004). Specimens were soaked in supersaturated staining solutions such that barium and sulfate ions diffused and concentrated within void space in the tissue – e.g., vasculature and cracks – which acted as a “micro-reactor” and provided an abundance of heterogeneous nucleation sites on surfaces of the extracellular matrix. The presence of BaSO_4 was verified by BEI and EDS (Fig. 4). Furthermore, individual crystals less than $5 \mu\text{m}$ in size were observed on the surfaces of propagating cracks at high magnification (Fig. 5(a)). These crystals appeared similar to those prepared under more

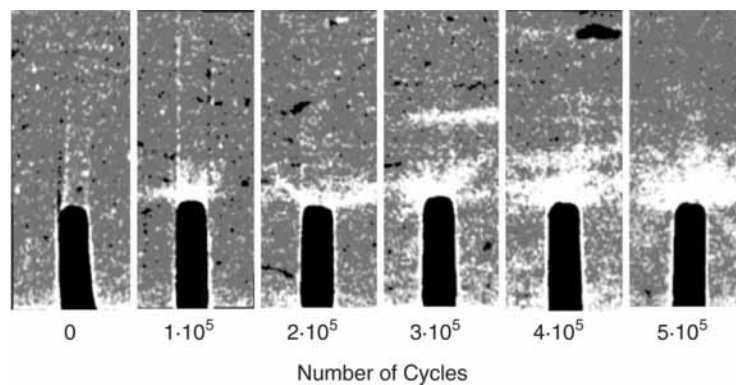


Fig. 6 – Representative two-dimensional micro-CT images from different specimens showing changes in the stained region ahead of the notch with the number of loading cycles. The images were taken from specimens loaded to 0 (control), 1×10^5 , 2×10^5 , 3×10^5 , 4×10^5 and 5×10^5 cycles (left to right). The width of each image is 1.2 mm.

Table 1 – Non-linear regression of the BaSO₄ relative peak intensity with the number of loading cycles using a power law, $y = A \cdot x^b$. The region of analysis included either the micro-CT image of the entire specimen cross-section or a subregion that excluded the free surfaces of beams and endosteal vasculature, as shown in Fig. 2. Specimens regarded as outliers included two specimens that were observed to be over-stained and four specimens that exhibited macroscopic cracks propagating from the imaged notch (Fig. 8)

Specimens	Region of analysis	A	b	p	r ²
All (n = 24)	Entire cross-section	0.165	0.041	<0.05	0.23
All (n = 24)	Subregion	0.063	0.121	<0.0001	0.56
Outliers removed (n = 18)	Entire cross-section	0.162	0.045	<0.005	0.41
Outliers removed (n = 18)	Subregion	0.062	0.124	<0.0001	0.61

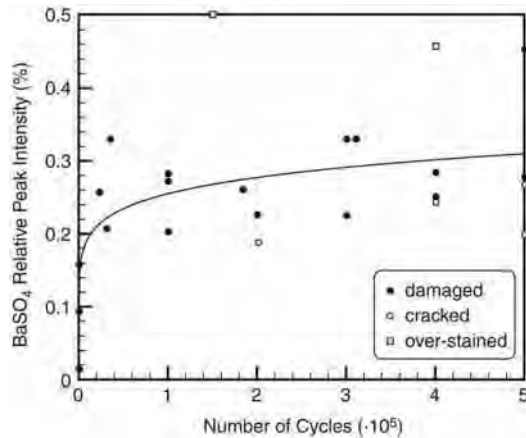


Fig. 8 – Power-law regression of the BaSO₄ relative peak intensity with the number of loading cycles using the image subregion and including all specimens, $y = 0.063x^{0.121}$ ($p < 0.0001$, $r^2 = 0.56$). Data points considered as outliers in subsequent regression analyses, shown in Table 1, included two specimens that were observed to be over-stained and four specimens that exhibited macroscopic cracks propagating from the imaged notch.

highly controlled conditions (Leng et al., 2004). Staining was not observed in tissue ahead of the notch in unloaded control specimens or far away from the notch in loaded specimens (Fig. 4). Therefore, the observed staining of tissue ahead of the notch tip in loaded specimens suggests that damage resulted in the extra-cellular matrix having an increased permeability to the staining solutions due to ultrastructural (“diffuse”) damage. Higher-magnification SEM micrographs revealed “diffuse staining” and “diffuse damage” (Fig. 5(b)) similar to observations with BEI using a lead-uranyl acetate stain (Schaffler et al., 1994) and ultraviolet light or confocal microscopy using fluorescent stains or chelating agents (Boyce et al., 1998; Martin, 2003; Wang and Niebur, 2006; Zioupos and Currey, 1994).

The region of diffuse staining ahead of the notch tip did not extend as far ahead of the notch in specimens where a macroscopic crack propagated from the notch (Fig. 2(b), Fig. 4(c) and Fig. 8). In such cases, the crack propagated laterally from the notch, due to the orientation of the notch relative to the plexiform (or fibrolamellar) structure of bovine cortical bone, and the crack plane was able to be imaged using longitudinal slices in micro-CT (Fig. 9). The smaller

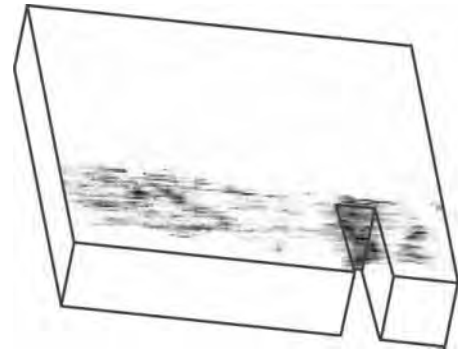


Fig. 9 – Three-dimensional micro-CT image reconstructed from longitudinal slices of a specimen loaded to 5×10^5 cycles and stained with BaSO₄, showing a crack propagating laterally from the notch. Note that the specimen is the same as that shown in Fig. 2(b) and Fig. 4(c).

region of diffuse staining ahead of the notch in cracked specimens suggests that damage accumulation occurred primarily before, rather than during, crack propagation. Similarly, studies investigating the toughness of cortical bone during crack propagation (R-curve behavior) have concluded that microcracking contributes relatively little as a toughening mechanism, per se (Ager et al., 2006; Nalla et al., 2004, 2005). Thus, the role of microcracking is more likely as a precursor to crack propagation (Ager et al., 2006; O'Brien et al., 2005) rather than a toughening mechanism during crack propagation (Vashishth et al., 1997, 2000).

The amount of BaSO₄ staining was correlated with the number of loading cycles using a power-law regression (Fig. 8, Table 1). The power-law relationship was not surprising since specimens were loaded under displacement control, where damage accumulation was expected to lower the beam stiffness and thus the applied load with increasing loading cycles. Since BaSO₄ staining was shown to be due to microdamage, the amount of BaSO₄ staining was considered a relative, but not an absolute, measure of damage. This was a limitation of the study design where only one unbroken notch from each specimen was consistently suitable for imaging microdamage and was stained only with BaSO₄. If loaded specimens were sectioned lengthwise prior to staining, matching pairs could be stained and imaged by both micro-CT using BaSO₄ and ultraviolet light microscopy using a fluorescent stain or chelating agent. Thus, a direct correlation could be made between each measure of damage, and such a study is in progress.

The strength and significance of the correlation for the amount of BaSO₄ staining with the number of loading cycles was substantially improved using a subregion that excluded non-specific staining of the free surfaces of beams and endosteal vasculature (Table 1). In particular, the presence and amount of endosteal vasculature was randomly distributed amongst specimens, but had a profound influence on the staining volume when present (cf. Fig. 2(a) vs. (b)). The correlation was also improved by excluding six specimens exhibiting atypical behavior that was ascribed to the study methods. On average, the four specimens with macroscopic cracks propagating laterally from the unbroken notch exhibited less diffuse staining ahead of the notch (Figs. 2 and 8), for reasons discussed above. On the other hand, the reason for the apparent over-staining of two specimens was not clear. These specimens exhibited homogeneous staining of up to one-half the specimen cross-section that was clearly unrelated to the notch, loading or tissue microstructure.

Each loaded beam exhibited a continuous decrease in stiffness with the number of loading cycles, as expected. The amount of staining was correlated with the total (%) stiffness loss using a power-law regression ($p < 0.05$ for all sets of data shown in Table 1). However, the total (%) loss in stiffness was not correlated with the number of loading cycles ($p = 0.51$ and 0.26 for $n = 24$ and 18 , respectively). There are a couple of plausible explanations for this unexpected behavior. Specimens with macroscopic cracks propagating laterally from the unbroken notch exhibited less diffuse staining ahead of the notch, as described above, but a greater and more rapid stiffness loss. This explanation logically leads to a question of why the unbroken notch in most specimens exhibited damage accumulation ahead of the notch, but several specimens exhibited cracks propagating from the notch. The use of double-notched beams is a clever experimental technique that was previously used to characterize conditions ahead of the unbroken notch after static loading with the assumption that conditions ahead of the unbroken notch are reflective of the broken notch just prior to failure (Nalla et al., 2003, 2005). In this study, double-notched beams were loaded in displacement controlled fatigue and the same assumption was made. Thus, the results of this study may call this assumption into question, perhaps due to the heterogeneity of bone tissue ahead of each notch.

In summary, BaSO₄ staining enabled non-destructive and three-dimensional detection of microdamage in cortical bone using micro-CT. The amount of staining was qualitatively and quantitatively correlated with microdamage accumulation. Therefore, the methods in this study may be useful for future *in vitro* studies into the role of microdamage in bone fragility by enabling correlation of the spatial density of microdamage accumulation to local variations in mechanical loading, bone mineral density (BMD) or microarchitecture. Extension of this technique to *in vivo* detection of microdamage will require improved specificity, biocompatibility, deliverability and x-ray dosage. Staining by BaSO₄ precipitation was non-specific for damage, including all void spaces such as vasculature and free surfaces, and the staining solutions were not biocompatible. Specificity could be greatly improved by molecular or particulate contrast agents with functional

groups that enable preferential binding to calcium exposed on the surfaces of microcracks or diffuse damage (Parkesh et al., 2007). Such a contrast agent could be delivered during the accumulation of damage in bone *in situ*. Finally, the x-ray dosage of current micro-CT scanners is not yet suitable for imaging *in vivo*, though it is not known whether a suitable contrast agent could enable the detection of damaged tissue using clinical CT scanners.

5. Conclusions

Non-destructive and three-dimensional detection of fatigue microdamage accumulation in notched cortical bone specimens was enabled *in vitro* using micro-CT with a precipitated BaSO₄ contrast agent. Reconstructed images showed a distinct region of bright voxels around the notch tip or along propagating cracks due to the presence of BaSO₄, which was verified by backscattered electron imaging and energy dispersive spectroscopy. The shape of the stained region ahead of the notch tip was qualitatively consistent with principal strain contours calculated by finite element analysis. The relative volume of the stained region was correlated with the number of loading cycles by non-linear regression using a power law. The new methods demonstrated in this study may be useful for future *in vitro* studies into the role of microdamage in bone fragility.

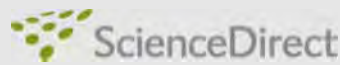
Acknowledgements

This research was supported by the National Institutes of Health (AR049598) and U.S. Army Medical Research and Materiel Command (W81XWH-06-1-0196) through the Department of Defense Peer Reviewed Medical Research Program (PR054672).

REFERENCES

- Ager III, J.W., Balooch, G., Ritchie, R.O., 2006. Fracture, aging, and disease in bone. *J. Mater. Res.* 21 (8), 1878–1892.
- Boyce, T.M., Fyhrie, D.F., Glotkowski, M.C., Radin, E.L., Schaffler, M.B., 1998. Damage type and strain mode associations in human compact bone bending fatigue. *J. Orthop. Res.* 16 (5), 322–329.
- Burr, D.B., Martin, R.B., Schaffler, M.B., Radin, E.L., 1985. Bone remodeling in response to *in vivo* fatigue microdamage. *J. Biomech.* 18, 189–200.
- Burr, D.B., Stafford, T., 1990. Validity of the bulk-staining technique to separate artefactual from *in vivo* bone microdamage. *Clin. Orthop. Rel. Res.* (260), 305–308.
- Burr, D.B., Forwood, M.R., Fyhrie, D.P., Martin, R.B., Schaffler, M.B., Turner, C.H., 1997. Bone microdamage and skeletal fragility in osteoporotic and stress fractures. *J. Bone Miner. Res.* 12, 6–15.
- Jee, W.S.S., 2001. Integrated bone tissue physiology: anatomy and physiology. In: Cowin, S.C. (Ed.), *Bone Mechanics Handbook*, second ed. CRC Press LLC, Boca Raton, pp. 1.1–1.68.
- Jepsen, K.J., Davy, D.T., 1997. Comparison of damage accumulation measures in human cortical bone. *J. Biomech.* 30 (9), 891–894.
- Lee, T.C., Arthur, T.L., Gibson, L.J., Hayes, W.C., 2000. Sequential labelling of microdamage in bone using chelating agents. *J. Orthop. Res.* 18, 322–325.

- Leng, H., Wang, X., Niebur, G.L., Roeder, R.K., 2004. Synthesis of a barium sulfate nanoparticle contrast agent for micro-computed tomography of bone microstructure. *Ceram. Trans.* 159, 219–229.
- Leng, H., VanDersarl, J.J., Niebur, G.L., Roeder, R.K., 2005. Microdamage in bovine cortical bone measured using micro-computed tomography. *Trans. Orthop. Res. Soc.* 30, 665.
- Lewis, G., 1997. Properties of acrylic bone cement: State of the art review. *J. Biomed. Mater. Res. (Appl. Biomater.)* 38, 155–182.
- Li, J., Miller, M.A., Hutchins, G.D., Burr, D.B., 2005. Imaging bone microdamage in vivo with positron emission tomography. *Bone* 37 (6), 819–824.
- Martin, R.B., Burr, D.B., 1982. A hypothetical mechanism for the stimulation of osteonal remodelling by fatigue damage. *J. Biomech.* 15 (3), 137–139.
- Martin, R.B., 2003. Fatigue microdamage as an essential element of bone mechanics and biology. *Calcif. Tissue Int.* 73 (2), 101–107.
- Mori, S., Burr, D.B., 1993. Increased intracortical remodeling following fatigue damage. *Bone* 14, 103–109.
- Nalla, R.K., Kinney, J.H., Ritchie, R.O., 2003. Mechanistic fracture criteria for the failure of human cortical bone. *Nat. Mater.* 2, 164–168.
- Nalla, R.K., Kruzic, J.J., Ritchie, R.O., 2004. On the origin of the toughness of mineralized tissue: microcracking or crack bridging? *Bone* 34, 790–798.
- Nalla, R.K., Stölken, J.S., Kinney, J.H., Ritchie, R.O., 2005. Fracture in human cortical bone: local fracture criteria and toughening mechanisms. *J. Biomech.* 38, 1517–1525.
- O'Brien, F.J., Taylor, D., Dickson, G.R., Lee, T.C., 2000. Visualization of three-dimensional microcracks in compact bone. *J. Anat.* 197, 413–420.
- O'Brien, F.J., Taylor, D., Lee, T.C., 2002. An improved labelling technique for monitoring microcrack growth in compact bone. *J. Biomech.* 35, 523–526.
- O'Brien, F.J., Taylor, D., Lee, T.C., 2005. The effect of bone microstructure on the initiation and growth of microcracks. *J. Orthop. Res.* 23 (2), 475–480.
- Parkesh, R., Lee, T.C., Gunnlaugsson, T., Gowin, W., 2006. Microdamage in bone: Surface analysis and radiological detection. *J. Biomech.* 39, 1552–1556.
- Parkesh, R., Mohsin, S., Lee, T.C., Gunnlaugsson, T., 2007. Histological, spectroscopic, and surface analysis of microdamage in bone: Toward real-time analysis using fluorescent sensors. *Chem. Mater.* 19, 1656–1663.
- Reilly, D.T., Burstein, A.H., 1974. The mechanical properties of cortical bone. *J. Bone Joint Surg. Am.* 56 (5), 1001–1022.
- Schaffler, M.B., Radin, E.L., Burr, D.B., 1989. Mechanical and morphological effects of strain rate on fatigue of compact bone. *Bone* 10 (3), 207–214.
- Schaffler, M.B., Pitchford, W., Choi, K., Riddle, J.M., 1994. Examination of compact bone microdamage using back-scattered electron microscopy. *Bone* 15, 483–488.
- Silva, M.J., Uthgenannt, B.A., Rutlin, J.R., Wohl, G.R., Lewis, J.S., Welch, M.J., 2006. In vivo skeletal imaging of ¹⁸F-fluoride with positron emission tomography reveals damage- and time-dependent responses to fatigue loading in the rat ulna. *Bone* 39, 229–236.
- Skucas, J., 1989. Barium sulfate: Clinical Application, Barium sulfate: Toxicity and Complications. In: Skucas, J. (Ed.), *Radiographic Contrast Agents*, second ed. Aspen Publishers, Inc., Rockville, pp. 10–76.
- Vashishth, D., Behiri, J.C., Bonfield, W., 1997. Crack growth resistance in cortical bone: Concept of microcrack toughening. *J. Biomech.* 30, 763–769.
- Vashishth, D., Tanner, K.E., Bonfield, W., 2000. Contribution, development and morphology of microcracking in cortical bone during crack propagation. *J. Biomech.* 33, 1169–1174.
- Wang, X., Niebur, G.L., 2006. Microdamage propagation in trabecular bone due to changes in loading mode. *J. Biomech.* 39, 781–790.
- Wang, X., Masse, D.B., Leng, H., Hess, K.P., Ross, R.D., Roeder, R.K., Niebur, G.L., 2007. Detection of trabecular bone microdamage by micro-computed tomography. *J. Biomech.*, in press (doi:10.1016/j.jbiomech.2007.05.009).
- Zioupou, P., Currey, J.D., 1994. The extent of microcracking and the morphology of microcracks in damaged bone. *J. Mater. Sci.* 29, 978–986.

available at www.sciencedirect.comjournal homepage: www.elsevier.com/locate/jmbbm

Technical note

Detection of dentinal cracks using contrast-enhanced micro-computed tomography

Matthew D. Landrigan^a, John C. Flatley^a, Travis L. Turnbull^a, Jamie J. Kruzic^b,
Jack L. Ferracane^c, Thomas J. Hilton^c, Ryan K. Roeder^{a,*}

^a Department of Aerospace and Mechanical Engineering, University of Notre Dame, Notre Dame, IN 46556, USA

^b School of Mechanical, Industrial, and Manufacturing Engineering, Oregon State University, Corvallis, OR 97331, USA

^c Division of Biomaterials and Biomechanics, Department of Restorative Dentistry, School of Dentistry, Oregon Health and Science University, Portland, OR 97239, USA

ARTICLE INFO

Article history:

Received 12 June 2009

Received in revised form

17 September 2009

Accepted 1 October 2009

Published online 13 October 2009

ABSTRACT

A new technique using contrast enhanced micro-computed tomography (micro-CT) was developed to improve the ability to detect dentinal cracks in teeth and assess associated risks to oral health. Extracted, whole human molars that exhibited visual evidence of external cracks following extraction and machined, partially fractured elephant dentin specimens were labeled by BaSO₄ precipitation and imaged by micro-CT. Contrast-enhanced micro-CT was demonstrated *in vitro* to enable non-destructive, 3-D imaging of the presence, morphology and spatial location of dentinal cracks in whole human molars and machined specimens. BaSO₄ staining provided enhanced contrast for the detection of cracks that could not be detected prior to staining. Backscattered SEM micrographs showed that BaSO₄ was precipitated on the surfaces of dentinal cracks and within adjacent tubules. The new methods demonstrated in this study are expected to be useful for clinical and scientific studies investigating the etiology and treatment of dentinal cracks in teeth.

© 2009 Elsevier Ltd. All rights reserved.

1. Introduction

Cracked teeth are commonly observed in dental practice and are potentially symptomatic (Clark et al., 2003; Kahler, 2008; Snyder, 1976). Cracked teeth are the third most common cause of tooth loss after caries and periodontal disease (Braly and Maxwell, 1981; Hiatt, 1973). Treatment options are typically lengthy, expensive and include a risk of morbidity (Liu and Sidhu, 1995; Homewood, 1998;

Geurtsen and García-Godoy, 1999; Kahler, 2008), yet there is little definitive evidence to support the diagnosis of cracks requiring intervention or the effectiveness of interventions (e.g., Bader et al., 1996). Therefore, treatments may be either over-prescribed or prescribed too late.

Current methods for the diagnosis of cracks that may compromise teeth are all based on optical assessment, with or without the aid of surgical loupes, microscopes, dyes and/or transillumination (Clark et al., 2003; Kahler, 2008). Improvements in the detection and classification of cracks have been demonstrated using enhanced magnification

* Corresponding address: Department of Aerospace and Mechanical Engineering, University of Notre Dame, 148 Multidisciplinary Research Building, Notre Dame, IN 46556, USA. Tel.: +1 574 631 7003; fax: +1 574 631 2144.

E-mail address: rroeder@nd.edu (R.K. Roeder).

1751-6161/\$ - see front matter © 2009 Elsevier Ltd. All rights reserved.

doi:10.1016/j.jmbbm.2009.10.003

(Clark et al., 2003; Slaton et al., 2003) and transillumination (Wright et al., 2004). However, optical methods suffer from an inherent inability to assess the severity of cracks (e.g., crack depth), particularly sub-surface dentinal cracks. Moreover, dentinal cracks are generally not able to be detected in plain radiographs.

Micro-CT is useful for non-invasive, three-dimensional (3-D) imaging of the internal structure of mineralized tissues, due to relative differences in x-ray attenuation. Cone beam volumetric micro-CT was recently demonstrated to provide more accurate assessment of proximal caries lesion depth compared to conventional radiographs (Kalathing et al., 2007). Intra-oral systems limit the volume irradiated and thus achieve a low radiation dose to the patient; however, the spatial resolution is currently limited to 40 μm and the image contrast is low relative to conventional CT (Kalathing et al., 2007). High-resolution micro-CT systems are commercially available for both *in vivo* imaging of small animals and *in vitro* imaging of tissue specimens. The spatial resolution is typically on the order of 10 μm and systems with 1 μm resolution are now available. However, the detection of small cracks ($\sim 1 \mu\text{m}$ in width) in relatively large specimens (e.g., a molar) is limited by the resolution, maximum specimen size, and data collection time of the above instruments. X-ray tomography using high energy, monochromatic synchrotron radiation is able to image cracks in dentin (Kruzic et al., 2003), but is neither readily available nor amenable to imaging large numbers of tissue specimens that are relatively large in size.

Non-destructive, 3-D imaging of the presence, spatial location and accumulation of microdamage in bone tissue was recently demonstrated for the first time using contrast-enhanced micro-CT with a precipitated BaSO_4 stain (Leng et al., 2008; Wang et al., 2007). Although imaging of cracks and damage in bone had been previously demonstrated using high energy, monochromatic synchrotron radiation (Nalla et al., 2005), this approach enabled the use of commercially available bench top micro-CT instruments. BaSO_4 was precipitated within damaged tissue, cracks and vasculature, as verified by backscattered electron imaging and energy dispersive spectroscopy (Leng et al., 2008; Wang et al., 2007). Moreover, precipitated BaSO_4 enhanced the intensity of voxels in micro-CT due to the higher x-ray attenuation of BaSO_4 relative to bone tissue. The micro-CT scanner (10 μm resolution) was unable to detect microcracks or fatigue cracks without the use of the contrast agent. Therefore, contrast-enhanced micro-CT is expected to find increased use in the study of mineralized tissue mechanics, complementing or replacing methods of damage/crack detection that are inherently destructive, two-dimensional and tedious.

The objective of this study was to non-destructively and three-dimensionally image dentinal cracks using contrast-enhanced micro-CT. Extracted, whole human molars that exhibited visual evidence of external cracks following extraction and machined, partially fractured elephant dentin specimens were labeled by BaSO_4 precipitation and imaged by micro-CT using methods adapted from previous studies investigating microdamage in bone tissue (Leng et al., 2008; Wang et al., 2007).

2. Materials and methods

2.1. Elephant dentin

Two partially fractured, dehydrated compact-tension specimens of dentin from tusk shards of a single adult male elephant (*Loxodonta africana*) used in a previous study (Kruzic et al., 2003) provided well-characterized and highly controlled cracks for evaluating feasibility of the technique. Elephant dentin is similar to human dentin in containing tubules within an extracellular matrix of mineralized collagen fibers and avoids the specimen size limitations of human dentin. Compact-tension specimens were machined while hydrated to a thickness of $\sim 2.5 \text{ mm}$ and width of $\sim 15 \text{ mm}$. Specimens were polished to a 1200 grit finish, followed by 1 and 0.05 μm alumina suspensions. An initial notch was introduced with a low speed diamond wafer saw such that the crack growth direction was oriented perpendicular to the long axis of the tubules and the crack plane was in the plane of the tubules. A final notch with root radius $\sim 15 \mu\text{m}$ was achieved by repeatedly sliding a razor blade over the initial notch. Fracture resistance (R-curve) testing was conducted in *vacuo* ($\sim 10^{-4} \text{ Pa}$) in a scanning electron microscope (SEM). Specimens were rehydrated and stored in phosphate buffered saline upon receipt and during all interim periods before staining and micro-CT.

2.2. Whole human molars

Ten extracted human molars from different donors were provided by the Practice-based Research in Oral Health (PROH) practitioner network through the Oregon Health and Science University. Teeth were screened after extraction for evidence of external cracks upon inspection with 3.5X surgical loupes. All teeth were maintained hydrated in a 0.05% solution of chloramine T during all interim periods before staining and micro-CT.

2.3. Histological staining and imaging

Elephant dentin specimens and whole human molars were imaged before and after histological staining by micro-CT ($\mu\text{CT-80}$, Scanco Medical AG, Bassersdorf, Switzerland) at 10 μm resolution, 70 kVp voltage, 113 μA current, and 400 ms integration time. Grayscale images were smoothed by Gaussian filtering. High intensity voxels representative of BaSO_4 were segmented to highlight cracks in 3-D reconstructions. An image subregion was used to remove the effect of non-specific BaSO_4 staining on specimen free surfaces which would have otherwise obscured the visualization of internal features in 3-D reconstructions.

All specimens were stained by BaSO_4 precipitation, soaking in an equal parts mixture of 0.5 M barium chloride (Certified ACS crystal, Fisher Scientific, Fair Lawn, NJ) in de-ionized water, buffered saline, and acetone for 3 days, followed by an equal parts mixture of 0.5 M sodium sulfate (Anhydrous powder, Fisher Scientific, Fair Lawn, NJ) in de-ionized water, buffered saline, and acetone for 3 days, both under vacuum ($\sim 50 \text{ mm Hg}$). The staining mechanism was a precipitation reaction where $\text{BaCl}_2(\text{aq}) + \text{Na}_2\text{SO}_4(\text{aq}) \rightarrow \text{BaSO}_4(\text{s}) + 2\text{NaCl}(\text{aq})$. Barium and sulfate ions diffused into

and concentrated within void space in the dentinal tissue – e.g., tubules and cracks – which acted as a “micro-reactor” and provided an abundance of heterogeneous nucleation sites on tissue surfaces (Leng et al., 2004, 2008).

After staining and micro-CT, specimens were dehydrated in a graded series of alcohol solutions, dried overnight in an oven at 90 °C, embedded in poly(methyl methacrylate), sectioned with a low-speed diamond wafer saw, polished with a series of diamond compounds to a 1 µm finish, and coated with Au–Pd by sputter deposition for scanning electron microscopy (SEM). Specimens were imaged using backscattered electrons (Evo 50, LEO Electron Microscopy Ltd., Cambridge, UK) at an accelerating voltage of 20 kV and a working distance of 9–12 mm. Note that image contrast from backscattered electrons is primarily due to compositional differences in atomic number, with an increasing atomic number resulting in increased intensity. The elemental composition of the stain was verified by electron probe microanalysis using energy dispersive spectroscopy (EDS) (INCA x-sight model 7636, Oxford Instruments America, Concord, MA).

3. Results

Contrast-enhanced micro-CT enabled non-destructive, 3-D imaging of the presence, morphology and spatial location of dentinal cracks in machined specimens (Fig. 1) and whole human molars (Fig. 2). In both types of specimens, BaSO₄ staining provided enhanced contrast for the detection of cracks that were not able to be detected prior to staining (Figs. 1(b), (c), and 2(b)). Note that the entire 3-D volume of grayscale image slices for the specimens shown in Figs. 1 and 2 are available as movie files (.avi) in Electronic Annex 1 and 2, respectively, of the online version of this article. Backscattered SEM micrographs showed that BaSO₄ was precipitated on the surfaces of dentinal cracks and within adjacent tubules (Fig. 1(e)). The highest levels of image intensity for both micro-CT and backscattered SEM were shown to correspond to the presence of elemental barium and sulfur measured using EDS. At higher magnification, SEM revealed the presence of BaSO₄ crystals and aggregates, typically submicron but up to 5 µm in size, on the surfaces of propagating cracks and within adjacent tubules. BaSO₄ was also precipitated on all free surfaces, including the root canal and pulp chamber (Fig. 2(a)). Therefore, a subregion was used to remove staining of the outer specimen surfaces and reveal internal features, including cracks, in segmented 3-D reconstructions (Figs. 1(a), and 2(a)).

4. Discussion

The feasibility of non-destructive, 3-D imaging of dentinal cracks was demonstrated *in vitro* in machined, partially fractured specimens (Fig. 1) and whole human molars (Fig. 2) using contrast-enhanced micro-CT with a precipitated BaSO₄ stain. BaSO₄ precipitation on the surfaces of dentinal cracks and within adjacent tubules enhanced the intensity of voxels in micro-CT due to the higher x-ray attenuation of BaSO₄

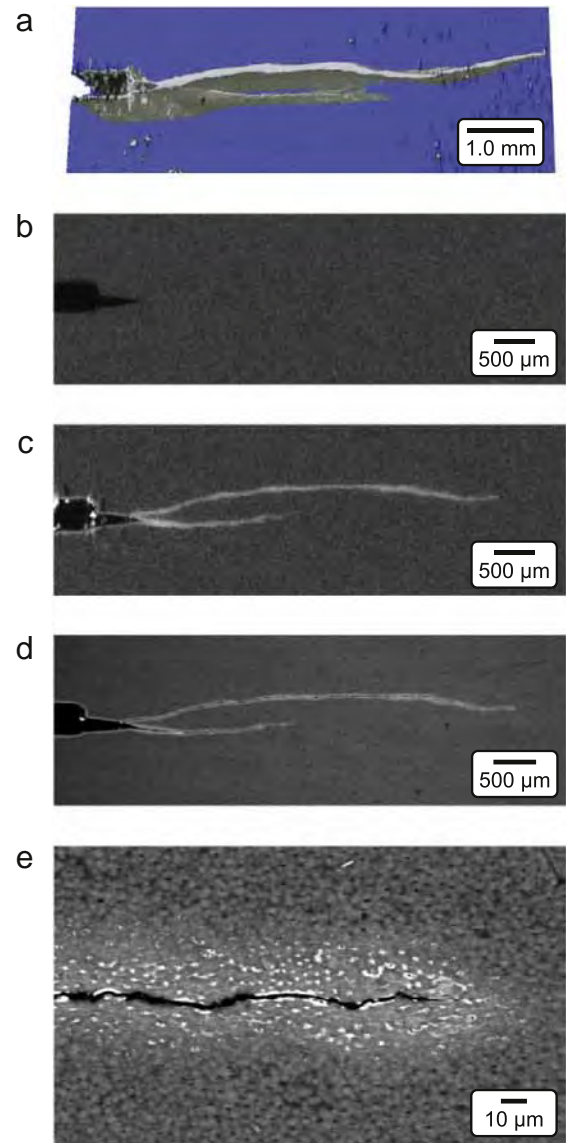


Fig. 1 – A branched crack that propagated from a notch (left) in a compact tension specimen of elephant dentin was imaged by micro-CT before and after staining by BaSO₄ precipitation, and by backscattered SEM after staining by BaSO₄ precipitation. (a) A segmented, three-dimensional micro-CT reconstruction showed crack surfaces stained with BaSO₄. Cross-sectional grayscale micro-CT images at the same depth approximately midway through the specimen thickness (b) before and (c) after staining by BaSO₄ precipitation showed that the crack was unable to be detected at this location without the use of the contrast agent. The contrast-enhanced micro-CT image in (c) was compared to (d) a backscattered SEM micrograph for the same specimen at approximately the same cross-sectional depth and magnification. (e) A backscattered SEM micrograph of the crack tip in (d) at higher magnification showed BaSO₄ penetration into microtubules. Note that the presence of elemental Ba and S was verified by EDS (not shown).

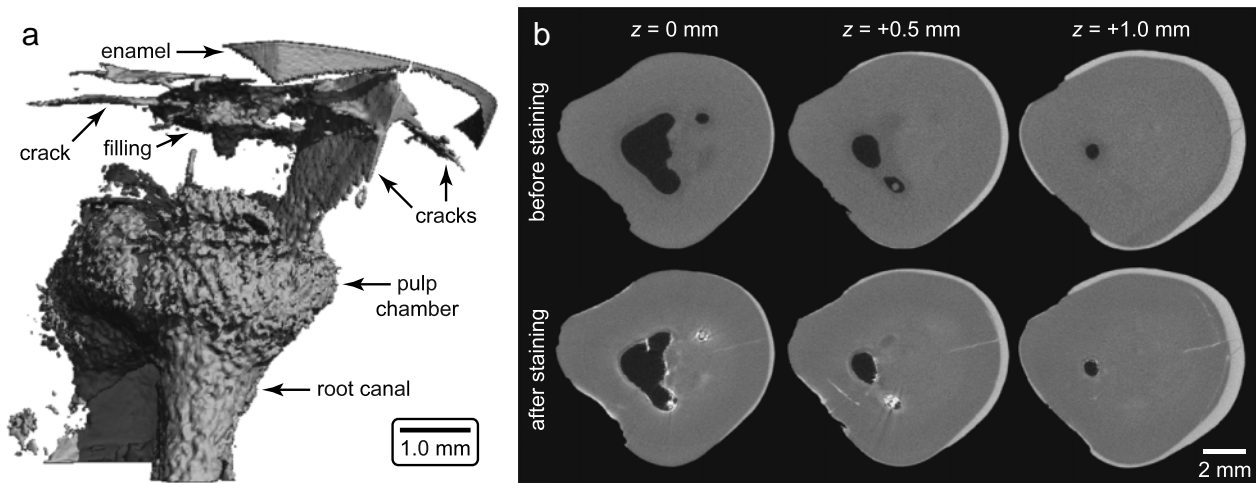


Fig. 2 – An extracted human molar which showed evidence of cracks upon visual inspection was imaged by micro-CT. (a) A segmented, three-dimensional micro-CT reconstruction revealed internal surfaces stained by BaSO_4 precipitation, including the root canal, pulp chamber and cracks, and other features exhibiting the highest x-ray attenuation, including the enamel and a composite filling. Note that the majority of the enamel crown of the tooth has been excluded from the image at the top. (b) Grayscale images of transverse cross-sections showed enhanced contrast for the detection of dentinal cracks after staining by BaSO_4 precipitation compared to the same image cross-section prior to staining.

relative to dentin. The BaSO_4 contrast agent enabled the detection of dentinal cracks that were otherwise not able to be detected using a standard benchtop micro-CT instrument at 10 μm resolution (Figs. 1(b), (c), and 2(b)). The total crack length measured at the free surface in the elephant dentin compact-tension specimens was unchanged before and after staining, which suggests that the staining process did not introduce artifactual damage. Furthermore, the absence of BaSO_4 within cracks during subsequent electron microscopy also enabled discrimination of artifactual cracks that formed during specimen preparation, for example during dehydration, from cracks that formed *in vivo* or during *in vitro* mechanical loading.

The new methods demonstrated in this study are expected to be very useful for *in vitro* scientific studies investigating the mechanical behavior of teeth, including the etiology and morphology of dentinal cracks. Insightful quantitative measurements of crack dimensions, volume, density, orientation, etc. can be subsequently obtained by applying common methods of image analysis to acquired micro-CT data. Such measurements would be extremely tedious, if not impossible, using conventional two-dimensional (2-D) histological techniques. Moreover, even in a highly controlled fracture test, crack length and branching, for example, may exhibit significant 3-D spatial variation that would be otherwise undetected by observation of the specimen surface or any single 2-D cross-section (Fig. 1(a)). Finally, additional potential exists for use of this technique *in vivo* for clinical studies, perhaps with some modification to the staining method or contrast agent. Indeed, cone beam micro-CT with 40 μm resolution is under investigation for clinical use (Kalathing et al., 2007).

Some limitations should be noted for the new methods demonstrated in this study. BaSO_4 precipitation was nonspecific for cracks, including all void spaces such as vasculature and free surfaces. Furthermore, under the conditions of this

study the BaSO_4 contrast agent was difficult to distinguish from the enamel, presumably due to comparable levels of x-ray attenuation. However, cracks in the enamel were readily detected by micro-CT both with and without the use of a contrast agent (Fig. 2(b)) due to the relatively low x-ray attenuation of the fluid space in the crack compared to the enamel. Therefore, the main limitation of the difficulty distinguishing BaSO_4 from enamel, as well as non-specific staining of exterior specimen surfaces with BaSO_4 , was the need to remove the outermost voxels using contouring and a subregion analysis in order to visualize internal features in segmented, 3-D reconstructions. Last, the barium chloride and sodium sulfate staining solutions may or may not be acceptable within the oral cavity with some modification, warranting future work and potentially limiting this technique to *in vitro* studies.

5. Conclusions

Contrast-enhanced micro-CT was demonstrated *in vitro* to enable non-destructive, 3-D imaging of the presence, morphology and spatial location of dentinal cracks in whole human molars and machined, partially fractured specimens. In both types of specimens, BaSO_4 staining provided enhanced contrast for the detection of cracks that were not able to be detected prior to staining. Backscattered SEM micrographs showed that BaSO_4 was precipitated on the surfaces of dentinal cracks and within adjacent tubules. The new methods demonstrated in this study are expected to be immediately useful for *in vitro* scientific studies investigating the etiology and treatment of dentinal cracks in teeth, and also possess potential for use in clinical studies with further development.

Acknowledgments

This research was partially supported by the U.S. Army Medical Research and Materiel Command (W81XWH-06-1-0196) through the Peer Reviewed Medical Research Program (PR054672).

Appendix. Supplementary data

Supplementary data associated with this article can be found, in the online version, at [doi:10.1016/j.jmbbm.2009.10.003](https://doi.org/10.1016/j.jmbbm.2009.10.003).

REFERENCES

- Bader, J.D., Shugars, D.A., Roberson, T.M., 1996. Using crowns to prevent tooth fracture. *Community Dent. Oral Epidemiol.* 24 (1), 47–51.
- Braly, B.V., Maxwell, E.H., 1981. Potential for tooth fracture in restorative dentistry. *J. Prosthet. Dent.* 45 (4), 411–414.
- Clark, D.J., Sheets, C.G., Parquette, J.M., 2003. Definitive diagnosis of early enamel and dentin cracks based on microscopic evaluation. *J. Esthet. Restor. Dent.* 15 (7), 391–401.
- Geurtsen, W., García-Godoy, F., 1999. Bonded restorations for the prevention and treatment of the cracked tooth syndrome. *Am. J. Dent.* 13 (6), 266–270.
- Hiatt, W.H., 1973. Incomplete crown-root fracture in pulpal-periodontal disease. *J. Periodontol.* 44 (6), 369–379.
- Homewood, C.I., 1998. Cracked tooth syndrome—Incidence, clinical findings and treatment. *Aust. Dent. J.* 43 (4), 217–222.
- Kahler, W., 2008. The cracked tooth conundrum: Terminology, classification, diagnosis, and management. *Am. J. Dent.* 21, 275–282.
- Kalathingall, S.M., Mol, A., Tyndall, D.A., Caplan, D.J., 2007. In vitro assessment of cone beam local computed tomography for proximal caries detection. *Oral Surg. Oral Med. Oral Pathol. Oral Radiol. Endod.* 104, 699–704.
- Kruzic, J.J., Nalla, R.K., Kinney, J.H., Ritchie, R.O., 2003. Crack blunting, crack bridging and resistance-curve fracture mechanics in dentin: Effect of hydration. *Biomaterials* 24 (28), 5209–5221.
- Leng, H., Wang, X., Niebur, G.L., Roeder, R.K., 2004. Synthesis of a barium sulfate nanoparticle contrast agent for micro-computed tomography of bone microstructure. *Ceram. Trans.* 159, 219–229.
- Leng, H., Wang, X., Ross, R.D., Niebur, G.L., Roeder, R.K., 2008. Micro-computed tomography of fatigue microdamage in cortical bone using a barium sulfate contrast agent. *J. Mech. Behav. Biomed. Mater.* 1 (1), 68–75.
- Liu, H.H., Sidhu, S.K., 1995. Cracked teeth—treatment rationale and case management: Case reports. *Quintessence Int.* 26 (7), 485–492.
- Nalla, R.K., Kruzic, J.J., Kinney, J.H., Ritchie, R.O., 2005. Mechanistic aspects of fracture and R-curve behavior in human cortical bone. *Biomaterials* 26 (2), 217–231.
- Slaton, C.C., Loushine, R.J., Weller, R.N., Parker, M.H., Kimbrough, W.F., Pashley, D.H., 2003. Identification of resected root-end dentinal cracks: A comparative study of visual magnification. *J. Endod.* 29 (8), 519–522.
- Snyder, D.E., 1976. The cracked-tooth syndrome and fractured posterior cusp. *Oral Surg. Oral Med. Oral Pathol.* 41 (6), 698–704.
- Wang, X., Masse, D.B., Leng, H., Hess, K.P., Ross, R.D., Roeder, R.K., Niebur, G.L., 2007. Detection of trabecular bone microdamage by micro-computed tomography. *J. Biomech.* 40 (15), 3397–3403.
- Wright, H.M., Loushine, R.J., Weller, R.N., Kimbrough, W.F., Waller, J., Pashley, D.H., 2004. Identification of resected root-end dentinal cracks: A comparative study of transillumination and dyes. *J. Endod.* 30 (10), 712–715.



Contrast-enhanced micro-computed tomography of fatigue microdamage accumulation in human cortical bone

Matthew D. Landrigan^a, Jiliang Li^b, Travis L. Turnbull^a, David B. Burr^{c,d}, Glen L. Niebur^a, Ryan K. Roeder^{a,*}

^a Department of Aerospace and Mechanical Engineering, University of Notre Dame, Notre Dame, IN 46556, USA

^b Department of Biology, Indiana University–Purdue University Indianapolis, Indianapolis, IN 46202, USA

^c Department of Anatomy and Cell Biology, Indiana University School of Medicine, Indianapolis, IN 46202, USA

^d Department of Orthopaedic Surgery, Indiana University School of Medicine, Indianapolis, IN 46202, USA

ARTICLE INFO

Article history:

Received 20 July 2010

Revised 22 September 2010

Accepted 8 October 2010

Available online 15 October 2010

Edited by: D. Fyhrie

Keywords:

Barium sulfate

Contrast agent

Cortical bone

Fatigue microdamage

Micro-computed tomography

ABSTRACT

Conventional methods used to image and quantify microdamage accumulation in bone are limited to histological sections, which are inherently invasive, destructive, two-dimensional, and tedious. These limitations inhibit investigation of microdamage accumulation with respect to volumetric spatial variation in mechanical loading, bone mineral density, and microarchitecture. Therefore, the objective of this study was to investigate non-destructive, three-dimensional (3-D) detection of microdamage accumulation in human cortical bone using contrast-enhanced micro-computed tomography (micro-CT), and to validate micro-CT measurements against conventional histological methods. Unloaded controls and specimens loaded in cyclic uniaxial tension to a 5% and 10% reduction in secant modulus were labeled with a precipitated BaSO₄ stain for micro-CT and basic fuchsin for histomorphometry. Linear microcracks were similarly labeled by BaSO₄ and basic fuchsin as shown by backscattered electron microscopy and light microscopy, respectively. The higher X-ray attenuation of BaSO₄ relative to the bone extracellular matrix provided enhanced contrast for the detection of damage that was otherwise not able to be detected by micro-CT prior to staining. Therefore, contrast-enhanced micro-CT was able to nondestructively detect the presence, 3-D spatial location, and accumulation of fatigue microdamage in human cortical bone specimens *in vitro*. Microdamage accumulation was quantified on segmented micro-CT reconstructions as the ratio of BaSO₄ stain volume (SV) to total bone volume (BV). The amount of microdamage measured by both micro-CT (SV/BV) and histomorphometry (Cr.N, Cr.Dn, Cr.S.Dn) progressively increased from unloaded controls to specimens loaded to a 5% and 10% reduction in secant modulus ($p < 0.001$). Group means for micro-CT measurements of damage accumulation were strongly correlated to those using histomorphometry ($p < 0.05$), validating the new methods. Limitations of the new methods in the present study included that the precipitated BaSO₄ stain was non-specific and non-biocompatible, and that micro-CT measurements exhibited greater variability compared to conventional histology. Nonetheless, contrast-enhanced micro-CT enabled non-destructive imaging and 3-D spatial information, which are not possible using conventional histological methods.

© 2010 Elsevier Inc. All rights reserved.

Introduction

Microdamage has been implicated in clinical fracture susceptibility, including stress fractures in active individuals, fragility fractures in the elderly, and the effects of long-term antiresorptive treatments for osteoporosis [1,2]. Microdamage can accumulate in bone tissue with aging [2–6] and/or repetitive mechanical loading, resulting in the degradation of mechanical properties, such as the elastic modulus [5–11] and fracture toughness [6,12,13], among others. The accumulation of fatigue damage is typically measured mechanically, by a reduction

in modulus or stiffness [8–12,14,15], and/or histologically, by microcrack density (Cr.Dn), microcrack length (Cr.Ln.), microcrack surface density (Cr.S.Dn), and diffuse damage [3–16].

Conventional methods used to image and quantify microdamage accumulation in bone are limited to histological sections, which are inherently invasive, destructive, two-dimensional (2-D), and tedious [17]. These methods include: transmitted light or epifluorescence microscopy using basic fuchsin stain [18–21]; epifluorescence microscopy using chelating fluorochromes [22–25]; and backscattered electron microscopy using a lead-uranyl acetate stain [26]. The various contrast agents are used to aid detection of microdamage and differentiate artifactual damage created during specimen preparation. Laser scanning confocal microscopy of damaged tissue labeled with fluorochromes provided enhanced depth of focus for three-dimensional (3-D) imaging [27,28], but remained limited to histological

* Corresponding author. Department of Aerospace and Mechanical Engineering, Bioengineering Graduate Program, 148 Multidisciplinary Research Building, University of Notre Dame, Notre Dame, IN 46556, USA. Fax: +1 574 631 2144.

E-mail address: rroeder@nd.edu (R.K. Roeder).

sections. Serial sectioning of damaged tissue labeled with fluorochromes enabled 3-D images to be reconstructed from 2-D serial images [29,30], but is destructive and labor intensive. The above limitations associated with conventional histological methods inhibit investigation of microdamage accumulation with respect to volumetric spatial variation in mechanical loading, bone mineral density, and microarchitecture. Moreover, a non-destructive, 3-D method for damage assessment could reduce the time and labor required for current histological methods.

Recent studies have begun to investigate methods for non-destructive, 3-D detection and imaging of microdamage in bone tissue. Fatigue microdamage generated in a rat forelimb was detected *in vivo* by positron emission tomography (PET) using a sodium fluoride (Na^{18}F) tracer [31,32], but may be limited in specificity due to the concomitant influence of metabolic activity. X-ray tomography using high energy, monochromatic synchrotron radiation has sufficient resolution to directly image microcracks in bone tissue [33–36], but may embrittle the tissue [36] and is neither readily available nor amenable to imaging large numbers of tissue specimens that are relatively large in size. Therefore, contrast agents have been investigated to enable the use of lower resolution, but commercially available, micro-computed tomography (micro-CT) instruments.

Micro-CT has been investigated for the detection of microdamage *in vitro* using iodinated molecules [17,37], precipitated lead sulfide [38,39], precipitated barium sulfate (BaSO_4) [40–42], and functionalized gold nanoparticles [43–45] as contrast agents with higher X-ray attenuation than the extracellular matrix of bone. Lead-based stains were adopted from prior use on 500 μm thick cortical bone sections for histology using electron microscopy [26] and were demonstrated as a micro-CT contrast agent in human femoral trabecular bone specimens which typically exhibit 100–200 μm thick trabeculae [39], but exhibited poor penetration into bulk (4 mm thick) cortical bone specimens [38]. Moreover, lead salts are among the most severe chemical hazards for human health and the environment [46]. Therefore, a new approach was developed for staining by BaSO_4 precipitation within damaged tissue, cracks, and vasculature, which was verified by backscattered electron imaging and energy dispersive spectroscopy [40–42]. Damage accumulation that was localized ahead of a notch in bovine cortical bone beams loaded in cyclic four-point bending was stained *in vitro* by precipitation of BaSO_4 and imaged using micro-CT [40]. However, the 3-D spatial location of damage accumulation ahead of the notch was to be expected *a priori* and micro-CT measurements were not validated by histology.

Therefore, the objectives of this study were to: (1) detect the 3-D spatial location and quantify the amount of microdamage accumulation within a uniformly stressed volume of human cortical bone using contrast-enhanced micro-CT with a precipitated BaSO_4 stain; and (2) validate micro-CT measurements against conventional histological methods. Human cortical bone specimens were loaded in cyclic uniaxial tension to predetermined levels of secant modulus degradation, which was correlated with the level of damage measured by micro-CT and conventional histology on specimens stained with BaSO_4 and basic fuchsin, respectively.

Materials and methods

Specimen preparation

Ninety specimens were sectioned from the femoral mid-diaphysis of three Caucasian men (62, 62 and 65 years of age) presenting no medical history of skeletal pathology or trauma. All tissues were obtained with donor's consent (National Disease Research Interchange, Philadelphia, PA) and all protocols were approved by the Notre Dame Human Subjects Institutional Review Board. Cylindrical specimens were machined to a 2.5 mm diameter by 5 mm gauge length on a computer numerical controlled lathe (4500 Series,

Sherline Products, Inc., Vista, CA). Specimens were randomly assigned to six experimental groups ($n = 15/\text{group}$), comprising an unloaded control and two mechanically loaded groups for both micro-CT and conventional histology. Specimens were wrapped in gauze, hydrated in phosphate buffered saline (PBS), and stored at -20°C in airtight containers during interim periods.

Fatigue loading

Mechanically loaded specimens were subjected to cyclic uniaxial tension ($R = 0$) at 2 Hz under load control on an electromagnetic test instrument (ElectroForce 3300, Bose Corp., Eden Prairie, MN) while hydrated with a de-ionized (DI) water drip at ambient temperature until achieving a 5% or 10% reduction in the secant modulus. Note that loading was completed within a relatively short duration (within 18 h for 26 specimens and within 5 days for 4 specimens), allowing the use of a DI water drip without significant effect on the tissue. The secant modulus was measured as the slope of the line connecting the minimum and maximum load and displacement for a given loading cycle. Displacements were measured via a cross-head linear variable displacement transducer (± 0.025 mm sensitivity), which was verified against measurements using an extensometer.

Specimens were first preconditioned at 60 MPa for 20 cycles and the initial secant modulus was measured as the average of the first 10 cycles. Maximum fatigue load levels were normalized to an initial maximum strain of 6400 ± 300 microstrain using the initial secant modulus. The secant modulus degradation during fatigue loading was measured as the percent reduction in secant modulus at a given number of loading cycles relative to the initial secant modulus. For specimens loaded to a 5% reduction in secant modulus, the average of five cycles was taken in order to filter noise and prevent premature stoppage of the test. Specimens loaded to a 10% reduction in secant modulus did not require averaging because a 10% reduction in secant modulus typically coincided with fatigue crack propagation prior to fracture. Thus, averaging multiple cycles would have resulted in catastrophic failure of many specimens. Finally, the total number of loading cycles was recorded upon reaching the predetermined secant modulus degradation for each specimen.

Barium sulfate staining and micro-CT

Unloaded controls and specimens loaded to a 5% and 10% reduction in secant modulus were stained by BaSO_4 precipitation. Specimens were soaked in a solution of equal parts buffered saline, acetone, and 0.5 M BaCl_2 (certified ACS crystal, Fisher Scientific, Fair Lawn, NJ) in DI water for 3 days, followed by a solution of equal parts buffered saline, acetone, and 0.5 M Na_2SO_4 (anhydrous powder, Fisher Scientific, Fair Lawn, NJ) in DI water for 3 days, both under vacuum (~ 50 mm Hg). Specimens were rinsed with DI water after each step to minimize ions or particles on specimen surfaces. The staining mechanism was a precipitation reaction where $\text{BaCl}_2(\text{aq}) + \text{Na}_2\text{SO}_4(\text{aq}) \rightarrow \text{BaSO}_4(\text{s}) + 2\text{NaCl}(\text{aq})$. Barium and sulfate ions diffused into and concentrated within void space in the tissue—e.g., microcracks, damaged tissue and vasculature—which provided an abundance of heterogeneous nucleation sites for precipitation on tissue surfaces [40].

The entire gauge length of each stained specimen was imaged by micro-CT ($\mu\text{CT}-80$, Scanco Medical AG, Brüttisellen, Switzerland) at 10 μm resolution, 70 kVp voltage, 113 μA current, and 400 ms integration time with slices taken perpendicular to the longitudinal specimen axis. Note that selected specimens were also imaged by micro-CT after mechanical loading but prior to staining in order to determine whether micro-CT could detect microdamage without the contrast agent. Grayscale images were smoothed by a Gaussian filter with $\sigma = 1.5$ and support = 3. The ratio of BaSO_4 stain volume (SV) to total bone volume (BV), SV/BV, was adopted as a measure of

damage. High intensity voxels representative of SV were segmented at a constant global threshold of 490, corresponding to a mean linear attenuation coefficient of 3.92 cm^{-1} or $\sim 1890 \text{ mg HA/cm}^3$, which was well above the tissue mineral density of human cortical bone [47]. Low intensity voxels representative of Haversian porosity were segmented at a constant global threshold of 270 (2.16 cm^{-1} or $\sim 839 \text{ mg HA/cm}^3$) prior to staining and 290 (2.32 cm^{-1} or $\sim 924 \text{ mg HA/cm}^3$) after staining. These thresholds were shown to provide similar measurements of porosity for the same specimen before and after staining due to an overall shift in image intensity. BV was measured from all voxels above the Haversian porosity threshold. In order to minimize the effect of non-specific BaSO_4 staining on specimen free surfaces, a cylindrical image subregion was analyzed with a radius reduced by $100 \mu\text{m}$ (10 voxels) from the specimen perimeter. The above parameters were determined to provide an optimal balance of sensitivity and noise suppression after a systematic evaluation described in detail elsewhere [48].

After micro-CT, selected specimens were prepared for scanning electron microscopy (SEM). These specimens were dehydrated in a graded series of alcohol solutions, dried overnight in an oven at 90°C , embedded in poly(methyl methacrylate), sectioned longitudinally with a low-speed diamond wafer saw, polished with a series of diamond compounds to a $1 \mu\text{m}$ finish, washed with ethanol, dried overnight in an oven at 90°C , and coated with Au-Pd by sputter deposition. Specimens were imaged using backscattered electron imaging (BEI) at an accelerating voltage of 20 kV and a working distance of 7 mm (Evo 50, LEO Electron Microscopy Ltd., Cambridge UK). Note that image contrast from backscattered electrons is primarily due to compositional differences in atomic number, with an increasing atomic number resulting in increased intensity. The elemental composition of the stain was verified by electron probe microanalysis (EPMA) using energy dispersive spectroscopy (EDS) (INCA x-sight model 7636, Oxford Instruments America, Concord, MA).

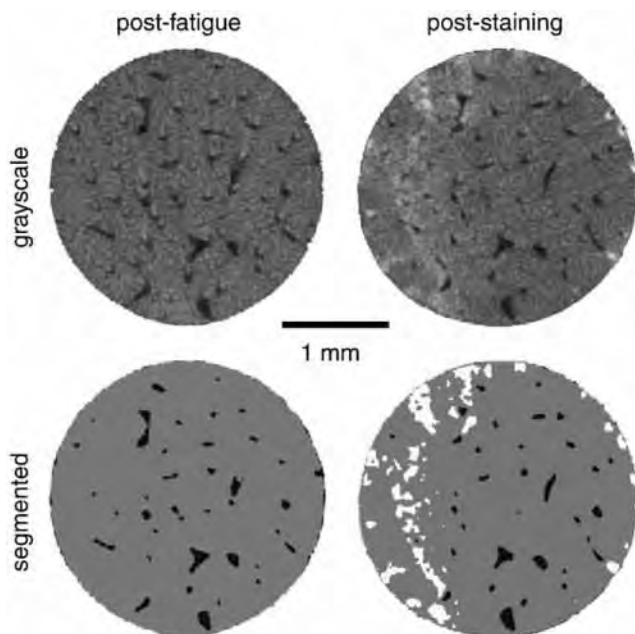


Fig. 1. Grayscale and segmented micro-CT images of the same specimen cross-section (2.5 mm diameter) after loading to a 10% reduction in secant modulus but prior to staining (post-fatigue), and after staining with BaSO_4 (post-staining), showing enhanced contrast (bright voxels) for the detection of damage that was not able to be detected prior to staining.

Validation by basic fuchsin staining

For validation by conventional histology, specimens were stained *en bloc* under vacuum ($15\text{--}20 \text{ mm Hg}$) by 1% basic fuchsin in a graded series of alcohol solutions (80%, 95%, and 100% ethanol) which were changed after 2 h in each [20]. After staining, specimens were rinsed in 100% ethanol, followed by 100% methyl methacrylate, for 4 h each under vacuum and embedded in poly(methyl methacrylate) with 3% dibutyl phthalate. Longitudinal serial sections, $80 \mu\text{m}$ in thickness, were prepared using a diamond wire saw (Delaware Diamond Knives, Wilmington, DE) and 5–7 sections within the gauge section of each specimen were assessed histologically for microdamage. Note that this technique is able to discriminate artifactual damage caused by histological preparation processes from prior fatigue microdamage [19].

Histomorphometry was carried out by a single individual blinded to group affiliation using transmitted light microscopy (Optiphot 2, Nikon) with a semiautomatic digitizing system (OSTEO 7.20.10, Bioquant Image Analysis Corp., Nashville, TN). Stained microcracks were identified by shape, depth of field, and permeation of the stain into crack surfaces. The crack density was measured as the number of linear microcracks normalized to bone area ($\text{Cr.Dn} = \text{Cr.N/bone area}$, $\#/\text{mm}^2$). Crack lengths (Cr.Le , μm) were measured and the mean Cr.Le was used to calculate the crack surface density (Cr.S.Dn , $\mu\text{m}/\text{mm}^2$) as the product of Cr.Dn and mean Cr.Le .

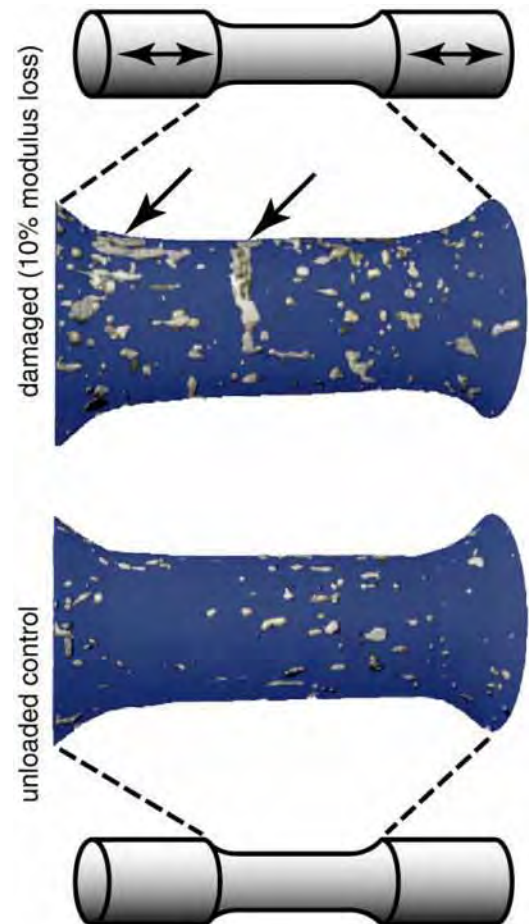


Fig. 2. Segmented, 3-D micro-CT reconstructions of the entire gauge section (2.5 mm in diameter by 5 mm in length) for an unloaded control specimen compared to a specimen loaded in cyclic uniaxial tension to a 10% reduction in secant modulus, showing the ability of micro-CT to detect spatial variation in damage accumulation. Arrows highlight regions of concentrated BaSO_4 staining characteristic of fatigue damage and/or propagating microcracks.

Statistical methods

Micro-CT (SV/BV) and histological (Cr.N, Cr.Le, Cr.Dn, and Cr.S.Dn) measurements of microdamage exhibited non-homogeneous variances. Therefore, experimental groups were compared using Kruskal–Wallis non-parametric analysis of variance (ANOVA) and post-hoc comparisons were performed using Mann–Whitney *U*-tests with a Bonferroni correction for multiple comparisons (JMP 8, SAS Institute Inc., Cary, NC). Linear least squares regression was used to correlate SV/BV, Cr.N, Cr.Dn, Cr.S.Dn, the number of loading cycles, and Haversian porosity. Spearman's rho was used to correlate the ranked group means for micro-CT (SV/BV) and histological measurements (Cr.N, Cr.Dn, and Cr.S.Dn) of microdamage accumulation. Eta-squared (η^2) was calculated as a correlation coefficient for the variance of histological measurements (Cr.N, Cr.Dn, and Cr.S.Dn) able to be predicted by SV/BV means. The level of significance for all tests was set at 0.05.

Results

The presence and spatial location of fatigue microdamage was non-destructively detected by micro-CT after staining with BaSO₄. Grayscale and segmented micro-CT images of the same specimen cross-section, after loading to a 10% reduction in secant modulus and after BaSO₄ staining (post-staining), showed enhanced contrast (bright voxels) for microdamage that was not able to be detected by micro-CT prior to staining (post-fatigue) (Fig. 1). Segmented, 3-D reconstructions of the entire gauge section showed the ability of micro-CT to detect spatial variation in damage accumulation (Fig. 2). Unloaded control specimens revealed non-specific BaSO₄ staining on free surfaces and within vasculature. Specimens loaded in cyclic uniaxial tension typically exhibited at least one distinct region of concentrated BaSO₄ stain which appeared characteristic of fatigue

damage and/or propagating microcracks (e.g., see arrows in Fig. 2). See the Appendix for movies showing cross-sectional grayscale image stacks using contrast-enhanced micro-CT for representative specimens from the unloaded control group and groups loaded to a 5% and 10% reduction in secant modulus.

Linear microcracks generated by cyclic uniaxial tension were similarly labeled by BaSO₄ (bright) and basic fuchsin (violet) as shown by backscattered electron microscopy and light microscopy, respectively, on separate specimens from paired experimental groups (Fig. 3). Therefore, bright voxels detected by micro-CT were confirmed by backscattered electron microscopy to be microcracks and/or diffuse damage labeled with BaSO₄ (Figs. 3a and 4a). Moreover, EDS confirmed elevated levels of Ba in stained versus unstained regions of tissue (Fig. 4b).

The amount of microdamage increased from the unloaded control group to groups loaded to a 5% and 10% reduction in secant modulus for both micro-CT (SV/BV) and histological (e.g., Cr.Dn) measurements of microdamage ($p < 0.001$, Kruskal–Wallis) (Fig. 5). All differences between experimental groups were statistically significant ($p < 0.05$, Mann–Whitney *U*-test). For example, SV/BV and Cr.Dn for specimens loaded to a 10% reduction in secant modulus exhibited a four- and ten-fold increase over controls, respectively. Histological measurements for the crack number (Cr.N) and crack surface density (Cr.S.Dn) exhibited similar trends as Cr.Dn (Table 1). However, the mean crack length (Cr.Le) was not statistically different between controls and specimens loaded to a 5% reduction in secant modulus, but was increased for a 10% reduction in secant modulus (Table 1).

The accumulation of microdamage measured by micro-CT (SV/BV) was correlated with Cr.Dn (Fig. 6), Cr.N, and Cr.S.Dn measured by conventional histology ($p < 0.05$, Spearman's rho) allowing prediction of Cr.Dn, Cr.N, and Cr.S.Dn from SV/BV group means ($\eta^2 = 0.78, 0.78$, and 0.65 , respectively). SV/BV was not correlated with the level of Haversian porosity ($p = 0.87$). The overall mean (\pm standard

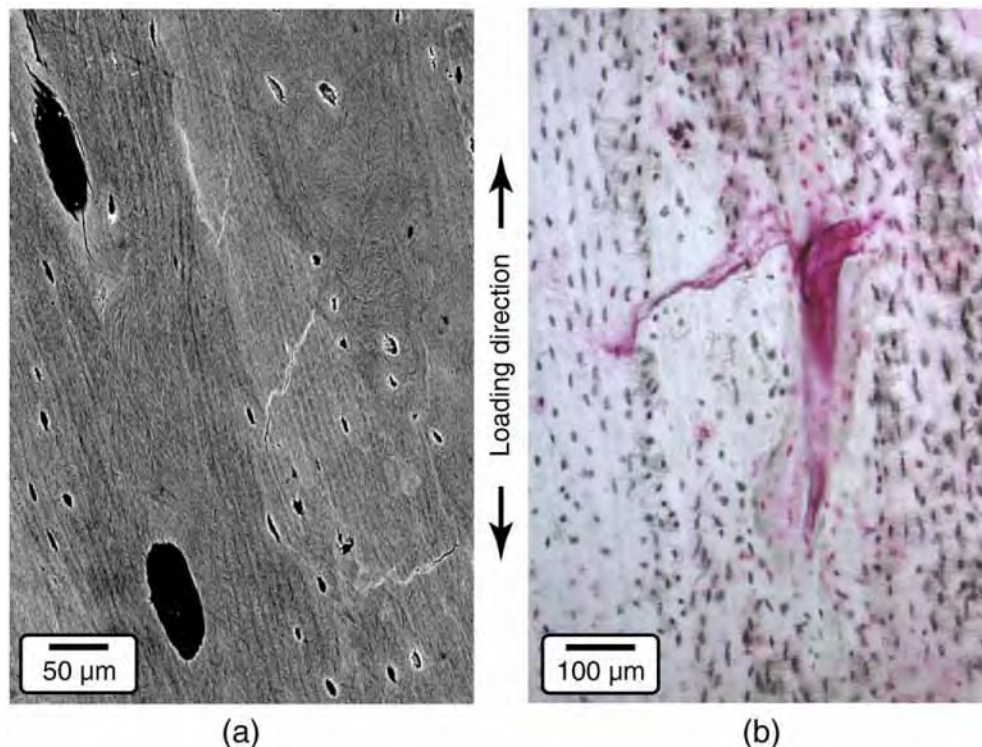


Fig. 3. Representative (a) backscattered SEM and (b) transmitted light micrographs for specimens loaded in cyclic uniaxial tension to a 5% reduction in secant modulus, showing transverse linear microcracks within interstitial tissue similarly labeled by BaSO₄ (bright) and basic fuchsin (violet), respectively.

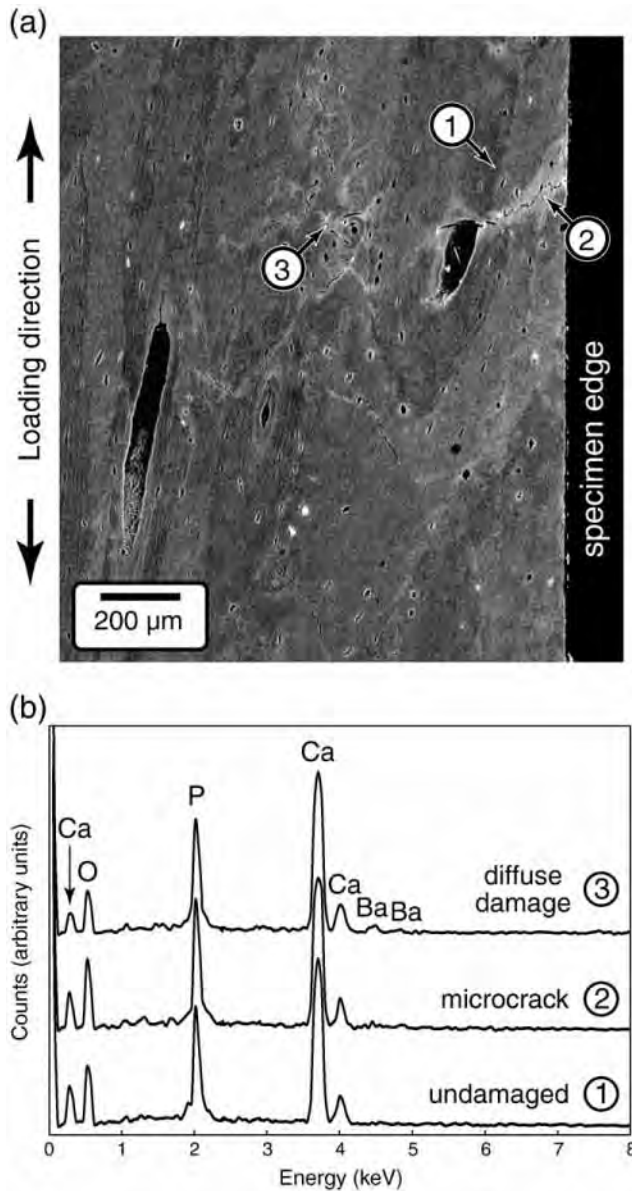


Fig. 4. (a) Backscattered SEM micrograph for a specimen loaded in cyclic uniaxial tension to a 10% reduction in secant modulus, showing (2) a microcrack that propagated between the specimen edge and a Haversian canal and (3) diffuse damage accumulated in interstitial tissue, both labeled by BaSO₄ (bright). (b) The elemental composition measured using EDS showed elevated levels of Ba associated with (2) linear microcracks and (3) diffuse damage compared to (1) undamaged tissue.

deviation) level of Haversian porosity was 2.54 (1.46) %, and differences between experimental groups were not statistically significant ($p=0.70$ Kruskal–Wallis). In mechanically loaded specimens, SV/BV was not correlated with the number of loading cycles ($p=0.16$), but the number of loading cycles exhibited a weak, negative correlation ($p<0.05$, $R^2=0.15$) with the level of Haversian porosity.

Discussion

The 3-D spatial location of microdamage within a uniformly stressed volume of human cortical bone was non-destructively detected and quantified *in vitro* using contrast-enhanced micro-CT with a precipitated BaSO₄ stain. A previous study, using similar staining and imaging methods, demonstrated the detection of microdamage that was localized ahead of a notch in bovine cortical bone

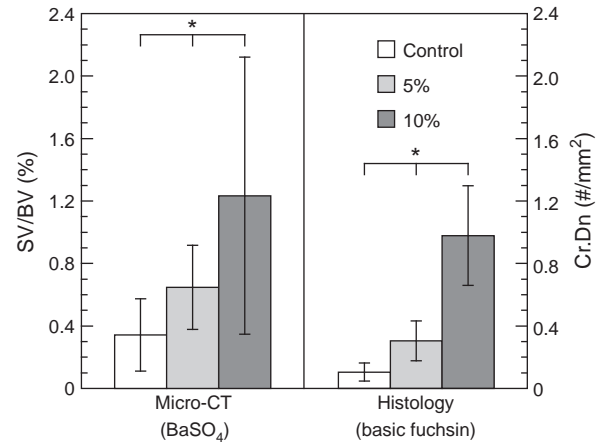


Fig. 5. The amount of microdamage increased from the unloaded control group to groups loaded to a 5% and 10% reduction in secant modulus for both micro-CT (SV/BV) and histological (Cr.Dn) measurements of microdamage ($p<0.001$, Kruskal–Wallis). Error bars span one standard deviation. Asterisks denote statistically significant differences between groups ($p<0.05$, Mann–Whitney *U*-test).

beams loaded in cyclic four-point bending [40]. However, the spatial location of microdamage accumulation was known *a priori* due to the use of notched beams, and the quantification of microdamage accumulation rapidly saturated due to crack initiation from the notch and the use of displacement-controlled fatigue. In the present study, the use of load-controlled fatigue on a uniformly stressed volume demonstrated the feasibility of detecting of the 3-D spatial location (Figs. 1–2) and progressive accumulation (Fig. 5) of microdamage in human cortical bone. Of the 15 specimens per experimental group, 12 and 14 specimens loaded in cyclic uniaxial tension to a 5% and 10% reduction in secant modulus, respectively, exhibited at least one distinct region of concentrated BaSO₄ stain which appeared indicative of fatigue damage and/or propagating microcracks (e.g., see arrows in Fig. 2). Regions of concentrated BaSO₄ stain were located near the center or ends of the gauge length in 13 specimens each, and the mean SV/BV was not statistically different between each location for specimens loaded to either a 5% and 10% reduction in secant modulus ($p=0.4$ and 0.9 , respectively, *t*-test). Thus, tissue in the specimen gauge section was confirmed to be uniformly stressed and damage accumulated with equal probability at any location within the tissue volume.

BaSO₄ staining provided enhanced contrast for the detection of damage that was otherwise not able to be detected using a polychromatic, cone-beam micro-CT scanner at 10 μm resolution (Fig. 1). Typical microcracks in cortical bone tissue are elliptical, with a width and length on the order of 100–500 μm [28,30], and a thickness on the order of 1 μm [18,26,35]. The thickness of microcracks in this study was also observed by electron and optical microscopy to be on the order of 1 μm (Figs. 3 and 4a), which was well below the 10 μm voxel size of the micro-CT scanner. BaSO₄ precipitation within microcracks, and penetration into adjacent tissue, enhanced the intensity of voxels in micro-CT due to the higher X-ray attenuation of BaSO₄ relative to the extracellular matrix (Fig. 4) [40–42]. Moreover,

Table 1

The mean (\pm standard deviation) crack number (Cr.N), crack length (Cr.Le), crack density (Cr.Dn), and crack surface density (Cr.S.Dn) for the unloaded control group and groups loaded to a 5% and 10% reduction in secant modulus using conventional histology after staining by basic fuchsin. Groups not connected by the same superscript letter exhibited statistically significant differences ($p<0.05$, Mann–Whitney *U*-test).

Group	Cr.N (#)	Cr.Le (μm)	Cr.Dn (#/mm ²)	Cr.S.Dn (μm/mm ²)
Control	5 (3) ^a	84 (10) ^a	0.10 (0.06) ^a	9 (5) ^a
5%	14 (6) ^b	85 (21) ^a	0.30 (0.13) ^b	26 (11) ^b
10%	44 (13) ^c	100 (19) ^b	0.98 (0.32) ^c	101 (48) ^c

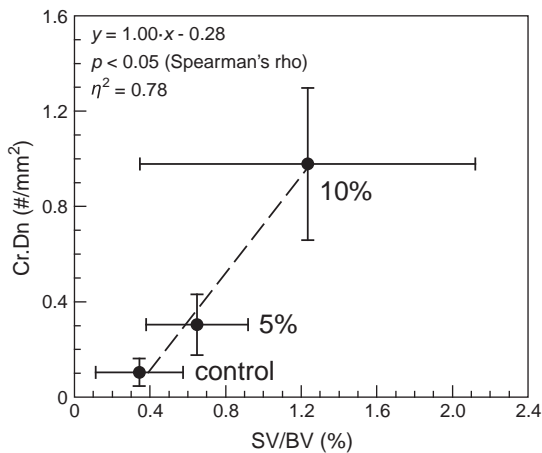


Fig. 6. The accumulation of microdamage measured by micro-CT (SV/BV) was correlated with the microcrack density (Cr.Dn) measured by conventional histology ($p < 0.05$, Spearman's rho) allowing prediction of Cr.Dn from SV/BV group means ($\eta^2 = 0.78$). Data points show the mean and one standard deviation ($n = 15/\text{group}$) for the unloaded control group and groups loaded to a 5% and 10% reduction in secant modulus.

artifactual microcracks resulting from subsequent histological specimen preparation were not labeled by BaSO₄ and were therefore able to be distinguished from pre-existing microcracks, since BaSO₄ staining was conducted on tissue specimens *en bloc* immediately after mechanical loading.

Contrast-enhanced micro-CT was able to detect and quantify the progressive accumulation of fatigue microdamage from unloaded control specimens to those loaded to a 5% and 10% reduction in secant modulus (Fig. 5). Group means for micro-CT measurements of damage accumulation (SV/BV) exhibited a strong correlation with those using histomorphometry (e.g., Cr.Dn), validating the new methods (Fig. 6). However, note that this correlation may not be generally applicable for prediction of Cr.Dn from SV/BV since measurements of the SV are dependent on the staining and imaging methods, as described in further detail below.

Post hoc power analysis using the root mean square error, total number of specimens, and $\alpha = 0.05$ for the unloaded control specimens and those loaded to a 5% reduction in secant modulus resulted in a power of 0.89 for a difference of 0.302 between the group means for SV/BV, which corresponded to an 87% (1.9-fold) increase in SV/BV over the unloaded control group. For the same level of power, *post hoc* power analysis suggested that histology (Cr.Dn) was able to detect a 115% increase (2.2-fold) in Cr.Dn over the unloaded control group. Therefore, the level of damage incurred by a 5% reduction in secant modulus was just above the minimum level that could be expected to be detected by contrast-enhanced micro-CT for the sample size and methods used in this study, and the sensitivity of contrast enhanced micro-CT was not unlike that that exhibited by conventional histological measurements.

Histological measurements of microdamage have been correlated to a reduction in modulus (or stiffness) in surprisingly few studies and with varied results. In whole canine femora loaded in cyclic four-point bending to a 5–45% reduction in stiffness, microdamage was not observed histologically until a 15% reduction in stiffness [9]. The crack area (Cr.Ar) was positively and significantly correlated with the stiffness degradation, but other histological measures (Cr.Dn, Cr.Le, etc.) did not exhibit a statistically significant difference from unloaded control specimens nor a correlation with the stiffness degradation [9]. In human femoral cortical bone specimens subjected to tensile overloading to a 0–10% reduction in elastic modulus, Cr.N and Cr.Le exhibited a positive but weak ($R^2 = 0.15$ – 0.24) correlation with the modulus degradation [8]. Whole rat ulnae loaded in cyclic bending exhibited a statistically significant increase in Cr.Dn, Cr.Le, and Cr.S.Dn

in loaded groups compared to unloaded controls, but differences between groups loaded to a 20% and 40% reduction in stiffness were not statistically significant [10]. Bovine tibial cortical bone specimens loaded in cyclic uniaxial compression exhibited a statistically significant increase in Cr.Dn, Cr.Le, and Cr.S.Dn for specimens loaded to a 10% reduction in elastic modulus compared to unloaded controls, as well as interesting trends with the number of loading cycles [7]. Finally, bovine tibial cortical bone specimens loaded in cyclic four-point bending exhibited a statistically significant increase in Cr.Dn for compressive loading, but no difference for tensile loading, between a 20% and 50% degradation in the elastic modulus determined using linear elastic beam theory [12]. In light of these prior studies, the strong correlation of both micro-CT (SV/BV) and histological (Cr.N, Cr.Dn, Cr.S.Dn) measurements of microdamage with the modulus degradation (Fig. 5) in the present study was itself a significant result. A reduction in secant modulus greater than 10% could not be reliably achieved prior to fracture of the specimens in the present study, which was similar to the most closely related prior study [7]. The wide variation in mechanical degradation observed amongst the other studies is most likely due to differences in loading mode [12] and tissue source, as well as systematic experimental errors [15].

Unloaded control specimens exhibited a mean microcrack length and density (Table 1) that was comparable to prior measurements for microdamage in human femoral cortical bone tissue from donors of similar age [3,5,8]. Specimens loaded to a 5% reduction in secant modulus primarily exhibited transverse microcracks in interstitial tissue, which terminated at cement lines, and longitudinal microcracks along cement lines (Fig. 4). Specimens loaded to a 10% reduction in secant modulus exhibited transverse propagating microcracks or fatigue cracks (e.g., Fig. 4a). These cracks appeared to originate at the specimen surface and propagate inward, normal to the direction of loading, as expected for fatigue failure in cyclic uniaxial tension. The number of loading cycles required to reach the designated reduction in secant modulus for loaded specimens exhibited a negative correlation with the level of Haversian porosity, suggesting that Haversian porosity may have provided stress concentrations for primary crack initiation and/or secondary crack initiation ahead of a propagating microcrack (Fig. 3b) [49] especially when located near the specimen surface (Fig. 4a).

This study was not without several limitations. Staining by BaSO₄ precipitation was non-specific for microdamage, including all void spaces, such as vasculature and free surfaces, and the staining solutions were not biocompatible. Therefore, the new methods demonstrated in this study are limited to use *in vitro*. However, functionalized gold [43–45] and BaSO₄ nanoparticles are being investigated for a deliverable, targeted X-ray contrast agent for damaged bone tissue.

The amount of damage measured by micro-CT (SV/BV) exhibited greater variability, and decreased relative differences between experimental groups, compared to conventional histology (Cr.Dn) (Fig. 5). The most likely contributing factors were the relatively lower resolution of micro-CT and non-specific BaSO₄ staining. Unloaded control specimens exhibited scattered, small volumes of BaSO₄ staining on free surfaces and within vasculature (Fig. 2). However, SV/BV was not correlated with the amount of Haversian porosity in individual specimens. Further work is required to determine whether SV/BV would be influenced by higher levels of Haversian porosity than that exhibited by the tissue specimens in this study. Alternatively, a segmented reconstruction of Haversian porosity imaged prior to staining could be overlaid or subtracted from segmented reconstructions imaged after staining.

The subregion and threshold for analysis and segmentation, respectively, required careful selection. A parametric study was used to determine the effects of the image subregion size and threshold value on the magnitude and variability of SV/BV [48]. The effects of non-specific staining on the specimen free surfaces were minimized

by analyzing a subregion with a radius reduced by 100 μm (10 voxels) from the specimen perimeter. However, the removal of this tissue from analysis also excluded SV that was due to microdamage and may have contributed to the increased variability in SV/BV with an increased reduction in secant modulus, since propagating microcracks were typically observed at or near the specimen surface. The optimal threshold (3.92 cm^{-1}) for segmenting the SV corresponded to an equivalent density of $\sim 1890\text{ mg}$ hydroxyapatite per cubic centimeter, which was well above the tissue mineral density of human cortical bone [47].

Finally, microdamage accumulation was quantified by micro-CT as SV/BV, but a true crack density and crack dimensions could not be measured. The resolution and absorption contrast limits of a polychromatic, cone-beam micro-CT with $10\text{ }\mu\text{m}$ resolution did not allow imaging of individual microcracks or discrimination between microdamage and non-specific staining, though the latter may be feasible using morphological criteria. The use of higher resolution and/or monochromatic radiation could enable dimensional measurements of microcracks, but only at the cost of sample volume and radiation dose. However, SV/BV was shown to be strongly correlated with the crack density measured histologically (Fig. 6). Therefore, a greater impact for contrast-enhanced micro-CT could be realized by extension to instruments with lower resolution and lower radiation doses in order to enable non-invasive, 3-D detection of microdamage in whole bones using preclinical instruments for small animals, or even clinical instruments.

In conclusion, contrast-enhanced micro-CT was able to detect the presence, spatial location, and progressive accumulation of fatigue microdamage in human cortical bone specimens *in vitro* using a precipitated BaSO_4 stain, and was validated against conventional histological methods using basic fuchsin. Limitations of the new methods in the present study included that the precipitated BaSO_4 stain was non-specific and non-biocompatible, and that micro-CT measurements exhibited greater variability compared to conventional histology. Nonetheless, contrast-enhanced micro-CT enabled non-destructive imaging and 3-D spatial information, which are not possible using conventional histological methods. Therefore, contrast-enhanced micro-CT is immediately useful in the study of bone tissue mechanics, including the etiology of fatigue and fragility fractures.

Supplementary materials related to this article can be found online at doi:10.1016/j.bone.2010.10.160.

Acknowledgments

This research was supported by the U.S. Army Medical Research and Materiel Command (W81XWH-06-1-0196) through the Peer Reviewed Medical Research Program (PR054672).

References

- [1] Chapurlat BD, Delmas PD. Bone microdamage: a clinical perspective. *Osteoporos Int* 2009;20:1299–308.
- [2] Burr DB, Forwood MR, Fyhrie DP, Martin RB, Schaffler MB, Turner CH. Bone microdamage and skeletal fragility in osteoporotic and stress fractures. *J Bone Miner Res* 1997;12:6–15.
- [3] Norman TL, Wang Z. Microdamage of human cortical bone: incidence and morphology in long bones. *Bone* 1997;20:375–9.
- [4] Schaffler MB, Choi K, Milgrom C. Aging and matrix microdamage accumulation in human compact bone. *Bone* 1995;17:521–5.
- [5] Sobelman OS, Gibeling JC, Stover SM, Hazelwood SJ, Yeh OC, Shelton DR, Martin RB. Do microcracks decrease or increase fatigue resistance in cortical bone? *J Biomech* 2004;37:1295–303.
- [6] Zioupos P. Accumulation of *in-vivo* fatigue microdamage and its relation to biomechanical properties in ageing human cortical bone. *J Microsc* 2001;201(Pt 2):270–8.
- [7] O'Brien FJ, Taylor D, Lee TC. Microcrack accumulation at different intervals during fatigue testing of compact bone. *J Biomech* 2003;36:973–80.
- [8] Akkus O, Knott DF, Jepsen KJ, Davy DT, Rinnac CM. Relationship between damage accumulation and mechanical property degradation in cortical bone: microcrack orientation is important. *J Biomed Mater Res* 2003;65A:482–8.
- [9] Burr DB, Turner CH, Naick P, Forwood MR, Ambrosius W, Hasan MS, Pidaparti R. Does microdamage accumulation affect the mechanical properties of bone? *J Biomech* 1998;31:337–45.
- [10] Danova NA, Colopy SA, Radtke CL, Kalscheur VL, Markel MDR, Vanderby J, McCabe RP, Escarcega AJ, Muir P. Degradation of bone structural properties by accumulation and coalescence of microcracks. *Bone* 2003;33:197–205.
- [11] Forwood MR, Parker AW. Microdamage in response to repetitive torsional loading in the rat tibia. *Calcif Tissue Int* 1989;45:47–53.
- [12] Diab T, Vashishth D. Effects of damage morphology on cortical bone fragility. *Bone* 2005;37:96–102.
- [13] Norman TL, Yeni YN, Brown CU, Wang X. Influence of microdamage on fracture toughness of the human femur and tibia. *Bone* 1998;23:303–6.
- [14] Boyce TM, Fyhrie DF, Glotkowski MC, Radin EL, Schaffler MB. Damage type and strain mode associations in human compact bone bending fatigue. *J Orthop Res* 1998;16:322–9.
- [15] Landrigan MD, Roeder RK. Systematic error in mechanical measures of damage during four-point bending fatigue of cortical bone. *J Biomech* 2009;42:1212–7.
- [16] Diab T, Condon KW, Burr DB, Vashishth D. Age-related change in the damage morphology of human cortical bone and its role in bone fragility. *Bone* 2006;38:427–31.
- [17] Lee TC, Mohsin S, Taylor D, Parkesh R, Gunnlaugsson T, O'Brien FJ, Giehl M, Gowin W. Detecting microdamage in bone. *J Anat* 2003;203:161–72.
- [18] Frost HM. Presence of microscopic cracks *in vivo* in bone. *Henry Ford Hosp Med Bull* 1960;8:25–35.
- [19] Burr DB, Stafford T. Validity of the bulk-staining technique to separate artefactual from *in vivo* bone microdamage. *Clin Orthop Relat Res* 1990;260:305–8.
- [20] Burr DB, Hooser M. Alterations to the en bloc basic fuchsin staining protocol for the demonstration of microdamage produced *in vivo*. *Bone* 1995;17:431–3.
- [21] Lee TC, Myers ER, Hayes WC. Fluorescence-aided detection of microdamage in compact bone. *J Anat* 1998;193:179–84.
- [22] Lee TC, Arthur TL, Gibson LJ, Hayes WC. Sequential labelling of microdamage in bone using chelating agents. *J Orthop Res* 2000;18:22–35.
- [23] O'Brien FJ, Taylor D, Lee TC. An improved labelling technique for monitoring microcrack growth in compact bone. *J Biomech* 2002;35:523–6.
- [24] Parkesh R, Mohsin S, Lee TC, Gunnlaugsson T. Histological, spectroscopic, and surface analysis of microdamage in bone: toward real-time analysis using fluorescent sensors. *Chem Mater* 2007;19:1656–63.
- [25] Parkesh R, Lee TC, Gunnlaugsson T. Fluorescence imaging of bone cracks (microdamage) using visibly emitting 1, 8-naphthalimide-based PET sensors. *Tetrahedron Lett* 2009;50:4114–6.
- [26] Schaffler MB, Pitchford WC, Choi K, Riddle JM. Examination of compact bone microdamage using back-scattered electron microscopy. *Bone* 1994;15:483–8.
- [27] Zioupos P, Currey JD. The extent of microcracking and the morphology of microcracks in damaged bone. *J Mater Sci* 1994;29:978–86.
- [28] O'Brien FJ, Taylor D, Dickson GR, Lee TC. Visualization of three-dimensional microcracks in compact bone. *J Anat* 2000;197:413–20.
- [29] Bigley RF, Singh M, Hernandez CJ, Kazakia GJ, Martin RB, Keaveny TM. Validity of serial milling-based imaging system for microdamage quantification. *Bone* 2008;42:212–6.
- [30] Mohsin S, O'Brien FJ, Lee TC. Microcracks in compact bone: a three-dimensional view. *J Anat* 2006;209:119–24.
- [31] Li J, Miller MA, Hutchins GD, Burr DB. Imaging bone microdamage *in vivo* with positron emission tomography. *Bone* 2005;37:819–24.
- [32] Silva MJ, Uthgenannt BA, Rutlin JR, Wohl GR, Lewis JS, Welch MJ. *In vivo* skeletal imaging of ^{18}F -fluoride with positron emission tomography reveals damage- and time-dependent responses to fatigue loading in the rat ulna. *Bone* 2006;39:229–36.
- [33] Nalla RK, Kruzic JJ, Kinney JH, Ritchie RO. Mechanistic aspects of fracture and R-curve behavior in human cortical bone. *Biomaterials* 2005;26:217–31.
- [34] Thurner PJ, Wyss P, Voide R, Stauber M, Stamparoni M, Sennhauser U, Müller R. Time-lapsed investigation of three-dimensional failure and damage accumulation in trabecular bone using synchrotron light. *Bone* 2006;39:289–99.
- [35] Voide R, Schneider P, Stauber M, Wyss P, Stamparoni M, Sennhauser U, van Lenthe GH, Müller R. Time-lapsed assessment of microcrack initiation and propagation in murine cortical bone at submicrometer resolution. *Bone* 2009;45:164–73.
- [36] Barth HD, Launey ME, MacDowell AA, Ager JW, Ritchie RO. On the effect of X-ray irradiation on the deformation and fracture behavior of human cortical bone. *Bone* 2010;46:1475–85.
- [37] Parkesh R, Lee TC, Gunnlaugsson T, Gowin W. Microdamage in bone: surface analysis and radiological detection. *J Biomech* 2006;39:1552–6.
- [38] Leng H. Micro-computed tomography of microdamage in cortical bone. University of Notre Dame, Notre Dame, IN: Ph.D. Dissertation; 2006.
- [39] Tang SY, Vashishth D. A non-invasive *in vitro* technique for the three-dimensional quantification of microdamage in trabecular bone. *Bone* 2007;40:1259–64.
- [40] Leng H, Wang X, Ross RD, Niebur GL, Roeder RK. Micro-computed tomography of fatigue microdamage in cortical bone using a barium sulfate contrast agent. *J Mech Behav Biomed Mater* 2008;1:68–75.
- [41] Wang X, Masse DB, Leng H, Hess KP, Ross RD, Roeder RK, Niebur GL. Detection of trabecular bone microdamage by micro-computed tomography. *J Biomech* 2007;40:3397–403.
- [42] Landrigan MD, Flatley JC, Turnbull TL, Kruzic JJ, Ferracane JL, Hilton TJ, Roeder RK. Detection of dental cracks using contrast-enhanced micro-computed tomography. *J Mech Behav Biomed Mater* 2010;3:223–7.
- [43] Zhang X, Ross RD, Roeder RK. Preparation of functionalized gold nanoparticles as a targeted X-ray contrast agent for damaged bone tissue. *Nanoscale* 2010;2:582–6.
- [44] Ross RD, Roeder RK. Binding affinity of surface functionalized gold nanoparticles for hydroxyapatite. *J Biomed Mater Res*, submitted.

- [45] Ross RD, Roeder RK. Functionalized gold nanoparticles for targeted labeling of damaged bone tissue in X-ray tomography. *Trans Orthop Res Soc* 2010;35: 1368.
- [46] Swanson MB, Davis GA, Kincaid LE, Schultz TW, Bartness JE, Jones SL, George EL. A screening method for ranking and scoring chemical by potential human health and environmental impacts. *Environ Toxicol Chem* 1997;16:372–83.
- [47] Deuerling JM, Rudy DJ, Niebur GL, Roeder RK. Improved accuracy of cortical bone mineralization measured by polychromatic micro-computed tomography using a novel high mineral density composite calibration phantom. *Med Phys* 2010;37: 5138–45.
- [48] Landrigan MD. Evaluation of methods for measuring microdamage accumulation in cortical bone. University of Notre Dame, Notre Dame, IN: Ph.D. Dissertation; 2009.
- [49] Fleck C, Eifler D. Deformation behaviour and damage accumulation of cortical bone specimens from the equine tibia under cyclic loading. *J Biomech* 2003;36: 179–89.



Systematic error in mechanical measures of damage during four-point bending fatigue of cortical bone[☆]

Matthew D. Landrigan, Ryan K. Roeder^{*}

Department of Aerospace and Mechanical Engineering, The University of Notre Dame, Notre Dame, IN 46556, USA

ARTICLE INFO

Article history:

Accepted 12 March 2009

Keywords:

Fatigue microdamage

Compact bone

Cortical bone

Elastic modulus

Creep

Four-point bending

ABSTRACT

Accumulation of fatigue microdamage in cortical bone specimens is commonly measured by a modulus or stiffness degradation after normalizing tissue heterogeneity by the initial modulus or stiffness of each specimen measured during a preloading step. In the first experiment, the initial specimen modulus defined using linear elastic beam theory (LEBT) was shown to be nonlinearly dependent on the preload level, which subsequently caused systematic error in the amount and rate of damage accumulation measured by the LEBT modulus degradation. Therefore, the secant modulus is recommended for measurements of the initial specimen modulus during preloading. In the second experiment, different measures of mechanical degradation were directly compared and shown to result in widely varying estimates of damage accumulation during fatigue. After loading to 400,000 cycles, the normalized LEBT modulus decreased by 26% and the creep strain ratio decreased by 58%, but the normalized secant modulus experienced no degradation and histology revealed no significant differences in microcrack density. The LEBT modulus was shown to include the combined effect of both elastic (recovered) and creep (accumulated) strain. Therefore, at minimum, both the secant modulus and creep should be measured throughout a test to most accurately indicate damage accumulation and account for different damage mechanisms. Histology revealed indentation of tissue adjacent to roller supports, with significant sub-surface damage beneath large indentations, accounting for 22% of the creep strain on average. The indentation of roller supports resulted in inflated measures of the LEBT modulus degradation and creep. The results of this study suggest that investigations of fatigue microdamage in cortical bone should avoid the use of four-point bending unless no other option is possible.

© 2009 Elsevier Ltd. All rights reserved.

1. Introduction

Various methods have been used to measure the accumulation of fatigue microdamage via changes in mechanical properties. The elastic modulus or stiffness degradation is most commonly reported as a ratio or percent loss measured by (1) the maximum beam deflection using linear elastic beam theory (LEBT) (Boyce et al., 1998; Danova et al., 2003; Diab et al., 2006; Diab and Vashishth, 2005), (2) the secant modulus or stiffness (Cotton et al., 2005; Fleck and Eifler, 2003; Gibson et al., 1995; Moreno et al., 2006; Pattin et al., 1996; Schaffler et al., 1989; Schaffler et al., 1990; Winwood et al., 2006a,b; Zioupos et al., 1996), (3) the tangent modulus or stiffness (Akkus et al., 2003; Burr et al., 1998; Gibson et al., 1995; Jepsen and Davy, 1997; Pidaparti et al., 2000), and (4) the unloading modulus or stiffness (Fleck and Eifler, 2003).

[☆] Funding Sources: US Army Medical Research and Materiel Command (W81XWH-06-1-0196) through the Peer Reviewed Medical Research Program (PR054672), National Institutes of Health (AR049598).

^{*} Corresponding author. Tel.: +1 574 631 7003; fax: +1 574 631 2144.

E-mail address: roeder@nd.edu (R.K. Roeder).

Other mechanical measures of fatigue damage have included creep or “plastic” strain (Cotton et al., 2003, 2005; Fleck and Eifler, 2003; Moreno et al., 2006; Winwood et al., 2006a,b), cyclic energy dissipation (Pattin et al., 1996) or elastic strain amplitude (Fleck and Eifler, 2003; Winwood et al., 2006a,b), and viscoelastic relaxation or recovery (Jepsen and Davy, 1997; Joo et al., 2007).

The initial modulus or stiffness of a specimen is often measured prior to fatigue testing in order to normalize tissue heterogeneity to a prescribed maximum strain (Boyce et al., 1998; Caler and Carter, 1989; Cotton et al., 2005; Diab et al., 2006; Diab and Vashishth, 2005; Gibson et al., 1995; Pattin et al., 1996; Pidaparti et al., 2000; Sobelman et al., 2004). Cyclic preloading at 100 N for 20 cycles has been commonly adopted for this purpose whether utilizing uniaxial loading with a cross-sectional area of 7–8 mm² (Caler and Carter, 1989; Cotton et al., 2005; Pattin et al., 1996) or four-point bending with a 4 × 4 mm beam cross section (Boyce et al., 1998; Diab et al., 2006; Diab and Vashishth, 2005). Under these conditions the maximum stress of the non-uniform stress distribution in four-point bending is approximately four times greater than the uniform stress of 12–14 MPa produced by uniaxial loading. In four-point bending of machined beams, the

specimen modulus during preloading and fatigue is often calculated using LEBT as

$$E = \frac{3PL}{4bh^2\varepsilon} \quad (1)$$

where P is the applied load, L is the outer support span, $L/4$ is the distance between the inner and outer supports, b is the specimen width, h is the specimen height, and ε is the maximum strain based on the beam deflection (Boyce et al., 1998; Diab et al., 2006; Diab and Vashishth, 2005; Gibson et al., 1995; Griffin et al., 1999; Sobelman et al., 2004). The measured initial modulus and a prescribed maximum initial strain are then used to determine a normalized applied load for fatigue testing using Eq. (1).

In an increasing number of studies, specimens are loaded to a specified modulus or stiffness degradation to generate controlled levels of damage (Boyce et al., 1998; Danova et al., 2003; Diab and Vashishth, 2005). However, this practice assumes that measures of modulus or stiffness degradation are free of systematic error. Therefore, the objective of this study was to examine sources of systematic error in mechanical measures of microdamage during cyclic four-point bending fatigue via two experiments. The aim of the first experiment was to establish the effect of the preload level on the initial specimen modulus defined using LEBT and the subsequent modulus degradation during fatigue. The aim of the second experiment was to directly compare different mechanical measures of damage accumulation. The results of these experiments suggested several recommendations for standardization of fatigue testing methods.

2. Methods

2.1. Experiment 1: effects of the preload level

Ten parallelepiped beams, nominally $4 \times 4 \times 50$ mm, were prepared from the mid-diaphysis of bovine tibiae on a computer numerical controlled mini-mill and randomly assigned to two groups. All specimens were wrapped in gauze, hydrated, and stored at -20°C in airtight containers during interim periods.

The effect of the preload level on the initial specimen modulus defined using LEBT was determined by loading two groups of five specimens in four-point bending fatigue with a minimum load of 4 N and a maximum load that either increased from 40 to 300 N by 20 N every 30 cycles, or decreased from 300 to 40 N by 20 N every 30 cycles. All specimens were preloaded with the periosteal surface in tension under cyclic four-point bending at 2 Hz in de-ionized water at ambient temperature using an electromagnetic test instrument (ELF 3300, Bose Corporation, Eden Prairie, MN). The loading fixture comprised 6.35 mm diameter roller supports with a 40 mm outer span and a pivoting 20 mm inner span. All preloading tests were concluded within a 4 min. total duration, eliminating concerns due to testing in de-ionized water (Gustafson et al., 1996). The initial LEBT modulus was calculated from the maximum load and deflection using Eq. (1) and reported as the mean (\pm standard deviation) for each preload level. Beam deflections were measured via a linear variable displacement transducer (± 0.025 mm sensitivity) at the inner supports and converted to strain using LEBT as

$$\varepsilon = \frac{6h\delta}{L^2} \quad (2)$$

where h is the specimen height, δ is the maximum deflection at the inner supports, and L is the outer support span.

Specimens in both preloading groups were randomly reassigned to two groups of five specimens that were tested in four-point bending fatigue under load control with a minimum load of 4 N and the maximum load normalized to 6000 μstrain using Eq. (1) and the initial LEBT modulus (E_0) determined from a preload of either 100 or 200 N (Fig. 1). All tests were conducted at 2 Hz in phosphate buffered saline at 37°C and were concluded at 400,000 cycles without failure. The level of strain for normalization was chosen to not exceed the monotonic yield point of the specimens, which was determined to range between 8000 and 11,000 μstrain on specimens originating from the same tissue source.

2.2. Experiment 2: mechanical measures of damage accumulation

Ten additional specimens were prepared from bovine tibiae as described above. All specimens were loaded with the periosteal surface in tension under cyclic four-point bending at 2 Hz in phosphate buffered saline at 37°C for 400,000

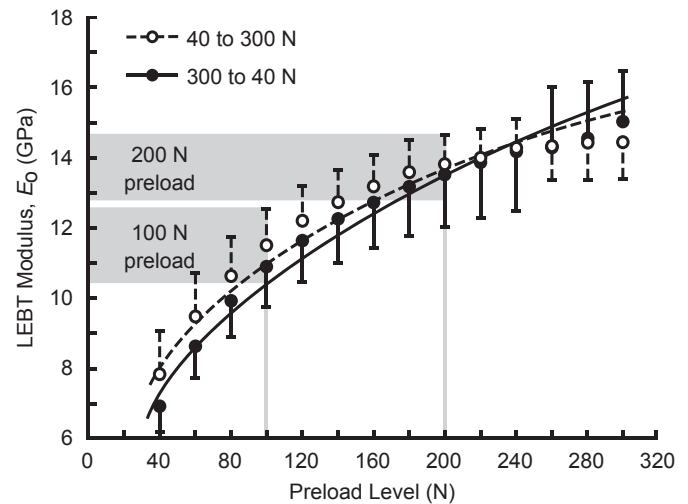


Fig. 1. The dependence of the initial specimen modulus measured using linear elastic beam theory (LEBT) on the magnitude of the applied preload for specimens loaded from 40 to 300 N and 300 to 40 N, increasing or decreasing, respectively, the load by 20 N every 30 cycles. Error bars show one standard deviation. Data was fit by nonlinear least squares regression using a power law ($R^2 = 0.78$ and 0.80 , respectively). Shaded regions show the range of initial specimen moduli, E_0 , for preload levels of 100 and 200 N employed for the measurements in Fig. 3.

cycles without failure. Specimens were preloaded at 175 N for 20 cycles to measure the initial LEBT modulus, followed by load-controlled fatigue with a minimum load of 4 N and the maximum load normalized to 6000 μstrain . Note that the maximum load ranged 171–208 N (81–100 MPa) for various specimens.

The LEBT modulus, secant stiffness, loading stiffness, unloading stiffness, and creep strain were determined from data collected at 250 points per loading cycle (Fig. 2). The LEBT modulus was calculated from the maximum load and deflection (Fig. 2a) using Eqs. (1) and (2). The secant stiffness was measured as the slope of the line connecting the minimum and maximum load and deflection for a given loading cycle. The loading and unloading stiffness was determined by a linear least squares fit to the initial loading and unloading portion of each hysteresis loop from 6 to 25 N (~ 3 –14%) and 140 to 170 N (~ 82 –95%), respectively. Creep strain was defined as the accumulated strain during fatigue and determined from the minimum deflection for a given loading cycle (Fig. 2b).

The modulus or stiffness degradation at a given number of loading cycles was normalized by the initial value measured for the first loading cycle, making a given measure of stiffness degradation equivalent to modulus degradation. Moreover, note that for load control and normalization, the measured LEBT modulus degradation, secant modulus degradation, and creep were equivalent to the strain ratios

$$\text{LEBT: } \frac{E}{E_0} = \frac{\varepsilon_{e,o} + \varepsilon_{p,o}}{\varepsilon_{e,n} + \varepsilon_{p,n}} \quad (3)$$

$$\text{Secant: } \frac{E}{E_0} = \frac{\varepsilon_{e,o}}{\varepsilon_{e,n}} \quad (4)$$

$$\text{Creep: } \frac{\varepsilon_{p,o}}{\varepsilon_{p,n}} \quad (5)$$

where e and p are used by common convention to denote the elastic (recovered) and “plastic” (accumulated) strains, and o and n denote the initial and n th loading cycle, respectively. Note that the accumulated deformation during fatigue is hereafter, and more accurately, termed creep. Eqs. (3)–(5) enabled direct comparison of the measured modulus degradation to the creep strain ratio. Finally, note that each reported strain ratio was equivalent to the corresponding deflection ratio (Fig. 2b), since the dimensions of all specimens were identical.

The total number of linear microcracks, microcrack density (Cr.Dn), and microcrack length (Cr.Ln) were measured for all fatigue specimens and an additional ten unloaded control specimens. Specimens were stained for 16 h in a 0.5 mM calcein (ICN Biomedicals Inc., Aurora, OH) solution under vacuum (~ 50 mm Hg) (O’Brien et al., 2003). Each specimen was subsequently dried by serial alcohol dehydration, followed by 90°C in a vacuum oven overnight, and embedded in poly(methylmethacrylate) (Sample-kwick[®], Buehler Ltd., Lake Bluff, IL). Embedded specimens were sectioned longitudinally into 250- μm -thick sections using a low-speed diamond wafer saw, ground to 150 μm and polished to 1 μm final finish. Each section was mounted on a slide and imaged at 100X magnification using an optical microscope (Eclipse ME600L, Nikon Instruments

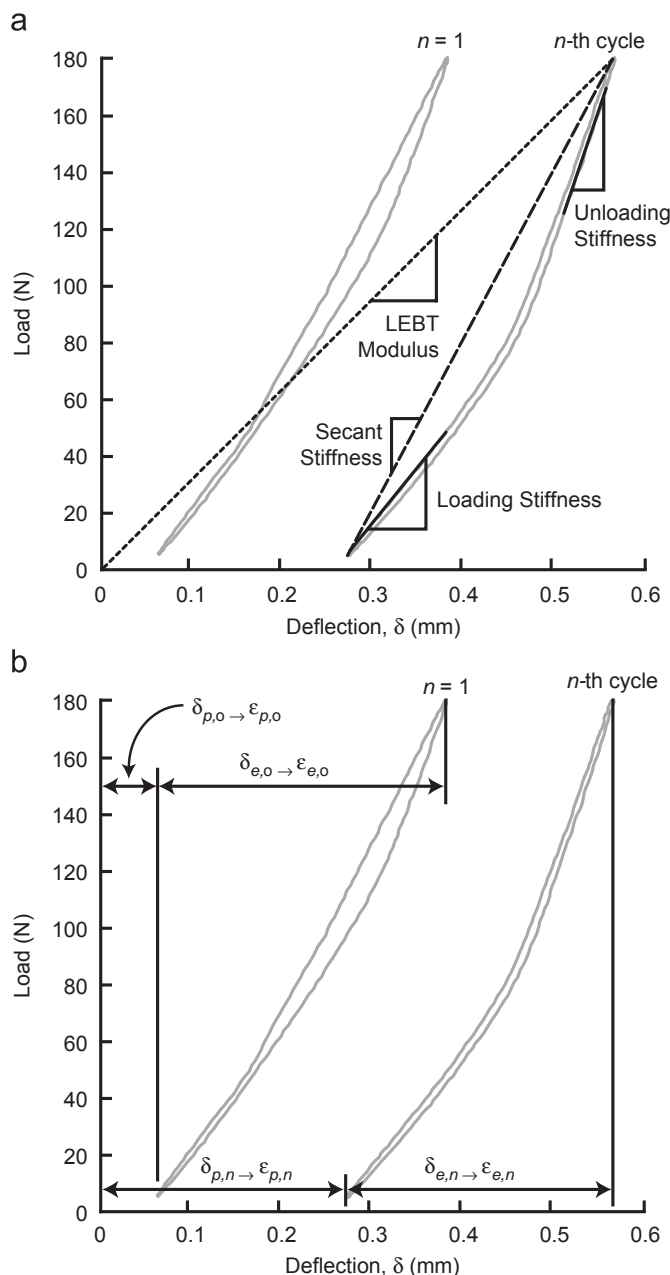


Fig. 2. Hysteresis loops for cyclic four-point bending fatigue of a representative specimen at the initial and final loading cycle showing various mechanical measures of damage in terms of (a) stiffness or modulus, and (b) deflection or strain for elastic, e , (recovered) and “plastic”, p , (accumulated) deformation at the initial, o , and n th loading cycle. Note that the accumulated deformation during fatigue is hereafter, and more accurately, termed creep. Also, note that in the second experiment conversion of a beam deflection into strain was not necessary since all measures of mechanical degradation were reported by a normalized stiffness or strain ratio (Eqs. (3)–(5)), which was equivalent to the corresponding deflection ratio since the dimensions of all specimens were identical.

Inc., Melville, NY) under green epifluorescence with a fluorescein isothiocyanate (FITC) filter with 460–500 nm excitation and 510–560 nm emission. The number and length of microcracks stained by calcein were measured (O’Brien et al., 2003; Lee et al., 1998), not including microcracks within tissue immediately adjacent to roller supports.

2.3. Statistical methods

Experimental groups were compared using one and two-way analysis of variance (ANOVA) (JMP 5.1, SAS Institute Inc., Cary, NC). Post-hoc comparisons were performed using an unpaired Student’s t -test or, in the case of microcrack

density, a Wilcoxon rank-sum test. The level of significance for all tests was set at 0.05. For experiment 1, the initial LEBT modulus was fit to the applied preload by nonlinear least squares regression using a power law.

3. Results

3.1. Experiment 1: effects of the preload level

The initial specimen modulus defined by LEBT increased nonlinearly with an increased preload level ($p < 0.0001$, ANOVA) (Fig. 1). The difference in LEBT modulus between groups with an increasing and decreasing preload level was not statistically significant overall ($p = 0.22$, ANOVA) or at any preload level ($p > 0.23$, t -test), indicating that damage did not accumulate during the course of preloading. Thus, variability for a given preload level was simply due to tissue heterogeneity and the specimens were randomly reassigned to two new groups for fatigue testing. Specimens normalized to 6000 μ strain by an initial modulus measured at a 200 N preload level exhibited a 24% higher initial LEBT modulus (Fig. 1) and were consequently tested in fatigue at a correspondingly higher load level than those normalized using the conventional 100 N preload level. Therefore, specimens that were normalized by measuring the initial specimen modulus at a 200 N preload level experienced a 39% greater relative modulus degradation, or an 8% absolute difference, after 400,000 cycles compared to specimens preloaded at 100 N ($p < 0.05$, t -test) (Fig. 3). Overall, the modulus degradation of specimens normalized by the two preload levels exhibited a statistically significant difference by group ($p < 0.0001$, ANOVA) and interaction with the number of cycles ($p < 0.05$, ANOVA).

3.2. Experiment 2: mechanical measures of damage accumulation

Different mechanical measures of damage resulted in widely varying estimates of damage accumulation during fatigue. Changes in each mechanical measure of damage were most apparent in the first 50,000 cycles, continuing less rapidly and nearly linearly thereafter (Figs. 4 and 5). The normalized LEBT modulus decreased by 26% ($p < 0.0001$, t -test), the normalized secant modulus experienced no degradation ($p = 0.51$, t -test), and the creep strain ratio decreased by 58% ($p < 0.0001$, t -test), after

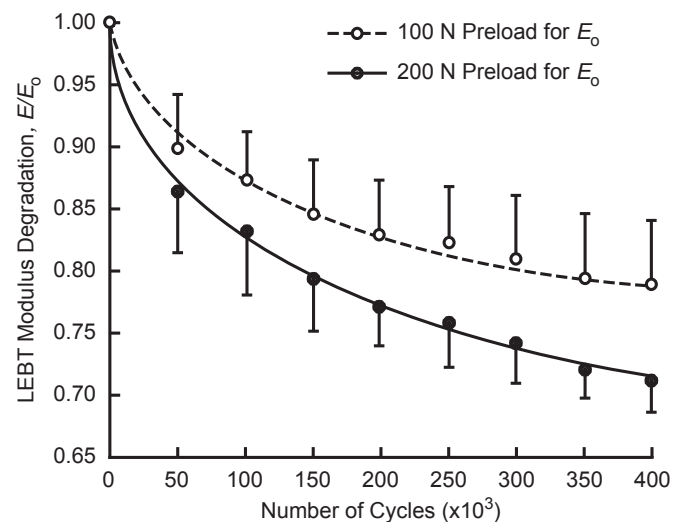


Fig. 3. Modulus degradation, E/E_0 , measured using LEBT during load-controlled four-point bending fatigue of specimens normalized to an initial maximum strain of 6000 μ strain using an initial specimen modulus determined at a preload of either 100 or 200 N (Fig. 1). Error bars show one standard deviation.

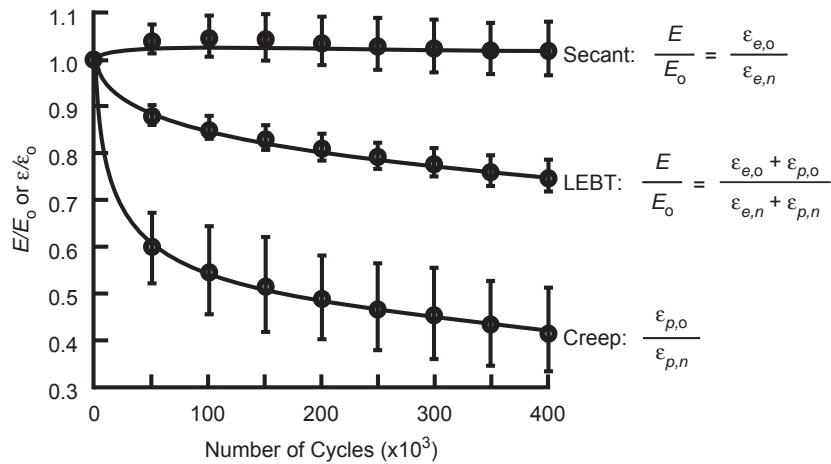


Fig. 4. Mechanical degradation based on measurements of the LEBT modulus (or total strain), secant modulus (or elastic strain), and creep (or accumulated strain) during four-point bending fatigue. Error bars show one standard deviation. Note that the normalized LEBT and secant moduli were equivalent to strain ratios enabling a direct comparison to the creep strain ratio.

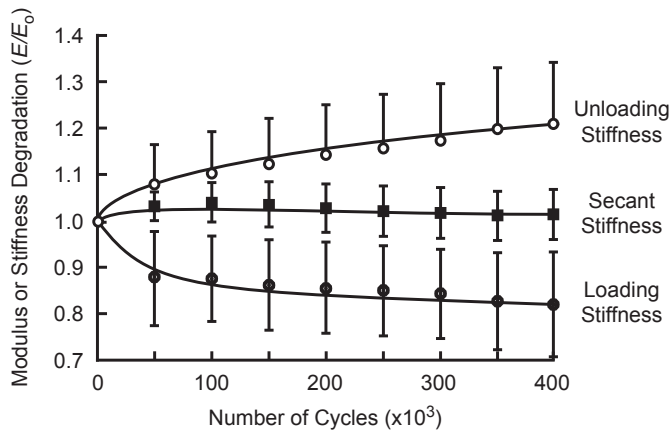


Fig. 5. Mechanical degradation based on measurements of the secant, loading, and unloading stiffness during four-point bending fatigue. Error bars show one standard deviation.

400,000 cycles (Fig. 4). Note that the normalized LEBT and secant moduli were equivalent to strain ratios enabling a direct comparison to the creep strain ratio (Fig. 4). Therefore, the LEBT modulus included effects of both elastic (recovered) and creep (accumulated) strain. The loading and unloading stiffness decreased and increased, respectively, during fatigue ($p < 0.0001$, ANOVA) (Fig. 5).

Histology revealed that the microcrack density (Cr.Dn) of specimens loaded to 400,000 cycles at a load normalized to 6000 μ strain was not significantly different from the unloaded control group ($p = 0.40$, Wilcoxon rank-sum) (Table 1). The mean crack length (Cr.Ln) increased from $41 \pm 22 \mu\text{m}$ for the unloaded control group to $108 \pm 63 \mu\text{m}$ for the loaded group ($p < 0.05$, t -test). Histology further revealed indentation of tissue adjacent to roller supports, with significant sub-surface damage beneath large indentations (Fig. 6). The mean indentation depth per specimen was measured to range between 10 and 63 μm ($27 \pm 19 \mu\text{m}$) and was positively correlated to the creep strain by linear regression ($p = 0.06$, $R^2 = 0.48$).

4. Discussion

Mechanical measures for the accumulation of damage in bovine cortical bone during cyclic four-point bending fatigue

Table 1

The total number of linear microcracks, microcrack density, and microcrack length (mean \pm one standard deviation) measured on longitudinal sections for unloaded control specimens compared to specimens loaded to 400,000 cycles with four-point bending fatigue.

Group	Pre-existing (Control)	Loaded	p-Value
Cr.Dn (#/cm ²)	0.26 ± 0.68	0.26 ± 0.45	$p = 0.40^a$
Cr.Ln (μm)	41 ± 22	108 ± 63	$p < 0.05^b$

^a Wilcoxon rank-sum test.

^b Unpaired t -test.

were shown to be highly dependent on the methods employed. Therefore, the following recommendations should be considered for standardized four-point bending fatigue tests with cortical bone:

4.1. Preloading and normalization

The common protocol using a 100 N preload for 20 cycles significantly underestimated the amount of damage accumulation compared to the use of a higher preload level, which was closer to the level of load employed during the fatigue test after normalizing to the prescribed strain (Fig. 3). Thus, if the LEBT modulus is to be used to normalize tissue heterogeneity, the preload level should be chosen as near as possible to the load level employed during the fatigue test without exceeding the elastic limit for the tissue. The above recommendation minimizes the difference between the level of strain or load employed during preloading and fatigue loading. For example, the 175 N preload level employed in the second experiment corresponded to $5300 \pm 300 \mu\text{strain}$ compared to $5900 \pm 130 \mu\text{strain}$ for the initial loading cycles of the fatigue test after normalization to the LEBT modulus.

Alternatively, the secant modulus should be used to determine the initial specimen modulus during preloading instead of the LEBT modulus. The nonlinear dependence of the initial LEBT modulus on the preload level (Fig. 1) caused systematic error in the amount and rate of damage accumulation measured by the LEBT modulus degradation (Fig. 3). However, the secant modulus measured for the same specimens shown in Fig. 1 was independent of the preload level at $17.8 \pm 1.8 \text{ GPa}$, which was significantly

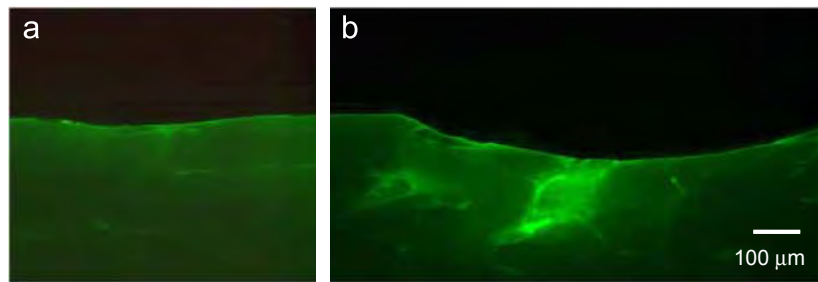


Fig. 6. Optical micrographs using green epifluorescence of calcein-stained longitudinal beam sections showing (a) minimal and (b) significant indentation adjacent to the roller supports. Note the prominence of vasculature within the tissue underlying the larger indentation.

greater than the LEBT modulus measured at any other preload level (Fig. 1).

The nonlinear dependence of the LEBT modulus on the load level (Fig. 1) was not expected and initially thought to be due to strain rate effects (Schaffler et al., 1989), since the strain rate increased with increasing load level. Therefore, an additional five specimens were prepared and loaded from 40 to 300 N in 20 N increments at a constant strain rate by adjusting the frequency at each load level to match the strain rate for a 200 N load at 2 Hz. The LEBT modulus still increased nonlinearly with an increased preload level ($p < 0.0001$, ANOVA) suggesting that the dependence was not due to strain rate effects, but indentation of the roller supports into the tissue as discussed further below.

Finally, it is worth reminding that preloading protocol for normalizing fatigue loads to a prescribed strain may account for variability in the initial specimen modulus, but cannot account for differences in the mode of loading (e.g., uniaxial versus bending) and specimen size (e.g., Weibull modulus) between various studies. Moreover, variability in the number of cycles to a prescribed modulus degradation or failure remains high (Boyce et al., 1998; Cotton et al., 2005; Diab et al., 2006; Gibson et al., 1995; Pattin et al., 1996; Pidaparti et al., 2000; Sobelman et al., 2004), with no apparent differences from typical fatigue test data without a normalization procedure.

4.2. Mechanical measures of damage accumulation

Degradation of the LEBT modulus did not alone adequately characterize damage accumulation, but included the combined effect of elastic (recovered) and creep (accumulated) strain (Fig. 4). While the normalized LEBT modulus decreased by 26% and the creep strain ratio decreased by 58% after 400,000 cycles, the normalized secant modulus experienced no degradation and histology revealed no significant differences in microcrack density (Table 1). Therefore, at minimum, both secant modulus and creep should be measured throughout a test to most accurately indicate damage accumulation and account for different damage mechanisms. Fatigue damage due to elastic (recovered) and creep (accumulated) strain is generally thought to correspond to quasi-brittle microcracking and viscoplasticity, respectively (Lemaitre and Desmorat, 2005). Creep observed in cortical bone fatigue has been suggested to be due to microcrack propagation and/or diffuse damage formation (Winwood et al., 2006a,b), which was supported by an increase in the mean crack length measured in this study (Table 1).

The secant modulus did not change during the course of fatigue testing (Fig. 4), which suggested that damage accumulation due to quasi-brittle microcracking was insignificant, as was confirmed through histological analysis. This was not expected for a test normalized to 6000 μ strain after 400,000 cycles (Boyce et al., 1998; Diab et al., 2006; Diab and Vashishth, 2005; Gibson

et al., 1995; Sobelman et al., 2004), but a couple of possible explanations exist. First, as mentioned above, the initial LEBT modulus used to normalize fatigue loads to 6000 μ strain was significantly lower than the initial secant modulus. If the specimens in the second experiment had been normalized using the initial secant modulus, the applied fatigue loads would have been at least 20% greater than those employed. Second, the relative effects of elastic and creep strains were only previously investigated in uniaxial fatigue loading of osteonal human cortical bone (Cotton et al., 2003, 2005; Winwood et al., 2006a,b). In this study, fatigue damage of plexiform bovine cortical bone in four-point bending was dominated by viscoplastic creep (Fig. 4).

Differences in the secant, loading, and unloading stiffness degradation (Fig. 5) were due to the presence of asymmetric hysteresis loops (Fig. 2). Hysteresis loops are typically symmetric about the secant, as previously reported for uniaxial tension and compression (Pattin et al., 1996), and therefore exhibit a similar loading and unloading stiffness. However, all specimens in this study exhibited a distinct change in stiffness approximately mid-way through the hysteresis loop which became more prominent with an increased number of loading cycles (Fig. 2), leading to the unexpected increase in unloading stiffness during fatigue (Fig. 5). If not for this behavior, changes in the unloading stiffness would be expected due to purely elastic recovery, even following prior inelastic deformation, providing a potentially insightful measure of fatigue damage.

The only other group to report hysteresis loops for four-point bending fatigue of cortical bone observed the same asymmetric behavior (Gibson et al., 1995; Griffin et al., 1999). The asymmetry was attributed to the formation of “wear grooves” at fixed load supports and was reported to be minimized by using roller supports (Griffin et al., 1997). However, the asymmetry was prominent in this study despite the use of roller supports. A decline in the hysteresis, or energy dissipated per cycle, was observed to occur within the first 50,000 cycles, followed by constant hysteresis thereafter. This behavior suggested the formation of indentations (Fig. 6), rather than “wear grooves.” Moreover, the mean indentation depth per specimen was calculated to account for 8 to 48% ($22 \pm 24\%$) of the creep strain. The largest indentations exhibited significant sub-surface damage, coinciding with prominent vasculature within the tissue adjacent to the roller supports (Fig. 6). In contrast, fully dense synthetic composites with an elastic modulus similar to cortical bone exhibited typical symmetric hysteresis loops during four-point bending fatigue using similar-sized specimens and the same loading fixture (Kane et al., 2008). Finally, since large creep strains were measured during fatigue (Fig. 4) even after accounting for roller support indentations, viscoplastic deformation may have also contributed to the asymmetric hysteresis by producing a curved beam with an altered neutral axis.

In summary, the presence of indentations at roller supports resulted in inflated measures of the LEBT modulus degradation

and creep. Therefore, considering all the above factors, investigations of fatigue microdamage in cortical bone should avoid the use of four-point bending unless no other option is possible. Other well-known limitations in the use of four-point bending tests include specimen size dependency and stressed volume effects.

5. Conclusions

Mechanical measures for the accumulation of damage in bovine cortical bone during four-point bending fatigue were shown to be highly dependent on the methods employed. Therefore, the following recommendations should be considered for standardized four-point bending fatigue of cortical bone:

- (1) The initial specimen modulus should not be measured from beam deflections using linear elastic beam theory (LEBT). The initial LEBT modulus was shown to be nonlinearly dependent on the preload level, which subsequently caused systematic error in the amount and rate of damage accumulation measured by the LEBT modulus degradation. The secant modulus was free of this error and is therefore recommended.
- (2) Both the secant modulus and creep, at minimum, should be measured throughout fatigue loading to most accurately indicate damage accumulation and account for different damage mechanisms. The LEBT modulus did not alone adequately characterize damage accumulation, but included a combined effect of both elastic (recovered) and creep (accumulated) strain.
- (3) Investigations of fatigue microdamage in cortical bone should avoid the use of four-point bending unless no other option is possible. Histology revealed indentation of tissue adjacent to roller supports, with significant sub-surface damage beneath large indentations, accounting for 22% of the creep strain on average. The indentation of roller supports resulted in inflated measures of the LEBT modulus degradation and creep.

Conflict of interest statement

I and my co-authors have no conflicts of interest to disclose regarding our submission entitled, "Systematic error in the measure of microdamage by modulus degradation during four-point bending fatigue of cortical bone," for publication in the *Journal of Biomechanics*.

Acknowledgements

This research was supported by the US Army Medical Research and Materiel Command (W81XWH-06-1-0196) through the Peer Reviewed Medical Research Program (PR054672), and the National Institutes of Health (AR049598).

References

Akkus, O., Knott, D.F., Jepsen, K.J., Davy, D.T., Rinnac, C.M., 2003. Relationship between damage accumulation and mechanical property degradation in cortical bone: microcrack orientation is important. *Journal of Biomedical Materials Research* 65A (4), 482–488.

- Boyce, T.M., Fyhrie, D.P., Clotkowski, M.C., Radin, E.L., Schaffler, M.B., 1998. Damage type and strain mode associations in human compact bone bending fatigue. *Journal of Orthopaedic Research* 16 (5), 322–329.
- Burr, D.B., Turner, C.H., Naick, P., Forwood, M.R., Ambrosius, W., Hasan, M.S., Pidaparti, R., 1998. Does microdamage accumulation affect the mechanical properties of bone? *Journal of Biomechanics* 31, 337–345.
- Caler, W.E., Carter, D.R., 1989. Bone creep-fatigue damage accumulation. *Journal of Biomechanics* 22, 625–635.
- Cotton, J.R., Zioupos, P., Winwood, K., Taylor, M., 2003. Analysis of creep strain during tensile fatigue of cortical bone. *Journal of Biomechanics* 36, 943–949.
- Cotton, J.R., Winwood, K., Zioupos, P., Taylor, M., 2005. Damage rate is a predictor of fatigue life and creep strain rate in tensile fatigue of human cortical bone samples. *Journal of Biomechanical Engineering* 127 (4), 213–219.
- Danova, N.A., Colopy, S.A., Radtke, C.L., Kalscheur, V.L., Markel, M.D., Vanderby, R., McCabe, R.P., Escarcega, A.J., Muir, P., 2003. Degradation of bone structural properties by accumulation and coalescence of microcracks. *Bone* 33, 197–205.
- Diab, T., Vashishth, D., 2005. Effects of damage morphology on cortical bone fragility. *Bone* 37, 96–102.
- Diab, T., Condon, K.W., Burr, D.B., Vashishth, D., 2006. Age-related change in the damage morphology of human cortical bone and its role in bone fragility. *Bone* 38 (3), 427–431.
- Fleck, C., Eifler, D., 2003. Deformation behaviour and damage accumulation of cortical bone specimens from the equine third metacarpus: mechanical property analysis. *Journal of Orthopaedic Research* 13, 861–868.
- Griffin, L.V., Gibeling, J.C., Gibson, V.A., Martin, R.B., Stover, S.M., 1997. Artificial nonlinearities due to wear grooves and friction in four-point bending experiments of cortical bone. *Journal of Biomechanics* 30 (2), 185–188.
- Griffin, L.V., Gibeling, J.C., Martin, R.B., Gibson, V.A., Stover, S.M., 1999. The effects of testing methods on the flexural fatigue life of human cortical bone. *Journal of Biomechanics* 32, 105–109.
- Gustafson, M.B., Martin, R.B., Gibson, V., Storms, D.H., Stover, S.M., Gibeling, J., Griffin, L., 1996. Calcium buffering is required to maintain bone stiffness in saline solution. *Journal of Biomechanics* 29 (9), 1191–1194.
- Jepsen, K.J., Davy, D.T., 1997. Comparison of damage accumulation measures in human cortical bone. *Journal of Biomechanics* 30 (9), 891–894.
- Joo, W., Jepsen, K.J., Davy, D.T., 2007. The effect of recovery time and test conditions on viscoelastic measures of tensile damage in cortical bone. *Journal of Biomechanics* 40, 2731–2737.
- Kane, R.J., Converse, G.L., Roeder, R.K., 2008. Effects of the reinforcement morphology on the fatigue properties of hydroxyapatite reinforced polymers. *Journal of the Mechanical Behavior of Biomedical Materials* 1 (3), 261–268.
- Lee, T.C., Myers, E.R., Hayes, W.C., 1998. Fluorescence-aided detection of microdamage in compact bone. *Journal of Anatomy* 193, 179–184.
- Lemaitre, J., Desmorat, R., 2005. *Engineering Damage Mechanics*. Springer, Berlin.
- Moreno, L.D., Waldman, S.D., Grynias, M.D., 2006. Sex differences in long bone fatigue using a rat model. *Journal of Orthopaedic Research* 24, 1926–1932.
- O'Brien, F.J., Taylor, D., Lee, T.C., 2003. Microcrack accumulation at different intervals during fatigue testing of compact bone. *Journal of Biomechanics* 36, 973–980.
- Pattin, C.A., Caler, W.E., Carter, D.R., 1996. Cyclic mechanical property degradation during fatigue loading of cortical bone. *Journal of Biomechanics* 29, 69–79.
- Pidaparti, R.M., Akyuz, U., Naick, P.A., Burr, D.B., 2000. Fatigue data analysis of canine femurs under four-point bending. *Biomedical Materials and Engineering* 10, 43–50.
- Schaffler, M.B., Radin, E.L., Burr, D.B., 1989. Mechanical and morphological effects of strain rate on fatigue of compact bone. *Bone* 10 (3), 207–214.
- Schaffler, M.B., Radin, E.L., Burr, D.B., 1990. Long-term fatigue behavior of compact bone at low strain magnitude and rate. *Bone* 11 (5), 321–326.
- Sobelman, O.S., Gibeling, J.C., Stover, S.M., Hazelwood, S.J., Yeh, O.C., Shelton, D.R., Martin, R.B., 2004. Do microcracks decrease or increase fatigue resistance in cortical bone? *Journal of Biomechanics* 37, 1295–1303.
- Winwood, K., Zioupos, P., Currey, J.D., Cotton, J.R., Taylor, M., 2006a. Strain patterns during tensile, compressive and shear fatigue of human cortical bone and implications for bone biomechanics. *Journal of Biomedical Materials Research* 79A, 289–297.
- Winwood, K., Zioupos, P., Currey, J.D., Cotton, J.R., Taylor, M., 2006b. The importance of the elastic and plastic components of strain in tensile and compressive fatigue of human cortical bone in relation to orthopaedic biomechanics. *Journal of Musculoskeletal and Neuronal Interaction* 6 (2), 134–141.
- Zioupos, P., Wang, X.T., Currey, J.D., 1996. The accumulation of fatigue microdamage in human cortical bone of two different ages in vitro. *Clinical Biomechanics* 11 (7), 365–375.

Improved accuracy of cortical bone mineralization measured by polychromatic microcomputed tomography using a novel high mineral density composite calibration phantom

Justin M. Deuerling, David J. Rudy, Glen L. Niebur, and Ryan K. Roeder^{a)}

Department of Aerospace and Mechanical Engineering, University of Notre Dame,
Notre Dame, Indiana 46556

(Received 12 April 2010; revised 22 July 2010; accepted for publication 22 July 2010;
published 31 August 2010)

Purpose: Microcomputed tomography (micro-CT) is increasingly used as a nondestructive alternative to ashing for measuring bone mineral content. Phantoms are utilized to calibrate the measured x-ray attenuation to discrete levels of mineral density, typically including levels up to 1000 mg HA/cm³, which encompasses levels of bone mineral density (BMD) observed in trabecular bone. However, levels of BMD observed in cortical bone and levels of tissue mineral density (TMD) in both cortical and trabecular bone typically exceed 1000 mg HA/cm³, requiring extrapolation of the calibration regression, which may result in error. Therefore, the objectives of this study were to investigate (1) the relationship between x-ray attenuation and an expanded range of hydroxyapatite (HA) density in a less attenuating polymer matrix and (2) the effects of the calibration on the accuracy of subsequent measurements of mineralization in human cortical bone specimens.

Methods: A novel HA-polymer composite phantom was prepared comprising a less attenuating polymer phase (polyethylene) and an expanded range of HA density (0–1860 mg HA/cm³) inclusive of characteristic levels of BMD in cortical bone or TMD in cortical and trabecular bone. The BMD and TMD of cortical bone specimens measured using the new HA-polymer calibration phantom were compared to measurements using a conventional HA-polymer phantom comprising 0–800 mg HA/cm³ and the corresponding ash density measurements on the same specimens.

Results: The HA-polymer composite phantom exhibited a nonlinear relationship between x-ray attenuation and HA density, rather than the linear relationship typically employed *a priori*, and obviated the need for extrapolation, when calibrating the measured x-ray attenuation to high levels of mineral density. The BMD and TMD of cortical bone specimens measured using the conventional phantom was significantly lower than the measured ash density by 19% ($p < 0.001$, ANCOVA) and 33% ($p < 0.05$, Tukey's HSD), on average, respectively. The BMD and TMD of cortical bone specimens measured using the HA-polymer phantom with an expanded range of HA density was significantly lower than the measured ash density by 8% ($p < 0.001$, ANCOVA) and 10% ($p < 0.05$, Tukey's HSD), on average, respectively.

Conclusions: The new HA-polymer calibration phantom with a less attenuating polymer and an expanded range of HA density resulted in a more accurate measurement of micro-CT equivalent BMD and TMD in human cortical bone specimens compared to a conventional phantom, as verified by ash density measurements on the same specimens. © 2010 American Association of Physicists in Medicine. [DOI: [10.1118/1.3480507](https://doi.org/10.1118/1.3480507)]

Key words: bone mineral density, cortical bone, hydroxyapatite, microcomputed tomography, mineralization

I. INTRODUCTION

The level of mineralization is an important determinant of the mechanical properties and fracture susceptibility of bone tissue.¹ Cortical bone mechanical properties—such as the elastic modulus, strength, and fracture toughness—are strongly influenced by mineralization.^{2–6} Moreover, a parametric study using a multiscale, micromechanical model demonstrated that the elastic modulus of cortical bone was most sensitive to the mineral density, among seven structural parameters investigated.⁷ Therefore, precise and reliable techniques are needed for measuring the level of mineralization in bone tissue.

Mineralization is most commonly and accurately measured by ashing bone tissue at a temperature sufficient to pyrolyze the organic matrix, leaving the bone mineral for gravimetric analysis. Unfortunately, this process is inherently invasive and destructive. Mineralization has also been measured using backscattered electron imaging in a scanning electron microscope^{8,9} and microradiography.^{9,10} These techniques are capable of very fine spatial resolution but are inherently invasive and two-dimensional. In contrast, peripheral quantitative computed tomography (pQCT) has enabled noninvasive, three-dimensional (3D) measurement of volumetric bone mineral density (BMD) but has a relatively low spatial resolution for examining levels of mineralization.¹¹

Synchrotron radiation computed tomography (SRCT) is capable of precise, 3D measurements of bone mineralization^{9,12,13} but is limited in availability and to a small specimen size.

Therefore, microcomputed tomography (micro-CT) has been proposed for nondestructive, 3D measurements of bone mineralization using a linear calibration of mineral density and x-ray attenuation.^{13–20} Both micro-CT and SRCT have sufficient spatial resolution to enable volumetric measurement of tissue mineral density (TMD), exclusive of porosity, in addition to BMD, inclusive of porosity.^{13,14} However, measurements of mineral density by micro-CT are complicated by beam hardening due to the use of polychromatic radiation. Beam hardening leads to an underestimation of x-ray attenuation, and subsequently mineral density, because the mean x-ray energy is higher for the specimen interior due to the preferential attenuation of low energy x rays at the specimen perimeter. Beam hardening correction algorithms are one approach used to mitigate this phenomenon, but may not be sufficient, especially at high levels of mineral density.^{13–16}

Mixtures of polymers with known quantities of hydroxyapatite (HA) crystals are commonly used in micro-CT imaging phantoms for the calibration of x-ray attenuation to HA density.^{13,14,17} Phantoms comprising HA are desirable because HA exhibits similar composition and x-ray attenuation compared to bone mineral. The measured x-ray attenuation versus the known HA density in the phantom is fitted by least-squares linear regression and this calibration is subsequently used to estimate the mineral density of bone specimens from the measured x-ray attenuation. Previous studies demonstrated strong correlations between micro-CT equivalent density and ash density measurements in trabecular and cortical bone; however, micro-CT underestimated TMD compared to the ash density.^{13,14} Aqueous solutions containing varying concentrations of potassium phosphate (K_2HPO_4) have also been used as a micro-CT calibration phantom.^{12,16,17,20} K_2HPO_4 was utilized due to exhibiting x-ray attenuation similar to HA and homogeneity throughout the liquid phantom.

Current HA-polymer and liquid K_2HPO_4 calibration phantoms share a common limitation. The range of mineral density commonly present in either HA-polymer composite (0–800 mg HA/cm³) (Refs. 13, 14, and 17) or K_2HPO_4 solution (0–1000 mg HA/cm³) (Refs. 12, 16, 17, and 20) phantoms encompasses levels of BMD observed in trabecular bone. However, levels of BMD observed in cortical bone and levels of TMD in cortical or trabecular bone typically exceed 1000 mg HA/cm³, requiring extrapolation of linear calibration regressions.^{13–16} Moreover, a nonlinear relationship between measured x-ray attenuation and known phantom mineral density has been observed even after the use of a beam hardening correction algorithm.¹⁶ The presence of a nonlinear calibration of measured x-ray attenuation and known phantom mineral density suggests that the use of an extrapolated linear calibration would result in increased un-

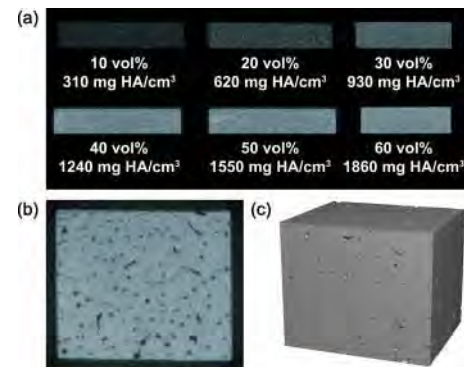


FIG. 1. Representative cross-sectional grayscale images for micro-CT of (a) the HA-polymer composite phantom showing increased brightness with increased HA density, as expected, and (b) a representative cortical bone specimen including (c) a segmented, three-dimensional reconstruction of the entire tissue specimen. Note that the vertical dimension of the phantom specimens in (a) is 2.5 mm, and the horizontal dimension of the tissue specimen in (b) and (c) is 5 mm.

derestimation of the mineral density in tissue specimens at high levels of mineral density, as has been observed in practice.^{13,14}

Therefore, the objectives of this study were to investigate (1) the relationship between x-ray attenuation and an expanded range of HA density (0–1860 mg HA/cm³) using a calibration phantom comprising 0–60 vol % HA crystals in a less attenuating polymer matrix and (2) the effects of the calibration on the accuracy of subsequent measurements of mineralization in human cortical bone specimens. The BMD and TMD of cortical bone specimens measured using the new HA-polymer calibration phantom were compared to measurements using a conventional HA-polymer phantom comprising 0–800 mg HA/cm³ and the corresponding ash density measurements on the same specimens.

II. MATERIALS AND METHODS

II.A. Calibration phantoms

HA reinforced high density polyethylene (HDPE) composites composed of 0, 10, 20, 30, 40, 50, and 60 vol % HA were prepared using methods described in detail elsewhere.^{21,22} The HA densities of the composites were calculated to be 0, 310, 620, 930, 1240, 1550, and 1860 mg HA/cm³ [Fig. 1(a), Table I], based on the known density of HDPE (960 mg/cm³) (Ref. 21) and HA crystals prepared using similar methods (3100 mg/cm³).^{23,24} The HA content in the composites was also verified using measurements from Archimedes' principle²⁵ and ashing.²²

Composite bars with cross-sectional dimensions of 10 × 2.5 mm were each positioned near the outer edge of a 20 mm diameter specimen holder such that the specimen was within 7–10 mm from the center of rotation and scanned individually using a benchtop micro-CT system (μ CT-80, Scanco Medical AG, Brüttisellen, Switzerland) equipped with a cone beam polychromatic x-ray source, 0.5 mm aluminum filter, and 2048 × 128 element charge-coupled device detector. Imaging was performed in de-ionized (DI) water

TABLE I. The new HA-polymer composite phantom with an expanded range of HA density encompassed levels of BMD characteristic of human cortical bone, and levels of TMD characteristic of both human cortical and trabecular bone. Measurements of the micro-CT equivalent mineral density for compositions of the new HA-polymer phantom using extrapolated linear or nonlinear calibrations for the conventional phantom (Fig. 2) significantly underestimated the known HA density ($p < 0.01$, paired t -test). The first standard deviation of mean values is given in parentheses, when applicable, and represents intrascan spatial variability for a single volume of interest.

HA-polymer phantom composition		Micro-CT measurements		
HA volume fraction (vol %)	HA density (mg HA/cm ³)	X-ray attenuation (cm ⁻¹)	Linear calibrated equivalent density ^a (mg HA/cm ³)	Nonlinear calibrated equivalent density ^b (mg HA/cm ³)
0	0	0.24(0.18)	-97 (68)	-72 (58)
10	310	1.05(0.39)	215 (151)	208 (127)
20	620	1.72(0.58)	475 (225)	464 (191)
30	930	2.34(0.52)	714 (201)	718 (171)
40	1240	2.88(0.53)	925 (214)	958 (174)
50	1550	3.40(0.53)	1124 (204)	1196 (174)
60	1860	3.88(0.56)	1310 (218)	1430 (184)

^aMeasured using an extrapolated linear calibration for the conventional phantom.

^bMeasured using an extrapolated nonlinear calibration for the conventional phantom.

soaked gauze at 70 kVp, 114 μ A, and 400 ms integration time for 200 slices with a 10 μ m voxel size. All parameters known to affect x-ray attenuation measurements—such as the tube voltage, detector distance, detector size, and imaging media¹⁷—were held constant. A beam hardening correction algorithm based on a HA-resin wedge phantom (1200 mg HA/cm³) was applied as provided by the micro-CT manufacturer. Analysis was conducted on a volume of interest, with boundaries reduced from the specimen outline by 50 pixels (0.5 mm) to remove partial volume artifacts, after applying a Gaussian filter (sigma=0.8, support =1.0) to minimize high frequency noise.

A conventional calibration phantom (QRM-microCT-HA, Quality Assurance in Radiology and Medicine, GmbH, Möhrendorf, Germany) provided by the micro-CT manufacturer comprised HA particles embedded in a proprietary epoxy resin (1130 mg/cm³) at 0, 100, 200, 400, and 800 mg HA/cm³ (Table II). All five HA compositions were embedded within a single, 35 mm diameter cylindrical block of the same epoxy resin, evenly spaced and centered about a 20 mm diameter from the center of rotation, and each individual HA composition was 6 mm in diameter. The conventional calibration phantom was scanned using identical methods to the HA-polymer phantom, except that the size of the conventional phantom necessitated lower resolution (18 μ m voxel size) and each HA composition could not be scanned individually. Therefore, in order to consider the effects of the lower resolution and specimen positioning, the HA-polymer phantom compositions were also rescanned with an 18 μ m voxel size either simultaneously (in parallel) or individually (in series) while placed the same distance from the center of rotation as the conventional phantom compositions.

Linear and nonlinear least-squares regression (STATVIEW 5.0.1, SAS Institute, Inc., Cary, NC) was used to correlate the measured x-ray attenuation with the known HA density in the calibration phantoms. Analysis of covariance (ANCOVA) was used to compare regressions. The known HA density within calibration phantoms was compared to the HA density

determined from the measured x-ray attenuation and the calibration provided for the conventional phantom using a paired t -test. The level of significance for all tests was set at 0.05.

II.B. Measurements of cortical bone mineralization

Thirty-seven cortical bone specimens, nominally 5 \times 5 \times 5 mm, were machined from the femoral diaphysis of three human male donors ages 62, 62, and 70, presenting no medical history of skeletal pathology or trauma. All tissues were obtained with donor's consent (National Disease Research Interchange, Philadelphia, PA) and all protocols were approved by the Notre Dame Human Subjects Institutional Review Board. The entire volume of each specimen was scanned by micro-CT [Figs. 1(b) and 1(c)] in DI water soaked gauze using the same methods and parameters described above for the calibration phantoms. X-ray attenua-

TABLE II. The conventional phantom provided by the micro-CT manufacturer comprised a range of HA density that encompassed levels of BMD characteristic of human trabecular bone only. Repeated measurements of the micro-CT equivalent mineral density for compositions of the phantom using the linear calibration were not statistically different than the HA density quoted by the phantom manufacturer ($p > 0.10$, paired t -test). The first standard deviation of mean values is given in parentheses, when applicable, and represents intrascan spatial variability for a single volume of interest.

Conventional phantom composition	Micro-CT measurements	
HA density ^a (mg HA/cm ³)	X-ray attenuation (cm ⁻¹)	Equivalent density ^b (mg HA/cm ³)
0	0.44(0.09)	−22 (34)
100	0.73(0.18)	94 (69)
200	1.00(0.21)	198 (82)
400	1.51(0.24)	396 (91)
800	2.45(0.23)	760 (88)

^aProvided by the phantom manufacturer.

^bRepeated measurement using the linear calibration for the conventional phantom.

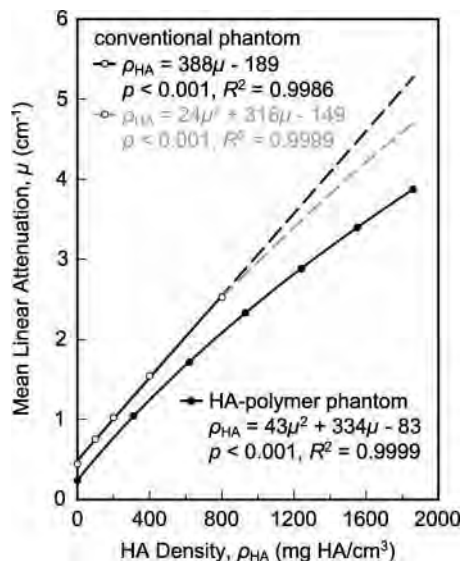


FIG. 2. The HA-polymer composite phantom with an expanded range of HA density exhibited a nonlinear relationship between the measured x-ray attenuation μ and the known HA density ρ_{HA} . The conventional phantom was fitted by a linear or a nonlinear relationship at the lower levels of HA density employed and extrapolated for higher levels of HA density. Therefore, calibration using the new HA-polymer phantom resulted in measurements of HA density that were significantly greater than those using extrapolated linear or nonlinear calibrations for the conventional phantom ($p < 0.01$, paired t -test) (Table I), and the differences became greater with increased HA density.

tion was evaluated over either the total volume (TV), inclusive of porosity, or bone volume (BV), exclusive of porosity. Tissue porosity was segmented from the BV using a global threshold value of 240 on the grayscale images for all specimens. This threshold was located at the toe of the bone peak in the image histogram and corresponded to an x-ray attenuation of 1.92 cm^{-1} or 553 mg HA/cm^3 using the conventional calibration phantom provided by the manufacturer. The mean (\pm standard deviation) Haversian porosity measured by micro-CT for the cortical bone specimens investigated in this study was $10.1 (\pm 7.1) \text{ vol } \%$. BMD and TMD were measured based on the TV and BV, respectively, using linear and nonlinear calibrations of measured x-ray attenuation and known mineral density from the calibration phantoms (Fig. 2).

The ash density for each specimen was measured as the ash mass divided by either the TV or BV, for comparison to micro-CT measurements of BMD or TMD, respectively. TV was measured using Archimedes' principle as the difference between the specimen mass when fully saturated with DI water (M) and the apparent mass when suspended in DI water (S).^{7,25,26} Each specimen was subsequently dehydrated in a graded series of alcohol solutions and dried in a vacuum oven at 100°C for 24 h. BV was also measured using Archimedes' principle as the difference between the dry specimen mass (D) and S .^{7,25,27} Specimens were finally ashed at 900°C for 48 h. The ash mass, as well as the above measures of specimen mass, was measured gravimetrically to a precision of 0.1 mg. Measured ash densities were compared to measured micro-CT equivalent densities using

ANCOVA (STATVIEW 5.0.1, SAS Institute, Inc., Cary, NC) or Tukey's HSD test, with a level of significance of 0.05.

III. RESULTS

III.A. Calibration phantoms

The HA-polymer composite phantom with an expanded range of HA density exhibited a nonlinear relationship between x-ray attenuation and HA density (Fig. 2). In contrast, the relationship between x-ray attenuation and HA density for the conventional phantom could be fitted by either a linear or a nonlinear relationship within the range of HA density in the phantom. Significant differences between the linear and nonlinear regressions were only observed upon extrapolation to HA density greater than the 800 mg HA/cm^3 upper limit of the phantom.

The HA-polymer phantom with an expanded range of HA density also utilized a lower density polymer that resulted in a significantly lower x-ray attenuation at any given HA density compared to the conventional phantom (Fig. 2). Therefore, calibration using the new HA-polymer phantom resulted in measurements of HA density that were significantly greater than those using extrapolated linear or nonlinear calibrations for the conventional phantom ($p < 0.01$, paired t -test) (Table I), and the differences became greater with increased HA density (Fig. 2).

The HA-polymer composite and conventional calibration phantoms in Fig. 2 were imaged with a 10 versus $18 \mu\text{m}$ voxel size and with the various HA compositions imaged individually (in series) versus simultaneously (in parallel), respectively, due to the size and design of the commercial phantom. In order to consider these effects, the HA-polymer phantom compositions were also rescanned with an $18 \mu\text{m}$ voxel size either individually (in series) or simultaneously (in parallel) while placed the same distance from the center of rotation as the conventional phantom compositions. The lower resolution and simultaneous imaging of the HA-polymer composite specimens resulted in increased measured x-ray attenuation for a given HA density, but the differences from conditions employed in Fig. 2 were not statistically significant ($p = 0.12$, ANCOVA) and the calibration remained nonlinear (Fig. 3). Therefore, subsequent measurements of cortical bone mineralization focused on the nonlinear calibration with HA-polymer composite phantom compositions imaged individually (in series) at the higher resolution (Fig. 2) in order to be most similar to the imaging methods employed for bone tissue specimens.

III.B. Measurements of cortical bone mineralization

The BMD of human cortical bone specimens measured by micro-CT was in closer agreement with the corresponding ash density using the nonlinear calibration for the HA-polymer phantom with an expanded range of HA density compared to extrapolated linear or nonlinear calibrations for the conventional phantom (Fig. 4). BMD measured using extrapolated linear or nonlinear calibrations for the conventional phantom was significantly lower than the measured

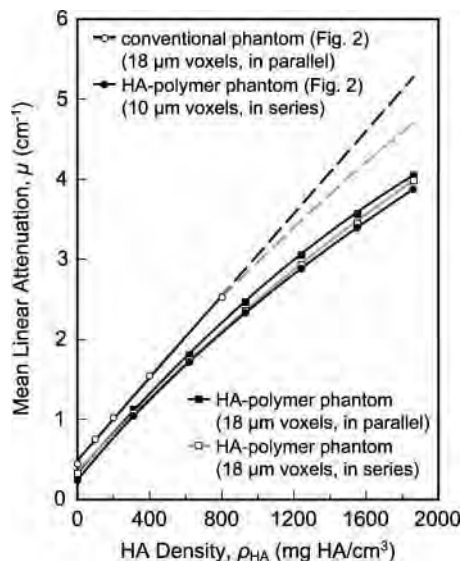


FIG. 3. The HA-polymer composite and conventional calibration phantoms in Fig. 2 were imaged with a 10 versus 18 μm voxel size, and with the various HA compositions imaged individually (in series) versus simultaneously (in parallel), respectively, due to the size and design of the commercial phantom. In order to consider these effects, the HA-polymer phantom compositions were also rescanned with an 18 μm voxel size either simultaneously (in parallel) or individually (in series) while placed the same distance from the center of rotation as the conventional phantom compositions. The lower resolution and simultaneous imaging of the HA-polymer composite specimens resulted in increased measured x-ray attenuation μ for a given HA density ρ_{HA} , but the differences from conditions employed in Fig. 2 were not statistically significant ($p=0.12$, ANCOVA) and the calibration remained nonlinear.

ash density ($p<0.001$, ANCOVA) by 19% or 17%, on average, respectively. BMD measured using the HA-polymer phantom with an expanded range of HA density was significantly greater than the measured ash density ($p<0.001$, ANCOVA) by 8%, on average. Micro-CT measurements of BMD were correlated with ash density measurements using both the nonlinear calibration for the HA-polymer composite phantom ($p<0.001$, $R^2=0.55$) and extrapolated linear or nonlinear calibrations with the conventional phantom ($p<0.001$, $R^2=0.56$).

The TMD of human cortical bone specimens measured by micro-CT was also in closer agreement with the corresponding ash density using the nonlinear calibration for the HA-polymer composite phantom with an expanded range of HA density compared to extrapolated linear or nonlinear calibrations for the conventional phantom (Fig. 5). Micro-CT measurements of TMD using either calibration phantom were not correlated with ash density measurements ($p>0.66$). However, TMD measured using extrapolated linear or nonlinear calibrations for the conventional phantom underestimated the ash density by 33% or 30%, on average, respectively, while TMD measured using the nonlinear calibration for the HA-polymer phantom underestimated the ash density by only 10%, on average ($p<0.05$, Tukey's HSD) (Fig. 6).

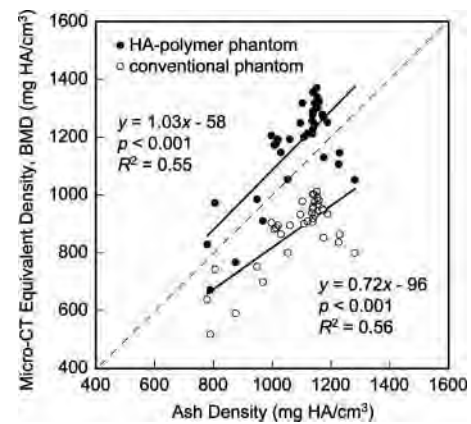


FIG. 4. The BMD of human cortical bone specimens measured by micro-CT equivalent density using the nonlinear calibration for the HA-polymer phantom with an expanded range of HA density was in greater agreement with the corresponding measured ash density (ash mass/TV) compared to using the extrapolated linear calibration for the conventional phantom. The micro-CT equivalent density measured by either calibration was correlated with the measured ash density. Note that measurements of the micro-CT equivalent density using the extrapolated nonlinear calibration for the conventional phantom exhibited only minor differences from the linear calibration (2% greater on average) that were not statistically significant and were therefore not shown for clarity.

IV. DISCUSSION

IV.A. Effects of the calibration phantom composition and imaging medium

The HA-polymer phantom used in this study enabled a more accurate calibration of x-ray attenuation and HA density (Fig. 2), and thus more accurate measurements of BMD and TMD in cortical bone specimens (Figs. 4–6), by virtue of employing (1) an expanded range of HA density

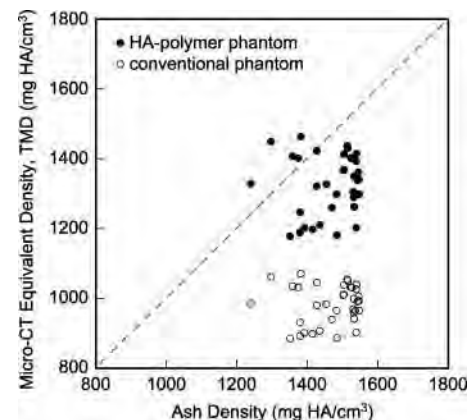


FIG. 5. The TMD of human cortical bone specimens measured by micro-CT equivalent density using the nonlinear calibration for the HA-polymer phantom with an expanded range of HA density was in greater agreement with the corresponding measured ash density (ash mass/BV) compared to using the extrapolated linear calibration for the conventional phantom. The micro-CT equivalent density measured by either calibration was not correlated with the measured ash density. Note that measurements of the micro-CT equivalent density using the extrapolated nonlinear calibration for the conventional phantom exhibited only minor differences from the linear calibration (3% greater on average) that were not statistically significant and were therefore not shown for clarity.

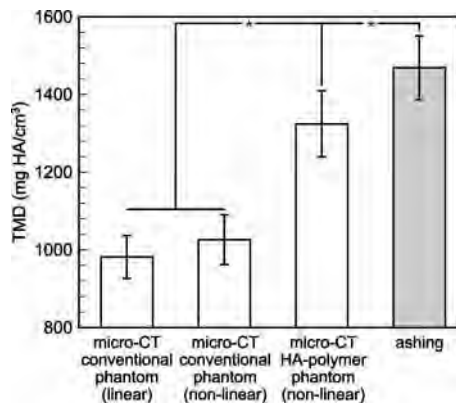


FIG. 6. The mean TMD of human cortical bone specimens measured by micro-CT equivalent density using extrapolated linear or nonlinear calibrations for the conventional phantom, and the nonlinear calibration for the HA-polymer phantom with an expanded range of HA density, compared to the corresponding ash density (ash mass/BV) of the same specimens. Error bars show one standard deviation. Asterisks denote statistically significant differences between groups ($p < 0.05$, Tukey's HSD).

(0–1860 mg HA/cm³) and (2) a less attenuating polymer phase. The range of HA density was inclusive of characteristic levels of BMD in cortical bone or TMD in cortical and trabecular bone. The BMD and TMD of human cortical bone specimens in this study ranged from approximately 700 to 1300 mg HA/cm³ and from 1200 to 1600 mg HA/cm³, respectively. However, the conventional calibration phantom included HA density only up to 800 mg HA/cm³, which may be suitable for the BMD of trabecular bone, but requires extrapolation for levels of BMD observed in cortical bone or levels of TMD in cortical and trabecular bone.

K₂HPO₄ solution phantoms have also been limited to equivalent HA density up to 800–1000 mg HA/cm³.^{16,17,20} Moreover, the solubility limit for K₂HPO₄ in water at 20 °C is 1670 mg/cm³,²⁸ which corresponds to ~1600 mg HA/cm³, depending on imaging parameters. This solubility limit prohibits the preparation of K₂HPO₄ solutions above this concentration and would limit the stability of solutions approaching this concentration. Other recent studies have prepared calibration phantoms comprising ~1200–2000 mg HA/cm³ by varying the level of porosity in pressed and sintered HA powder compacts.^{19,20} However, these phantoms were not able to be prepared at lower mineral density and thus required the use of a second phantom composed of different materials to calibrate HA density below 1200 mg HA/cm³. Moreover, the air or water in the pore space will not exhibit similar x-ray attenuation to macromolecules like collagen or synthetic polymers. Therefore, a HA-polymer composite phantom is expected to provide greater similarity to the extracellular matrix of bone tissue than liquid K₂HPO₄ or porous HA phantoms.

The HA-polymer phantom in this study utilized HDPE as the polymer phase, whereas the conventional phantom utilized a proprietary epoxy resin. The lower density of HDPE (960 mg/cm³) compared to the epoxy resin (1130 mg/cm³) resulted in less x-ray attenuation at a fixed HA density, which was evidenced by the vertical shift in calibration curves for

the two phantoms even at a HA density of zero (Fig. 2). Polyethylene has also received considerable use for tissue equivalent imaging phantoms.²⁹

The imaging medium surrounding phantom or tissue specimens was previously shown to affect the measured x-ray attenuation.¹⁷ In this study, water soaked gauze was used as the imaging medium and was held constant for both the HA-polymer phantom and cortical bone specimens. Furthermore, all phantom and tissue specimens were imaged separately to avoid interference. In contrast, the conventional phantom was comprised of mixtures of HA in an epoxy resin embedded within a single, larger resin block. Moreover, image projections for one HA density were not likely to be completely free from the influence of other HA densities positioned on the opposite side of the phantom (Fig. 3). These effects may have also contributed to the noticeable vertical shift in x-ray attenuation between the two calibration phantoms (Fig. 2). Thus, error due to differences in imaging media was minimized in this study when using the new HA-polymer phantom by scanning all phantom and tissue specimens separately and in the same imaging medium.

IV.B. Effects of the calibration nonlinearity

The relationship between x-ray attenuation and HA density was shown to be nonlinear for the HA-polymer calibration phantom comprising levels of HA density up to 1860 mg HA/cm³ (Fig. 2). A nonlinear relationship was previously reported for a K₂HPO₄ phantom comprising up to 800 mg HA/cm³ (Ref. 16) and was reported to slightly improve the calibration correlation coefficient for a pressed and sintered HA phantom comprising 1240–3050 mg HA/cm³.¹⁹ The results of the present study also showed a slight improvement in the calibration correlation coefficient (Fig. 2) and the accuracy of subsequent BMD and TMD (Fig. 6) measurements in cortical bone specimens when a quadratic rather than a linear relationship was used for the conventional phantom comprising up to 800 mg HA/cm³. However, a linear relationship was typically expected and employed *a priori* to calibrate measured x-ray attenuation to a known mineral density.^{13–20}

The most likely sources for the nonlinear behavior were beam hardening^{13–19} and scattering^{20,30–32} artifacts, which are dependent on the beam energy spectrum, the attenuation coefficient of the sample, the surrounding media, and the sample geometry. Note that nonlinearity was observed in spite of employing a beam hardening correction algorithm provided by the manufacturer, which is based on a HA-resin wedge phantom with 1200 mg HA/cm³. This algorithm was previously shown to reduce but not eliminate the effects of beam hardening compared to a 200 mg HA/cm³ wedge phantom.¹³ Thus, the results of this study add further weight to previous evidence that beam hardening due to a polychromatic x-ray source was not able to be fully corrected, especially at high levels of mineralization characteristic of TMD in cortical or trabecular bone.^{13–16}

The nonlinear calibration of x-ray attenuation and HA density for the HA-polymer phantom with an expanded

range of HA density was able to compensate for beam hardening artifacts not accounted for by the internal micro-CT correction algorithm, resulting in a more accurate measurement of micro-CT equivalent BMD and TMD in human cortical bone specimens (Figs. 4–6). In practice, the internal calibration provided by the micro-CT manufacturer can be readily corrected by simply applying the nonlinear calibration measured for the HA-polymer phantom with an expanded range of HA density (Fig. 2). For example, the HA density for the new HA-polymer phantom (ρ_{HA} , mg HA/cm³) was related to the HA density measured using the extrapolated linear calibration for the conventional phantom (ρ_{HA}°) as $\rho_{\text{HA}} = (2.89 \times 10^{-4}) \cdot (\rho_{\text{HA}}^{\circ})^2 + 0.97\rho_{\text{HA}}^{\circ} + 90.63$ ($p < 0.001$, $R^2 = 0.9999$). Note, however, that any calibration relationship must be recognized as being dependent on the instrument, imaging parameters, and specimen size, as has been well-documented.^{14–18}

IV.C. Other considerations

The HA-polymer calibration phantom described in this study enabled more accurate measurements of cortical bone mineralization. The micro-CT equivalent TMD of human cortical bone specimens measured using the HA-polymer phantom underestimated the corresponding ash density by 10%, on average (Fig. 6), exhibiting accuracy comparable to previous measurements using SRCT.¹³ While encouraging, other factors that may or may not contribute to this error must be considered for further improvement.

Differences in scanning parameters, such as x-ray tube voltage or detector distance, were previously shown to affect x-ray attenuation measurement¹⁷ but were held constant in this study. Moreover, repeated measurements of the conventional calibration phantom provided by the micro-CT manufacturer were in close agreement (Table II), ruling out systematic error. The cross-sectional dimensions of the HA-polymer phantom specimens (10 × 2.5 mm) were different from those of the cortical bone specimens (5 × 5 mm), though the cross-sectional area was held constant, which might be expected to result in a different proportion of the cross section influenced by beam hardening compared to the tissue specimens.¹⁵ However, the mean x-ray attenuation of the HA-polymer phantom was not different for a volume of interest at the specimen interior compared to the overall volume, minimizing this concern. Nonetheless, differences in the dimensions of tissue and phantom specimens should always be minimized or calibrated. Beam filtration can also be used to minimize the effects of beam hardening¹⁸ but requires longer image collection times.

The micro-CT equivalent TMD and the corresponding ash density may be subject to error via measurement of the BV, whether using micro-CT (Ref. 13) or Archimedes' principle.^{7,25,27} In this study, micro-CT was used by necessity to measure the BV for the equivalent TMD and Archimedes' principle was used to measure the BV for the corresponding ash density, where the latter was regarded as the most accurate assessment of the true tissue porosity. Micro-CT measurements of the tissue porosity were positively correlated

with measurements using Archimedes' principle ($p < 0.001$, $R^2 = 0.57$) but were approximately 16.3% lower, on average. An underestimation of tissue porosity by micro-CT was not unexpected due to the resolution limits of the instrument. The use of micro-CT measurements of BV for the corresponding ash density would have resulted in a decreased mean (\pm standard deviation) from 1469 (± 80) to 1225 (± 57) mg HA/cm³ (cf. Fig. 6), but the latter ash density would not be accurate and would not change the main results of this study. On the other hand, improvements in the accuracy of the BV measured by micro-CT would be expected to lead to decreased BV and consequently increased TMD, improving agreement between the micro-CT equivalent TMD and the corresponding ash density (Figs. 5 and 6). SRCT can be used to improve resolution limits and mitigate the underestimation of BV by micro-CT.¹³

The HA-polymer composite phantom in this study also utilized relatively large HA crystals compared to the size of apatite crystals in bone tissue. The HA crystals exhibited a whiskerlike morphology with mean dimensions of approximately 4–7 μm in length and 2 μm in width.²² Therefore, while the HA crystal size was smaller than the 10 μm voxel size for the micro-CT instrument, heterogeneity in x-ray attenuation was evident visually, especially at low HA density [Fig. 1(a)], as well as by the measured intrascan spatial variability in x-ray attenuation (Table I). The effect of heterogeneity within phantom specimens was assumed to be minimized by averaging over a relatively large volume of interest, but was not ideal. The use of nanoscale HA crystals in a polymer matrix could provide greater homogeneity to minimize scattering artifacts, similar to K₂HPO₄ solution phantoms,^{16,17,20} while retaining the advantages of a HA-polymer phantom mentioned above.

The correlation between the micro-CT equivalent BMD and the corresponding ash density (Fig. 4) was primarily due to variability in BMD caused by the range of porosity included within the TV. In contrast, the lack of a correlation between micro-CT equivalent TMD and the corresponding ash density (Fig. 5) was primarily due to limited variability in TMD resulting from exclusion of tissue porosity in the BV. The addition of other tissue types (e.g., trabecular tissue) and sources (e.g., bovine) could be used to further investigate the correlation of TMD measured by micro-CT and ashing.

V. CONCLUSIONS

A novel HA-polymer composite phantom was prepared comprising a lower attenuating polymer and an expanded range of HA density (0–1860 mg HA/cm³) inclusive of characteristic levels of BMD in cortical bone or TMD in cortical and trabecular bone. This HA-polymer composite phantom exhibited a nonlinear relationship between x-ray attenuation and HA density, rather than the linear relationship typically employed *a priori*, and obviated the need for extrapolation, when calibrating the measured x-ray attenuation to high levels of mineral density. Therefore, the new HA-polymer phantom resulted in more accurate measure-

ment of micro-CT equivalent BMD and TMD in human cortical bone specimens compared to a conventional phantom, as verified by ash density measurements on the same specimens.

ACKNOWLEDGMENTS

This research was supported by the U.S. Army Medical Research and Materiel Command (Contract No. W81XWH-06-1-0196) through the Peer Reviewed Medical Research Program (Contract No. PR054672) and a Lilly Presidential Fellowship from the University of Notre Dame. The authors thank Andres Laib of Scanco Medical AG for helpful conversations regarding this work.

- ^{a)} Author to whom correspondence should be addressed. Electronic mail: rroeder@nd.edu; Telephone: (574) 631-7003; Fax: (574) 631-2144.
- ¹ P. Ammann and R. Rizzoli, "Bone strength and its determinants," *Osteoporosis Int.* **14**, S13–S18 (2003).
- ² J. D. Currey, "The effect of porosity and mineral content on Young's modulus of elasticity of compact bone," *J. Biomech.* **21**(2), 131–139 (1988).
- ³ M. B. Schaffler and D. B. Burr, "Stiffness of compact bone: Effects of porosity and density," *J. Biomech.* **21**(1), 13–16 (1988).
- ⁴ J. Y. Rho, M. C. Hobatho, and R. B. Ashman, "Relations of mechanical properties to density and CT numbers in human bone," *Med. Eng. Phys.* **17**(5), 347–355 (1995).
- ⁵ C. J. Hernandez, G. S. Beaupré, T. S. Keller, and D. R. Carter, "The influence of bone volume fraction and ash fraction on bone strength and modulus," *Bone (Osaka)* **29**(1), 74–78 (2001).
- ⁶ O. Akkus, F. Adar, and M. B. Schaffler, "Age-related changes in physicochemical properties of mineral crystals are related to impaired mechanical function of cortical bone," *Bone (Osaka)* **34**, 443–453 (2004).
- ⁷ J. M. Deuerling, W. Yue, A. A. Espinoza Orías, and R. K. Roeder, "Specimen-specific multiscale model for the anisotropic elastic constants of human cortical bone," *J. Biomech.* **42**(13), 2061–2067 (2009).
- ⁸ R. D. Bloebaum, J. G. Skedros, E. G. Vajda, K. N. Bachus, and B. R. Constantz, "Determining mineral content variations in bone using back-scattered electron imaging," *Bone (Osaka)* **20**, 485–490 (1997).
- ⁹ P. Roschger, E. P. Paschalis, P. Fratzl, and K. Klaushofer, "Bone mineralization density distribution in health and disease," *Bone (Osaka)* **42**, 456–466 (2008).
- ¹⁰ G. Boivin and P. J. Meunier, "The degree of mineralization of bone tissue measured by computerized quantitative contact microradiography," *Calcif. Tissue Int.* **70**, 503–511 (2002).
- ¹¹ C. Schmidt, M. Priemel, T. Kohler, A. Weusten, R. Müller, M. Amling, and F. Eckstein, "Precision and accuracy of peripheral quantitative computed tomography (pQCT) in the mouse skeleton compared with histology and microcomputed tomography (microCT)," *J. Bone Miner. Res.* **18**, 1486–1496 (2003).
- ¹² S. Nuzzo, F. Peyrin, P. Cloetens, J. Baruchel, and G. Boivin, "Quantification of the degree of mineralization of bone in three dimensions using synchrotron radiation microtomography," *Med. Phys.* **29**, 2672–2681 (2002).
- ¹³ G. J. Kazakia, A. J. Burghardt, S. Cheung, and S. Majumdar, "Assessment of bone tissue mineralization by conventional x-ray microcomputed tomography: Comparison with synchrotron radiation microcomputed tomography and ash measurements," *Med. Phys.* **35**(7), 3170–3179 (2008).
- ¹⁴ A. J. Burghardt, G. J. Kazakia, A. Laib, and S. Majumdar, "Quantitative assessment of bone tissue mineralization with polychromatic micro-computed tomography," *Calcif. Tissue Int.* **83**, 129–138 (2008).
- ¹⁵ R. J. Fajardo, E. Cory, N. D. Patel, A. Nazarian, A. Laib, R. K. Manoharan, J. E. Schmitz, J. M. DeSilva, L. M. MacLachy, B. D. Snyder, and M. L. Bouxsein, "Specimen size and porosity can introduce error into μ CT-base tissue mineral density measurements," *Bone (Osaka)* **44**, 176–184 (2009).
- ¹⁶ L. Mulder, J. H. Koolstra, and T. M. G. J. Van Eijden, "Accuracy of microCT in the quantitative determination of the degree and distribution of mineralization in developing bone," *Acta Radiol.* **45**(7), 769–777 (2004).
- ¹⁷ A. Nazarian, B. D. Snyder, D. Zurakowski, and R. Müller, "Quantitative micro-computed tomography: A non-invasive method to assess equivalent bone mineral density," *Bone (Osaka)* **43**, 302–311 (2008).
- ¹⁸ J. A. Meganck, K. M. Kozloff, M. M. Thornton, S. M. Broski, and S. A. Goldstein, "Beam hardening artifacts in micro-computed tomography scanning can be reduced by x-ray beam filtration and the resulting images can be used to accurately measure BMD," *Bone (Osaka)* **45**, 1104–1116 (2009).
- ¹⁹ S. Schweizer, B. Hattendorf, P. Schneider, B. Aeschlimann, L. Gaukler, R. Müller, and D. Günther, "Preparation and characterization of calibration standards for bone density determination by micro-computed tomography," *Analyst (Cambridge, U.K.)* **132**, 1040–1045 (2007).
- ²⁰ W. Zou, J. Gao, A. S. Jones, N. Hunter, and M. V. Swain, "Characterization of a novel calibration method for mineral density determination of dentine by x-ray micro-tomography," *Analyst (Cambridge, U.K.)* **134**, 72–79 (2009).
- ²¹ R. K. Roeder, M. S. Sproul, and C. H. Turner, "Hydroxyapatite whiskers provide improved mechanical properties in reinforced polymer composites," *J. Biomed. Mater. Res.* **67A**(3), 801–812 (2003).
- ²² W. Yue and R. K. Roeder, "Micromechanical model for hydroxyapatite whisker reinforced polymer biocomposites," *J. Mater. Res.* **21**(8), 2136–2145 (2006).
- ²³ W. Suchanek, H. Sada, M. Yashimi, M. Kakihana, and M. Yoshimura, "Biocompatible whiskers with controlled morphology and stoichiometry," *J. Mater. Res.* **10**(3), 521–529 (1995).
- ²⁴ Powder Diffraction File Card No. 09-0432, $\text{Ca}_5(\text{PO}_4)_3\text{OH}$, hydroxylapatite (JCPDS–International Center for Diffraction Data, Newton Square, PA, 1997).
- ²⁵ ASTM Standard C 373-88, "Standard test method for water absorption, bulk density, apparent porosity, and apparent specific gravity of fired whiteware products" (American Society for Testing and Materials, West Conshohocken, PA, 1999), pp. 119–120.
- ²⁶ R. B. Ashman, S. C. Cowin, W. C. Van Buskirk, and J. C. Rice, "A continuous wave technique for the measurement of the elastic properties of cortical bone," *J. Biomech.* **17**(5), 349–361 (1984).
- ²⁷ X. Wang, R. A. Bank, J. M. TeKoppele, and C. M. Agrawal, "The role of collagen in determining bone mechanical properties," *J. Orthop. Res.* **19**, 1021–1026 (2001).
- ²⁸ *CRC Handbook of Chemistry and Physics*, edited by D. R. Lide (CRC, Boca Raton, FL, 1993), pp. 4–88.
- ²⁹ W. A. Kalender and C. Suess, "A new calibration phantom for quantitative computed tomography," *Med. Phys.* **14**(5), 863–866 (1987).
- ³⁰ S. Prevrhal, K. Engelke, and W. A. Kalender, "Accuracy limits for the determination of cortical width and density: The influence of object size and CT imaging parameters," *Phys. Med. Biol.* **44**, 751–764 (1999).
- ³¹ J. H. Siewerdsen, M. J. Daly, B. Bakhtiar, D. J. Mosely, S. Richard, H. Keller, and D. A. Jaffray, "A simple, direct method for x-ray scatter estimation and correction in digital radiography and cone-beam CT," *Med. Phys.* **33**, 187–197 (2006).
- ³² J. S. Bauer, T. M. Link, A. Burghardt, T. D. Henning, D. Mueller, S. Majumdar, and S. Prevrhal, "Analysis of trabecular bone structure with multidetector spiral computed tomography in a simulated soft-tissue environment," *Calcif. Tissue Int.* **80**, 366–373 (2007).

Functionalized Gold Nanoparticles for Targeted Labeling of Damaged Bone Tissue in X-Ray Tomography

¹Ross, R D; ⁺¹Roeder, R K

⁺University of Notre Dame, Notre Dame, IN
rroeder@nd.edu

INTRODUCTION:

Conventional methods used to image and quantify microdamage accumulation in bone are limited to thin histological sections, which are inherently invasive, destructive, tedious and two-dimensional [1]. Recent studies have begun to investigate methods for non-destructive, three-dimensional (3-D) detection and imaging of microdamage in bone tissue. The presence, spatial location and accumulation of fatigue microdamage in cortical and trabecular bone specimens was non-destructively detected using micro-CT after staining with barium sulfate [2-4]; however, specimens were stained *in vitro* via a precipitation reaction which was non-specific to damage and not biocompatible. Therefore, gold nanoparticles (Au NPs) were investigated as a potential damage-specific X-ray contrast agent due to their relative biocompatibility, ease of surface functionalization, colloidal stability, and high X-ray attenuation.

METHODS:

Au NPs were prepared from HAuCl₄·3H₂O and trisodium citrate dihydrate to a mean particle size of ~20 nm at [Au] ~0.5 mM using the citrate reduction method [5]. As-prepared Au NPs were functionalized by adding 1 mL of 0.01 M solution of either glutamic acid, 2-aminoethylphosphonic acid or alendronate, which exhibit a primary amine for binding gold opposite carboxylate, phosphonate or bisphosphonate groups, respectively, for targeting calcium (Fig. 1). Excess functionalization molecules were removed by dialysis. Samples were characterized by TEM, DLS, FT-IR, UV-vis, and zeta potential.

Binding affinity to a synthetic mineral analog was investigated by incubating hydroxyapatite crystals in DI water or FBS solutions containing functionalized Au NPs. The supernatant solution was collected after centrifugation and the gold concentration was measured using ICP-OES. Binding constants were derived using a half-reciprocal linearization of Langmuir isotherms. Specificity for labeling damaged bone tissue was demonstrated with bovine cortical bone specimens by masking machining damage with calcein, scratching the surface with a scalpel, and soaking in functionalized Au NP solutions. Scratched specimens were characterized using optical microscopy and backscattered SEM combined with EDS.

Fatigue microdamage labeled by functionalized Au NPs was imaged by X-ray tomography at 2.5 μ m resolution using a synchrotron light source at multiple energy levels just above and below the L_{III} edge of gold (11.918 keV). Specimens were sectioned from the femoral mid-diaphyses of a 58 year old female donor, turned down to a 1.5 mm diameter by 2.5 mm gauge length using a CNC mini-lathe, and prestained in calcein to mask machining damage. Specimens were loaded in cyclic uniaxial tension to a 10% reduction in secant modulus.

RESULTS:

Functionalized Au NPs were stable in physiological solutions and retained a mean particle size of ~20 nm in TEM (Fig. 2a), but the mean hydrodynamic diameter measured by DLS increased approximately two-fold, indicating the presence of functional groups. Binding constants for functionalized Au NPs in water were 3.82, 0.72 and 0.25 mg/L for alendronate, glutamic acid and phosphonic acid respectively, corresponding to a maximum of 7.33, 1.22 and 0.48 mg Au NPs bound per gram of hydroxyapatite. Thus, alendronate functionalized Au NPs exhibited the greatest specificity, as expected, and consequently provided the most visible labeling of damaged tissue (Fig. 2b,c). Fatigue microcracks labeled with bisphosphonate functionalized Au NPs were able to be detected by synchrotron X-ray tomography (Fig. 3).

DISCUSSION:

Functionalized Au NPs were prepared as a deliverable, damage-specific X-ray contrast agent. Bisphosphonate functionalized Au NPs exhibited the strongest binding affinity, followed by glutamic acid and phosphonic acid, which was in agreement with previous studies that investigated the hydroxyapatite binding affinity of modified proteins [6]. The small size (~20 nm) and colloidal stability of functionalized Au NPs enabled the contrast agent to readily diffuse into cortical bone tissue, which suggests that the contrast agent is deliverable. Diffusion was

verified by epifluorescence after conjugating Au NPs with fluorescein. However, due to the small size (~20 nm) and concentration required for deliverability and biocompatibility, damaged tissue labeled with functionalized Au NPs has not yet been detected using a commercially available polychromatic micro-CT scanner.

Detection of damage tissue labeled with functionalized Au NPs has thus far required a high resolution synchrotron light source to tune the energy of monochromatic X-rays to the L_{III} edge of gold. Therefore, the results of this study suggest that the ambitious goal of non-invasive (*in vivo*) imaging of microdamage in bone could be feasible with significant improvements in commercial scientific and clinical CT instruments. Moreover, a biocompatible, deliverable, damage-specific contrast agent with greater x-ray attenuation than bone could enable clinical assessment of bone quality and damage accumulation, and scientific study of damage processes *in situ*.

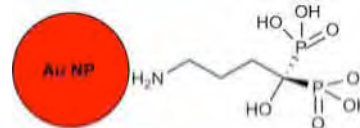


Fig. 1. Schematic diagram showing a Au NP surface functionalized with alendronate (not to scale). Note that the primary amine binds to the Au NP surface and is opposite bisphosphonate groups which bind to exposed bone mineral surfaces in damaged tissue.

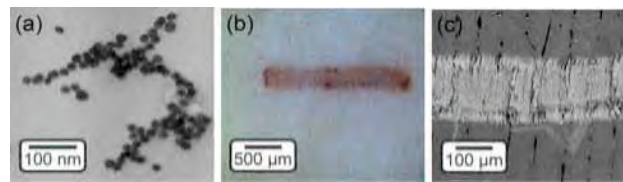


Fig. 2. (a) TEM micrograph of bisphosphonate functionalized Au NPs with a mean particle size of ~20 nm. (b) Optical micrograph and (c) backscattered SEM micrograph of a scratch on the surface of bovine cortical bone, where the red color and brightness, respectively, indicates targeted labeling by bisphosphonate functionalized Au NPs.

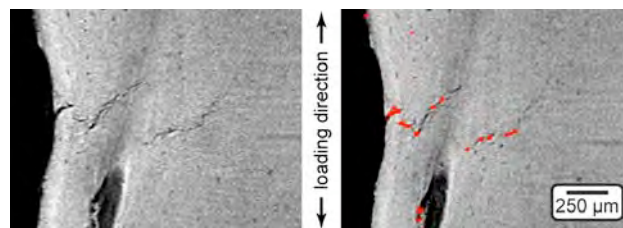


Fig. 3. Synchrotron x-ray tomography images of longitudinal cross-sections from a human cortical bone specimen loaded in cyclic uniaxial tension to a 10% reduction in secant modulus showing microcracks labeled by bisphosphonate functionalized Au NPs (red). The image on the left was taken at 12.018 keV, just above the L_{III} edge for gold, and the image on the right was generated by overlaying in red the subtraction of images taken above and below the L_{III} edge.

ACKNOWLEDGEMENTS:

This research was supported by the U.S. Army Medical Research and Materiel Command (W81XWH-06-1-0196) through the Peer Reviewed Medical Research Program (PR054672). Use of the Advanced Photon Source at Argonne National Laboratory was supported by the U.S. Department of Energy (DE-AC02-06CH11357).

REFERENCES:

- [1] Lee TC, *et al.*, *J. Anat.*, 203:161-172, 2003. [2] Wang, *et al.*, *J. Biomechanics*, 40:3397-3403, 2007. [3] Leng H, *et al.*, *J. Mech. Behav. Biomed. Mater.*, 1:68-75, 2008. [4] Landrigan MD, *et al.*, *Trans. Orthop. Res. Soc.*, 34:2143, 2009. [5] Turkevich J, *et al.*, *Discuss. Faraday Soc.* 11:55-75, 1951. [6] Uludag H, *et al.*, *Biotech. Progr.*, 16:258-267, 2000.

**Detection of fatigue microdamage in whole rat femora
using contrast-enhanced micro-computed tomography**

Travis L. Turnbull and Ryan K. Roeder

Department of Aerospace and Mechanical Engineering
University of Notre Dame
Notre Dame, IN 46556, USA

Submitted to: *Journal of Biomechanics*

Running Title: Micro-CT of whole bone fatigue microdamage

Keywords: Barium Sulfate; Contrast Agent; Fatigue Microdamage; Micro-Computed Tomography

Correspondence: Ryan K. Roeder, Ph.D.
Associate Professor
Department of Aerospace and Mechanical Engineering
Bioengineering Graduate Program
148 Multidisciplinary Research Building
Notre Dame, Indiana 46556

Phone: (574) 631-7003
Fax: (574) 631-2144
Email: rroeder@nd.edu

Funding Sources: U.S. Army Medical Research and Materiel Command (W81XWH-06-1-0196) through the Peer Reviewed Medical Research Program (PR054672)

Abstract

Microdamage in bone tissue results from repetitive mechanical loading, and the accumulation of microdamage has been implicated with increased fracture susceptibility, including stress fractures in active individuals and fragility fractures in the elderly. Conventional methods used to detect microdamage in bone are limited to thin histological sections, which are inherently invasive, destructive, tedious and two-dimensional. Contrast-enhanced micro-computed tomography was recently demonstrated to enable non-destructive, three-dimensional (3-D) detection of the presence, location and accumulation of microdamage in cortical and trabecular bone specimens *in vitro*. However, these prior studies only investigated machined specimens. Therefore, the objective of this study was to detect the presence, spatial location, and accumulation of fatigue microdamage in whole rat femora using micro-computed tomography (micro-CT) with a BaSO₄ contrast agent. Microdamage was detected and observed to vary spatially in all femora loaded in cyclic three-point bending to a 5 or 10% reduction in secant modulus after staining with BaSO₄ and non-destructively imaging with micro-CT. The ratio of the BaSO₄ stain volume (SV) to total volume (TV) was adopted as a measure of damage. The amount of microdamage measured by micro-CT (SV/TV) was significantly greater for both loaded groups compared to the control group ($p < 0.05$), but the difference between loaded groups was not statistically significant ($p > 0.4$). Limitations of this study included the non-specific and non-biocompatible nature of the BaSO₄ stain, as well as the large intra-group variability of SV/TV. Despite its limitations, this study demonstrated the non-destructive, 3-D microdamage detection capability of contrast-enhanced micro-CT for whole rat femora.

1. Introduction

Microdamage can accumulate in cortical bone tissue with aging and/or repetitive mechanical loading (Schaffler et al., 1995; Burr et al., 1997; Norman and Wang, 1997; O'Brien et al., 2003). The accumulation of microdamage in machined specimens *in vitro* has been shown to adversely affect mechanical properties, including the elastic modulus (Schaffler et al., 1989; Pattin et al., 1996) and fracture toughness (Norman et al., 1998), among others. Therefore, microdamage has been implicated with increased fracture susceptibility, including stress fractures in active individuals, fragility fractures in the elderly, and the effects of long-term antiresorptive treatments for osteoporosis (Burr et al., 1997; Chapurlat and Delmas, 2009). However, relatively few studies have investigated microdamage accumulation in whole bones, no matter whether loaded *in vitro* (Forwood and Parker, 1989; Burr et al., 1998) or *in vivo* (Silva et al., 2006; Uthgenannt and Silva, 2007).

Microdamage in bone tissue is conventionally imaged and quantified using histological sections, which are inherently invasive, destructive, tedious and two-dimensional (Lee et al., 2003). A non-destructive, three-dimensional (3-D) method would enable correlation of the spatial location and accumulation of microdamage with spatial variations in the mechanical loading (magnitude and stress state), bone mineral density, microarchitecture, and morphology of whole bones. Moreover, a non-destructive, 3-D damage assessment technique could also reduce the time and labor required for current histological methods.

Contrast-enhanced micro-computed tomography (micro-CT) was recently demonstrated to enable non-destructive, 3-D detection of the presence, spatial location, and accumulation of microdamage in cortical and trabecular bone specimens *in vitro* (Wang et al., 2007; Leng et al., 2008; Landrigan et al., 2011). Furthermore, measurements of damage accumulation by contrast-

enhanced micro-CT were strongly correlated ($p < 0.05$) with measurements by conventional histology using basic fuchsin, validating the new methods (Landrigan et al., 2011). However, previous studies using contrast-enhanced micro-CT have only investigated machined specimens. Therefore, the objective of this study was to detect the presence, spatial location, and accumulation of fatigue microdamage in whole rat femora using micro-CT with a BaSO₄ contrast agent. Whole rat femora were loaded in cyclic three-point bending *in vitro* to predetermined levels of secant modulus degradation, stained with BaSO₄, and imaged by micro-CT to measure levels of damage.

2. Materials and Methods

2.1 Specimen Preparation

Fresh-frozen hind limbs were obtained from eighteen mature Wistar rats exhibiting no skeletal pathology. All protocol were approved by the Institutional Animal Care and Use Committee at the University of Notre Dame. Femora were excised from right and left hind limbs, cleaned of all soft tissue, and randomly divided into a non-loaded control group and two loaded groups ($n = 10/\text{group}$). Specimens were stored at $\sim 20^{\circ}\text{C}$ in airtight containers containing an equal parts mixture of phosphate buffered saline (PBS) and ethanol during interim periods.

2.2 Fatigue Loading

Whole rat femora were thawed and rehydrated at ambient temperature for 24 h prior to mechanical loading. Femora were loaded in cyclic three-point bending at 2 Hz under load control on an electromagnetic test instrument (Bose ElectroForce 3300, Bose Corp., Eden Prairie, MN) in a PBS bath at ambient temperature until achieving a 5 or 10% reduction in the

secant modulus. The loading fixture employed a fixed support span of 14.5 mm and a concave, constant radius ($R = 2.5$ mm) upper load support which approximated the curvature of the diaphysis (Fig. 1). The lower supports were cylindrical with a 4 mm diameter and the upper load support had a major and minor diameter of 9 mm and 4 mm, respectively. Specimens were preconditioned (Tami et al., 2003) with a 27 N static compressive load sustained for 5 min, followed by cyclic three-point bending with a sinusoidal waveform at 2 Hz between a minimum and maximum load of 18 N and 36 N, respectively. The secant modulus measured from the final hysteresis loop during cyclic preconditioning was used to calculate the maximum fatigue load normalized to an initial maximum strain of $8,000 \pm 825$ microstrain. Flexural strains were approximated as $\varepsilon = 6\delta d/L^2$ (Turner and Burr, 1993; Moreno et al., 2006), where δ is the vertical deflection at the midspan, d is the specimen diameter and L is the support span. The secant modulus degradation during fatigue loading was calculated as the percent reduction in instantaneous secant modulus at a given number of loading cycles relative to the initial secant modulus. The initial secant modulus was defined as the maximum secant modulus measured in the first 1000 cycles. The total number of loading cycles was recorded upon reaching the predetermined secant modulus degradation for each specimen.

2.3 Contrast-Enhanced Micro-CT

Femora from both the non-loaded control and loaded groups were stained by BaSO₄ precipitation (Landrigan et al., 2011). Specimens were soaked in a solution of equal parts acetone, PBS, and 0.5 M BaCl₂ (certified ACS crystal, Fisher Scientific, Fair Lawn, NJ) in DI water for 3 d, followed by a solution of equal parts acetone, PBS, and 0.5 M Na₂SO₄ (anhydrous powder, Fisher Scientific, Fair Lawn, NJ) in DI water for 3 d, both under vacuum (~50 mm Hg). Specimens were rinsed with DI water after each step to minimize particles or ions on specimen

surfaces. The staining mechanism was a precipitation reaction where $\text{BaCl}_2(\text{aq}) + \text{Na}_2\text{SO}_4(\text{aq}) \rightarrow \text{BaSO}_4(\text{s}) + 2\text{NaCl}(\text{aq})$. Barium and sulfate ions diffused into, and concentrated within, void space in the tissue—e.g., microcracks, damaged tissue and vasculature—which provided an abundance of heterogeneous nucleation sites for precipitation on tissue surfaces (Leng et al., 2008).

An 8.5 mm segment of the femoral diaphysis, centered about the midspan from three-point bending, was imaged using micro-CT (μCT -80, Scanco Medical AG, Brüttisellen, Switzerland) at 10 μm resolution, 70 kVp voltage, 114 μA current, and 400 ms integration time with slices oriented transverse to the diaphysis. Selected specimens were also imaged by micro-CT after fatigue loading but prior to staining in order to determine whether micro-CT could detect microdamage without the contrast agent. Gray-scale images were smoothed by a Gaussian filter with sigma = 1.5 and support = 3. The total volume (TV) of cortical bone, inclusive of tissue porosity and exclusive of medullary volume, was measured after contouring the endosteal and periosteal surfaces (Fig. 2). The ratio of the BaSO_4 stain volume (SV) to TV (SV/TV) was adopted as a measure of damage. High intensity voxels representative of SV were segmented at a constant global threshold of 730, corresponding to a mean linear attenuation coefficient of 5.84 cm^{-1} or $\sim 3340 \text{ mg hydroxyapatite per cubic centimeter (mg HA/cm}^3\text{)}$ (Deuerling et al., 2010), which was well above the tissue mineral density of rat cortical bone which was measured in this study to be $\sim 1180 \text{ mg HA/cm}^3$.

Specimens exhibiting the median SV/TV for each group were also imaged using scanning electron microscopy (SEM). Specimens were dehydrated in a graded series of alcohol solutions, embedded in poly(methyl methacrylate), sectioned in the sagittal plane with a diamond wire saw, polished with a series of diamond compounds to a 9 μm finish, washed with ethanol, and coated

with Ir by sputter deposition. Specimens were imaged by SEM using backscattered electron imaging (BEI) at an accelerating voltage of 20 kV and a working distance of ~6 mm (Evo 50, LEO Electron Microscopy Ltd., Cambridge UK). Note that image contrast from backscattered electrons is primarily due to compositional differences in atomic number, with an increasing atomic number resulting in increased intensity. The elemental composition of the stain was verified by electron probe microanalysis (EPMA) using energy dispersive spectroscopy (EDS) (INCA x-sight model 7636, Oxford Instruments America, Concord, MA).

2.5 Statistical Methods

All experimental groups exhibited non-normal distributions of SV/TV and loaded groups exhibited non-normal distributions for the total number of loading cycles. Therefore, SV/TV and the number of loading cycles for experimental groups was compared using Kruskal–Wallis non-parametric analysis of variance (ANOVA) and *post hoc* comparisons were performed using Mann–Whitney U-tests with a Bonferroni correction for multiple comparisons (StatView, SAS Institute Inc., Cary, NC). SV/TV was correlated with the number of loading cycles using linear least squares regression. The level of significance for all tests was 0.05.

3. Results

Microdamage was detected and observed to vary spatially in all femora loaded in cyclic three-point bending after staining with BaSO₄ and non-destructively imaging with micro-CT. Microdamage was labeled by concentrated regions of BaSO₄ stain, which appeared as bright voxels in gray-scale micro-CT images, and was quantified in segmented images (Fig. 2). The spatial variation and accumulation of microdamage was observed in segmented, 3-D micro-CT reconstructions. Of the 10 specimens per experimental group, at least one distinct region of stain

was visible in 8 and 9 specimens loaded to a 5 and 10% degradation in secant modulus, respectively, whereas control specimens exhibited limited segmented stain volume (Fig. 3).

Bright voxels detected by micro-CT were confirmed by BEI to be microcracks and/or diffuse damage labeled with BaSO₄ (Fig. 4). EDS confirmed elevated levels of barium in damaged regions labeled with stain relative to undamaged, unlabeled tissue. Observation of multiple sagittal sections from the median specimen (SV/TV) in both loaded groups revealed that microcracks in the tensile surface of the cortex were predominantly transversely oriented, while microcracks in the compressive cortex were predominantly oriented longitudinally (Fig. 4).

The amount of microdamage measured by SV/TV increased from the non-loaded control group to the loaded groups ($p < 0.005$, Kruskal-Wallis). The mean ratio of BaSO₄ stain volume to the total bone volume (SV/TV) was significantly greater for both loaded groups compared to the control group ($p < 0.05$, Mann-Whitney *U*-test), but the difference between loaded groups was not statistically significant ($p > 0.4$, Mann-Whitney *U*-test) (Fig. 5). A significant difference did not exist between the mean total number of loading cycles for the two loaded groups ($p = 0.17$, Mann-Whitney *U*-test). SV/TV exhibited a weak positive correlation with the number of loading cycles for loaded specimens ($p = 0.08$, $R^2 = 0.16$).

4. Discussion

Microdamage resulting from *in vitro* cyclic three-point bending of rat femora was detected and observed to vary spatially using contrast-enhanced micro-CT with a precipitated BaSO₄ stain. Previous studies (Wang et al., 2007; Leng et al., 2008; Landrigan et al., 2011) have employed similar staining and imaging techniques to investigate microdamage within machined cortical and trabecular bone specimens. The present study demonstrated the ability of established methods to be adapted for microdamage detection within whole rat femora. The

results of the present study are encouraging as a first step toward the study of microdamage in whole human bone using non-destructive methods.

Similar to previous studies (Wang et al., 2007; Leng et al., 2008; Landrigan et al., 2011), BEI verified that the bright voxels in micro-CT images were due to the presence of BaSO₄ stain (Figs. 2-4). Likewise, elevated levels of barium measured by EDS in damaged regions further confirmed BaSO₄ labeling.

Variability in SV/TV (Fig. 5) was attributed to non-specific staining of soft tissue and porosity at or near endosteal surfaces, in addition to variability common to biological specimens. The use of threshold values for the SV less than that used in this study increased differences between the group means but also increased variability for SV/TV (cf., Fig. 5). The lack of an increase in SV/TV between specimens loaded to a 5 and 10% degradation in secant modulus suggested that staining methods adapted from previous studies (Wang et al., 2007; Leng et al., 2008; Landrigan et al., 2011) require further refinement for whole bones and/or the different specimen size. Interestingly, there was little non-specific staining observed on periosteal surfaces, most likely due to the periosteum. This observation contrasted the results of previous studies where machined specimens were prone to non-specific staining on exterior surfaces (Leng et al., 2008; Landrigan et al., 2011).

In the present study, cyclic three-point bending was used to generate microdamage despite known issues with cyclic bending tests (Landrigan and Roeder, 2009). The complex geometry of the rat femora necessitated a simple, reproducible test setup which was afforded by the three-point bending fixture. During preliminary testing, the original upper load support was found to leave an indentation in the specimen; therefore, a new upper load support was designed and manufactured to more closely approximate the curvature of the diaphysis (Fig. 1). The

modified upper load support alleviated the indentation issues; however, given the inherent differences in specimen geometry, the load support was unable to exactly match the curvature of each femur which led to variable contact and produced inconsistent staining in the region of the load support. The lower supports were not found to exhibit the same indentation issues as the upper load support, and furthermore, the 8.5 mm segment imaged by micro-CT did not include tissue which would have been directly affected by the lower supports.

5. Acknowledgements

This research was supported by the U.S. Army Medical Research and Materiel Command (W81XWH-06-1-0196) through the Peer Reviewed Medical Research Program (PR054672). Fresh-frozen rat hind limbs were kindly provided by Freimann Life Science Center at Notre Dame.

6. References

- Burr, D.B., Forwood, M.R., Fyhrie, D.P., Martin, R.B., Schaffler, M.B., Turner, C.H., 1997. Bone microdamage and skeletal fragility in osteoporotic and stress fractures. *Journal of Bone and Mineral Research* 12, 6-15.
- Burr, D.B., Turner, C.H., Naick, P., Forwood, M.R., Ambrosius, W., Hasan, M.S., Pidaparti, R., 1998. Does microdamage accumulation affect the mechanical properties of bone? *Journal of Biomechanics* 31, 337-345.
- Chapurlat, B.D., Delmas, P.D., 2009. Bone microdamage: a clinical perspective. *Osteoporosis International* 20, 1299-1308.
- Deuerling, J.M., Rudy, D.J., Niebur, G.L., Roeder, R.K., 2010. Improved accuracy of cortical bone mineralization measured by polychromatic microcomputed tomography using a novel high mineral density composite calibration phantom. *Medical Physics* 37, 5138-5145.
- Forwood, M.R., Parker, A.W., 1989. Microdamage in response to repetitive torsional loading in the rat tibia. *Calcified Tissue International* 45, 47-53.
- Landrigan, M.D., Roeder, R.K., 2009. Systematic error in mechanical measures of damage during four-point bending fatigue of cortical bone. *Journal of Biomechanics* 42, 1212-1217.
- Landrigan, M.D., Li, J., Turnbull, T.L., Burr, D.B., Niebur, G.L., Roeder, R.K., 2011. Contrast-enhanced micro-computed tomography of fatigue microdamage accumulation in human cortical bone. *Bone* 48, 443-450.
- Lee, T.C., Mohsin, S., Taylor, D., Parkesh, R., Gunnlaugsson, T., O'Brien, F.J., Giehl, M., Gowin, W., 2003. Detecting microdamage in bone. *Journal of Anatomy* 203, 161-172.
- Leng, H., Wang, X., Ross, R.D., Niebur, G.L., Roeder, R.K., 2008. Micro-computed tomography of fatigue microdamage in cortical bone using a barium sulfate contrast agent. *Journal of the Mechanical Behavior of Biomedical Materials* 1, 68-75.
- Moreno, L.D., Waldman, S.D., Gryn timer, M.D., 2006. Sex differences in long bone fatigue using a rat model. *Journal of Orthopaedic Research* 24, 1926-1932.
- Norman, T.L., Wang, Z., 1997. Microdamage of human cortical bone: Incidence and morphology in long bones. *Bone* 20, 521-525.
- Norman, T.L., Yeni, Y.N., Brown, C.U., Wang, X., 1998. Influence of microdamage on fracture toughness of the human femur and tibia. *Bone* 23, 303-306.
- O'Brien, F.J., Taylor, D., Lee, T.C., 2003. Microcrack accumulation at different intervals during fatigue testing of compact bone. *Journal of Biomechanics* 36, 973-980.

- Pattin, C.A., Calert, W.E., Carter, D.R., 1996. Cyclic mechanical property degradation during fatigue loading of cortical bone. *Journal of Biomechanics* 29, 69-79.
- Schaffler, M.B., Radin, E.L., Burr, D.B., 1989. Mechanical and morphological effects of strain rate on fatigue of compact bone. *Bone* 10, 207-214.
- Schaffler, M.B., Choi, K., Milgrom, C., 1995. Aging and matrix microdamage accumulation in human compact bone. *Bone* 17, 521-525.
- Silva, M.J., Uthgenannt, B.A., Rutlin, J.R., Wohl, G.R., Lewis, J.S., Welch, M.J., 2006. In vivo skeletal imaging of ¹⁸F-fluoride with positron emission tomography reveals damage- and time-dependent responses to fatigue loading in the rat ulna. *Bone* 39, 229-236.
- Tami, A.E., Nasser, P., Schaffler, M.B., Knothe Tate, M.L., 2003. Noninvasive fatigue fracture model of the rat ulna. *Journal of Orthopaedic Research* 21, 1018-1024.
- Turner, C.H., Burr, D.B., 1993. Basic biomechanical measurements of bone: a tutorial. *Bone* 14, 595-608.
- Uthgenannt, B.A., Silva, M.J., 2007. Use of the rat forelimb compression model to create discrete levels of bone damage in vivo. *Journal of Biomechanics* 40, 317-324.
- Wang, X., Masse, D.B., Leng, H., Hess, K.P., Ross, R.D., Roeder, R.K., Niebur, G.L., 2007. Detection of trabecular bone microdamage by micro-computed tomography. *Journal of Biomechanics* 40, 3397-3403.

Figure Captions

Fig. 1. Schematic diagram showing a segmented micro-CT reconstruction of a whole rat femur loaded in cyclic three-point bending with concave upper load support.

Fig. 2. Gray-scale and corresponding segmented micro-CT images for transverse cross-sections of a non-loaded control specimen, and femora loaded in cyclic three-point bending to a 5 and 10% reduction in secant modulus, showing regions labeled by BaSO₄ (bright voxels). Note that the images shown correspond to the midspan of the median specimen (SV/TV) in each group.

Fig. 3. Segmented, 3-D reconstructions of a non-loaded control specimen and a specimen loaded to a 5% degradation in secant modulus. A region of microdamage labeled by BaSO₄ was observed at the midspan on the tensile surface of all but three loaded specimens. Note that the loaded specimen is oriented such that the front surface was loaded in tension.

Fig. 4. Scanning electron micrographs using BEI showing (A) a longitudinal (coronal) microcrack on the compressive, periosteal surface and (B) a transverse microcrack (arrow) on the tensile, periosteal surface for the median (SV/TV) specimen loaded to a (A) 5 and (B) 10% reduction in secant modulus.

Fig. 5. The ratio of BaSO₄ stain volume to total volume (SV/TV) measured in segmented micro-CT images was increased for loaded groups compared to the non-loaded control group. Error bars show one standard deviation. * $p < 0.05$, Mann-Whitney U -test versus control.

